Doctoral Thesis


# Identification of singularities in the displacement field for damage detection in structures.

**Author:** Qiaoyu Ma
**Director:** Mario Solís Muñiz

Department of Continuum Mechanics and Structural Analysis
School of Engineering
University of Seville

Sevilla, 2019

Tesis Doctoral

# Identification of singularities in the displacement field for damage detection in structures.


Autor:

**Qiaoyu Ma**


A thesis submitted for the degree of
*Doctor of Philosophy*


Director:

**Mario Solís Muñiz**
Profesor Titular

Departamento de Mecánica de Medios Continuos y Teoría de Estructuras
Escuela Técnica Superior de Ingeniería
Universidad de Sevilla


2019

Tesis Doctoral: Identification of singularities in the displacement field for damage detection in structures.

Autor: Qiaoyu Ma
Director: Mario Solís Muñiz

El tribunal nombrado para juzgar la Tesis arriba indicada, compuesto por los siguientes doctores:

Presidente:

Vocales:

Secretario:

acuerdan otorgarle la calificación de:

El Secretario del Tribunal

Fecha:

# Preface

The present Ph.D. thesis has been completed during my Ph.D. study from June 2016 to May 2019 at the Department of Continuum Mechanics and Structural Analysis, University of Seville. It has been submitted for assessment in partial fulfillment of the requirements for the Ph.D. degree. The thesis is based on the five accepted or published scientific papers listed as follows. Parts of the papers are used directly or indirectly in the extended summary of the thesis. Some unpublished results are also included. As part of the assessment, co-author statements have been made available to the assessment committee and are also available at the Faculty. The thesis is not in its present form acceptable for open publication but only in limited and closed circulation as copyright may not be ensured.

The present thesis consists of the following five papers, listed in the chronological order of the conducted research:

A Solís, M., **Ma, Q.**, Galvín, P. (2018). "Damage detection in beams from modal and wavelet analysis using a stationary roving mass and noise estimation", *Strain*. 2018:e12266

B **Ma, Q.** and Solís, M. (2017). "Damage localization and quantification in simple supported beams using static test data", *Journal of Physics: Conference Series* 842 012007

C **Ma, Q.** and Solís, M. (2018). "Damage localization and quantification in beams from slope discontinuities in static deflections", *Smart Structures and Systems*, 22(3):291-302.

D **Ma, Q.** and Solís, M. (*accepted*). "Multiple damage identification in beams from full-field digital photogrammetry", *Journal of Engineering Mechanics.*

E **Ma, Q.** and Solís, M. (*accepted*). "Application of wavelet analysis for crack localization and quantification in beams using static deflections", *Lecture Notes in Mechanical Engineering*

*Qiaoyu Ma*
*Seville, 2019*

*A mi familia*
*To my family*
獻給我的家人

# Agradecimientos

En primer lugar, deseo expresar mi sincero agradecimiento al director de esta tesis doctoral, Mario Solís Muñiz, por su tiempo, dedicación, y consejos. Igualmente agradecer al tutor de la misma, Andrés Sáez Pérez, su disponibilidad en todo momento y los apoyos prestados.

He de expresar mi más sincero agradecimiento al Profesor Dionisio Bernal por haberme acogido en el *Structural Dynamics and System Identification Laboratory, Department of Civil and Environmental Engineering, Northeastern University, Boston, E.E.U.U.* y, también, antes de esta, por su dedicación y apoyo en mi Master Report. Además, fue él quien me presentó a Profesor Solís en IMAC XXXII en Orlando, E.E.U.U., 2014.

Este agradecimiento es extensible a la Consejería de Economía, Innovación, Ciencia y Empleo de Andalucía (Junta de Andalucía) por financiar el proyecto P12-TEP-2546 y las actividades academicas.

Gracias a todos mis amigos y aquellos con los que he trabajado durante estos años por sus ayudas en el idioma, cultura y muchas cosas más en la vida en España.

Pero sobre todo, quisiera agradecer a mis padres por su inmenso apoyo incondicional todo los años y sin el cual esta tesis nunca se habría escrito.

*Qiaoyu Ma*
*Sevilla, 2019*

# Acknowledgement

First and foremost, I would like to express my sincere gratitude to my advisor Prof. Mario Solís Muñiz for his continuous support, guidance and patience during my Ph.D. study, which made my experience in Spain a rewarding journey. The same to Prof. Andrés Saiz Perez, the tutor of the project. Without their enormous effort, I would not be able to embark on this research project, not to mention finishing it. I am very grateful to have worked for/with them in the past three years.

Special gratitude to Prof. Dionisio Bernal for not only hosting me as a visiting scholar at the *Structural Dynamics and System Identification Laboratory, Department of Civil and Environmental Engineering, Northeastern University, Boston, USA*, but also, before that, supervising my Master research. Additionally, it was Prof. Bernal who introduced me to Prof. Solís on the 32nd IMAC conference at Orlando, USA, in 2014.

The gratitude is extended to the Consejería de Economía, Innovación, Ciencia y Empleo de Andalucía, Spain who funded this research project P12-TEP-2546.

I sincerely appreciate my friends and colleagues for being my Spanish teachers, without whom, many things would be much more difficult.

Last but not the least, I would like to thank my parents for the unconditional love and immense support in my life, without which I would never achieved what I have today.

*Qiaoyu Ma*
*Seville, 2019*

# 致謝

首先衷心感謝我的博士生導師，馬里奧·索利斯 教授，在學業研究上對我的耐心指導與支持，以及對我在西班牙生活中的幫助與照顧。同時也感謝博士研究項目的負責人，安德烈斯·塞斯 教授，在整個博士研究期間提供的各種支持。很榮幸能夠與兩位共事並得到兩位的指導。

特別感謝我的碩士生導師，丹尼斯·伯爾納 教授，接受我去美國東北大學土木與環境學院結構動力實驗室做訪問學者。他對我在科研方面的指導（包括碩士學習期間）使我受益匪淺。二〇一四年參加第卅二屆結構動力學論壇期間，在他的介紹下與 索利斯 教授相識。

感謝安達盧西亞自治州政府對此研究項目(P12-TEP-2546)，以及相關學術活動提供的經濟資助。

此外，由衷的感謝在西班牙旅居期間遇到的各位好友和同僚，感謝他們對我在西班牙語學習上的幫助。

最後，感謝我的父母，對我在學術追求上的無條件支持，我今天的成就離不開他們的付出。

馬喬宇
貳零壹玖年于塞維利亞

# Abstract

In this thesis, the damage identification problem in beam-type structures through the displacement field and the relevant challenges are studied. The exploration includes one damage localization approach using mode shapes and two damage identification methodologies based on static measurements. The premise is that concentrated cracks introduce singularities in the displacement fields.

The first study on the detecting and locating damage using mode shapes with wavelet analysis is called the *Mode Shape-Wavelet* approach. The focus is to enhance the sensitivity of the wavelet coefficient to damage. An auxiliary mass was used in the experimental tests to probe the dynamic characteristics of the beam. The wavelet coefficient of all mode shapes and mass locations are combined as the damage localization indicator. Additionally, a weighting parameter which evaluates the noise effect is formulated into the calculation. The approach is tested with experimental mode shapes of a cantilever beam obtained by a set of accelerometers.

The investigation using static measurements is based on the deflection difference of the beam prior and posterior to damage. The associated state of the damaged beam that can produce the deflection variation is derived through a superposition scheme and named the Incremental State. Two damage identification methodologies are explored, namely the *Deflection-Spring* approach and the *Deflection-Wavelet* approach. The *Deflection-Spring* approach models the cracks by discrete rotational springs and locates them by finding the sudden change in the slope of the deflection difference. Furthermore, the crack depths are estimated through a spring characteristic function. In order to obtained reasonable slope change, a trend estimation for denoising purpose is needed. The *Deflection-Wavelet* approach locates the damage with a localization index based on the normalized wavelet coefficient for different scales and estimates the damage with a quantification index developed from the Lipschitz condition. Both methods are tested with experimental data of a simply supported beam. In addition, relevant issues regarding the application in statically indeterminate beams are discussed.

The static deflections of the structure in the laboratory tests were measured by a *Digital Image Correlation* (DIC) system. In the test, a procedure to obtain the whole displacement field of the structure by using partial measurements was explored. The measurements validate this procedure which can facilitate the application for in situ measurement of large scale structures.

Lastly, conclusions are drawn and the direction of possible future work is commented to close the thesis.

# Contents

# 1 Introduction

## 1.1 General background of SHM

In pursuing innovation in Civil/Structural Engineering, new material and novel structural systems are implemented for structures while minimizing the use of material. This leads to the increase of inspection or health monitoring of the structures to avoid catastrophic failure. The common routine inspection methods in the current industrial practice are visual inspection methods using acoustic, ultrasonic, magnet field, radiographs or thermal field [46]. In order to perform such inspections, the proximate locations of the damage should be known and the portion of the structure should be accessible. Due to these limitations, methods that can assess the integrity of structures through global structural responses are desired.

Structural Health Monitoring (SHM), in general consensus, is a system or methodology that can provide an evaluation of the physical status or performance of the structure through measurement data, such as acceleration, velocity, displacement, strain and etc. The process to obtain common structural characteristics, such as stiffness or flexibility matrix, natural frequencies, mode shapes and damping, is called structural system identification. Damage is defined as the change in the structural properties which leads to an adverse influence on the structural responses in service. Although such a change can be either an increase or a decrease of a structural property, generally, the term damage is referred to those that diminish the structural bearing capacity in one way or the other. Needless to say, the propagation of damage will further deteriorate the integrity of the structure and shorten its life expectancy. The objective of SHM is to understand the current state of the structure in order to make appropriate decisions for restoration or demolition.

During the lifespan of structures, their structural properties can be altered by many factors, such as cycling loads, impact loads, corrosion, temperature and etc. Among all the types of damage, cracking is one of the most commonly seen defects in structural engineering. The presence of cracks not only reduces the local stiffness of the structure but also exposes the interior of the structure to the environment, which accelerates the deterioration. It is one of the essential interest in the industry to know the information of such defects at their early stage. The revolved procedures that can acquire the information of such changes with regarded to their existence, locations, quantities and effects on the safety reliability are named damage identification. Generally, damage identification can be divided into four levels [66]:

1. detection: is there any damage?
2. localization: how many and where are they?
3. assessment: how severe are they?
4. consequence: what to do?

## 1.2 Motivation

After decades of research on damage identification, only a small portion of the proposed methods have reached to the level of industrial implementation, mainly due to measurement limits, boundary uncertainties, complexity of the structure or/and the applicability of the method. Depending on the features used in the identification process, the methods can be categorized into:

- dynamic-based methods, where features related to the dynamic characteristics of the structure are used, such as frequencies, mode shapes, damping, operational deflections, time-history response of acceleration, velocity and displacement, thorough fundamental reviews of the developments in this category were presented by Doebling et al. [24], Sohn et al. [68] and Fan and Qiao [26], and
- static-based methods, where static features are applied, for example, deflections and strain, which are less common in the industrial application due to some limits on the applicability of static tests on the full scale structure.

The first level of damage identification, the existence of the damage, is considered a forward problem which can be determined through the change in the structural properties. The primary feature proposed for such purpose was the natural frequency which provides the integrity information of the structure and can be easily and accurately obtained in practice. Although studies indicate that cracked structures have natural frequencies different from their healthy state [38], it has been reported in many cases that they are not sensitive to local stiffness changes unless the damage is severe enough to make an impact on the global stiffness, partly because they are factors of the whole structure and partly because the sensitivity of the modes to damage also depends on the locations of the damage [9, 69]. Some experimental tests of real bridges can be found in References [21, 27].

One way to determine the number of the damage as well as their locations and extents is by solving an inverse problem based on model updating methods which are complex tasks and have a high computational cost. As damage is a local feature, the lack of knowledge of the location demands a large number of candidate parameters [29]. In many cases, the inverse method suffers the difficulties of solving an ill-posed problem whose solutions are not unique. In other words, it is possible that damage at two different locations with different severities cause the same amount of change in the responses or characteristics. The fundamental idea and challenges of model updating method can be found in Reference [54, 67].

Therefore, this thesis focuses on the development of damage identification methodologies based on direct displacement measurements of the structure. Moreover, due to the development of digital photogrammetric measuring system in engineering application, which has facilitated the static response measuring, static deflection is considered a base for the development of the methods. In addition, the use of static measurements has the advantage of achieving the complete estimate of the flexibility matrix, which is essentially difficult for dynamic-based approaches.

## 1.3 Scope of the thesis

The aim of the present thesis is to develop methodologies for detecting, locating and/or assessing single or multiple damage in beams through the displacement field. The behavior of the beam is considered linear for both the states prior and posterior to damage. The damage is assumed to be stable once it is formed and does not propagate during the tests.

### 1.3.1 Damage definition

The target damage is limited to isolated cracks in beams, which can be treated as individual concentrated damage. Capillary and smeared cracks are not included in the scope of this thesis.

This type of damage leads to singularities in the displacement field of the structure at the damage locations. In structures of homogeneous material, cracks form at the maximum stress location, usually at the surface of the structure. If the material is not homogeneous, the formation of cracks is more complex as the profile of the crack, namely the shape, location and propagation direction, is irregular. For simplicity, prismatic steel beams are used in this research. The crack is defined as a regular cut with uniform width and depth through the cross-section. Other names of such artificial cracks, such as slots, notches and transversal cracks, can be found in literature. The damage severity is defined as the crack depth to beam height ratio, which should be treated as an equivalent damage severity since a crack in the regular form as the artificial crack is barely seen in industrial applications.

As mentioned before, damage is defined through the changes in the structural geometry or material properties, which leads to an adverse change in the structural response. In this sense, damage is a relative term defined by comparing two different states of the structure. One is the reference state, which is usually considered undamaged, and the other is the current state, which is commonly assumed to be damaged. Strictly speaking, all damage detection approaches have a reference state as the baseline. The term "non-baseline" in many research articles are based on the assumption that the flexural rigidity distribution of the beam is smooth such that no sudden change in the cross-section or material properties along the length of the beam [81]. If the undamaged beam is homogeneous and has a uniform cross-section, the damaged displacement can be used for identification purpose without introducing the baseline since no other singularities exits in the displacement field. Therefore, to distinguish the newly induced changes in the structural features, the input data is taken as the difference in the structural responses between the reference state and the damaged state, i.e. mode shapes difference and static deflection difference, in this thesis.

### 1.3.2 Damage modelling

In order to accurately assess the damage severity, a relationship between the crack depth and the damage quantification feature is required, which is usually established with some types of models. Comprehensive reviews of crack modelling and stiffness loss modelling approaches were presented by Dimarogonas [23], Ostachowicz and Krawczuk [56], and Friswell [30]. The approaches can be classified into three categories [30]:

**1.** local stiffness reduction;

**2.** discrete spring models;

**3.** complex 2D or 3D models.

The first class is the simplest approach for finite element models that contains complete stiffness reduction of the damaged elements. The accuracy of this approach is related to the mesh density which can be problematic in practice when the location of damage is unknown. Another main issue is to match the stiffness loss to crack depth in the quantification process. The second class of methods is a simplified model used in beam type structures as the structure is divided into two parts connected by a rotational spring at the crack location. In this approach, the crack size, shape and relative location of the cross-section are ignored as well as the shear deformation. The advantage is that the crack severity is directly related to the rotational stiffness of the spring model. Depending on the behavior of the beam, the spring model can be characterized into linear, nonlinear or bilinear for opening crack, closed crack and open-closed crack respectively. Alternatively, more accurate results and estimates of the responses can be obtained through complex 2D or 3D models.

In the present thesis, two types of models are adopted for the quantification purpose in the proposed methodologies. One method uses some characteristic functions of the rotational discrete spring model proposed by other researchers [11, 19, 28, 57, 63] to estimate the crack depth. In the other method, a reference map is obtained through a 3D finite element model of the crack.

## 1.4 Related literature review

For simple beam-type structures, either the static displacement or the modal displacement of the structure can be used for damage identification purpose. The local stiffness loss induced by the crack generates discrepancy in mode shapes and deflections.

Among the mode shape based damage detection features, the Modal Assurance Criterion (MAC) [4] is one of the common index for comparing mode shapes, which indicates the overall difference between two sets of mode shapes through their correlation. However, it is found that, similar to natural frequencies, the MAC is not a sensitive damage indicator since its value between the mode shapes of the pre-damage state and post-damage state is almost unity, which means that the two mode shapes are almost identical from the overall perspective [69]. Pandey [60] first indicated that cracks in beams create discontinuities in the modal curvature and thereby can be used as a damage localization feature. The idea was validated with a numerical case study, in which the damage was modelled by a reduction in the modulus of elasticity of the damaged section and the curvature was calculated by the central difference approximation. The results also showed that although the absolute modal curvature difference indicates the existence and locations of the damage, the absolute modal shape difference fails to provide similar information. Later on, Abdel Wahab and De Roeck [1] applied the idea with experimental data of a real damaged bridge and suggested to average the modal curvature difference over all identified mode shapes in order to reduce the noise influence. Moreover, similar to the modal curvature, it has been pointed out that the slope of mode shapes [3] and their higher order derivatives [80] also contain discontinuities at the damage locations and, therefore, can be used as damage localization indicators as well. However, the use of the modal curvature as damage feature suffers the difficulty of quantifying the crack severity through the discontinuities due to the lack of consistency of the modal curvature difference values for different modes [20]. In addition, for a beam with two individual cracks (multiple damage scenario), the relative relationship of the modal curvature difference of the two cracks can be reverse from one mode to another, that is to say, the modal curvature difference of one crack can be bigger than the other in one mode and smaller than the other in another [7]. This issue can be avoid by using the static response of the structure.

Similar to MAC, the overall difference between the displacements between two states of the beam can be evaluated by the Displacement Assurance Criterion (DAC) [35]. Different from the mode shape difference, the absolute static deflection difference of the beam can clearly disclose the locations of the damage. An elastic damage load theorem (EDLT) can be derived as the shape of displacement variation of a beam due to damage equals to the influence line of the moment on its conjugate beam at the point where the damage occurs [18]. Further, Caddemi and Morassi [12, 13] derived an analytical solution for the deflection difference of a beam with single or multiple cracks using the discrete rotational spring as the damage model. The deflection variation is resulted by applying a set of moments at the damaged locations of the damaged beam. Through the solution, the damage can be located by solving an inverse problem and the extent can be evaluated by using a rotational spring characteristic function.

One of the critical parameters in the use of the static displacement field is the number of measurement points. One common way to solve this issue is by using advanced measuring technologies such as laser scanning measuring systems or optical measuring systems. Moreover, based on the Maxwell Betti's reciprocity theorem, one can also convert the problem from the sparsity of measuring positions to the sparsity of loading positions. In this way, the deflection can be obtained by using only one sensor with a quasi-static moving load traversing from one end of the beam to the other [36, 72]. Furthermore, similar to the mode shapes, the derivatives of the deflection difference can be used for damage localization. One additional advantage of using the derivatives instead of the deflection difference by itself is that they can identify damage at intermediate supports of multi-span beams [71].

In practical applications, another main challenge is the measurement noise which can not only mask the actual singularities in the derivatives due to damage but also result unacceptable error in the derivative calculation by the central difference approach [16]. The actual trend of the displacement data needs to be estimated with proper denoising techniques [1]. The main challenge is that applying a curve fitting algorithm directly to the measurement data tends to smooth the local discontinuities at the damage locations. Alternatively, other methods that can detect the discontinuities directly in the displacement field are used, such as wavelet analysis and Lipschitz exponent [50]. Compared with other digital differentiator filters, the wavelet functions are advantageous in terms of simplicity due to its characteristics [51]. The static deflection [5, 6, 61, 65, 70, 77, 79, 82], mode shapes [14, 15, 17, 32, 40, 42, 64, 69, 76, 83, 85] and operational deflection [87] can be treated as signal in space domain for the wavelet analysis. At the crack locations where discontinuities exist, the wavelet transform coefficients exhibit local maximum values. The issues in the implementation of the wavelet analysis, such as the selection of the mother wavelet function, the number of vanishing moments, the sampling interval, scale numbers, boundary effects, the crack size sensitivity, the mode order sensitivity, etc. can be found in References [31, 39, 43, 52, 53, 61, 62, 73]. However, to the author's knowledge, most of the relevant topics remain opened.

Furthermore, the absolute values of the wavelet coefficients at the damage locations are proposed for damage quantification purpose by comparing with reference values from numerical models [58, 59, 77]. In these applications, a limitation on the use of the reference damage index is the requirement of knowledge about the damage location since the absolute value of the wavelet coefficient depends on the damage location and the scale number. A location independent but scale dependent damage index can be developed based on the static deflection, which is defined as the ratio between the wavelet coefficient at the damage location and its corresponding curvature of the undamaged beam [6]. To avoid the scale dependency, the wavelet coefficients at the damage location can be normalized over selected scales [5]. Another scale independent damage quantification method is to use the Lipschitz condition of the displacement as damage index. At the crack location, the local maximum wavelet coefficient is proportional to the scale in logarithmic form [50]. The slope of this linear relationship which is the Lipschitz exponent can be used to locate and estimate the damage [37]. Later, the intersection of the y-axis of this linear relationship can be used as a damage quantification index [25, 48, 86]. The drawback of these techniques is the reference value for mapping can be only obtained based on the model with the correct damage locations. Although the damage localization always comes before the quantification process, it is still of interest to develop a damage quantification index that is both scale and damage location independent.

Some other damage detection methods based on static displacements can be found in References [2, 10, 22, 33, 47].

## 1.5 Contribution of the thesis

This thesis presents three damage identification methodologies using either the modal displacement measurements or the static deflection measurements, namely the Mode Shape-Wavelet approach, the Deflection-Spring approach and the Deflection-Wavelet approach.

1. The **Mode Shape-Wavelet approach** is a model independent damage localization scheme using wavelet analysis with the mode shape difference, which
    - uses a weighting parameters to consider the noise effect on each measured mode shape;
    - utilizes a stationary roving mass traversing along the beam to alter the dynamic behaviors of the beam [84];
    - locates the damage through a combination of weighted wavelet coefficients of all modes and mass positions.

2. The **Deflection-Spring approach** is a static-based damage identification method with the use of a discrete rotational spring model, which
   - locates the damage at the discontinuities in the slope of the deflection difference;
   - estimates the damage severity by using a rotational spring characteristic functions;
   - requires a trend estimation algorithm for localization purpose.
3. The **Deflection-Wavelet approach** is a damage identification method using wavelet analysis with the static deflection difference, which
   - locates the damage by a damage localization index which takes into account the influence of different scales;
   - develops a damage location, wavelet scale and external load independent damage quantification index based on the linear relationship between the wavelet coefficients and their scales in logarithm form.
   - requires the reference values of the damage quantification index which can be obtained with a 3D finite element model of a beam with the same dimension and boundary conditions.

In addition to these three main contributions, this thesis also tests the feasibility of obtaining whole deflection by the Partial Measurement Procedure in the use of a Digital Image Correlation system for static measurements because it is likely that only parts of the structure can be captured by the measuring system for in situ measurements of a large scale structure [8, 41, 78].

4. The **Partial Measurement Procedure** is an experimental procedure which divides the whole structure into several parts for measuring. The partial measurements are combined to construct the displacement field of the whole structure.

## 1.6 Outline of the thesis

The remainder of the thesis is composed of five chapters that contain the theoretical backgrounds, proposed methodologies and their applications, four appendices that consist of the papers which constitute the body of the thesis and an appendix with the static measurement data. The content of each component is summarized as follows:

**Chapter 2** presents the background of the crack effect in the displacement field as well as two singularity detection techniques, wavelet analysis and the central difference approach.

**Chapter 3** introduces the Mode Shape-Wavelet scheme which proposes a modified wavelet coefficient and the implementation of an auxiliary mass to improve the sensitivity of the method. The scheme is examined based on laboratory tests with a cantilever steel beam with a single crack.

**Chapter 4** presents two static based methodologies, the Deflection-Spring approach and the Deflection-Wavelet approach. An experimental case study of the beam with two different cracks is provided to demonstrate the application and performance of the two methods. The issues in the application of statically indeterminate beams are also discussed.

**Chapter 5** concludes the thesis with a summary and a discussion on the future work.

**Appendix A** contains the paper by Solís, Ma and Galvín (2018), that is "Damage detection in beams from modal and wavelet analysis using a stationary roving mass and noise estimation".

**Appendix B** contains the paper by Ma and Solís (2017), that is "Damage localization and quantification in simply supported beams using static test data".

**Appendix C** contains the paper by Ma and Solís (2018), that is "Damage localization and quantification in beams from slope discontinuities in static deflections".

**Appendix D** contains the paper by Ma and Solís (in press), that is "Multiple damage identification in beams from full-field digital photogrammetry".

**Appendix E** contains the paper by Ma and Solís (2019), that is "Application of wavelet analysis for crack localization and quantification in beams using static deflections".

**Appendix F** contains the static deflection measurements.

**Appendix G** contains the corrections of the errors in the published papers.

# 2 Singularity detection in the displacement field

## 2.1 Continuity and differentiability

A function, $f(x)$, is said to be continuous in interval $[a, b]$ ($a \in \mathbb{R}, b \in \mathbb{R}$) if it satisfies the followings:

$$\lim_{x \to c^-} f(x) = f(c) = \lim_{x \to c^+} f(x) \quad \text{with} \quad a < c < b \tag{2.1}$$

and

$$\begin{aligned} \lim_{x \to a^+} f(x) &= f(a) \\ \lim_{x \to b^-} f(x) &= f(b) \end{aligned} \tag{2.2}$$

to ensure continuity at the boundaries, where superscript signs "$-$" and "$+$" represents the left approach and the right approach, respectively. The function is differentiable at $c \in (a, b)$ if its derivative $f'(c)$ exist, which is defined as:

$$f'(c) = \lim_{h \to 0} \frac{f(c+h) - f(c)}{h} \tag{2.3}$$

The smoothness of the function is classified by its differentiability. The function is said to be of class $C^k$ if its derivatives, $f^{(0)}, f^{(1)}, \cdots, f^{(k)}$, are continuous.

## 2.2 Discontinuity in the displacement field

For beam-type structures, the compatibility (kinematic) of the physics enforces the deformations and mode shapes of the beam to be part of a continuous function in the interval of its dimension.

### 2.2.1 Crack in solid beams

At the location of a crack in a solid beam, the sudden change in the geometry of the beam introduces a local stiffness reduction and consequently leads to a change in the deflection. In the vicinity of the crack, the slope of the deflection and the curvature of the beam change continuously and rapidly within a relative small region named damage affected region (Fig. 2.1).

### 2.2.2 Discrete rotational spring model

From the macro perspective, this affected region of notch type cracks, i.e. regular V-shaped or U-shaped cuts, can be simplified by a rotational spring with a constant rotational constraint (Fig. 2.2).

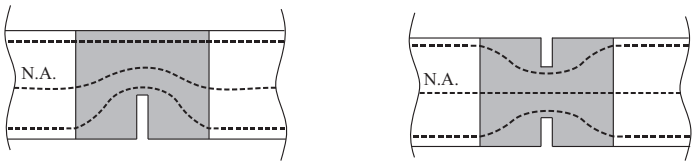


**Figure 2.1** The damage affected region and its stress flow of (a) single-sided crack case; (b) double-sided crack case (N.A. stands for Neutral Axis).

This idealization of the damage can be taken as the beam is split into two segments at the crack location and connected by the spring. The discrete rotational spring model introduces discontinuity in the slope of the deflection at its location and approximates the deflection with a continuous function of class $C^0$. Therefore, the sudden change in the slope of the deflection can be used as a damage indicator.

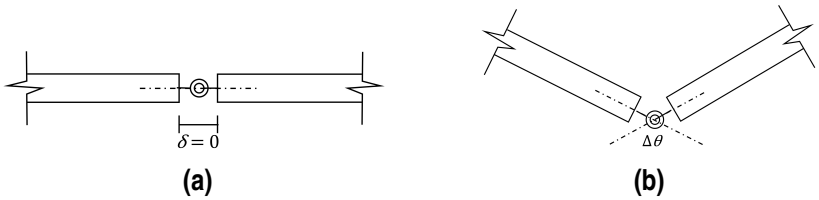


**Figure 2.2** Ideal lumped damage model: (a) undeformed; (b) deformed.

### 2.2.3 Discrete data

In numerical computations, the input function is not known at all coordinate values but is characterized by a uniform sampling which approximates the input function at a resolution that depends upon the sampling interval. When a function is approximated at a finite resolution, strictly speaking, it is not meaningful to speak about discontinuities or singularities. This is illustrated by the fact that through the discrete data, no information in between two points is observed. This condition becomes more critical in practice when experimental measurements are limited by the number of sensors. However, in practice, we still can use mathematical tools that describe discontinuities and singularities. The baseline of applying wavelet analysis in damage detection is that the measured data is a discrete sample set of a continuous function.

## 2.3 Wavelet analysis approach

Mallat [49] provided a thorough elaboration of wavelet analysis and its application in singularity detection and denoising. A brief introduction of this technique is provided in this section as the basic theoretical background. Proofs and details of this technique as well as its application can be found in Reference [49].

### 2.3.1 Wavelet and wavelet transform

A function $\psi(x)$ is said to be wavelet if and only if its Fourier transform $\hat{\psi}(\omega)$ satisfies

$$\int_0^{+\infty} \frac{|\hat{\psi}(\omega)|^2}{|\omega|} \mathrm{d}\omega = \int_{-\infty}^{0} \frac{|\hat{\psi}(\omega)|^2}{|\omega|} \mathrm{d}\omega < +\infty \tag{2.4}$$

which means that function $\psi(x)$ has a zero mean and finite length (compact support)

$$\int_{-\infty}^{+\infty} \psi(x)\mathrm{d}x = 0 \tag{2.5}$$

The real or complex function $\psi(x)$ is used to create a family of wavelets $\psi_{u,s}(x)$, defined as

$$\psi_{v,s}(x) = \frac{1}{\sqrt{s}}\psi\left(\frac{x-v}{s}\right) \tag{2.6}$$

where real number $s$ and $v$ are the scale and translation parameters respectively. The family of wavelet functions is a dilated or stretched version of the mother wavelet $\psi(x)$.

For a given signal $f(x)$, where $x$ is a spatial coordinate, the Continuous Wavelet Transform (CWT) is obtained by integrating the product of the signal function and the wavelet function

$$Wf(v,s) = \frac{1}{\sqrt{s}}\int_{-\infty}^{+\infty} f(x)\psi^*\left(\frac{x-v}{s}\right)\mathrm{d}x \tag{2.7}$$

where $\psi^*(x)$ is the complex conjugate of the wavelet function. $Wf(v,s)$ is called the wavelet coefficient for wavelet $\psi_{v,s}(x)$ and it measures the content of the signal in the vicinity of $v$ of function $f$ with scale (size) $s$.

### 2.3.2 Vanishing moments

In singularity detection, the vanishing moments (VM) has an important influence. A wavelet has $n$ vanishing moments if

$$\int_{-\infty}^{+\infty} x^k\psi(x)\mathrm{d}x = 0, \quad k = 0,1,2,...,n-1 \tag{2.8}$$

which states that a wavelet with $n$ vanishing moments is orthogonal to polynomials of degree up to $n-1$. From Eq. (2.8), one has $\int_{-\infty}^{+\infty} x^k\psi(x)\mathrm{d}x = i^k\hat{\psi}^{(p)}(0)$. Therefore, for any integer $p < n$, $\hat{\psi}(\omega)$ can be factorized into

$$\hat{\psi}(\omega) = (-i\omega)^p\hat{\vartheta}(\omega) \tag{2.9}$$

whose form, in the spatial domain, is

$$\psi(x) = (-1)^p\frac{\mathrm{d}^p\vartheta(x)}{\mathrm{d}x^p} \tag{2.10}$$

and the Fourier transform of function $\vartheta(x)$ satisfies Eq. (2.4). From Eq. (2.10), one can derive

$$\bar{\psi}_s(x) = s^p\frac{\mathrm{d}^p\bar{\vartheta}_s(x)}{\mathrm{d}x^p} \quad \text{with} \quad \bar{\psi}_s(x) = \frac{1}{\sqrt{s}}\psi\left(\frac{-x}{s}\right) \tag{2.11}$$

If the $p$th derivative of function $f(x)$ is well defined, the wavelet transform can be written as

$$Wf(v,s) = f * \bar{\psi}_s(v) = \frac{\mathrm{d}^p}{\mathrm{d}v^p}(f * s^p\bar{\vartheta}_s)(v) = s^p\left(\frac{\mathrm{d}^p f}{\mathrm{d}v^p} * \bar{\vartheta}_s\right)(v) \tag{2.12}$$

It means that the CWT of $f(x)$ computed with the wavelet $\psi(x)$ is equal to the CWT of the $p$th derivative of $f(x)$ with respect to the wavelet $\vartheta(x)$ and multiplied by $s^p$. Equation (2.12) is called the multi-scale differential operator than constructs the relationship between the $Wf(v,s)$ and $s$.

### 2.3.3 Detection of singularities

If the signal has a singularity, or it is not differentiable at certain point $v_0$, then the wavelet coefficients at that point will have locally maximum values (apex values) for fine scales. The wavelet analysis approach detects and locates the singularities by finding the abscissa where the wavelet coefficients exhibit local maximum values, named wavelet maximum. The $\|Wf(v_0,s_0)\|$ at point $v_0$, is a local maximum in both the left and right neighborhoods. This implies that

$$\frac{\partial Wf(v_0,s_0)}{\partial v} = 0 \tag{2.13}$$

The line form by the local maximums over the scales is called the maxima line. To better understand the influence of the vanishing moments, the wavelet transform is written as the multi-scale differential operator

$$Wf(v,s) = s^p \frac{\mathrm{d}^p}{\mathrm{d}v^p}(f * \bar{\vartheta}_s)(v) \tag{2.14}$$

If the wavelet has one vanishing moment, the wavelet maxima are the maxima of the first-order derivative of $f(x)$ smoothed by $\hat{\vartheta}_s$. If the wavelet has two vanishing moments, the maxima corresponds to the maxima of curvatures.

### 2.3.4 Quantification of singularities

The decay of $|Wf(v,s)|$ in the neighborhood of $v_0$ is controlled by the decay of the wavelet maxima included in the cone $|v - v_0| \leq Cs$, supposed that the wavelet function $\psi(x)$ has a compact support equal to $[-C, C]$. The Lipschitz regularity of $f(x)$ is defined as $f(x)$ is uniformly Lipschitz $\alpha$ in the neighborhood of $v$ if and only if there exists $A > 0$ such that each wavelet maximum in the cone satisfies

$$|Wf(v,s)| \leq As^{\alpha+1/2} \tag{2.15}$$

which can be written as

$$\log_2 |Wf(v,s)| \leq \log_2 A + (\alpha + 1/2)\log_2 s \tag{2.16}$$

The Lipschitz regularity at $v_0$ is the maximum slope of $\log_2 |Wf(v,s)|$ as a function of $\log_2 s$ along the maxima lines, which implies

$$\log_2 |Wf(v_0,s)| = \log_2 A + (\alpha + 1/2)\log_2 s \tag{2.17}$$

Due to this linear relationship between the wavelet coefficient and scales in logarithmic form, the intersection of this linear line and the y-axis can be used as a damage index [25, 48, 86]. One should note that the scale is a positive value.

### 2.3.5 Choice of mother wavelet

Rucka and Wilde [64, 65] provided a Table of the characteristic of some real wavelets and a table of their feasibility for damage detection application. A brief combined version of the two tables is provided in this thesis for some common wavelets used in the literature (Table 2.1). Studies on this issue have shown that, for damage detection purpose, the wavelet should have not less than 2 vanishing moments [37].

### 2.3.6 Wavelet scale and sampling

At the locations of the singularities, Eq. (2.12) shows that the wavelet coefficient increases with the scale. Small scales correspond to the "compressed" wavelets. The more compressed the

**Table 2.1** The real wavelet characteristics and possibilities in damage detection.

| Wavelet name | Order $N$ | No. of V.M. | Symmetry | Support width | Possibility |
|---|---|---|---|---|---|
| Haar | - | 1 | Asymmetry | 1 | Yes |
| Daubechies $N$ | $1,2,\cdots$ | $N$ | No | $2N-1$ | Yes |
| Symlet $N$ | $2,3,\cdots$ | $N$ | Near from | $2N-1$ | Yes |
| Coiflet $N$ | 1,2,3,4,5 | $2N$ | Near from | $6N-1$ | Yes |
| Gaussian $N$ | $1,2,\cdots$ | $N$ | Yes (even) Asymmetry (odd) | 10 | Yes |
| Mexican hat | - | 2 | Yes | 16 | Yes |

wavelet, the shorter the portion of the signal with which it is being compared, and therefore the finer the signal features measured by the wavelet coefficients. The support of wavelet $\psi(x)$ equals to $[v-Cs, v+Cs]$. In the use of numerical sampling, we take the Gaussian wavelet whose support width is $10s$ (Table 2.1) as an example. When $s=1$, ten sampling points are covered by the wavelet and when $s=2$, twenty sampling points are covered by the wavelet. Therefore, in the application with noise contaminated data, small scales provide higher resolution on locating singularities but is more sensitive to noise while high scales are more robust to noise but provide lower location resolution. In the multiple damage case, the largest scale is controlled by the support width of the wavelet which should be smaller than the distance between two adjacent damage to prevent having other singularities affect the wavelet coefficient $Wf(v,s)$. One challenge of using wavelet analysis for detecting multiple cracks in beams is the selection of scales.

### 2.3.7 Wavelet boundary effect

Applying the CWT (Eq. (2.7)) to a finite length signal results in extreme high values at the two ends of the signal, which is commonly known as the boundary effects. The affected region can be estimated as a half width of the wavelet for each scale. The basic idea to avoid this issue is to extend the signal beyond the boundaries, which can be achieved through the following four methods:

1. **boundary value padding** repeats the boundary value of the signal;
2. **symmetrical padding** replicates the signal symmetrically;
3. **anti-symmetrical padding** replicates the signal anti-symmetrically;
4. **periodic padding** treats the signal as a periodic signal;
5. **extrapolation padding** extends the signal by using a polynomial fit.

In this research, the anti-symmetrical padding method is adopted to deal with the boundary effects.

### 2.3.8 Scalogram

The wavelet coefficients obtained from Eq. (2.7) contains the translation and scale parameters, which can be plotted either in regular 3D coordinate or a 2D colored picture named scalogram. In damage location detection, only the relative relationships among the wavelet coefficient values are needed. Hence, the 2D scalogram is adopted to review the results in Paper A (Appendix A). The x-axis represents the position along the beam normalized to unity and the y-axis represents the scale values. The color in the picture indicates the amplitude of the coefficients, with warm and bright colors represent high values and dark colors for low values.

Since higher scales result higher wavelet coefficients, the change of the coefficients with low scale values on the scalogram can not be observed. In order to highlight the local maximum values in the wavelet coefficients with different scale values, the coefficients are normalized to its maximum, which provides a ridge of the peak values at the damage location through all the scales. This ridge

of the local maximums is called the maxima line. The actual mathematical meaning of the wavelet coefficients is lost with the normalization process, but this is irrelevant since they are used as a relative indicator of the presence of damage.

## 2.4 Central difference approach

In the continuous displacement field, let the location of the damage be $x_0$, the discontinuity at $x_0$ in the first-order derivatives of the displacement is:

$$\Delta\theta(x_0) = \lim_{x\to x_0^+} \theta(x_0) - \lim_{x\to x_0^-} \theta(x_0) \tag{2.18}$$

where the left approach and the right approach of slope at $x_0$ can be derived from Eq. 2.3

$$\lim_{x\to x_0^-} \theta(x_0) = \lim_{h\to 0} \frac{f(x_0) - f(x_0 - h)}{h} \tag{2.19}$$

$$\lim_{x\to x_0^+} \theta(x_0) = \lim_{h\to 0} \frac{f(x_0 + h) - f(x_0)}{h} \tag{2.20}$$

with $f(x)$ taken as either the static deflection difference or the mode shape difference.

For discrete numerical data, the rotational discontinuity at $x_0$ can be calculated through the central difference approach (Eq. (2.21)) assuming $\Delta x$ is the distance between two consecutive measurements which is a constant.

$$\begin{aligned} \Delta\theta_i &= \theta(x_0^+) - \theta(x_0^-) \\ &= \frac{f(x_0 + \Delta x) - f(x_0)}{\Delta x} - \frac{f(x_0) - f(x_0 - \Delta x)}{\Delta x} \\ &= \frac{f(x_0 - \Delta x) - 2f(x_0) + f(x_0 + \Delta x)}{\Delta x} \end{aligned} \tag{2.21}$$

# 3 Mode Shape-Wavelet approach

Parts of this chapter have been published in

- Paper A by Solís, M., Ma, Q., Galvín, P. (2018) in Appendix A.

## 3.1 Mode shape-Wavelet approach

In the application of wavelet analysis in detecting damage in mode shapes, this research continues the work of Solís et al. [69] and aims at enhancing the sensitivity of the use of wavelet analysis in detecting damage in beams.

### 3.1.1 Mode shapes

The equation of motion of a homogeneous elastic beam of length $L$ without damping is

$$\rho A \frac{\partial^2 u(x,t)}{\partial t^2} + EI \frac{\partial^4 u(x,t)}{\partial x^4} = q(x,t), \quad 0 \leq x \leq L \tag{3.1}$$

where $A$ is the cross section area, $\rho$ is the mass density and $A$ is the cross section area (assumed to be uniform). Form the eigenvalue problem with the assumption that the displacement of the beam can be written in the form

$$u(x,t) = w(x)e^{-i\omega t}, \quad i = \sqrt{-1} \tag{3.2}$$

where $\omega$ is the natural frequency (eigenvalue) and $w$ is the mode shape (eigenfunction). Substituting Eq. 3.2 into Eq. 3.1 with $q(x,t) = 0$ (free vibration) yields the eigen equation

$$\rho A \omega^2 w(x) = EI \frac{\partial^4 w(x)}{\partial x^4} \tag{3.3}$$

For nonzero eigenvalues, the corresponding eigenfunction can be written as

$$w(x) = C_1 \cos \zeta x + C_2 \sin \zeta x + C_3 \cosh \zeta x + C_4 \sinh \zeta x \tag{3.4}$$

where

$$\zeta^4 = \omega^2 \frac{\rho A}{EI} \tag{3.5}$$

where the constants $C_1, C_2, C_3, C_4$ are determined by the boundary conditions, and sinh and cosh are the hyperbolic sine and cosine functions, respectively.

### 3.1.2 Modified wavelet coefficient

For each mode, two weighted factors are considered for improving the sensitivity of the wavelet coefficient to damage, one is based on the frequency change, $\eta_\omega$, defined in Eq. (3.6) and the other is based on the signal to noise ratio (SNR), $\eta_{SNR}$, defined in Eq. (3.7).

$$\eta_\omega = \left(1 - \frac{\omega_u}{\omega_d}\right)^2 \tag{3.6}$$

$$\eta_{SNR} = 10\log\left(\frac{P_{mode}}{P_{noise}}\right) \tag{3.7}$$

where $\omega_u$ and $\omega_d$ stand for the natural frequencies of the mode shapes at the undamaged state and damaged state, respectively; and $P_{mode}$ and $P_{noise}$ are the power of the mode shape and the noise, defined as:

$$P_{mode} = \frac{\sum_{k=1}^{n} x_k^2}{n} \tag{3.8}$$

$$P_{noise} = \frac{\sum_{k=1}^{n} \left(x_k - x_k^{ref}\right)^2}{n} \tag{3.9}$$

where $x_k$ is the $k$th component of the mode shape vector and $n$ is the number of its components; and $x_k^{ref}$ is the $k$th component of a reference noise-free mode shape vector which is taken as the cubic spline interpolation of the corresponding measured mode shape.

In the application of the auxiliary mass, for each damage case, a set of mode shapes can be obtained for each position of the additional mass. As the mass traversing from one end of the beam to the other, the dynamic characteristics of the beam are altered due to the change of the mass and stiffness distribution. It is assumed that those modes that are more sensitive to damage exhibit higher frequency change and a larger variation in mode shapes. The use of SNR is to emphasize those less noisy mode shapes. If no noise is presented, the wavelet coefficient is highly sensitive to small change in the signal. Therefore, the weighted wavelet coefficient for mode $i$ with the auxiliary mass at location $j$ is written as

$$W\phi^{ij}_{weighted}(v,s) = \left|W\phi^{ij}_{diff}(v,s)\right| \cdot \eta^{ij}_{\omega} \cdot \eta^{ij}_{SNR} \tag{3.10}$$

where $W\phi^{ij}_{diff}(v,s)$ is the wavelet transform coefficient of the mode shape difference (Eq. (2.7)).

To examine the effect of the auxiliary stationary roving mass on each mode, the wavelet coefficients of the same mode order for all mass locations are combined and normalized. Thus, for a single mode $i$, the modified wavelet coefficient can be computed by

$$W\phi^{i}_{sum}(v,s) = \sum_{j=1}^{M}\left(W\phi^{ij}_{weighted}(v,s)\right) \tag{3.11}$$

$$W\phi^{i}_{norm}(v,s) = \frac{W\phi^{i}_{sum}(v,s)}{\max|W\phi^{i}_{sum}(v,s)|_s} \tag{3.12}$$

where $M$ is the number of roving mass locations. When analyzing identified modes separately, the challenge is that not all the modes are equally sensitive to damage due to noise or the location of the crack, which means that no mode shape can be determined as the best for damage identification. It is more practical to examine all the available information. The combined results of all identified

modes are proposed since it provides a more global result

$$W\phi_{sum}(v,s) = \sum_{i=1}^{N}\sum_{j=1}^{M}\left(W\phi^{ij}_{weighted}(v,s)\right) \tag{3.13}$$

$$W\phi_{norm}(v,s) = \frac{W\phi_{sum}(v,s)}{\max|W\phi_{sum}(v,s)|_s} \tag{3.14}$$

where $N$ is the number of identified modes. The normalization process of Eqs. (3.12) and (3.14) are carried out after the addition is performed, which retains the original values of the wavelet coefficients so that relative difference between different modes and roving mass positions are preserved.

## 3.2 Experiment setup

The aim of the tests was to obtain experimental estimates for the modal parameters, i.e. natural frequencies and mode shapes, of a cantilever beam with a single crack. The test beam has a length ($L$) of 800 mm, a width ($W$) of 30 mm and a height ($H$) of 10 mm. The Young's modulus is 210 GPa ($E$) and density 7850 kg/m$^3$ ($\rho$).

The beam is clamped at one end with two metallic blocks and free on the other (Fig. 3.1(a)). A total of 32 measurement points distributed along the beam with equal distance of 25 mm leaving 10 mm to both ends were considered. A set of 16 accelerometers (general purpose piezoelectric type with 100 mV/g nominal sensitivity and a mass of 4g) were used to measure the dynamic response of the beam. The accelerometers were first mounted on odd positions of the beam for the test and changed to the even positions for another test. By doing so, the mass distribution of the beam together with the accelerometers was different in those two setups. Since the total weight of the accelerometers is around 3% of the beam, 16 dummy masses (screws of the same weight) were used in both setups to complement the equilibrium (Fig. 3.1(b)). The impulse excitation was applied at the free end with an impact hammer (Fig. 3.1(c)). Two different blocks of 5% and 10% of the mass of the beam were used as the auxiliary stationary roving mass (Fig. 3.1(d)). In each test, the mass was fixed on the beam as a nonstructural mass. Eleven equidistant positions were chosen for the mass. The crack was set at $0.4L$ (320 mm) from the fixed end, just in between two measurement points. Three levels of damage severities ($\xi(\%)$), 10%, 20% and 50%, were introduced progressively (Fig. 3.1(e)). The excitation force is applied at the free end of the beam with an impact hammer and the averaged Frequency Response Functions (FRFs) are obtained from 5 impacts for the 16 measuring points of each set-up. The mode shapes and natural frequencies are identified by applying the Poly-reference Least Squares Complex Frequency Domain (plSCF) algorithm.

## 3.3 Experimental results

In this study, the Daubechies wavelet with 2 vanishing moments is selected for the wavelet analysis. The scale $s \in \mathbb{N}$ is taken from 1 to 8. The modified wavelet coefficient (Eq. (3.13)) is obtained and the results are shown in Fig. 3.2 and Fig. 3.3. Fig. 3.2 shows that with the auxiliary roving mass, the wavelet local maxima at the damage location $x/L = 0.4$ appears to be more obvious than the noise resulted local maxima at position $x/L = 0.6$. The heavier the auxiliary mass, the more outstanding the wavelet local maxima at the damage location. The comparison of different crack severities in Fig. 3.3 indicates that, in this case, the minimum detectable damage severity in this case is 20%. More results and details of the experiment can be found in Paper A (Appendix A).

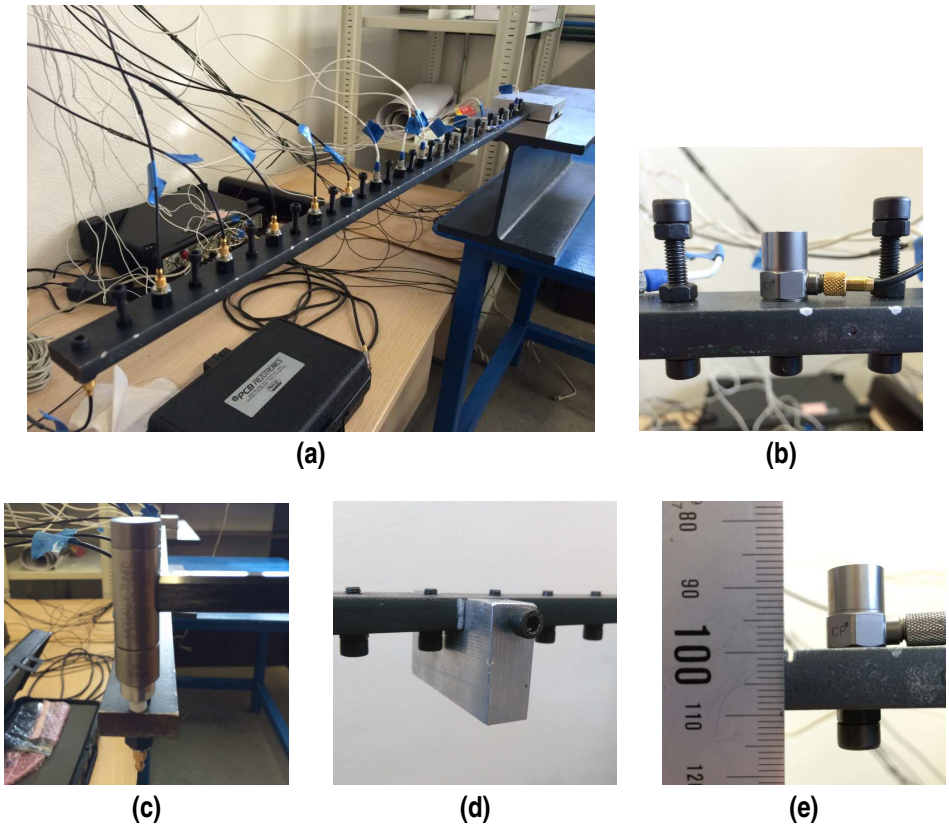


**Figure 3.1** Dynamic experimental test of the cantilever beam: (a) setup; (b) sensors and dummy mass; (c) the impact hammer; (d) the roving mass; (e) the crack.

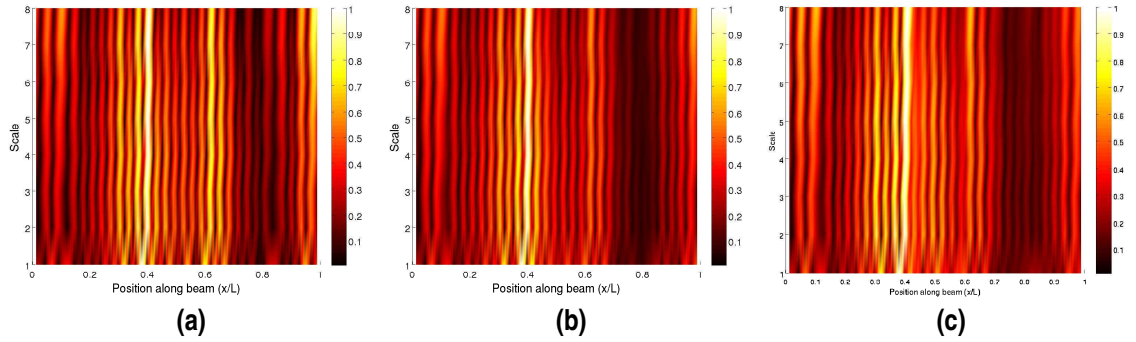


**Figure 3.2** The modified wavelet coefficients for crack depth 50% (a) with no auxiliary roving mass, (b) with 5% auxiliary roving mass and (c) with 10% auxiliary roving mass.

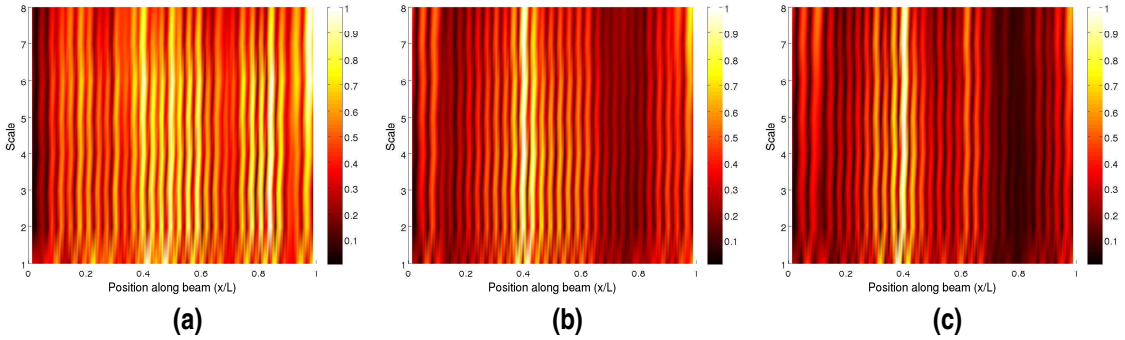


**Figure 3.3** The modified wavelet coefficients with 5% auxiliary roving mass for (a) crack depth 10%, (b) crack depth 20% and (c) crack depth 50%.

# 4 Deflection-Spring/Wavelet scheme

Parts of this chapter are taken from the following papers

- Paper B by Ma, Q. and Solís, M. (2017) in Appendix B.
- Paper C by Ma, Q. and Solís, M. (2018) in Appendix C.
- Paper D by Ma, Q. and Solís, M. (2018) in Appendix D.
- Paper E by Ma, Q. and Solís, M. (2018) in Appendix E.

and the experimental measurements of the static tests are provided in Appendix F

## 4.1 Superposition scheme in static problem

For a cracked beam subjected to external forces with well-established boundaries, named the Damaged State, the generated displacements and internal forces can be treated as the superposition of the results of two states. One is the beam subjected to the same load and boundary conditions before the formation of the crack, namely the solutions of the beam at the Reference State. At this state, the external forces result internal tractions at the potential crack position. The other state, named Incremental State in this thesis, is the beam subjected to these tractions at the crack surface due to the open of the crack [34]. These three states of the beam, hereinafter referred to as State D, State R and State I, respectively, are defined as follows

**State D:** the beam, after the occurrence of damage, is under the external load $P$ which generates the internal bending moment distribution $m_D(x)$ and the beam deflection $u_D(x)$;

**State R:** the beam, before the occurrence of damage, is under the same external load $P$ which generates the internal bending moment distribution $m_R(x)$ and the beam deflection $u_R(x)$;

**State I:** the beam, after the occurrence of damage, is under a series of self-equilibrated bending moments $M_R(b_i)$ applied at the damaged cross-sections $b_i$, respectively, which generates the internal bending moment distribution $m_I(x)$ and the beam deflection $u_I(x)$ ($i = 1,2,\cdots,n$ with $n$ being the damage number).

$M_R(b_i) = m_R(b_i)$ (the capital letter $M$ representing the moment applied as the external force and the lower case $m$ standing for the generated internal bending moment). The following expressions can be written based on the superposition scheme

$$u_D(x) = u_R(x) + u_I(x) \tag{4.1}$$

$$m_D(x) = m_R(x) + m_I(x) \tag{4.2}$$

To better illustrate the superposition scheme, an example of a beam with single damage modelled by a spring of rotational is depicted in Fig 4.1(a) where $0 < b < L$ is the location of the damage and $K_{eq}$ is the corresponding stiffness. The beam is assumed to be well constrained with a rotational spring and a translational spring with constrains $K_r$ and $K_t$, respectively, and the subscripts 0 and $L$ represent the left and right ends, respectively. The external load distribution is represented by $q(x)$ applied at a random position on the beam.

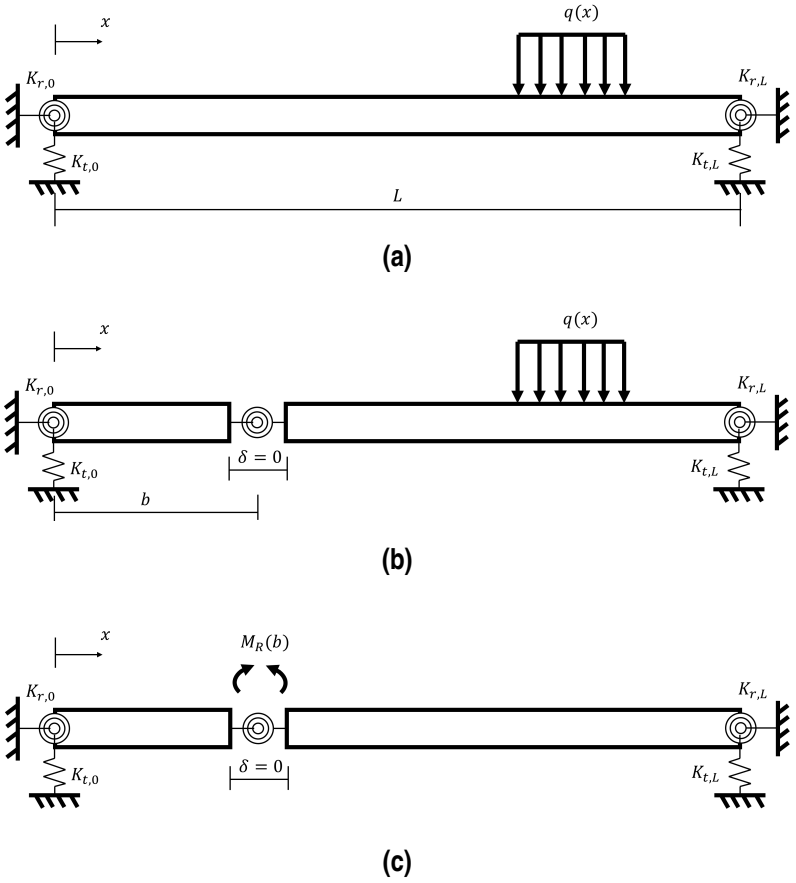


**Figure 4.1** Superposition scheme of a beam with a single crack idealized by rotational springs at: (a) State R; (b) State D; (c) State I.

### 4.1.1 The Reference State (State R)

Assuming the beam is undamaged at its Reference State, through classic beam theory (Euler-Bernoulli beam theory), the relationship between the transverse displacement, $u_R$, and the applied static load distribution, $q$, is governed by

$$\frac{\mathrm{d}^2}{\mathrm{d}x^2}\left(E(x)I(x)\frac{\mathrm{d}^2 u_R(x)}{\mathrm{d}x^2}\right) = q(x), \quad x \in [0, L] \tag{4.3}$$

where $E$ is the Young's modulus, $I$ is the second moment of area (moment of inertia) and $L$ is the length of the beam. The shear deformation is neglected for a slender beam subjected to bending. If the flexural rigidity, $E(x)I(x)$, is uniform along the beam, then the following static response can be

derived:

$$\theta_R(x) = EI\frac{\mathrm{d}u_R(x)}{\mathrm{d}x} \tag{4.4}$$

$$m_R(x) = EI\frac{\mathrm{d}^2u_R(x)}{\mathrm{d}x^2} = EI\kappa_R(x) \tag{4.5}$$

$$v_R(x) = EI\frac{\mathrm{d}^3u_R(x)}{\mathrm{d}x^3} \tag{4.6}$$

where $\theta$ is the rotation or slope of the beam, $\kappa$ is the curvature and $v$ is the internal shear force.

The boundary conditions of left end ($x = 0$) and right end ($x = L$) can be established as follows

$$K_{r,0}\frac{\mathrm{d}u_R(0)}{\mathrm{d}x} - EI\frac{\mathrm{d}^2u_R(0)}{\mathrm{d}x^2} = 0, \qquad K_{r,0}u(0) + EI\frac{\mathrm{d}^3u_R(0)}{\mathrm{d}x^3} = 0 \tag{4.7}$$

$$K_{r,L}\frac{\mathrm{d}u_R(L)}{\mathrm{d}x} + EI\frac{\mathrm{d}^2u_R(L)}{\mathrm{d}x^2} = 0, \qquad K_{r,L}u_R(L) - EI\frac{\mathrm{d}^3u_R(L)}{\mathrm{d}x^3} = 0 \tag{4.8}$$

where for ideal boundary conditions, taking the three common types for instance, one has

| | |
|---|---|
| simply supported end: | $K_r = 0$ and $K_t = \infty$; |
| fixed end: | $K_r = \infty$ and $K_t = \infty$; |
| free end: | $K_r = 0$ and $K_t = 0$; |

### 4.1.2 The Damaged State (State D)

Assuming one individual damage occurred at location $b$ where $0 < b < L$, the deflection of the beam at State D is governed by

$$EI\frac{\mathrm{d}^4u_D(x)}{\mathrm{d}x^4} = q(x), \quad x \in [0, b) \cup (b, L] \tag{4.9}$$

with the following relationships at the damage location $b$

$$u_D(b) = u_D(b^-) = u_D(b^+) \tag{4.10}$$

$$\theta_D(b^-) \neq \theta_D(b^+) \tag{4.11}$$

$$m_D(b) = m_D(b^-) = m_D(b^+) \tag{4.12}$$

Let $K_{eq}$ be the equivalent rotational stiffness of the damage, based on Hooke's law at the damage, one can derive

$$m_D(b) = Keq \cdot [\theta_D(b^+) - \theta_D(b^-)] \tag{4.13}$$

### 4.1.3 The Incremental State (State I)

From Eq. (4.1), the deflection of the beam at State I can be written as

$$u_I(x) = u_D(x) - u_R(x), \quad x \in [0, L] \tag{4.14}$$

By subtracting Eq. (4.3) from Eq. (4.9), the governing differential equation of $u_I$ can be obtained

$$EI\frac{\mathrm{d}^4u_I(x)}{\mathrm{d}x^4} = 0, \quad x \in [0, b) \cup (b, L] \tag{4.15}$$

with the following static response at the damage location $b$

$$\theta_I(b^-) \neq \theta_I(b^+) \tag{4.16}$$
$$m_I(b^-) = m_I(b^+) \neq m_I(b) \tag{4.17}$$

which means the deflection difference of a beam contains first-order and second-order discontinuities at the damage location. The locations of the cracks can be determined through identifying the discontinuities in the slope of $u_I$.

At State I, the response at the spring shown in Fig. 4.2 spring satisfies the following relationships:

$$M_R(b_i) = m_I(b^-) + m_I(b) = m_I(b^+) + m_I(b) \tag{4.18}$$
$$m_I(b) = Keq \cdot [\theta_I(b^+) - \theta_I(b^-)] \tag{4.19}$$

where $m_I(b) = m_D(b)$.

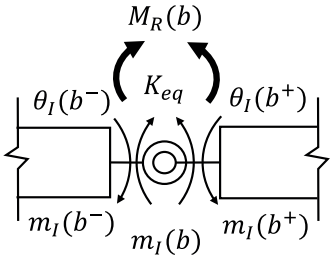


**Figure 4.2** The equilibrium detail of the spring at State I.

The deflection $u_I$ is resulted from the released bending moments at the cracks and its shape is influenced by the boundary conditions. From Eq. (4.15), the deformation of each part can be represented by a polynomial of third-order, the deflection difference $u_I$ thereby can be assembled with a set of third order polynomial curves. The kinks or turning points in $u_I$ are associated with the damage locations. For statically determinate systems whose moment diagram is independent from the flexural rigidity

$$m_D(x) = m_R(x), \quad x \in [0, L] \tag{4.20}$$
$$m_I(x) = 0, \quad x \in [0, b) \cup (b, L] \tag{4.21}$$

which implies the displacement of the undamaged parts are given by rigid body translations, in other words, $u_I$ is piecewise linear.

## 4.2 Deflection-Spring approach

### 4.2.1 Identification

This approach locates the damage at the discontinuities in the slope of the deflection difference $u_I$. The changes in the slope are estimated by using the center difference approach (Eq. (2.21)). The stiffness of the spring is representative of the stiffness of the damage affected region. Furthermore, with the damaged bending moment at each damage location, the equivalent rotational stiffness value can be obtained via Eq. (4.22) using Hooke's law. The crack depth can be estimated through a relationship between the crack depth and the equivalent rotational stiffness.

$$K_{eq,i} = \frac{m_D(b_i)}{\Delta\theta_{I,i}} \tag{4.22}$$

In the literature review, five rotational spring models for one-sided crack with uniform depth $d$ in rectangular cross-section of width $B$ and height $H$ are used in this study. The equivalent rotational stiffness is defined as a function of the damage severity ($\xi = d/H$). The characteristic functions can be generally expressed as

$$K_{eq} = \frac{EI}{H}\frac{1}{J(\xi)} \tag{4.23}$$

where $E$ is the Young's modulus of the material of the beam and $I$ is the moment of inertia of the cross-section. The damage parameter $J(\xi)$ are:

- Model 1 by Rizos et al. [63]:

$$\begin{aligned} J_R(\xi) =& 5.346(1.8624\xi^2 - 3.95\xi^3 + 16.375\xi^4 - 37.226\xi^5 \\ &+ 76.81\xi^6 - 126.9\xi^7 + 172\xi^8 - 143.97\xi^9 + 66.56\xi^{10}) \end{aligned} \tag{4.24}$$

- Model 2 by Ostachowicz and Krawczuk [57]:

$$\begin{aligned} J_O(\xi) =& 6\pi\xi^2(0.6384 - 1.035\xi + 3.7201\xi^2 - 5.1773\xi^3 \\ &+ 7.553\xi^4 - 7.332\xi^5 + 2.4909\xi^6) \end{aligned} \tag{4.25}$$

- Model 3 by Chondros et al. [19]:

$$\begin{aligned} J_C(\xi) =& 6\pi(1-\nu^2)(0.6272\xi^2 - 1.04533\xi^3 + 4.5948\xi^4 - 9.9736\xi^5 \\ &+ 20.2948\xi^6 - 33.0351\xi^7 + 47.1063\xi^8 - 40.7556\xi^9 + 19.6\xi^{10}) \end{aligned} \tag{4.26}$$

- Model 4 by Fernández-Sáez et al. [28]:

$$J_F(\xi) = 2\left(\frac{\xi}{1-\xi}\right)^2\left(5.93 - 19.69\xi + 37.14\xi^2 - 35.84\xi^3 + 13.12\xi^4\right) \tag{4.27}$$

- Model 5 by Bilello [11]:

$$J_B(\xi) = \frac{\xi(2-\xi)}{0.9(\xi-1)^2} \tag{4.28}$$

The equivalent rotational stiffness and the damage parameter are in inverse proportion. The results of $1/J$ for $\xi = 0.05$ to $0.5$ are plotted in Fig. 4.3. With an experimental estimated equivalent rotational stiffness, Model 1 to 4 provide similar results and Model 5 provides relative small estimates of crack depth. Details of the quantification results are referred to Paper B to E in Appendix B and E.

### 4.2.2 Trend estimation

With the noise contaminated data, the change of slope can not be computed directly through Eq. (2.21). It is necessary to apply some curve fitting tool to diminish the noise effect. As aforementioned, the deflection different $u_I$ can be taken as a set of segments of third order polynomials with consistent values at the joints. For a beam with $n$ cracks located at $0 < x_1 < x_2 < \cdots < x_n < L$, the beam can be divided into $(n+1)$ segments. Denote $x_0 = 0$ as the left end of the beam and $x_{n+1} = L$ as the right end of the beam. Each segment can be written as a third order polynomial function that contains four parameters

$$f_i(x) = A_i x^3 + B_i x^2 + C_i x + D_i, \quad x_{i-1} \le x \le x_i \tag{4.29}$$

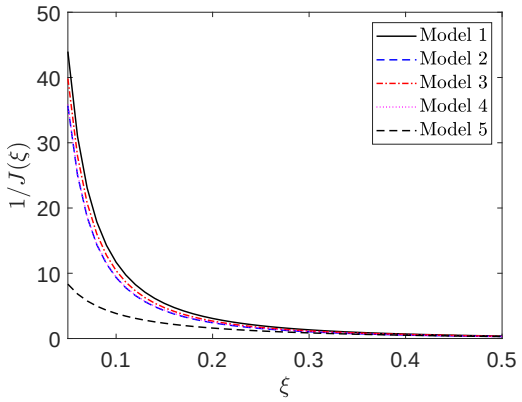


**Figure 4.3** The damage parameter $1/J$ of five different spring models proposed in the literatures.

where $i = 1, 2, \cdots, n+1$. The estimate of $u_I$ is written as $f(x) = [f_1, f_2, \cdots, f_{n+1}]$ for $x \in [0, L]$. Let $A = [A_1, A_2, \cdots, A_n + 1]$, $B = [B_1, B_2, \cdots, B_n + 1]$, $C = [C_1, C_2, \cdots, C_n + 1]$ and $D = [D_1, D_2, \cdots, D_n + 1]$ and denote the coordinates of the damages by $X = [x_1, x_2, \cdots, x_n]$ and $Y = [y_1, y_2, \cdots, y_n]$, the optimization problem can be written as

$$\min_{A,B,C,D,X,Y} Q(A,B,C,D,X,Y) = ||f(A,B,C,D,X,Y) - u_I||_2 \tag{4.30}$$

subjected to the constraints at the joints $(x_i, y_i)$

$$f_i(x_i) = f_{i+1}(x_i) = y_i \quad \text{for} \quad i = 1, \cdots, n \tag{4.31}$$

as well as the boundary conditions

$$f_1(0) = u_I(0) \quad \text{and} \quad f_{n+1}(L) = u_I(L) \tag{4.32}$$

The minimization of the cost function $Q$ can be solved by different methods, such as Nelder-Mead simplex algorithm [55], Multi-directional direct search algorithm [75], quasi-Newton method or genetic algorithm. For statically determinate structures, of which the deflection difference is piecewise linear, the optimization problem can be solved by using Lasso regression method. In this thesis, a linear trend estimation designed by Kim et al. [44] is adopted in this thesis for nonparametric regression.

The linear trend estimation tool designed by Kim et al. is, hereinafter, referred to as the $l1$ Trend Filtering [44]. It is a mathematical curve fitting tool which has the capability to estimate the local linear trend of the data through minimizing the objective function

$$(1/2)\sum_{k=1}^{N}(u_{I,k} - u_{I,k}^{l1})^2 + \lambda \sum_{k=2}^{N-1} |u_{I,k-1}^{l1} - 2u_{I,k}^{l1} + u_{I,k+1}^{l1}|, \quad \lambda \in [0, \infty) \tag{4.33}$$

where $u_{I,k}$ is the experimental value of the deflection variation at measurement point $k$, $u_{I,k}^{l1}$ is the estimate of the $l1$ Trend Filtering and $N$ is the number of measurement points. $\lambda$ is a regularization parameter which controls the trade-off between the "smoothness" of the estimate ($|u_{I,k-1}^{l1} - 2u_{I,k}^{k} + u_{I,k+1}^{l1}|$) and the residual between the measurement and the estimate $(u_{I,k} - u_{I,k}^{l1})^2$. It is obvious that as $\lambda$ changes from 0 to $\infty$, the estimate changes from the input data to its linear regression fit. The value of $\lambda$ is essential to the fitness of the estimate in this approach. If $\lambda$ is too small, the estimate tends to be overfitted while if $\lambda$ is too high, the estimate tends to be underfitted. It is also proved

that the $l1$ trend estimation converges for a finite value of $\lambda$ which is defined as

$$\lambda_{max} = \left|\left|(DD^T)^{-1}Du_I\right|\right|_\infty \tag{4.34}$$

$$D = \begin{bmatrix} 1 & -2 & 1 & & & \\ & 1 & -2 & 1 & & \\ & & \ddots & \ddots & \ddots & \\ & & & 1 & -2 & 1 \end{bmatrix}_{(N-2)\times N} \tag{4.35}$$

where $||x||_p = (\sum_{i\in\mathbb{N}} |x_i|^p)^{(1/p)}$ is the $p$th-norm. This maximum value $\lambda_{max}$ can be computed with $O(n)$ arithmetic steps (see Reference [44] Section 5.1). The $l1$ Trend Filtering can be applied with a MATLAB function provided by the authors [45]. To evaluate the influence of $\lambda$ to the estimate, an error function $R$ and its change rate $\mathrm{d}R/\mathrm{d}\lambda$ are defined as

$$R(\lambda_i) = ||u_I - u_I^{l1}(\lambda_i)||_2 \tag{4.36}$$

$$\frac{\mathrm{d}R(\lambda)}{\mathrm{d}\lambda} \approx \frac{R(\lambda_{i+1}) - R(\lambda_i)}{\lambda_{i+1} - \lambda_i} \tag{4.37}$$

with $0 \leq \lambda_1 < \cdots < \lambda_i < \cdots \lambda_n \leq \lambda_{max}$. Some more details of this trend filtering in the estimation of piecewise polynomial can be found in Reference [74].

## 4.3 Deflection-Wavelet approach

This section explores the application of wavelet analysis introduced in Chapter 2 in locating and identifying damage based on static measurements. In the use of wavelet analysis for damage location with experimental data, the main challenge is dealing with the noise influence. Small scales are sensitive to noise while high scales have a larger support width which may be an issue in multiple damage localization. Therefore, a localization index is taken as the sum of the normalized wavelet coefficients

$$Wf_n(v,s) = \frac{|Wf(v,s)|}{\max\limits_v(|Wf(v,s)|)} \tag{4.38}$$

$$\mathrm{LI}(v) = \sum_s Wf_n(v,s) \tag{4.39}$$

and the potential damage locations are taken where the local maximum values appear in the localization index, i.e. $\partial \mathrm{LI}(v)/\partial v = 0$.

Another challenge of using the static response is that the amplitude of the wavelet coefficient maxima is not only related to scale but also related to the external loads. The idea is to establish a damage index that is independent from the external loading. As shown in Section 4.1, we know that the deflection difference is a result of the rotation deformation of the damaged cross-sections. Therefore, a damage quantification index is developed based on the normalized wavelet coefficient to the damaged bending moment at the damage locations. Therefore, Equation (2.15) can be written as

$$\left|\frac{Wf(v,s)}{m_D(v)}\right| \leq \frac{A}{|m_D(v)|} \cdot s^{\alpha+1/2} \tag{4.40}$$

which implies that at the damage location $b$, one has

$$\log_2\left|\frac{Wf(b,s)}{m_D(b)}\right| = \log_2\left(\frac{A}{|m_D(b)|}\right) + (\alpha+1/2)\log_2 s \tag{4.41}$$

where the external load independent damage index is taken as the interception

$$\mathrm{DI}(b) = \log_2\left(\frac{A}{|m_D(b)|}\right) \tag{4.42}$$

A reference correlation map between the crack depth and DI can be established through a numerical model.

## 4.4 Experiment

A brief description of the static experimental tests, including the information of the beams and the measuring approaches applied, is presented in this section. The test beam is prismatic and made of steel. The beam is 1200 mm long ($L$), 800 mm wide ($W$) and 20 mm high ($H$). The Young's modulus is 210 GPa ($E$). The objective of the tests was to obtain experimental static deflections of a simple supported beam for single and multiple damage scenarios with a Digital Image Correlation (DIC) system. The author would like to state that in the published version of Paper B, Paper C and Paper D, the width of the beam was mistaken as 100 mm. This error results no change in the localization results but has some little influence on the quantification results. The correct values of the crack depth estimates for the experimental cases in Paper B, Paper C and Paper D are provided in Appendix G.

### 4.4.1 Setup

A concentrated static load is applied by hanging a mass at the bottom of the beam. A total number of 21 points, distributed at a spacing of 50 mm with 100 mm to both ends, were selected as loading positions (Fig. 4.4(a)). A concentrated load of 120 kg was applied at the load positions to generate the deflection. The maximum deflection of the beam under 120 kg load at the midspan is 3 mm, which is smaller than the serviceability limit. The deflections of the beam were measured by a DIC system named Pontos from GOM company (https://www.gom.com/3dsoftware/gom-correlate.html). The system contains two cameras of 8 mm lens with 5 Megapixel resolution placed at a distance of 300 mm (Fig. 4.4(b)). The measurement targets are high-contrast circle shaped stickers which consist of a black circle of 10 mm diameter with a white circle of 5 mm diameter at the center. The central point of the target is automatically identified by the DIC system (Fig. 4.4(c)). The side of the beam was covered by 241 measurement targets aligned in two lines, 121 points above the neutral axis and 120 points below, spacing at 5 mm. For each measure, 20 images were captured at a sample rate of 1 Hz. The system provides the coordinates of the targets in each measure. Erratic images were discarded and the average coordinate value is computed to enhance the accuracy of the measurement. The deflection of the beam was obtained by subtracting the coordinates of the targets at the unloaded state from those at the loaded one. The calibration of the system coordinate is done by using a calibration pattern (Fig. 4.4(d)).

### 4.4.2 Damage scenario

In this test, a total number of four cracks were introduced to the test beam progressively at locations 425 mm, 775 mm, 625 mm and 525 mm from the left end (shown in Fig 4.5). The maximum crack spacing was reduced from 350 mm to 100 mm in this progression. For each crack, five levels of damage severities $\xi(\%)$ were investigated step by step, namely, 5%, 10%, 20%, 35% and 50%. The new damage was introduced to the beam when the previously introduced crack reached to $\xi = 50\%$. Therefore, the experimental cases are denoted as Case $X.\xi$ where $X$ represents the order of the latest introduced crack and $\xi$ stands for its severity. For example, Case 2.20 is referring to the case of two cracks which one 50% crack at 425 mm and one 20% crack at 775 mm.

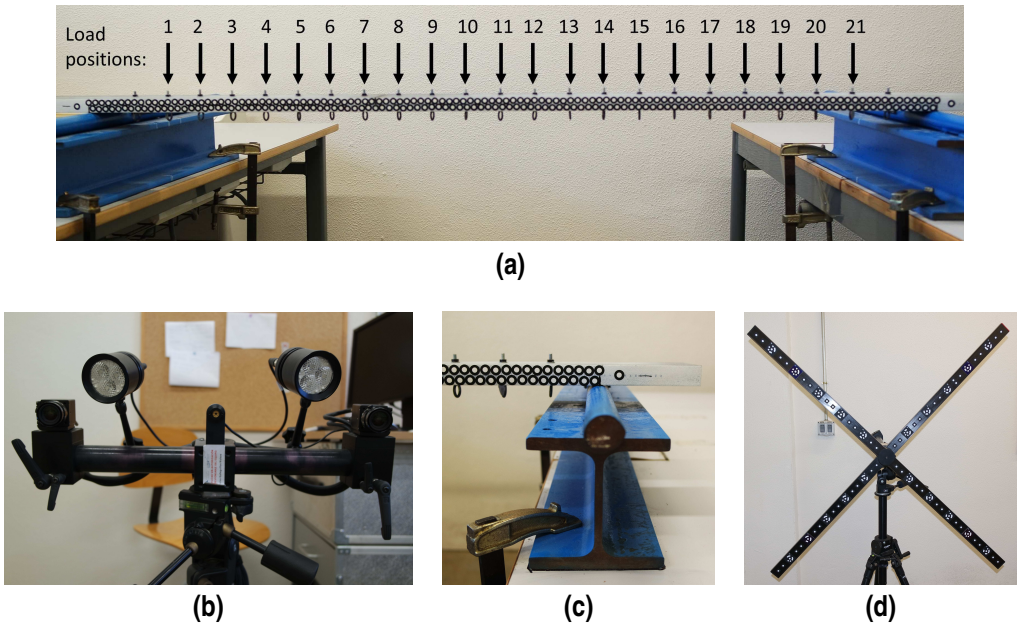


**Figure 4.4** Static experimental test of the simply supported beam: (a) beam with measurement targets; (b) the measuring cameras; (c) the measurement targets; (d) the calibration pattern.

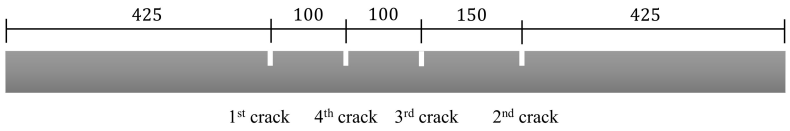


**Figure 4.5** Crack location scheme of quadruple damage scenario.

**Table 4.1** Definition of the experimental cases.

| Crack location (mm) | 425 | 525 | 625 | 775 |
|---|---|---|---|---|
| Crack order ($X$) | 1 | 4 | 3 | 2 |
| Case 1.$\xi$ | $\xi$ | – | – | – |
| Case 2.$\xi$ | 50% | – | – | $\xi$ |
| Case 3.$\xi$ | 50% | – | $\xi$ | 50% |
| Case 4.$\xi$ | 50% | $\xi$ | 50% | 50% |

### 4.4.3 Measuring approach

For single damage scenario, Case 1.$\xi$, the camera was placed at 1300 mm from the measurement targets (Fig. 4.6). At this distance, the whole deflection of the beam can be captured at one time.

For multiple damage scenarios, the measuring camera was placed at $750-800$ mm from the beam. At this distance, only half of the beam can be measured at one time (Fig. 3.1). In this case, the beam is divided into two parts for measuring and the whole deflection of the beam was obtained by combining the left and right half measurements.

### 4.4.4 Data process and review

The calibration of the DIC system establishes a coordinate system for the measuring volume. Once the targets fall within the measuring volume, the coordinates of the targets can be obtained from the

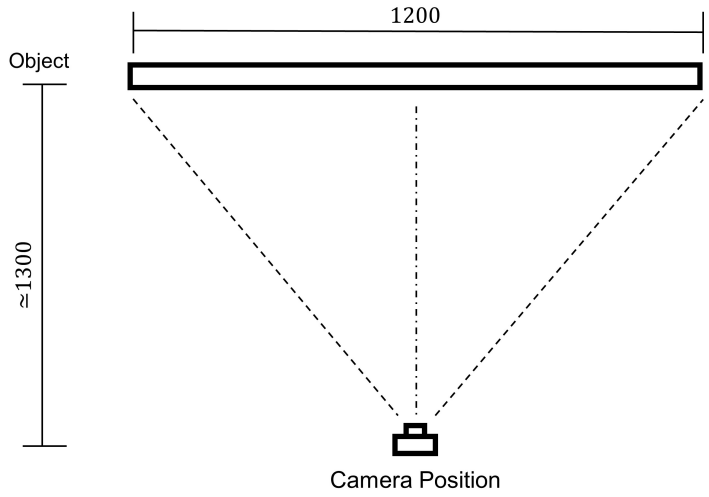


**Figure 4.6** Static experiment setup of single damage scenario (top view).

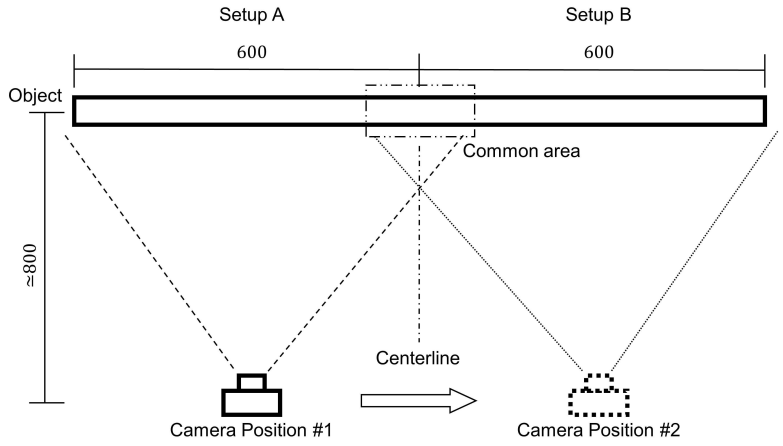


**Figure 4.7** Static experiment setup of multiple damage scenario (top view).

measuring system. During the tests, the cameras stayed at the same location for the unloaded and loaded structures. The subtraction of these two sets of coordinate values is the deflection of the beam under the applied load. Following this procedure, the deflections of the beam at its Reference State and Damaged State can be obtained. The sum of the deflections and their difference of all the load positions are plotted in Appendix F. The deflection measurements in Fig. F.1-F.4 show that the damage effect can barely be seen except for those cases of 50% damage. By taking the difference between the deflections, the noise exhibit a much higher influence than on the deflection measurements (Fig.. F.1-F.4). In the multiple damage scenarios (Fig. F.2-F.4), the main challenge is to identify the smaller damage with the presence of one or multiple more severe damage. Results in Fig. F.1-F.4 also show that the Partial Measuring procedure provides good measurements.

## 4.5 Experimental results: Case 2.20

In this section, the experimental Case 2.20 is used as an example for illustration purpose. Case 2.20 contains one 50% cracks at 425 mm, and one 20% crack at 775 mm.

### 4.5.1 Deflection-Spring approach

The deflection difference of the beam and the change in its slope, calculated by Eq. (2.21) are plotted in Fig. 4.8. It is clear that the 20% crack can not be spotted directly through observation to the measurement deflection difference. Moreover, the direct use of the central difference approach is not practicable.

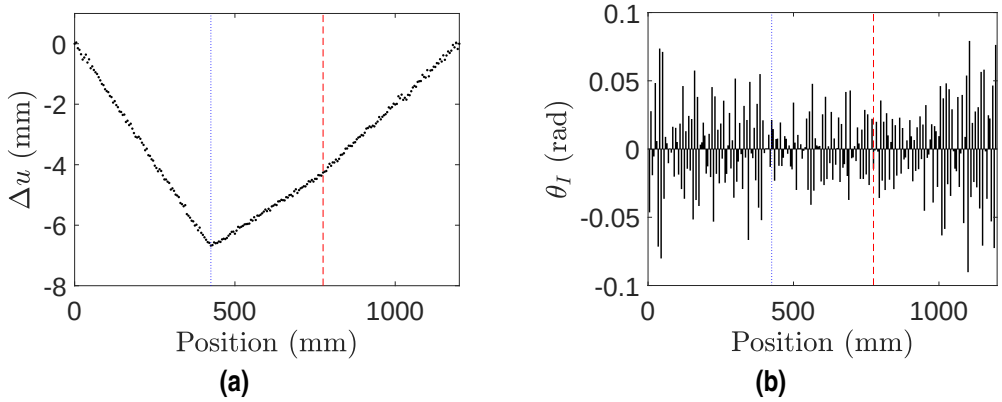


**Figure 4.8** Experimental measurements of Case 4.20: (a) deflection difference of the beam $\Delta u$; (b) change in the slope of $\Delta u$ (the red dashed line marks the 20% crack and the blue dotted line marks the 50% crack).

To estimate the piecewise linear trend of the deflection difference, the Nelder-Mead simplex search method is adopted. The algorithm can be achieved with predetermined Matlab function 'fminsearch'. In Fig. 4.9, the initial guess of the damage and the estimates are plotted. It can be seen that the algorithm return to the damage location directly. With either exact of or larger than the actual damage number as initial guess, the method returns to accurate results.

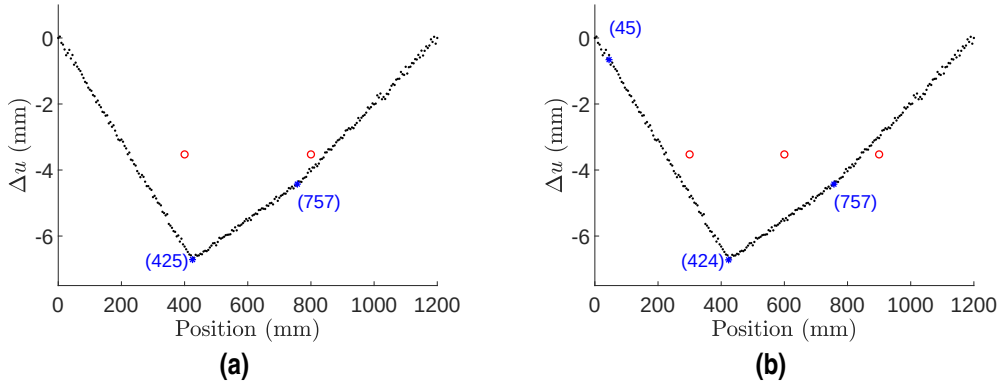


**Figure 4.9** Estimates by using the Nelder-Mead simplex search method: (a) with exact number of damage as the initial guess; (b) with one extra number of damage as the initial guess (the black dots (·) are measurements, the red circles (o) are the initial guess kinks, the blue stars (∗) are the estimates).

In the use of $l1$ Trend Filtering, the error function $R$ (Eq. (4.36)) and its change rate $\mathrm{d}R/\mathrm{d}\lambda$ are examined over a series of $\lambda$ values from 2 to 64. Through the illustration results in Fig. 4.10, one can see that the error $R$ monotonically increases as $\lambda$ increases but its increasing rate $\mathrm{d}R/\mathrm{d}\lambda$ exhibits a minimum. At that $\lambda$ value, the change of error $R$ is the least sensitive to the change of $\lambda$. In this

case, this value is $\lambda = 10$. The corresponding estimate $u_I^{l1}$ of the data is provided in Fig. 4.11(a). It

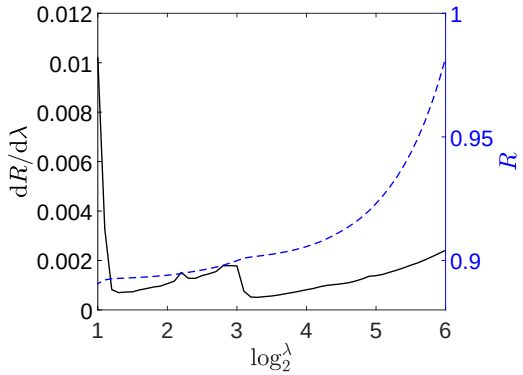


**Figure 4.10** The change rate of the error $\mathrm{d}R/\mathrm{d}\lambda$ (the black solid line) and the error $R$ (the blue dashed line) over $\lambda$ from the application of $l1$ Trend Filtering.

can be seen that the estimate fits the data fairly. The change in the slope can be calculated using Eq (2.21) based on $u_I^{l1}$. Furthermore, the estimate crack depths through spring Model 1 (Eq. (4.23) and (4.24)) can be obtained (Fig. 4.11). It can be seen that there is one crack of 9.5 mm at 425 and one crack of 3.9 mm at 755 mm.

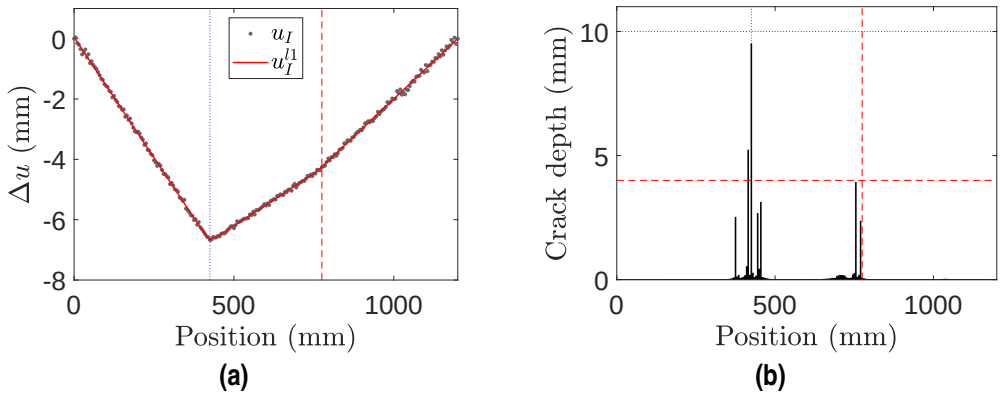


**Figure 4.11** (a) The estimate of $l1$ Trend Filtering with $\lambda = 10$: (b) the estimate crack depth with spring Model 1 (the red dashed lines mark the location and actual depth of the 20% crack and the blue dotted lines mark the location and actual depth of the 50% crack).

### 4.5.2 Deflection-Wavelet approach

Since the deflection difference is piecewise linear, the Gaussian wavelet with two vanishing moments is taken for the analysis. The number of scales are taken as $s = 2, 4, 6, 8$. The wavelet coefficient of the CWT is shown in Fig. 4.12(a). At both damage locations, the wavelet coefficients exhibit local maximum values over the scales. However, the 20% crack can not be clearly separated from other noise contaminated locations. It is worthy to note that at the noise contaminated locations, the local maximum wavelet coefficients do not necessarily increase with the increasing of the scale. The damage localization index from Eq. (4.39) is shown in Fig. 4.12(b), through which only 50% crack can be identified. Therefore, the trend estimate results provided previously ($u_I^{l1}$) is taken as the input data.

The wavelet coefficient and its LI with the estimate $u_I^{l1}$ are plotted in Fig. 4.13. The damage is located at 425 mm and 760 mm, clearly.

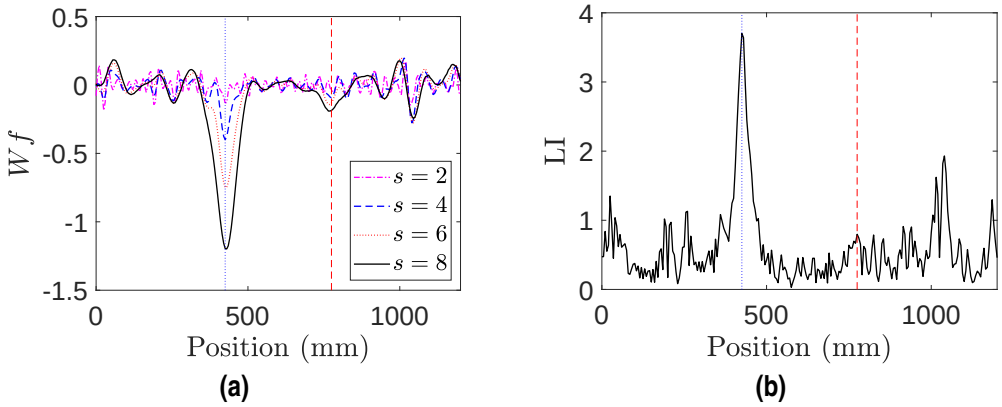


**Figure 4.12** Wavelet analysis of $u_I$: (a) wavelet coefficients; (b) damage localization indices (the red dashed line marks the location of the 20% crack and the blue dotted line marks the location of the 50% crack).

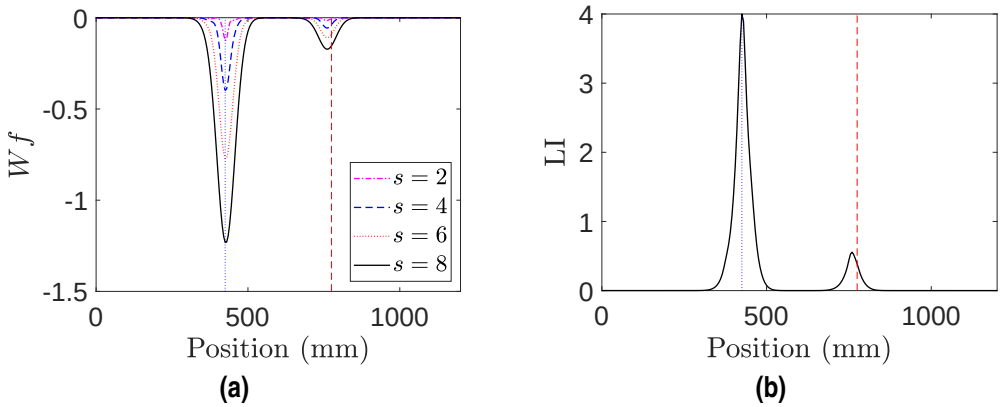


**Figure 4.13** Wavelet analysis of $u_I^{l1}$: (a) wavelet coefficients: (b) damage localization indices (the red dashed line marks the location of the 20% crack and the blue dotted line marks the location of the 50% crack).

Hence, the damage index of each crack can be obtained through Eq. (4.42) by examining the wavelet maximum over the scales in their logarithmic form. The DI of crack at 425 mm is $-16.5$ and the DI of crack at 760 mm is $-19.5$. Comparing the DI with the reference value Fig. E.10 in Paper E (Appendix E), the estimate crack depths are 9.2 mm at 425 mm and 3.6 mm at 760 mm.

## 4.6 Statically indeterminate beams

For statically indeterminate beams, the main challenge comes from two aspects. One is in the estimation of the change in the slope of the deflection difference. Since the deflection difference is a piecewise polynomial, the number of unknown parameters in the optimization problem is more than the linear problem. The other comes from the estimation of the damaged bending moments, for which the bending moment distribution can not be calculated easily, especially when there are boundary uncertainties. A direct solution is to experimentally compute the bending moment by measuring strain directly at the damage locations with strain gages, which requires the knowledge of the damage locations beforehand.

On the other hand, the bending moment distribution at State R can be computed based on the

curvatures of the undamaged deflection measurements or from classic beam theory. In Paper D (Appendix D), it is proposed to use the undamaged bending moments in place of the damaged bending moments in the quantification process. To better understand the error generated by this substitution, a beam of the same dimension as the test beam with a single damage situated at the midspan is used as an example.

Two sets of boundary conditions are considered. One is the perfectly fixed-fixed ends as the ideal boundary conditions and the other is elastic ends with rotational constraint to model the true boundary conditions (also known as the imperfect boundary conditions). For simplicity, the two constraints of the elastic ends are set to be equal. The State R and State D of the beam with these two sets of boundary conditions are sketched in Fig. 4.14. The internal bending moments at the damage for the ideal State R and State D are denoted by $m_R$ and $m_D$, respectively. The internal bending moments at the damage for the true State R and State D are denoted by $\tilde{m}_R$ and $\tilde{m}_D$, respectively.

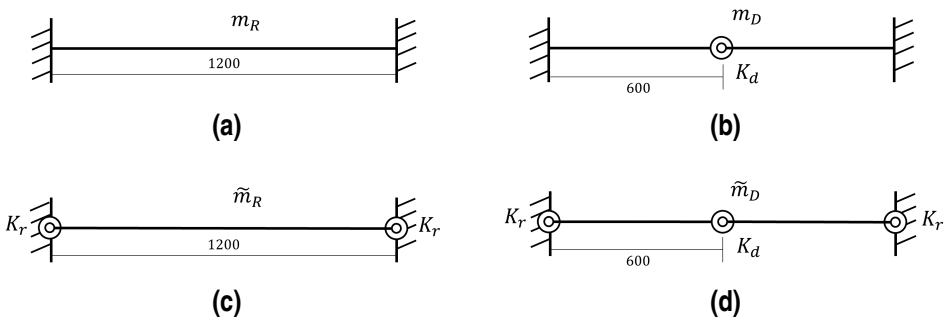


**Figure 4.14** The beam with ideal fixed-fixed ends (a) ideal State R; (b) ideal State D; and the beam with true elastic ends (c) true State R; (d) true State D.

First, the influence of the boundary uncertainties on the deflection of the beam is examined by comparing the deflections of the beam at true State R (Fig. 4.14(c)) with at ideal State R (Fig. 4.14(a)). The load condition is taken as the same as the experimental test. Three different values of $K_r = 200EI/L$, $300EI/L$, $400EI/L$ are selected and their corresponding deflections of the beam are plot in Fig. 4.15(a). The deflection differences between the beam with elastic ends and with fixed-fixed ends are shown in Fig. 4.15(b). We take $K_r = 300EI/L = 2.80\text{e}^6$ as the imperfect boundary conditions.

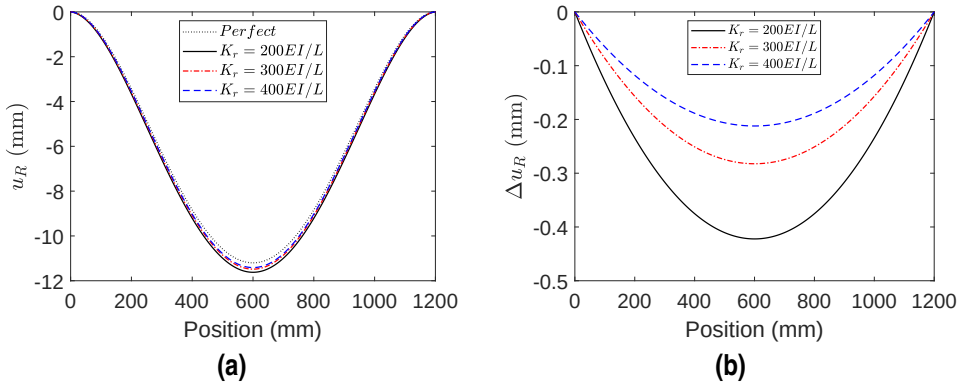


**Figure 4.15** (a) The deflection of the beam with different boundaries; (b) the deflection differences of the beam between true State R and ideal State R.

The damage is modelled by a rotational spring with constraint $K_d$. Four levels of damage ($\xi =$

10%, 20%, 35%, 50%) are considered and simulated with spring Model 2 (Eq. (4.23) and (4.25)). The equivalent rotational stiffness values are provided in Table 4.2. The deflection differences between State R and State D of the beam with the ideal boundary conditions and the imperfect boundary conditions are shown in Fig. 4.16. Table 4.3 shows that if the boundary is perfectly fixed-fixed, by using $m_R$ in place of $m_D$ produce a very small error. If the true boundary conditions

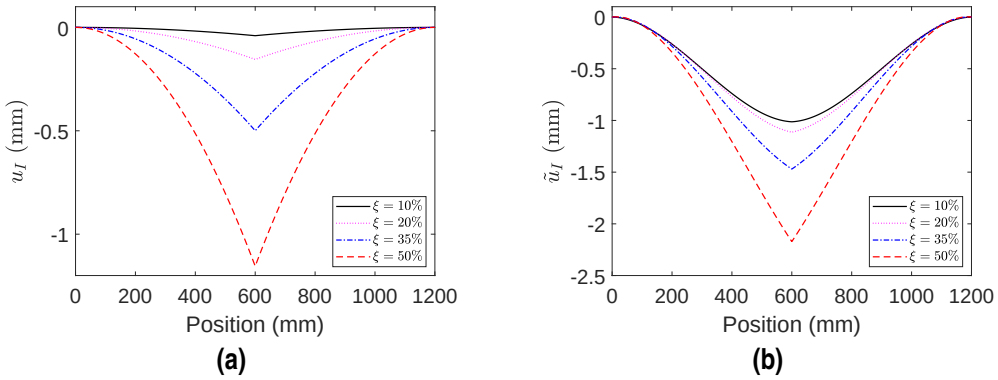


**Figure 4.16** The deflection differences of the beam with (a) ideal boundary conditions; (b) imperfect boundary conditions.

are imperfect and assuming that the boundary uncertainties $K_r$ are not known, we can estimate $\tilde{m}_R$ from the measurement of the true State R (Fig. 4.14(c)) and $m_R$ through analytical calculation of the ideal State R (Fig. 4.14(a)). Through the comparison in Table 4.3, it can be seen that using $m_R$ to substitute $\tilde{m}_D$ leads to similar error as using $\tilde{m}_R$. Both of the substitutions results underestimation of $\tilde{m}_D$ but the errors are small in this case.

**Table 4.2** Equivalent rotational stiffness of the damage.

| Damage severity $\xi$ (%) | 10 | 20 | 35 | 50 |
|---|---|---|---|---|
| $K_d$ (N·m/rad) | 5.23e$^6$ | 1.35e$^6$ | 4.12e$^5$ | 1.73e$^6$ |

**Table 4.3** The bending moment at damage location of beam with different boundary conditions.

| Damage severity | Bending moments at the damage (kN·m) | | | | Moment ratios | | |
|---|---|---|---|---|---|---|---|
| $\xi$ (%) | $m_R$ | $m_D$ | $\tilde{m}_R$ | $\tilde{m}_D$ | $m_R/m_D$ | $\tilde{m}_R/\tilde{m}_D$ | $m_R/\tilde{m}_D$ |
| 10 | −1.404 | −1.401 | −1.421 | −1.596 | 1.002 | 0.891 | 0.880 |
| 20 | −1.404 | −1.394 | −1.421 | −1.588 | 1.007 | 0.895 | 0.884 |
| 35 | −1.404 | −1.373 | −1.421 | −1.564 | 1.023 | 0.909 | 0.898 |
| 50 | −1.404 | −1.332 | −1.421 | −1.518 | 1.054 | 0.937 | 0.925 |

# 5 Conclusions and future work

## 5.1 Conclusions

In this thesis, one mode shape based damage localization method and two static based damage identification methods are presented. The premise is that the damage effect can be treated as a singularity in the displacement field. All three methods can locate the damage accurately without the use of numerical or analytical model. The main conclusions are drawn from those in the preceding chapters and the observations made in the papers provided in Appendix A to E.

The **Mode Shape-Wavelet approach** examines the mode shape differences of the structure between the states prior and posterior to the damage by using the continuous wavelet transform coefficients. It is proposed to use the wavelet coefficient of all identified mode shapes as the damage localization index. Two weighting parameters are applied to each mode in the summation calculation. One takes into account the damage effect on the change of natural frequencies and the other considers the noise influence on the measurement data. Moreover, an auxiliary mass is used in the experimental tests to probe the dynamic behaviors of the structure. The mode shapes obtained from the structure with the mass attached on different positions were used for the damage localization index calculation. The combined wavelet coefficient includes the wavelet coefficients for all modes and all mass locations. The results show that the use of the stationary roving mass helps to enhance the sensitivity of the methodology to damage.

The **Deflection-Spring approach** uses a discrete spring for damage modelling and locates the damage by identifying the discontinuities in the slope of the static deflection difference of the beam between State D and State R. Through a superposition scheme, the characteristic of the deflection difference can be derived and used for the formulation of the denoising problem. In the experimental case study, a direct search optimization algorithm named Nelder-Mead simplex algorithm is adopted to solve the denoising problem. Additionally, for statically determinate structures particularly, a trend filtering method based on the Lasso regression method is also examined with the experimental data. Both of the algorithms identified the damage locations accurately. Through an established characteristic function of the spring model, the crack depth can be assessed by using the estimated equivalent rotational stiffness of the crack from the experimental measurements.

The **Deflection-Wavelet approach** inspects the static deflection difference of the beam between the pre-damage state and post-damage state with the wavelet analysis. A damage localization index defined as the combination of the normalized wavelet coefficients for all scales is proposed to locate the damage. A damage quantification index which is damage location and external load independent is developed based on the Lipschitz condition. The interception with the y-axis of the linear relationship between the wavelet coefficient and the scales in logarithmic form can be taken as the damage index. The relationship between the damage index and the crack depth can be established by using a 3D finite element model of the beam with same dimension and boundary

conditions. The experimental case studies show that this method can identify the cracks at correct positions of accurate severity.

**In addition**, the experimental measurements in Appendix E indicate that it is feasible to use the DIC system for static measuring though the Partial Measuring Procedure. Finally, a simple numerical example shows that, for statically indeterminate beams with boundary uncertainties, the damaged bending moment at the crack can be approximated by the estimate of the undamaged bending moment from either experimental measurements or analytical calculation. The substitution results in a small error in the estimation of the damaged bending moment.

## 5.2 Future work

The scope of this thesis is grounded on the fundamental research on the damage identification using the displacement field of beam-type structures. Although experimental results show that the proposed methodologies perform reasonably well, there is still a big void to fill in order to achieve application in the industrial level. Some suggestions for the future work directions are given in this section.

Generally, the proposed methodologies should be tested with real damaged structures. Although the methods perform well with laboratory test results, the notch crack used in the current study is rarely seen in the industrial applications. The application of the DIC measuring system can be extended to measure the motion of the beams and the out of plane deflections of plate-type structures.

The superposition scheme for the static problem can be extended to the dynamic response. The concentrated damage introduces discontinuities in the derivatives of the mode shape differences between the reference state and damaged state. The feasibility of using the mode shape differences for the quantification purpose needs further studies.

For the Deflection-Spring approach, it is critical to estimate the trend of the deflection difference properly. The proposed Nelder-Mead simplex algorithm exhibits a lack of robustness for high dimension optimization problems. More robust algorithms need to be developed to address the denoising problem with high number of unknowns. Moreover, the approach can be modified for regional damage, the reduction of stiffness at a certain length of the beam, in which a new damage index needs to be developed. The bending moments at the boundaries of the damaged region might not be self-equilibrated. Thus, they should be balanced by the shear forces at the boundaries.

For the Deflection-Wavelet approach, the damage index can be simplified to a factor that is only related to the damage severity, mother wavelet function and the geometry of the cross-section. The current damage index is also related to the material of the beam and the boundary conditions besides those aforementioned. Furthermore, the wavelet analysis can be applied to 2D plate-type structures with concentrated damage. A new damage index for 2D structures needs to be developed.

# Bibliography


[1] Abdel Wahab, M., and De Roeck, G. Damage detection in bridges using modal curvatures: application to a real damage scenario. *J. Sound Vib. 226*, 2 (1999), 217–235.

[2] Abdo, M. A.-B. Parametric study of using only static response in structural damage detection. *Eng. Struct. 34* (2012), 124–131.

[3] Abdo, M.-B., and Hori, M. A numerical study of structural damage detection using changes in the rotation of mode shapes. *J. Sound Vib. 251*, 2 (mar 2002), 227–239.

[4] Allemang, R. J., and Brown, D. L. A correlation coefficient for modal vector analysis. In *Proc. 1st International Modal Anal. Conf.* (1982), pp. 110–116.

[5] Andreaus, U., Baragatti, P., Casini, P., and Iacoviello, D. Experimental damage evaluation of open and fatigue cracks of multi-cracked beams by using wavelet transform of static response via image analysis. *Struct. Control Heal. Monit. 24*, 4 (2017), 1–16.

[6] Andreaus, U., and Casini, P. Identification of multiple open and fatigue cracks in beam-like structures using wavelets on deflection signals. *Contin. Mech. Thermodyn. 28*, 1-2 (2016), 361–378.

[7] Babu, K. R. P., Kumar, B. R., Narayana, K. L., and Rao, K. M. Multiple crack detection in beams from the differences in curvature mode shapes. *APRN J. Eng. Appl. Sci. 10*, 4 (2015), 1701–1710.

[8] Baqersad, J., Poozesh, P., Niezrecki, C., and Avitabile, P. Photogrammetry and optical methods in structural dynamics – A review. *Mech. Syst. Signal Process. 86* (2017), 17–34.

[9] Barad, K. H., Sharma, D. S., and Vyas, V. Crack detection in cantilever beam by frequency based method. *Procedia Eng. 51*, 2013 (2013), 770–775.

[10] Bernal, D. Load Vectors for Damage Localization. *J. Eng. Mech. 128*, 1 (2002), 7–14.

[11] Bilello, C. *Theoretical and experimental investigation on damaged beams under moving systems*. Ph.d. thesis, Universitá degli Studi di Palermo, Italy, 2001.

[12] Caddemi, S., and Morassi, A. Crack detection in elastic beams by static measurements. *Int. J. Solids Struct. 44*, 16 (2007), 5301–5315.

[13] Caddemi, S., and Morassi, A. Detecting multiple open cracks in elastic beams by static tests. *J. Eng. Mech. 137*, 2 (2011), 113–124.

[14] Cao, M. S., Xu, W., Ren, W. X., Ostachowicz, W., Sha, G. G., and Pan, L. X. A concept of complex-wavelet modal curvature for detecting multiple cracks in beams under noisy conditions. *Mech. Syst. Signal Process. 76-77* (2016), 555–575.

[15] Castro, E., García-Hernandez, M. T., and Gallego, A. Damage detection in rods by means of the wavelet analysis of vibrations: Influence of the mode order. *J. Sound Vib. 296*, 4-5 (2006), 1028–1038.

[16] Chance, J., Tomlinson, G., and Worden, K. A simplified approach to the numerical and experimental modelling of the dynamics of a cracked beam. In *Proc. 12th Int. Modal Anal. Conf.* (Honolulu, HI, 1994), pp. 778–785.

[17] Chang, C. C., and Chen, L. W. Detection of the location and size of cracks in the multiple cracked beam by spatial wavelet based approach. *Mech. Syst. Signal Process. 19*, 1 (2005), 139–155.

[18] Choi, I.-Y., Lee, J. S., Choi, E., and Cho, H.-N. Development of elastic damage load theorem for damage detection in a statically determinate beam. *Comput. Struct. 82*, 29-30 (2004), 2483–2492.

[19] Chondros, T., Dimarogonas, A., and Yao, J. A continuous cracked beam vibration theory. *J. Sound Vib. 215* (1998), 17–34.

[20] Dawari, V. B., and Vesmawala, G. R. Structural damage identification using modal curvature differences. *IOSR-JMCE* (2013), 33–38.

[21] De Roeck, G. The state-of-the-art of damage detection by vibration monitoring: The SIMCES experience. *J. Struct. Control 10*, 2 (2003), 127–134.

[22] Di Paola, M., and Bilello, C. An integral equation for damage identification of Euler-Bernoulli beams under static loads. *J. Eng. Mech. 130*, 2 (2004), 225–234.

[23] Dimarogonas, A. D. Vibration of cracked structures: A state of the art review. *Eng. Fract. Mech. 55*, 5 (1996), 831–857.

[24] Doebling, S. W., Farrar, C. R., Prime, M. B., and Shevitz, D. W. Damage identification and health monitoring of structural and mechanical systems from changes in their vibration characteristics: A literature review. Tech. Rep. May, Los Alamos National Laboratory, New Mexico, 1996.

[25] Douka, E., Loutridis, S., and Trochidis, A. Crack identification in beams using wavelet analysis. *Int. J. Solids Struct. 40*, 13-14 (2003), 3557–3569.

[26] Fan, W., and Qiao, P. Vibration-based damage identification methods: A review and comparative study. *Struct. Heal. Monit. 10*, 1 (2011), 83–111.

[27] Farrar, C. R., and Jauregui, D. A. Comparative study of damage identification algorithms applied to a bridge: I. Experiment. *Smart Mater. Struct. 7*, 98 (1998), 704–719.

[28] Fernández-Sáez, J., Rubio, L., and Navarro, C. Approximate calculation of the fundamental frequency for bending vibrations of cracked beams. *J. Sound Vib. 225*, 2 (1999), 345–352.

[29] Friswell, M. I. Damage identification using inverse methods. *Philos. Trans. R. Soc. A Math. Phys. Eng. Sci. 365*, 1851 (2007), 393–410.

[30] Friswell, M. I., and Penny, J. E. T. Crack modeling for Structural Health Monitoring. *Struct. Heal. Monit. An Int. J. 1*, 2 (2002), 139–148.

[31] Gentile, A., and Messina, A. On the continuous wavelet transforms applied to discrete vibrational data for detecting open cracks in damaged beams. *Int. J. Solids Struct. 40*, 2 (2003), 295–315.

[32] Ghanbari Mardasi, A., Wu, N., and Wu, C. Experimental study on the crack detection with optimized spatial wavelet analysis and windowing. *Mech. Syst. Signal Process. 104* (2018), 619–630.

[33] Ghrib, F., Li, L., and Wilbur, P. Damage identification of Euler-Bernoulli beams using static reponse. *J. Eng. Mech. 138*, 5 (2012), 405–15.

[34] Gudmundson, P. The dynamic behaviour of slender structures with cross-sectional cracks. *J. Mech. Phys. Solids 31*, 4 (1983), 329–345.

[35] Ha, T. M., and Fukada, S. Nondestructive damage detection in deteriorated girders using changes in nodal displacement. *J. Civ. Struct. Heal. Monit. 7*, 3 (2017), 385–403.

[36] He, W.-Y., and Zhu, S. Moving load-induced response of damaged beam and its application in damage localization. *J. Vib. Control 22*, 16 (2015), 3601–3617.

[37] Hong, J. C., Kim, Y. Y., Lee, H. C., and Lee, Y. W. Damage detection using the Lipschitz exponent estimated by the wavelet transform: Applications to vibration modes of a beam. *Int. J. Solids Struct. 39*, 7 (2002), 1803–1816.

[38] Ismail, F., Ibrahim, A., and Martin, H. R. Identification of fatigue cracks from vibration testing. *J. Sound Vib. 140*, 2 (1990), 305–317.

[39] Janeliukstis, R., Rucevskis, S., Wesolowski, M., and Chate, A. Experimental structural damage localization in beam structure using spatial continuous wavelet transform and mode shape curvature methods. *Meas. J. Int. Meas. Confed. 102* (2017), 253–270.

[40] Janeliukstis, R., Rucevskis, S., Wesolowski, M., and Chate, A. Multiple damage identification in beam structure based on wavelet transform. *Procedia Eng. 172* (2017), 426–432.

[41] Jiang, R., Jáuregui, D. V., and White, K. R. Close-range photogrammetry applications in bridge measurement: Literature review. *Measurement 41*, 8 (2008), 823–834.

[42] Jiang, X., Ma, Z. J., and Ren, W.-X. Crack detection from the slope of the mode shape using complex continuous wavelet transform. *Comput. Civ. Infrastruct. Eng. 27*, 3 (2012), 187–201.

[43] Kim, H., and Huo, X. Optimal sampling and curve interpolation via wavelets. *Appl. Math. Lett. 26*, 7 (2013), 774–779.

[44] Kim, S.-J., Koh, K., Boyd, S., and Gorinevsky, D. l1Trend Filtering*. *SIAM Rev. 51*, 2 (2009), 339–360.

[45] Koh, K., Kim, S.-J., and Boyd, S. l1 Trending Filtering function Matlab, 2008.

[46] Kroworz, A., and Katunin, A. Non-destructive testing of structures using optical and other methods : A review. *SDHM 12*, April (2018), 1–17.

[47] Lee, E.-T., and Eun, H.-C. Damage detection of damaged beam by constrained displacement curvature. *J. Mech. Sci. Technol. 22* (2008), 1111–1120.

[48] Loutridis, S., Douka, E., and Trochidis, A. Crack identification in double-cracked beams using wavelet analysis. *J. Sound Vib. 277*, 4-5 (2004), 1025–1039.

[49] Mallat, S. *A Wavelet tour of signal processing*, 3rd ed. Academic Press, 2009.

[50] Mallat, S., and Hwang, W. L. Singularity detection and processing with wavelets. *IEEE Trans. Inf. Theory 38*, 2 (1992), 617–643.

[51] Messina, A. Detecting damage in beams through digital differentiator filters and continuous wavelet transforms. *J. Sound Vib. 272*, 1-2 (2004), 385–412.

[52] Messina, A. Refinements of damage detection methods based on wavelet analysis of dynamical shapes. *Int. J. Solids Struct. 45*, 14-15 (2008), 4068–4097.

[53] Montanari, L., Basu, B., Spagnoli, A., and Broderick, B. M. A padding method to reduce edge effects for enhanced damage identification using wavelet analysis. *Mech. Syst. Signal Process. 52-53*, 1 (2015), 264–277.

[54] Mottersheard, J., and Friswell, M. I. Model updating in structural dynamics: A survey. *J. Sound Vib. 167*, 2 (1993), 347–375.

[55] Nelder, J. A., and Mead, R. A simplex method for function minimization. *Comput. J. 7* (1965), 308–313.

[56] Ostachowicz, W., and Krawczuk, M. On Modelling of Structural Stiffness Loss Due to Damage. *Key Eng. Mater. 204-205* (2001), 185–200.

[57] Ostachowicz, W. M., and Krawczuk, M. Analysis of the effect of cracks on the natural frequencies of a cantilever beam. *J. Sound Vib. 150*, 2 (1991), 191–201.

[58] Pakrashi, V., Basu, B., and O' Connor, A. Structural damage detection and calibration using a wavelet-kurtosis technique. *Eng. Struct. 29*, 9 (2007), 2097–2108.

[59] Pakrashi, V., O'Connor, A., and Basu, B. A study on the effects of damage models and wavelet bases for damage identification and calibration in beams. *Comput. Civ. Infrastruct. Eng. 22*, 8 (2007), 555–569.

[60] Pandey, A., Biswas, M., and Samman, M. Damage detection from changes in curvature mode shapes. *J. Sound Vib. 145*, 2 (1991), 321–332.

[61] Quek, S. T., Wang, Q., Zhang, L., and Ang, K. K. Sensitivity analysis of crack detection in beams by wavelet technique. *Int. J. Mech. Sci. 43*, 12 (2001), 2899–2910.

[62] Quek, S. T., Wang, Q., Zhang, L., and Ong, K. H. Practical issues in the detection of damage in beams using wavelet. *Smart Mater. Struct 10* (2001), 1009–1017.

[63] Rizos, P. F., Aspragathos, N., and Dimarogonas, A. D. Identification of crack location and magnitude in a cantilever beam from the vibration modes. *J. Sound Vib. 138*, 3 (1990), 381–388.

[64] Rucka, M., and Wilde, K. Application of continuous wavelet transform in vibration based damage detection method for beams and plates. *J. Sound Vib. 297* (2006), 536–550.

[65] Rucka, M., and Wilde, K. Crack identification using wavelets on experimental static deflection profiles. *Eng. Struct. 28* (2006), 279–288.

[66] Rytter, A. *Vibrational based inspection of civil engineering structures*. PhD thesis, Aalborg Universitet, 1993.

[67] Simoen, E., De Roeck, G., and Lombaert, G. Dealing with uncertainty in model updating for damage assessment: A review. *Mech. Syst. Signal Process. 56* (2015), 123–149.

[68] Sohn, H., Farrar, C. R., Hemez, F. M., Shunk, D. D., Stinemates, D. W., Nadler, B. R., and Czarnecki, J. J. A review of structural health monitoring literature: 1996-2001. Tech. rep., Los Alamos National Laboratory, 2004.

[69] Solís, M., Algaba, M., and Galvín, P. Continuous wavelet analysis of mode shapes differences for damage detection. *Mech. Syst. Signal Process. 40*, 2 (2013), 645–666.

[70] Spanos, P. D., Failla, G., Santini, A., and Pappatico, M. Damage detection in Euler-Bernoulli beams via spatial wavelet analysis. *Struct. Control Heal. Monit. 13*, 1 (2006), 472–487.

[71] Štimac, I., and Kožar, I. Damage detection from displacement-in-time function. In *4th Youth Symp. Exp. Solid Mech.* (Castrocaro Terme, Italy, 2005), University of Rijeka, Croatia, pp. 5–6.

[72] Stöhr, S., Link, M., Rohrmann, R., and Rücker, W. Damage detection based on static measurements of bridge structures. In *Proc. Int. Modal Anal. Conf. IMAC XXIV* (St. Luis, Missouri, USA, 2006).

[73] Swamy, S., Reddy, D. M., and Prakash G, J. Damage detection and identification in beam structure using modal data and wavelets. *World J. Model. Simul. 13*, 1 (2017), 52–65.

[74] Tibshirani, R. J. Adaptive piecewise polynomial estimation via trend filtering. *Ann. Stat. 42*, 1 (2014), 285–323.

[75] Torczon, V. J. *Multi-directional search: a direct search algorithm for parallel machines*. PhD thesis, Rice University, 1989.

[76] Ulriksen, M. D., Tcherniak, D., Kirkegaard, P. H., and Damkilde, L. Operational modal analysis and wavelet transformation for damage identification in wind turbine blades. *Struct. Heal. Monit. 15*, 4 (2016), 381–388.

[77] Umesha, P., Ravichandran, R., and Sivasubramanian, K. Crack detection and quantification in beams using wavelets. *Comput. Civ. Infrastruct. Eng. 24*, 8 (2009), 593–607.

[78] Valença, J., Júlio, E. N., and Araújo, H. J. Applications of photogrammetry to structural assessment. *Exp. Tech. 36*, 5 (2012), 71–81.

[79] Wang, Q., and Deng, X. Damage detection with spatial wavelets. *Int. J. Solids Struct. 36*, 23 (1999), 3443–3468.

[80] Whalen, T. M. The behavior of higher order mode shape derivatives in damaged, beam-like structures. *J. Sound Vib. 309* (2008), 426–464.

[81] Worden, K., Farrar, C. R., Manson, G., and Park, G. The fundamental axioms of structural health monitoring. *Proc. R. Soc. A Math. Phys. Eng. Sci. 463*, January (2007), 1639–1664.

[82] Wu, N., and Wang, Q. Experimental studies on damage detection of beam structures with wavelet transform. *Int. J. Eng. Sci. 49*, 3 (2011), 253–261.

[83] Xu, Y. F., Zhu, W. D., Liu, J., and Shao, Y. M. Identification of embedded horizontal cracks in beams using measured mode shapes. *J. Sound Vib. 333*, 23 (2014), 6273–6294.

[84] Zhong, S., and Oyadiji, S. O. Identification of cracks in beams with auxiliary mass spatial probing by stationary wavelet transform. *J. Vib. Acoust. 130*, 4 (2008), 041001.

[85] Zhong, S., and Oyadiji, S. O. Crack detection in simply supported beams using stationary wavelet transform of modal data. *Struct. Control Heal. Monit. 18* (2011), 169–190.

[86] Zhu, L.-f., Ke, L.-l., Zhu, X.-q., Xiang, Y., and Wang, Y.-s. Crack identification of functionally graded beams using continuous wavelet transform. *Compos. Struct.* (2018).

[87] Zhu, X. Q., and Law, S. S. Wavelet-based crack identification of bridge beam from operational deflection time history. *Int. J. Solids Struct. 43*, 7-8 (2006), 2299–2317.

# Appendix A
# Paper A

Solís, M., Ma, Q., Galvín, P. (2018). "Damage detection in beams from modal and wavelet analysis using a stationary roving mass and noise estimation", *Strain*. 2018:e12266

The original paper can be found on: https://onlinelibrary.wiley.com

DOI: 10.1111/str.12266

Journal: Strain

ISSN: 0039-2103, 1475-1305

Journal Citation Reports (2017): Impact factor: 1.605

- Materials Science, Characterization & Testing: Q2 (15/33)

SCIMAGO (2017)

- Mechanical Engineering: Q1 (121/950)
- Mechanics of Materials: Q2 (98/480)

# Damage detection in beams from modal and wavelet analysis using a stationary roving mass and noise estimation

M. Solís, Q. Ma and P. Galvín

Department of Continuum Mechanics and Structural Analysis,
Escuela Técnica Superior de Ingeniería, Universidad de Sevilla,

**Abstract** This paper uses the Continuous Wavelet Transform Analysis on mode shapes for damage identification. The wavelet analysis is applied to the difference in the mode shapes between a healthy and a damaged state. The paper also includes a novel methodology for estimating the level of noise of the experimental mode shapes based on a standard Signal to Noise Ratio (SNR). The estimated SNRs are used for identifying and making emphasis on the less noisy data. Moreover, a mass attached to the structure is considered to enhance the sensitivity of the structure to damage. Modal analysis is performed for different positions of the mass along the beam. The results obtained for all the positions of the mass are combined so an averaging process is implicitly applied. The paper presents the results from an experimental test of a cantilever steel beam with different severity levels of damage at the same location. The results show that the use of the attached mass reduces the effect of noise and increases the sensitivity to damage. Little damage can be identified with the proposed methodology even using a small number of sensors and only the first five bending modes.

**Keywords** Damage detection and localization, beams, wavelet analysis, modal analysis, structural health monitoring

## A.1 Introduction

It is well known that the presence of damage (cracks) in a beam implies a change in its dynamic properties. Based on this fact, vibration based damage detection techniques try to detect the presence of damage by analyzing the change in natural frequencies, mode shapes and/or damping ratios. Some pioneering damage detection techniques [4] were based on the analysis of changes in natural frequencies, which are the most simple dynamic parameters to be measured. However, the natural frequencies are not sensitive to damage. Only a significant damage would induce a significant change in the natural frequencies. Moreover, the effect of damage may be masked by the effect of changes on environmental conditions, experimental noise, uncertainties, etc. On the other hand, natural frequencies are a global parameter of the structure, and therefore they can only provide information about the presence of damage but not about its location. In order to locate damage, the mode shapes of the structure may be used. From an experimental point of view, the identification of mode shapes requires a larger amount of sensors (more complex and expensive experimental set-ups) as well as more sophisticated system identification methods. This paper uses traditional piezoelectric accelerometers for the experimental modal analysis. However, it should be noted that developing Fiber Bragg Grating (FBG) sensors provide advantages for practical applications because of their light weight and multiplexing capabilities. Thus, the use of FBG sensors is rapidly increasing in the last years within the Structural Health Monitoring (SHM) community (see for instance [5, 17]). Despite of the experimental and mathematical efforts for modal identification, the changes in mode shapes induced by damage are usually subtle (unless severe damage is present) so damage can not be identified from mode shapes in a straightforward way. There is a significant number of papers that propose different techniques and damage detection parameters to analyze the information provided by mode shapes [4].

The wavelet transform is a rather new mathematical tool that has been developed from the 90s for signal processing and information encoding [25]. The wavelet transform is sensitive to local changes in the original signal. The wavelet coefficients show a singular behavior, ridges or peaks, when a discontinuity or a sudden change occurs. Thus, they can be used as an indicator of damage when applied to mode shapes, assuming that damage leads a discontinuity in mode shapes. Several authors have made different proposals to damage detection in structures by applying wavelet transform to mode shapes, time response, static deflection, etc., after the pioneering work by Surace and Ruotolo [26]. The state-of-the-art in wavelet transform exploring the possibilities of this technique for SHM was reviewed by Taha et al. [27] and Katunin [9]. The researches have been focused on the choice of the wavelet function, the severity of the identified defect, the experimental noise and the spatial sampling interval (i.e. the number of sensors).

For beam type structures, Rucka [20] presented a numerical and experimental study of a cantilever beam with damage depth of 20%, 10% and 5% of the beam height. She analyzed the first eight mode shapes and the influence of the mode order on the effectiveness of damage detection by the Continuous Wavelet Transform (CWT). From this analysis, the smallest detectable defect was found to be of a depth of 10% of the beam height and its localization was only possible at higher vibration modes. Moreover, the methodology was more effective using wavelets with smaller numbers of vanishing moments. Cao et al. [3] used the wavelet transform coupled with the Teager energy operator to detect multiple damage in beams. The methodology is based on the curvature mode shapes since this parameter showed stronger immunity to noise and greater sensitivity to damage. The authors identified multiple damage of small dimensions in beams in high-noise conditions from this approach. Recently, Ulriksen and Damkilde [28] introduced a damage localization method composed of two signal processing steps, a CWT and the application of a generalized discrete Teager Kaiser energy operator, and a subsequent statistical evaluation step to discriminate between damage-induced discontinuities and other signal irregularities. The authors showed the applicability of the method in the context of an experimental work with a scaled wind turbine blade. This methodology requires a relatively fine measurement density.

For two dimensional structures, Rajendran and Srinivasan [18] studied the detection of damage, modeled as an added mass, in glass fiber reinforced polymer plates employing two-dimensional wavelet packet transform, using rotational mode shape as an input. The proposed algorithm was sensitive to damage in a noisy environment with 5% noise. Katunin and Przystaka [12] presented an approach for damage identification in composite plates based on the fractional wavelet transform of modal displacements. They improved the sensitivity of the method by considering spatial fractional B-spline wavelets with optimized parameters. After, Katunin et al. [11] presented a method for automated damage identification and classification from the computed tomography scans using a wavelet-based algorithm. The authors tested two plates made of composite materials. The plates contained damages produced by cutting the circular holes by the water-jet method. The advantage of this methodology is the possibility of automated extraction and classification of predefined types of defects and it is also possible to evaluate the direction of damage propagation. Later, Katunin [10] proposed a method for the identification of damages in cross-ply epoxy laminated plates reinforced with E-glass cloth caused by stone impacts using wavelet analysis of modal data with quincunx non-separable wavelets. The obtained results showed that the impact damages, both cracks and delaminations, are well recognizable for even low energies of an impact. The main advantage of the application of quincunx wavelets of optimally selected fractional order for damage identification was the increasing sensitivity of the method with simultaneous decreasing of the computational time.

Regarding the required number of sensors, Montanari et al. [15] examined the effect of the spatial sampling interval in damage detection by CWT. A parametric study was carried out by analyzing the first three mode shapes of two set-ups for a beam varying the sampling interval, the noise level, the padding method, the wavelet function, the crack depth and position along the beam, and the

mechanical and geometrical beam parameters. The coiflet wavelet function with four vanishing moments was found to be the most effective one. The authors determined the minimum optimal number of sampling points in relation to the beam deflection shape and the damage location.

Solis et al. [23] have previously proposed a simple damage detection technique based on the wavelet analysis of the difference in mode shapes between a healthy and a damaged state. The main idea of this technique is to combine all the information provided from the wavelet analysis of all the identified mode shapes and the natural frequencies by a weighted addition of the wavelet coefficients according to the changes in the natural frequencies for each mode. This methodology was successfully applied to cracked steel beams. In this paper, the authors include some new ideas for making the proposed damage detection method more robust and sensitive to little damage.

Firstly, a mass is attached to the structure and modal analysis is performed for different positions of the mass. The mass is at a fixed position for each experimental test (it is not a moving load) but it changes its position from one test to another. Zhong and Oyadiji [34, 36] previously used this idea for damage detection in beams and first used the term 'stationary roving mass'. This term is also used in this paper as an acknowledgement. The response of the damaged beam depends on its stiffness, mass distribution and boundary conditions. Hence, the presence of the additional mass changes the modal properties (natural frequencies and mode shapes) of the beam. The natural frequencies and mode shapes from all the mass positions are analyzed in order to enhance the sensitivity to damage: at some positions of the mass, the dynamic response of the beam (and therefore its modal properties) is more affected by the presence of the mass so it is easier to detect the damage if compared to the situation in which no mass is added. Secondly, an estimation of the level of noise for each mode (Signal to Noise Ratio (SNR)) is performed by comparing the experimental mode shapes with a set of reference mode shapes obtained from a smoothed spline interpolation of the experimental mode shapes. The mode shapes that exhibit a higher SNR are considered more reliable for damage detection and their information should be specially analyzed. Finally, the proposed methodology combines the information obtained from all positions of the roving mass and the estimated SNRs. It analyzes the results for each mode individually and also for all the modes together.

The outline of the paper is as follows. Firstly, the proposed damage detection method is described from a mathematical and practical point of view. Secondly, the experimental work is described and the experimental results are presented and discussed. Finally, some conclusions are drawn.

## A.2 Mathematical definition of the proposed damage detection method

The proposed damage detection method is based on the wavelet analysis of mode shapes. The CWT of a function $f(x)$ can be defined as:

$$CWT_f(u,s) = \frac{1}{\sqrt{s}} \int_{-\infty}^{+\infty} f(x) \Psi^* \left( \frac{x-u}{s} \right) dx \tag{A.1}$$

where $\Psi$ is the wavelet function. Expression (A.1) is a convolution integral in which the resulting wavelet transform depends on two fundamental parameters of the wavelet function: the translation parameter ($u$) and the scale parameter ($s$). By changing the translation parameter, the wavelet function 'moves' along the $x$ coordinate, whereas by changing the scale parameter, the wavelet function stretches or shrinks. In the end, the values of the resulting wavelet transform indicate how similar is the original function to the wavelet function for each value of the translation and scale parameters. A more in depth description of the mathematics of the wavelet transform and its applications can be found elsewhere [16, 19, 23, 27, 28, 31].

From a structural damage detection perspective, the usefulness of the wavelet analysis is that it is sensitive to local and subtle changes in the original signal. Thus, it can be used for instance to indicate the effect of damage on mode shapes, since the changes induced by damage will induce a

singular behavior of the wavelet coefficients (local increase on their values). The selection of the wavelet function can affect the obtained results. The shape of the wavelet function should be as close as possible to the change induced by damage, so the wavelet coefficients exhibit the highest values at damage locations. However, it is not usually feasible to know the actual effect of damage. In most applications, the choice of the wavelet function is made by trial and error or based on previous applications (a review of different used wavelets can be found in previous works [21, 27]). There are also some papers that have addressed this issue from a more rigorous mathematical point of view [9, 12, 16, 20], but up to now there is a lack of a robust criteria for selecting the best wavelet function. In a previous work [23], where an open crack was also introduced on a steel beam, the authors compared the results obtained with Daubechies, Gauss and Symlet wavelets with 2 and 3 vanishing moments. Daubechies wavelet was more sensitive to damage and provided better results, so Daubechies wavelet with 2 vanishing moments is chosen in the present analysis, as the type of damage is similar to the previous work.

The wavelet coefficients of the wavelet function are related to the derivatives of the input signal of the same order as the number of vanishing moments of the wavelet function [6, 14, 22]. Therefore, by selecting 2 vanishing moments, the CWT coefficients of mode shapes differences give information about the change in the second derivatives of mode shapes (modal curvatures) which is a well-known sensitive feature for damage detection. Thus, the relation between the obtained wavelet coefficients using a Daubechies wavelet with 2 vanishing moments and the changes in modal curvatures justifies the sensitivity of the proposed methodology to damage. However, this paper also shows results obtained with other wavelets in order to validate the wavelet choice.

The proposed methodology applies the wavelet transform to detect changes in the dynamic properties of the structure between two different states: a reference state and a possible damaged one. Thus, the wavelet transform is applied to the difference between the damaged mode shape and the undamaged one ($\Phi^i_{diff}$) for each mode $i$:

$$CWT^i_{\Phi_{diff}}(u,s) = \frac{1}{\sqrt{s}} \int_{-\infty}^{+\infty} \Phi^i_{diff}(x) \Psi^* \left( \frac{x-u}{s} \right) dx \tag{A.2}$$

In order to avoid the so-called edge effect in the wavelet transform, an anti-symmetric extension of the signal is applied at both of its ends [23, 25]. When analyzing the wavelet coefficients, only those corresponding to the original part of the mode shapes are considered, whereas those out of that part (that are affected by the edge effect) are disregarded. On the other hand, the mode shapes are also mathematically transformed through a cubic spline interpolation. This transformation reduces the influence of the experimental random and local noise, which is a major concern when trying to identify the effect of a potential damage that may be masked by noise. It also allows to obtain additional modal information at interpolation points, which allows obtaining a more clear information from wavelet analysis [23, 28, 31, 35].

The wavelet coefficients obtained from Expression (A.2) are usually plotted in a 2D colored picture (scalogram) where the axes are the positions along the beam and the scale. The colors in the picture indicate the values of the coefficients for each position and scale. This paper applies a simple tool proposed by the authors to analyze the coefficients for all scales in one single picture [23]. It consists of the use of absolute values and the normalization to the maximum value for each scale. If no normalization is performed, higher values are obtained for higher scales, so no information about the singularities and ridges can be observed from the color map of the scalogram for low scales. By normalizing the values for each scale, one can see the oscillations appearing at each scale and the effect of damage can be more easily detected. Therefore, when the coefficients from all modes are combined and normalized for each scale, the effect of damage can be noticed for all scales and is clearly detected when maximum values (unity) are obtained for every scale at a certain location. The actual mathematical meaning of the wavelet coefficients is lost with the normalization

process, but this is irrelevant since they are used as a relative indicator of the presence of damage, and no interpretation is obtained from their actual numerical values.

This paper also introduces the attachment of a mass to the structure at certain positions along the beam, so the mode shapes are obtained for all those positions. It should be noted at this point that the structure changes (the mass distribution changes) when the mass is moved from one position to another. However, an experimental modal analysis is performed for each position of the mass for the reference and for the damaged state and the wavelet transform is applied to the difference in mode shapes for each mass position. Therefore, the difference in the mode shapes is theoretically (if there is no noise effect) coming only from the effect of damage and not from a different mass distribution. The change induced by the mass position is consequently canceled out, and all the performed wavelet analysis are consistent and pointing to the damage location, and not to the mass position. At each step of the wavelet analysis, the analyzed structure is the same, except for the damage. In addition, the added mass will emphasize the effect of damage at certain positions.

However, it is not feasible from a practical point of view to predict which are the most relevant positions of the mass for damage detection. Actually, they will depend on the damage position, the mode shape and the boundary conditions. Thus, the results obtained for each position are combined in a single scalogram by adding up the scalograms for each mass position. This addition reduces the effect of the random noise in the mode shapes along the beam. It also allows considering more favorable scenarios for damage detection when compared to the situation where no roving mass is considered, because of the amplification of the effect of damage for some positions of the mass. Moreover, the attached mass can also provide some additional benefits in real applications. For instance, it can enforce cracks to be permanently opened during the tests, so its effect can be more easily identified. This can be specially advantageous for prestressed beams, in which the effect of a crack on the dynamic properties of the beam is reduced [13, 29]. However, the effect of the roving mass should be specifically analyzed since the sensitivity of the methodology could be affected depending on the capability of the mass to keep the crack open or not during the tests.

When computing the addition of wavelet coefficients, the authors proposed in a previous work [24] that the coefficients are weighted through a coefficient based on the shift in natural frequency between the reference and the damaged state. Since the change in natural frequency is an indicator of how the damage has affected the structure, then the information coming from the most affected mode shapes is emphasized.

In addition to that, this paper also introduces a novel weighting parameter for the addition of wavelet coefficients. It is based on the estimated noise of each mode, so the less noisy mode shapes are also emphasized. The noise in mode shapes is a key issue affecting the sensitivity to damage. If no noise is present, the proposed method is extremely sensitive to little damage [24]. Therefore, the sensitivity to damage is enhanced by estimating the noise level on the mode shapes in order to evaluate their accuracy and subsequently highlight the information provided by the less noisy mode shapes. Thus, for a single mode $i$, the resulting scalogram can be computed as:

$$CWT^{i}_{sum}(u,s) = \sum_{j=1}^{M} \left| CWT_{\Phi^{ij}_{diff}}(u,s) \right| \cdot \left( 1 - \frac{\omega_u^{ij}}{\omega_d^{ij}} \right)^2 \cdot \mathrm{SNR}_{ij} \tag{A.3}$$

where subindex $j$ is related to each position of the added mass, $\omega_u$ and $\omega_d$ are the natural frequencies for the undamaged and damaged states respectively, and $\mathrm{SNR}_{ij}$ is the estimated Signal to Noise Ratio. The obtained normalized scalogram ($CWT^{i}_{sum\_norm}$) is obtained from Equation (A.4) and it can be used for analyzing the information provided by mode $i$ for damage detection.

$$CWT^{i}_{sum\_norm}(u,s) = \frac{CWT^{i}_{sum}(u,s)}{max|CWT^{i}_{sum}(u,s)|_s} \tag{A.4}$$

The $\mathrm{SNR}_{ij}$ is defined in its usual form for experimental data analysis [2]:

$$\mathrm{SNR}_{ij}[\mathrm{dB}] = 10\log\left(\frac{P^{ij}_{mode}}{P^{ij}_{noise}}\right) \tag{A.5}$$

where $P^{ij}_{mode}$ is the power of the mode shape $i$ for the mass position $j$, defined as the square of its Root Mean Square value:

$$P^{ij}_{mode} = \frac{\sum_{k=1}^{n} x_k^{ij^2}}{n} \tag{A.6}$$

where $x_k^{ij}$ is the $k$th component of the mode shape vector and $n$ is the number of its components, and $P^{ij}_{noise}$ is the estimated power of the noise:

$$P^{ij}_{noise} = \frac{\sum_{k=1}^{n}\left(x_k^{ij} - x_k^{ij^{ref}}\right)^2}{n} \tag{A.7}$$

where $x_k^{ij^{ref}}$ is the $k$th component of a reference noise-free mode shape vector. In this paper, the cubic spline interpolation of the corresponding mode shape $i$ for the mass location $j$ is used as a reference noise-free mode.

The previous definition of the SNR is usually applied to experimentally acquired signals. In this case, the mode shapes are considered as noisy experimental signals, although they are not a directly acquired experimental signal. The noise in mode shapes comes from the original noise of the accelerometers and impact hammer signals, and also from the numerical process of the modal analysis. At this point, it should be noted that wavelet analysis is well-known mathematical tool for denoising signals (usually the Discrete Wavelet Transform). Therefore, it could be also used for filtering the acquired recordings from the sensors and increase their resulting SNR [8, 33]. However, this enhancement is not likely to have a significant effect on the identified mode shapes since no filtering should be applied at frequencies close to the natural frequencies of the structure. On the other hand, this paper is interested in the SNR of the mode shapes and not of the signals from the accelerometers. Then, the Continuous Wavelet Transform is applied for detecting changes in mode shapes induced by damage and not for denoising.

The normalized scalogram obtained for each experimentally identified mode shape can be analyzed separately in order to look for potential damage effects. Unfortunately, not all the modes may be sensitive to damage. Some of them may clearly indicate the presence of damage whereas some others do not exhibit any influence from damage and they may show irregular behavior of the wavelet coefficients because of the noise. In real applications, where the actual position of the damage is not really known, it may not be possible to distinguish between the effect of noise and the effect of damage and eventually to properly choose the mode shapes that are really sensitive to damage. The results from the less noisy mode shapes is more accurate, and especially in those regions where they exhibit maximum modal amplitudes, since those regions are more sensitive to damage.

Finally, the information coming from all the identified mode shapes can also be combined to obtain a global result that can also provide some additional information about the presence of damage and also some implicit information on which mode is more reliable and sensitive to damage, as far as it is similar to the result obtained with any individual mode:

$$CWT_{sum}(u,s) = \sum_{i=1}^{N} CWT^{i}_{sum}(u,s) = \sum_{i=1}^{N}\sum_{j=1}^{M}\left|CWT_{\Phi^{ij}_{diff}}(u,s)\right| \cdot \left(1 - \frac{\omega_u^{ij}}{\omega_d^{ij}}\right)^2 \cdot \mathrm{SNR}_{ij} \tag{A.8}$$

where subindex $i$ and $j$ are related to each mode shape ($N$ is the number of experimentally identified

mode shapes) and each position of the added mass ($M$ is the number of positions considered for the mass), respectively, whereas $u$ and $d$ stand for the undamaged and the damaged case, respectively. The final scalogram obtained from Equation (A.8) is also normalized for every scale according to Equation (A.9), and the obtained normalized scalogram ($CWT_{sum\_norm}(u,s)$) can be used to analyze the whole information from all the identified mode shapes in just one single picture.

$$CWT_{sum\_norm}(u,s) = \frac{CWT_{sum}(u,s)}{max|CWT_{sum}(u,s)|_s} \tag{A.9}$$

It is worth to mention at this point that the normalization process of Equations (A.4) and (A.9) are carried out after the addition is performed for all positions of the mass, and after the addition for all positions of the mass and all the mode shapes, respectively. Therefore, during the addition process, the original values of the wavelet coefficients are kept, so the relative differences between different mode shapes and mass positions are kept, though they are modulated through the weighted coefficients related to the shift in natural frequencies and SNR.

The interpretation of the normalized scalogram for damage detection is further discussed from a practical point of view in the following section, where experimental damage detection results are presented.

## A.3 Experimental results

### A.3.1 Test set-up and experimental modal analysis

This section presents the experimental results obtained for a steel cantilever beam with a cross section of 30 mm $\times$ 10 mm and a length ($L$) of 800 mm. Figure A.1 shows pictures of the real test and a scheme of the tested beam. The damage is artificially induced by a saw cut (2 mm width approximately through all the beam width) at a distance of $0.4L$ from the fixed end of the beam. Increasing depths of the cut were considered during the experimental campaign: 1 mm, 2 mm and 5 mm depths that correspond to 10%, 20% and 50% of the height of the beam are the three damage scenarios.

The dynamic response of the beam was measured at 32 measuring points by using two set-ups of 16 roving accelerometers (general purpose piezoelectric type with 100mV/g nominal sensitivity and a mass of 4 grams). The measuring points were distributed along the beam every 25mm leaving 10mm from the fixed and from the free end. The accelerometers were located at the odd positions in one set-up and at the even positions in the other. The accelerometers were fixed to the beam through a threaded screw.

The location of the damage is just in the middle of two adjacent measuring points, which is a demanding situation for damage detection. If the damage location was coincident with a measuring point, the damage would be more easily identified [23].

Two different values of the attached mass have used for the tests: a 5% and a 10% of the total mass of the beam (1.884kg). In this case, an aluminium device was designed to be hanged from the beam at different positions, as shown in Figure A.2. Eleven equally distributed positions were considered along the beam.

The excitation force is applied at the free end of the beam with an impact hammer and the averaged Frequency Response Functions (FRFs) are obtained from 5 impacts for the 16 measuring points of each set-up. The mode shapes and natural frequencies are identified by applying the Poly-reference Least Squares Complex Frequency Domain (plSCF) algorithm [7] to the FRF matrix of the whole beam (32 measuring points) obtained from the assemble of the FRF matrices of both set-ups. Table A.1 shows the identified first five natural frequencies for each damage scenario and the reference state and Table A.2 shows the Modal Assurance Criterion (MAC) values of each

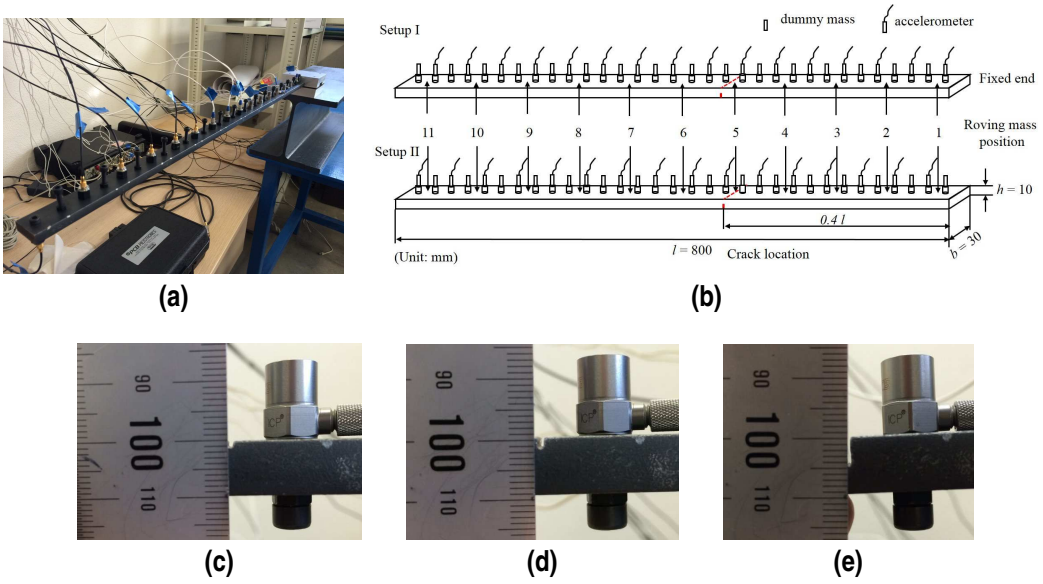


**Figure A.1** (a) Picture of the experimental setup (b) scheme of the tested beam (c) 10% crack (d) 20% crack (e) 50% crack.

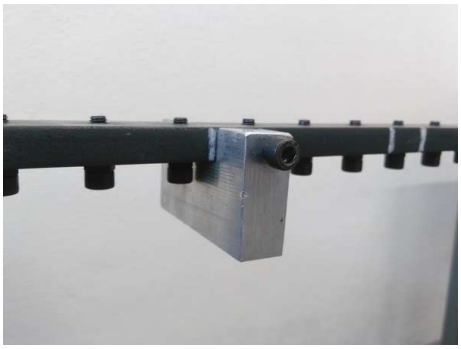

**Figure A.2** Picture of the added roving mass.

mode shape between its damaged and reference states. Figure A.3 illustrates the obtained FRFs by showing the results at the free end of the beam for the undamaged and the damaged states. For the sake of brevity, these tables and figure include only the results without roving mass. Similar values and conclusions are obtained with the roving mass attached at all different positions. From the tables, it can be seen that the change of natural frequencies induced by damage, even for a 50% crack, is less than 2%, so the damage can not be detected from such a global and simple parameter. The MAC values are all higher than 0.98, which means that they are very well correlated and similar to each other. Figure A.3 also shows that the effect of damage is very little on the structural response. The FRF for each damaged state is very similar to the undamaged situation. Only a slight shift in the natural frequencies is observed for the 50% crack.

Figure A.4 shows the five identified mode shapes for the undamaged and the 50% damage scenarios without the roving mass. Modes shapes are normalized to unit maximum amplitude in order to obtain a more consistent information from different states of the beam (different damages and mass positions). It can be seen that the effect of damage is negligible in the mode shapes even for such a severe damage, so any advanced mathematical analysis (for instance wavelet analysis) is necessary to detect the subtle and local changes induced by damage. From a practical point of view,

**Table A.1** Experimental natural frequencies [Hz] for each damage scenario (no added mass).

| Mode\Scenario | Intact | 10% | 20% | 50% |
|---|---|---|---|---|
| 1 | 11.70 | 11.68 | 11.64 | 11.53 |
| 2 | 72.97 | 72.68 | 72.53 | 70.43 |
| 3 | 206.63 | 206.44 | 206.41 | 205.47 |
| 4 | 402.84 | 402.28 | 401.02 | 391.87 |
| 5 | 662.47 | 661.21 | 660.04 | 651.52 |

**Table A.2** MAC values of each mode of each damage scenario with the corresponding undamaged one (no added mass) damage scenario.

| Mode\Scenario | 10% | 20% | 50% |
|---|---|---|---|
| 1 | 0.9879 | 0.9966 | 0.9981 |
| 2 | 0.9999 | 0.9997 | 0.9994 |
| 3 | 0.9997 | 0.9995 | 0.9993 |
| 4 | 0.9996 | 0.9995 | 0.9975 |
| 5 | 0.9997 | 0.9978 | 0.9931 |

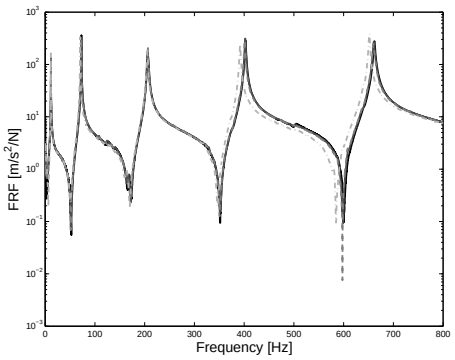


**Figure A.3** FRF of the free end of the beam for the undamaged (solid black line), 10% crack (solid gray line), 20% crack (dashed gray line) and 50% crack (dashed-dotted gray line) states (no added mass).

it should be mentioned at this point that because of the light weight of the structure, even the small mass of the attached accelerometers (4 grams) influence the dynamic response of the structure. This effect would not be relevant if all the accelerometers were always at a fixed position, because their effect would be the same in both the reference and the damaged state. For the same reason, the holes and their corresponding screws for attaching the accelerometers do not affect the damage detection results, since they are always present. However, because of the slightly different distribution of the mass of the accelerometers for each set-up, the identified mode shapes for the two set-ups did not match properly between each other. In order to solve this issue, equivalent dummy masses were added at each measuring point where no accelerometer was present at each set-up. These additional masses consisted of an additional nut and a screw attached to the screw at each measuring point where an accelerometer was not present for each set-up (Figure A.5). It can be seen in Figure A.4, therefore, that no discontinuity can be observed in the mode shapes because of a different mass distribution for the two set-ups. On the other hand, the cables (Figure A.1(a)) were hanged from an auxiliary structure to minimize their effect on the beam response.

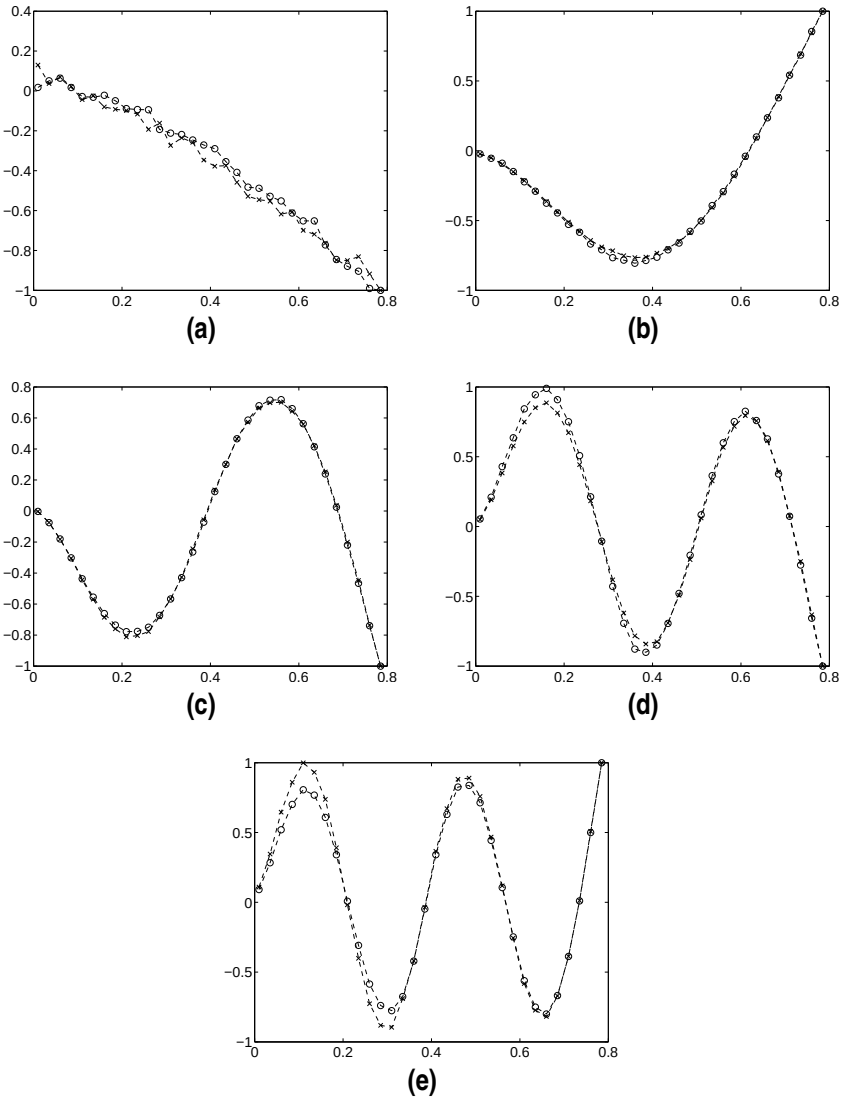


**Figure A.4** Identified mode shapes for the undamaged (-x-) and the 50% damage (-○-) state (no roving mass).

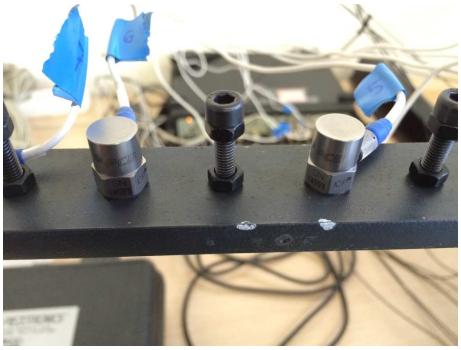

**Figure A.5** Picture of the accelerometer and the dummy accelerometer masses.

Figure A.4 shows that the experimental noise is apparently very small for modes 2 to 5. The mode

shapes are smooth and well identified. However, both the undamaged and 50% damage states show appreciable noise in mode 1. An hypothesis for the noise in mode 1 is an imprecise operation of the accelerometers in such a low frequency range. Nevertheless, this noisy information will serve as a proof of the ability of the proposed methodology to detect damage even when some noisy results are obtained, as it will be discussed in the next section.

At this point, the actual level of noise in the experimental results is estimated by comparing the experimentally identified mode shapes with numerically obtained mode shapes for the undamaged state. This preliminary analysis is useful to identify which modes are expected to be more reliable for damage detection. In addition, the estimation of this real level of noise can be useful for comparison purposes with future researches and also for providing reference values in researches where artificial noise is introduced to numerically obtained mode shapes. Firstly, a numerical model is developed including the non structural masses (roving mass, mass of the accelerometers and dummy masses) as well as a rotational spring at the fixed end of the beam, in order to match as closely as possible the experimental results. The model is built using a Matlab toolbox developed by Yang [32]. An optimum value of $1.8 \cdot 10^5$ Nm/rad was found for the stiffness of the rotational spring by a manual calibration. Table A.3 shows the MAC values between the experimental and the analytical mode shapes for all positions of the roving mass. Figure A.6 illustrates how similar are the experimental and numerical mode shapes by showing them when no roving mass is present. The very high values of MAC and the mode shapes from Figure A.6 show that the numerical model represents very accurately the real test. Thus, the numerical modes can be considered as a set of reference noise free modes to estimate the SNR of the experimental mode shapes by applying Equations (A.5), (A.6) and (A.7).

**Table A.3** MAC values between numerical and experimental modes (undamaged state) for each mode and for each position of the roving mass.

| Mass Position\Mode | 1 | 2 | 3 | 4 | 5 |
|---|---|---|---|---|---|
| 1 | 0.9955 | 0.9988 | 0.9973 | 0.9950 | 0.9919 |
| 2 | 0.9957 | 0.9983 | 0.9976 | 0.9956 | 0.9694 |
| 3 | 0.9963 | 0.9985 | 0.9970 | 0.9950 | 0.9925 |
| 4 | 0.9964 | 0.9989 | 0.9977 | 0.9959 | 0.9833 |
| 5 | 0.9951 | 0.9988 | 0.9976 | 0.9957 | 0.9877 |
| 6 | 0.9940 | 0.9983 | 0.9973 | 0.9946 | 0.9908 |
| 7 | 0.9906 | 0.9989 | 0.9977 | 0.9956 | 0.9852 |
| 8 | 0.9979 | 0.9990 | 0.9977 | 0.9954 | 0.9913 |
| 9 | 0.9909 | 0.9987 | 0.9980 | 0.9944 | 0.9875 |
| 10 | 0.9967 | 0.9987 | 0.9981 | 0.9955 | 0.9872 |
| 11 | 0.9981 | 0.9983 | 0.9970 | 0.9930 | 0.9855 |

The obtained SNR values are shown in Table A.4. The estimated values are in the range $40-70$ dB. It can be seen mode 2 is clearly the least noisy (highest SNR values) and it is expected to be the most reliable mode for damage detection. In practical applications, building a reliable model of the undamaged structure might not be feasible. In addition, modeling the damaged state is even more difficult since the location, and severity of damage is unknown, unless a model updating process is carried out. Since the proposed methodology is aimed at being model-free and avoid complex modeling strategies, it is proposed to use the cubic spline approach of each experimental mode shape as the reference noise-free mode shape. In order to evaluate the performance of the proposed strategy, the SNR values obtained from the proposed method for the undamaged beam are shown in Table A.5. It can be seen that the values of Tables A.4 and A.5 are similar. Thus the proposed methodology is valid for estimating the SNR of the mode shapes.

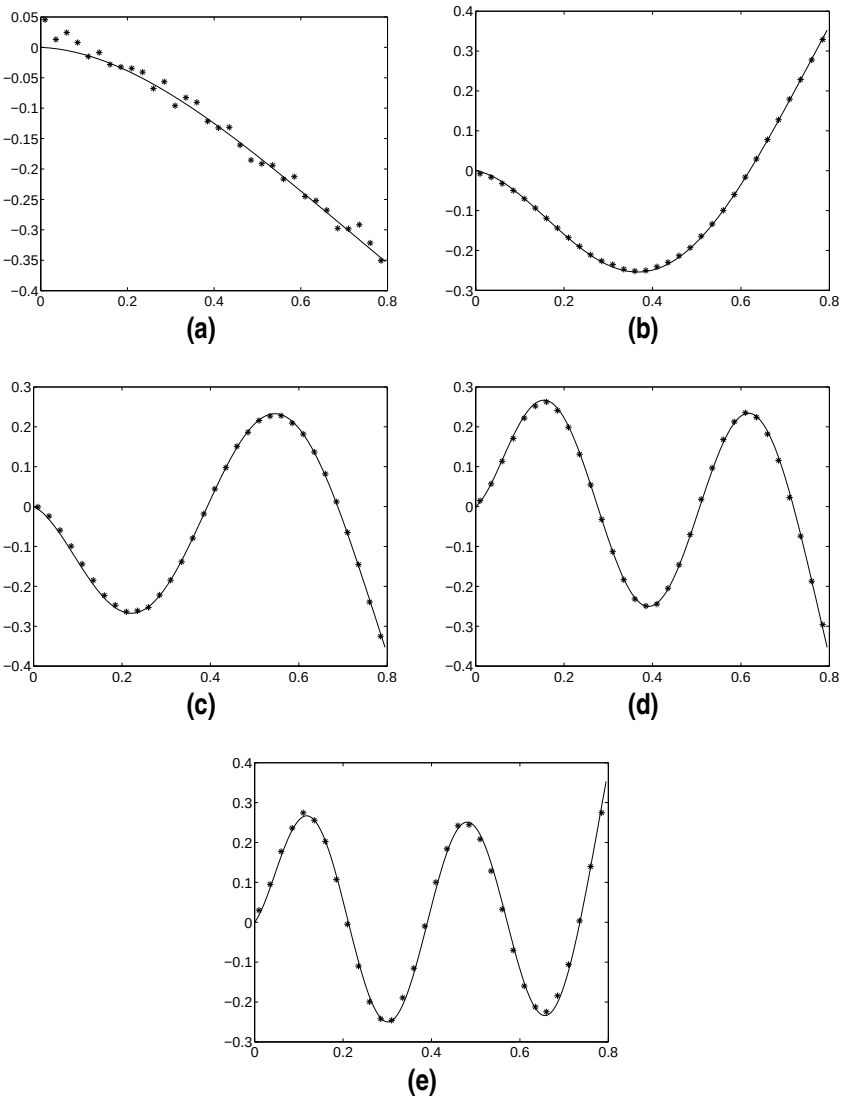


**Figure A.6** Experimental ($*$) and numerical (solid line) mode shapes of undamaged state (no roving mass).

### A.3.2 Damage detection

In this section, the results obtained for each damage scenario are presented. The resulting scalograms for each mode and for the combination of all modes are analyzed. Each result is defined by the depth of the crack (expressed in % of the beam height) and the value of the roving mass (expressed in % of the mass of the beam).

For the damage identification from the scalograms, it must be pointed out that the effect of damage is present at every scale, whereas the effect of noise (experimental noise in the sensors, uncertainties in the modal identification process, numerical instabilities in the interpolation process, etc.) affects only certain scales. This phenomenon has been reported and addressed in previous works [1, 30]. Therefore, a singular behavior (peak or ridge) of wavelet coefficients is observed at damage location for every scale. At the same time, local peaks or ridges can be observed due to noise at different locations and for certain scales. The peak values of wavelet coefficients due to noise can be higher than the peak values due to damage, but the criteria for identifying the damage location is a singular behavior for all the scales.

**Table A.4** SNR values [dB] of experimental modes with respect to numerical modes (undamaged state) for each position of the roving mass.

| Mass Position\Mode | 1 | 2 | 3 | 4 | 5 |
|---|---|---|---|---|---|
| 1 | 55 | 67 | 59 | 52 | 48 |
| 2 | 51 | 63 | 60 | 54 | 40 |
| 3 | 54 | 65 | 58 | 53 | 48 |
| 4 | 55 | 68 | 60 | 54 | 40 |
| 5 | 53 | 66 | 60 | 54 | 43 |
| 6 | 58 | 63 | 59 | 52 | 46 |
| 7 | 46 | 68 | 60 | 54 | 42 |
| 8 | 63 | 69 | 60 | 53 | 47 |
| 9 | 46 | 66 | 62 | 51 | 43 |
| 10 | 53 | 66 | 62 | 54 | 43 |
| 11 | 55 | 63 | 58 | 50 | 42 |

**Table A.5** SNR values [dB] of experimental modes (undamaged state) with respect to their corresponding cubic spline approach for each position of the roving mass.

| Mass Position\Mode | 1 | 2 | 3 | 4 | 5 |
|---|---|---|---|---|---|
| 1 | 57 | 69 | 67 | 62 | 59 |
| 2 | 57 | 58 | 68 | 60 | 58 |
| 3 | 53 | 61 | 62 | 57 | 57 |
| 4 | 54 | 68 | 68 | 59 | 58 |
| 5 | 54 | 62 | 68 | 60 | 58 |
| 6 | 57 | 66 | 65 | 58 | 59 |
| 7 | 60 | 61 | 66 | 60 | 57 |
| 8 | 56 | 68 | 64 | 60 | 58 |
| 9 | 54 | 63 | 64 | 60 | 59 |
| 10 | 58 | 69 | 68 | 57 | 54 |
| 11 | 57 | 70 | 64 | 54 | 57 |

Thus, the normalized scalograms make it easier to observe the results for each scale of the scalogram and to eventually discern between the effect of possible damage and noise. However, as a consequence, the normalization process can make the scalogram to look similar for different scales. The information of the values of the wavelet coefficients at every scale is lost because of the normalization, but the damage identification process analyzes the relative peaks of wavelet coefficients at every scale, instead of their actual values.

In the normalized scalograms, if no noise was present, clear peaks would be observed solely at damage locations for all scales. In real applications, when noise is present, additional peak values can be observed at different locations and at certain scales. From a practical point of view, the challenge is to make the effect of noise as small as possible, in order to avoid masking the actual effect of damage. If the noise level is high (or the damage severity is small), the high values of wavelet coefficients may extend in the scale dimension and lead to 'false positives' (possible damages identified at locations where is no damage). This phenomenon may also occur when the source of the noise is not random but it is due to a specific reason at a certain location (for instance a faulty sensor, cable, etc.)

The presented damage detection approach is aimed at reducing the effect of noise so more clear scalograms are obtained for damage detection, in order to enhance the sensitivity to damage. The

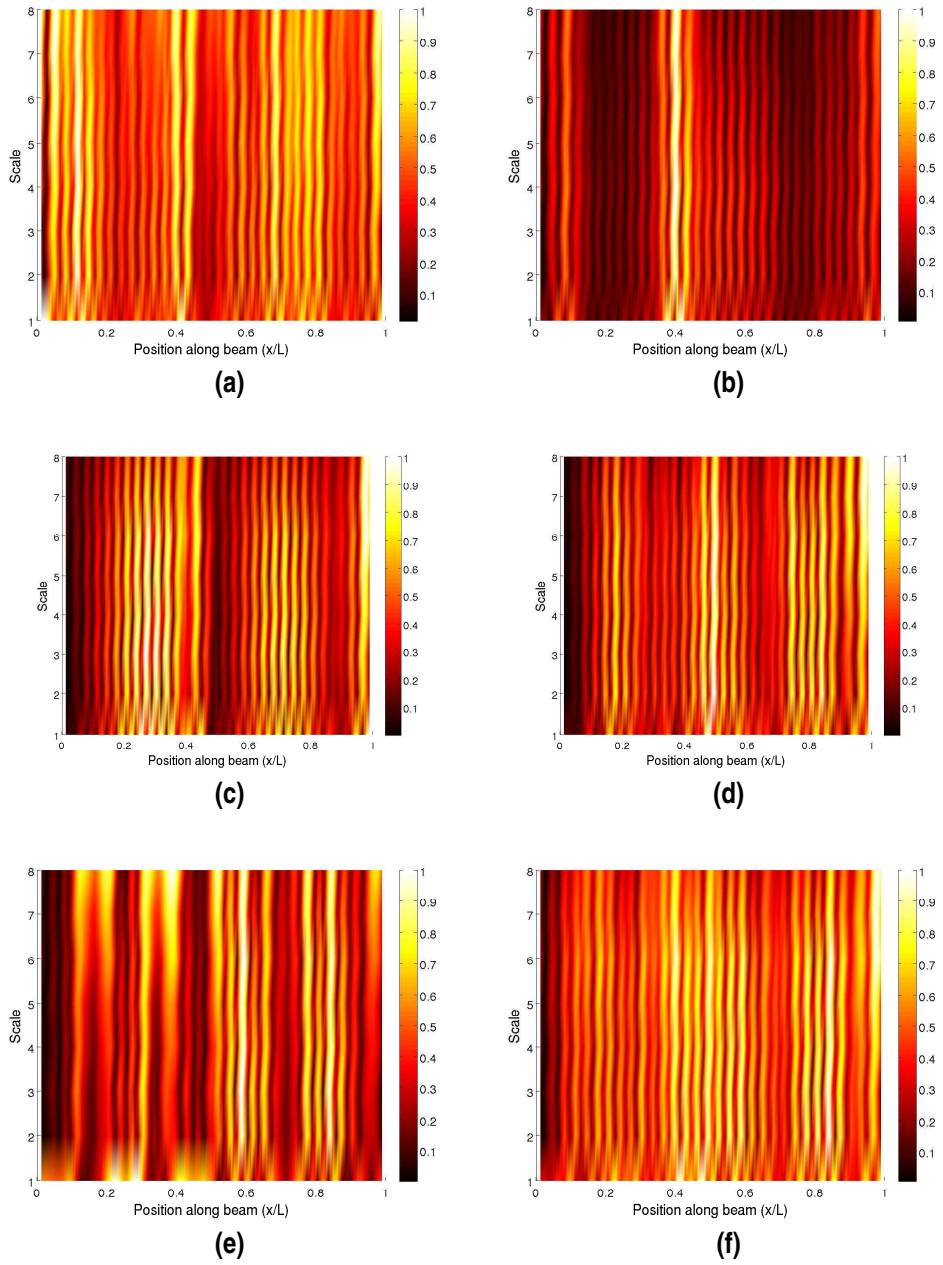


**Figure A.7** Normalized weighted addition of wavelet coefficients for crack depth 10% and 5% mass for (a) mode 1, (b) mode 2, (c) mode 3, (d) mode 4, (e) mode 5 and (f) combination of all mode shapes.

performance and limits of the proposed methodology are explored in this section. Results are presented for all identified modes and for all scales for different damage scenarios, in order to illustrate the capabilities of the method in a real application where no prior information is known about the properties of any existing damage.

It can be seen from Figure A.7 that when the crack is very small (only 10% of the height of the beam), the damage can not be detected except from mode 2. As it was shown in the previous section (Table A.4), this mode is indeed the least contaminated by noise, so it indicates that noise is probably masking the effect of damage in the rest of mode shapes. The level of noise is also relevant

enough to contaminate the results obtained from the combination of all modes. In addition, mode 2 indicates the true damage location at 0.4L which is in a region where this mode exhibits maximum amplitude and therefore it is sensitive to damage. Thus, taking into account both features (low noise and damage in a sensitive area), it can be concluded that mode 2 is providing a reliable damage detection result.

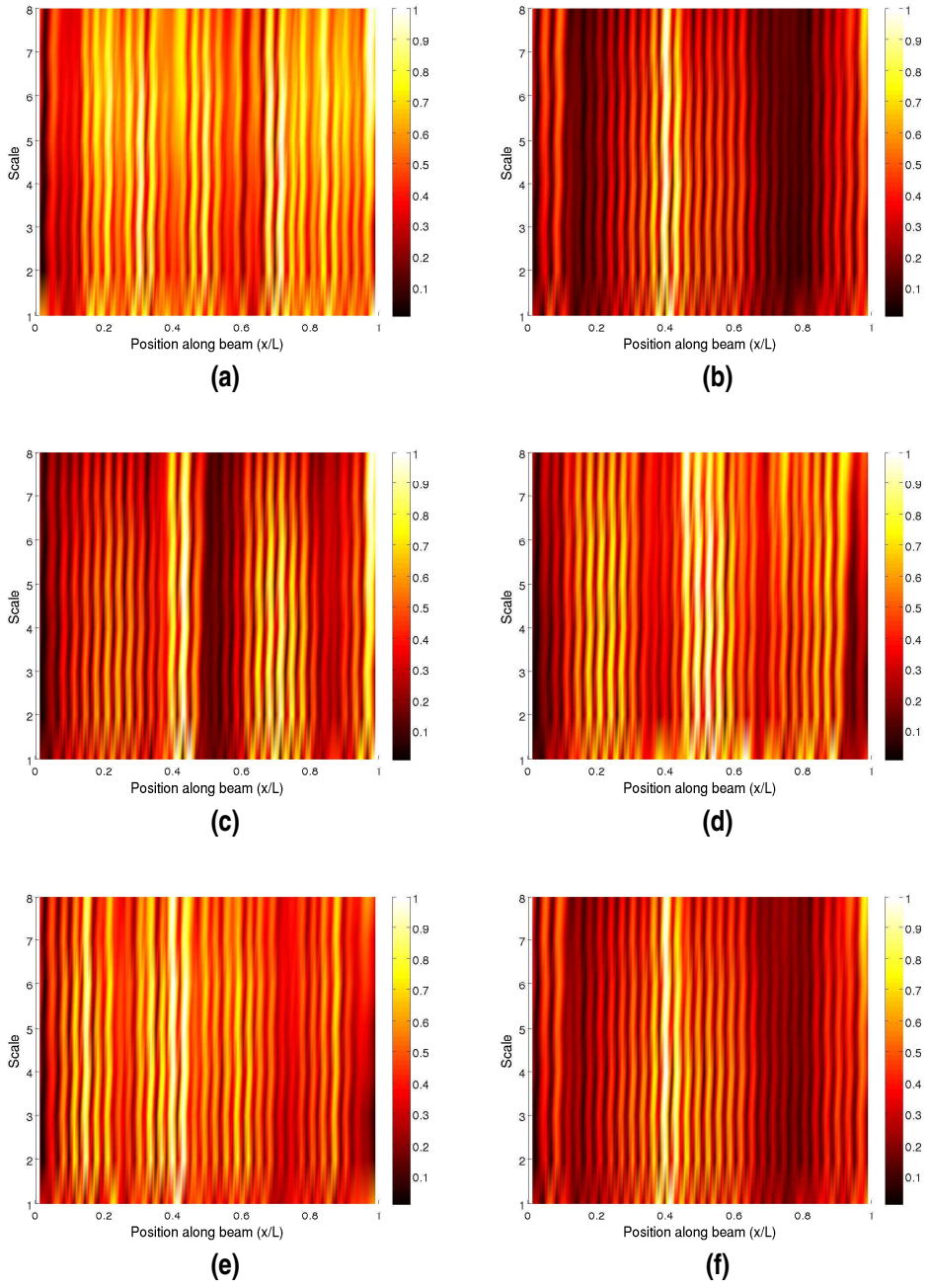


**Figure A.8** Normalized weighted addition of wavelet coefficients for crack depth 20% and 5% mass for (a) mode 1, (b) mode 2, (c) mode 3, (d) mode 4, (e) mode 5 and (f) combination of all mode shapes.

Figure A.8 shows that when damage is more severe the damage is also detected by mode 3 (Figure

A.8.(c)) and less clearly by mode 5 (Figure A.8.(e)). However, mode 2 gives the most reliable information because of its sensitivity and its low noise. Thus, the result obtained when combining all modes (Figure A.8.(f)) is very similar to the one obtained with mode 2.

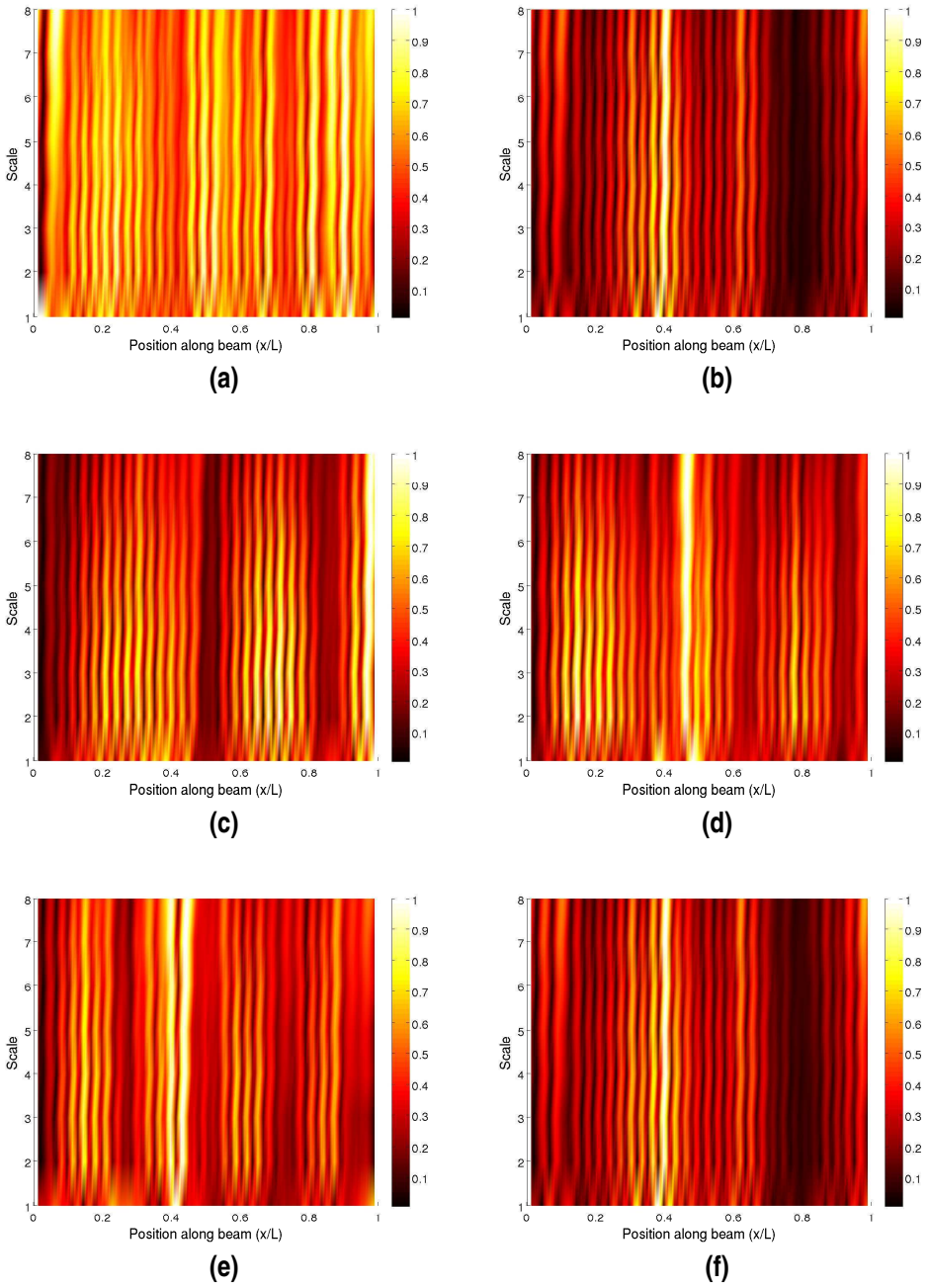


**Figure A.9** Normalized weighted addition of wavelet coefficients for crack depth 50% and 5% mass for (a) mode 1, (b) mode 2, (c) mode 3, (d) mode 4, (e) mode 5 and (f) combination of all mode shapes.

For the most severe damage scenario, modes 2 and 5 (Figure A.9.(b) and Figure A.9.(e)) are again sensitive to damage, whereas mode 3 (Figure A.9.(c)) can not detect damage.

Mode 4 (Figures A.7.(d), A.8.(d) and A.9.(d)) is not pointing to the damage location even though

it also exhibits high modal amplitudes at damage location. This is likely to be due to noise in the mode shape, so the effect of noise is masking the effect of damage. However, this noise effect is diminished when results from all mode shapes are combined because of the weighting coefficient based on the SNR of each mode shape.

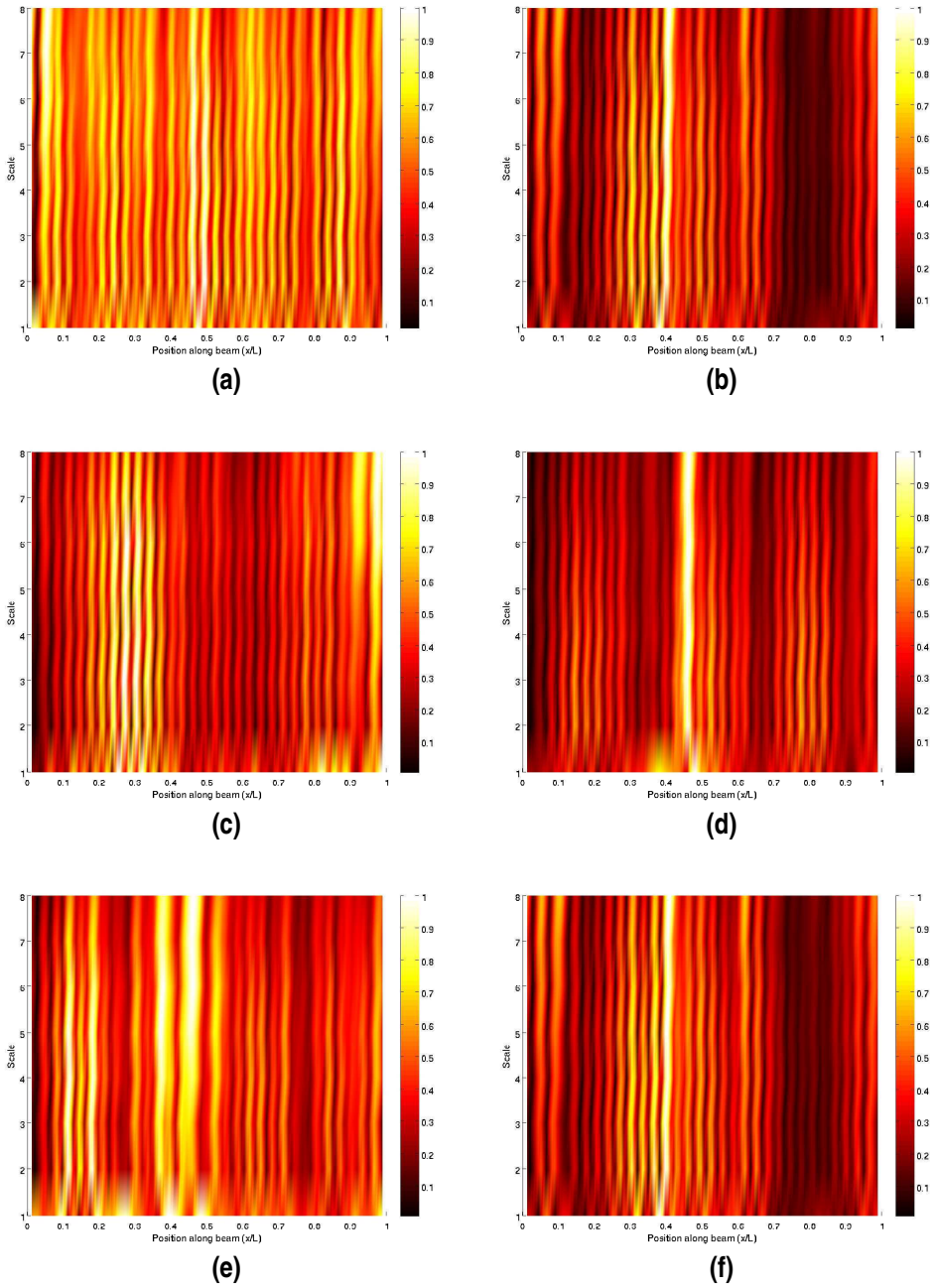


**Figure A.10** Normalized weighted addition of wavelet coefficients for crack depth 50% and 10% mass for (a) mode 1, (b) mode 2, (c) mode 3, (d) mode 4, (e) mode 5 and (f) combination of all mode shapes.

Figure A.10 shows the results for a crack depth of 50% when using a higher value of the roving mass (10% of the mass of the beam). It can be seen that the results are very similar to those obtained for the 5% mass (Figure A.9). Theoretically, a higher value of the mass increases the effect of

the attached mass on the structural response and therefore can highlight more clearly the effect of damage. On the other hand, if the mass is too small, it may not make any difference on the structural response and it turns out to be useless. However, from a practical point of view, the value of the mass is limited because its size may be too big, and it may be difficult to handle and to be attached to the structure. These factors may even lead to some undesirable consequences such as inducing non-linear effects because of contact or geometrical non-linearities. Therefore, there is a trade off between the practical size of mass and its effect on the structure. According to the presented results, values between 5 and 10% provide successful results.

Figure A.11 shows the results obtained for a crack of 50% depth when no roving mass is used. By comparing Figures A.9, A.10 and A.11 it can be seen that the use of the roving mass reduces the effect of noise and increases the sensitivity to damage for mode 2, the one with lowest noise level. Moreover, the result of the combination of all modes with the roving mass is clearer than the one without roving mass. Hence, the use of the roving mass is useful for mitigating the effect of noise.

In order to illustrate the effect of the wavelet choice in the final results, Figure A.12 shows the result of the combination of all mode shapes for all mass positions for a 50% crack and 5% mass when different wavelets are considered: Gauss with 2 vanishing moments, Coiflet with 2 and 4 vanishing moments and Daubechies with 3 and 4 vanishing moments. The presented results show that similar results are obtained for all the considered wavelet function with 2 vanishing moments. However, slightly better results are obtained for the Daubechies (Figure A.9(f)) than for Gauss (Figure A.12(a)) and Coiflet (Figure A.12(b)). When the number of vanishing moments increases, the oscillatory nature of the wavelet function expands and the effect of the damage in the scalogram is also slightly expanded (Figure A.12(c), (d) and (e)). These results are consistent with those presented in [23].

In order to show the performance of the method with smaller number of measuring points, Figure A.13 shows the results when only one set-up of sensors (16 measuring points) is used. The results show that the method is able to detect damage when using even such a small number of sensors. For the 10% crack, the results are even better than when 32 sensors are used (Figure A.7(a)). Even though the sensitivity to damage detection is theoretically improved by increasing the number of sensors, however, if less sensors are used, it is possible that there are less noisy data and whereas the effect of damage is still detected by the remaining sensors. This phenomenon has been previously reported in [23].

## A.4 Conclusions

This paper applies a damage detection technique based on the wavelet analysis of the mode shapes obtained from healthy and damaged states. The experimental results indicate that the method can successfully detect the damage location (even when it is in the middle of two adjacent measuring points). The results also show how the noise for each mode influences the performance of this damage identification methodology. The least noisy modes are the most reliable ones, especially in the areas where they show maximum amplitudes.

For the experimental tests included in the paper, results from mode 2 for all three damage scenarios clearly offer the correct damage location, while the modes with higher noise level did not provide much useful information since the damage effect was masked by the noise. Therefore the estimated level of noise (SNR) should be used for a rigorous analysis. Except for the 10% severity damage, the combination of wavelet coefficients of all modes provides a more reliable result for the damage detection than each mode individually. Nevertheless, both the combined results and the results from modes with lower noise level should be investigated in the analysis since the combined result may not be sensitive to light level of structural damage. In addition, when the roving mass is used, the summation process reduces the effect of noise and increase the sensitivity of the methodology to damage.

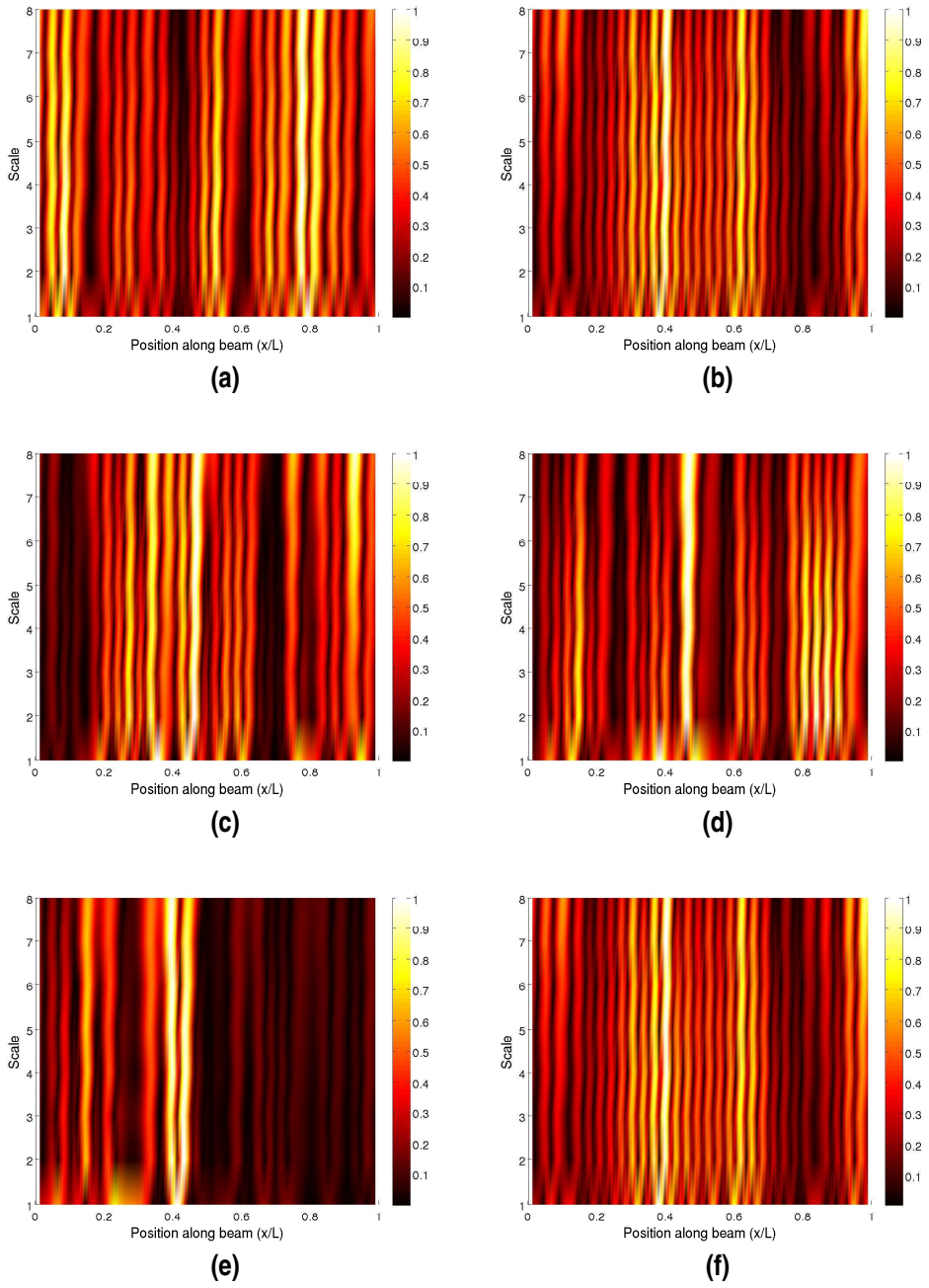


**Figure A.11** Normalized weighted addition of wavelet coefficients for crack depth 50% and no roving mass for (a) mode 1, (b) mode 2, (c) mode 3, (d) mode 4, (e) mode 5 and (f) combination of all mode shapes.

Thus, the main original contributions of the paper (namely the use of estimated SNR in mode shapes and the roving mass) can be applied to other damage detection approaches in 1D, 2D or 3D structures to enhance their sensitivity to damage. The obtained results can also be better than those presented in this paper if more measuring points are used, higher order modes are identified, the accuracy of the measuring system is better, etc. The effect of prestressing in the proposed methodology should be studied from the experimental analysis of concrete beams.

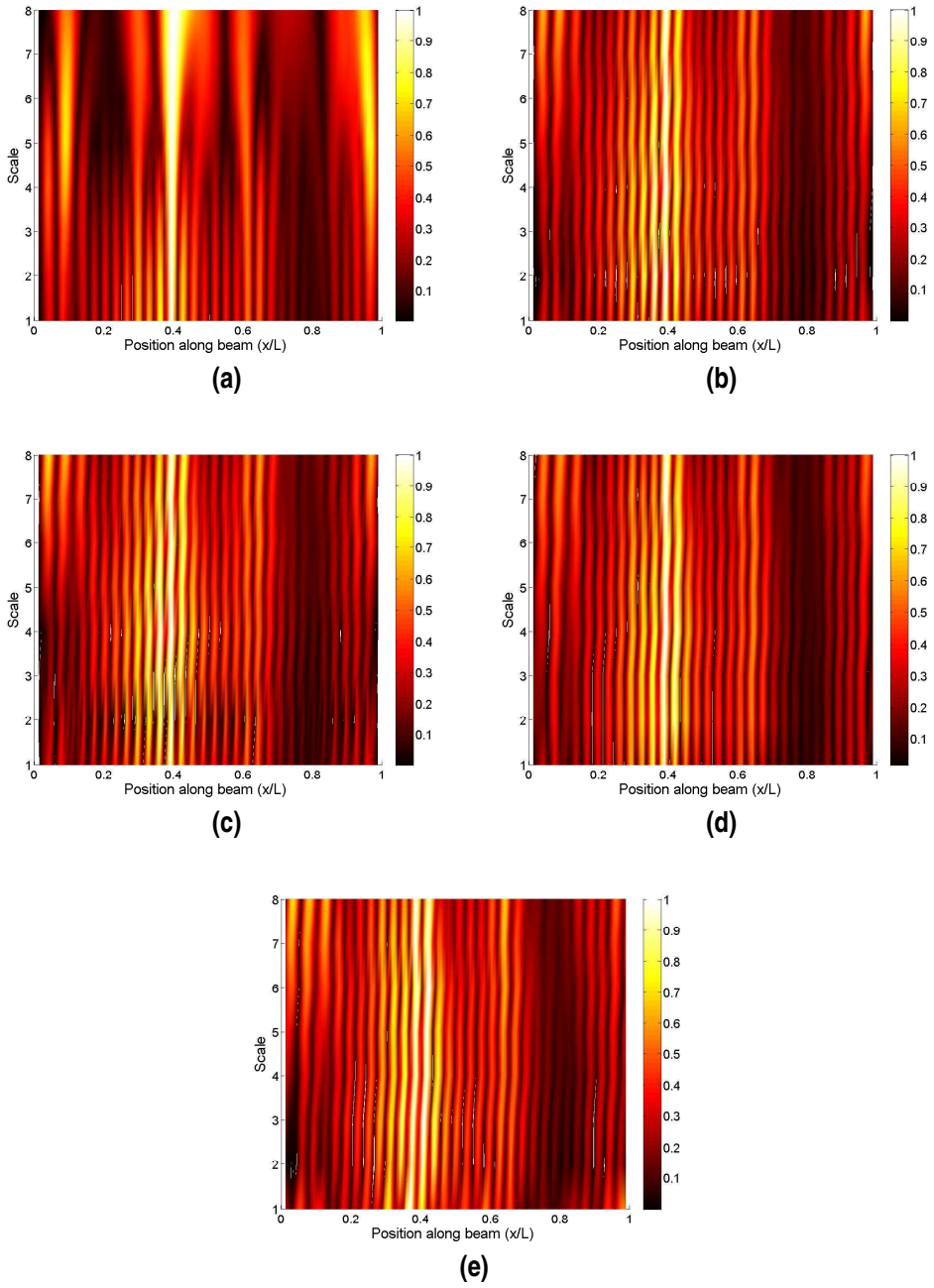


**Figure A.12** Normalized weighted addition of wavelet coefficients for all mode shapes for crack depth 50% and 5% mass using wavelet (a) Gauss with 2 vanishing moments, (b) Coiflet with 2 vanishing moments, (c) Coiflet with 4 vanishing moments, (d) Daubechies with 3 and (e) Daubechies with 4 vanishing moments.

## Acknowledgments

The authors deeply appreciate all the reviewers' and editor comments, ideas and suggestions, which have certainly permitted to raise the manuscript quality.

This work was supported by the Consejería de Economía, Innovación, Ciencia y Empleo of Andalucía (Spain) under project P12-TEP-2546 and the Ministerio de Economía y Competitividad

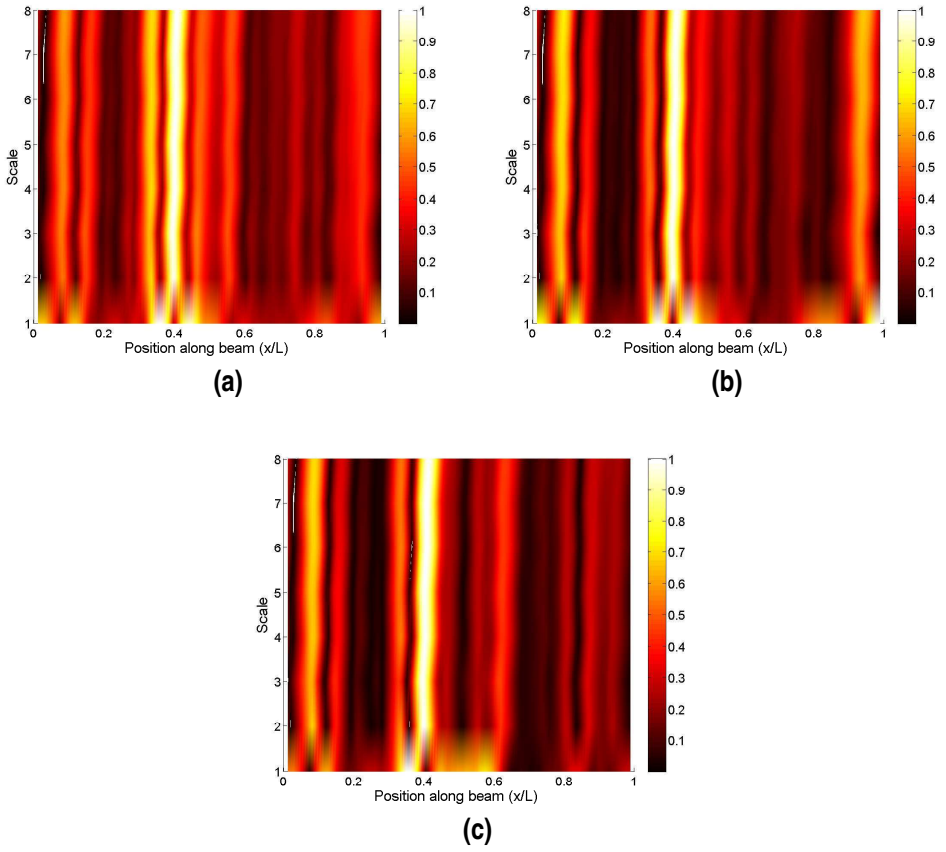


**Figure A.13** Normalized weighted addition of wavelet coefficients for all mode shapes for 5% added mass using wavelet Daubechies with 2 vanishing moments and 16 sensors for (a) 10% crack, (b) 20% crack and (c) 50% crack.

through research projects BIA2013-43085-P and BIA2016-75042-C2-1-R. Financial support is gratefully acknowledged.

## References

[1] Andreaus, U., Baragatti, P., Casini, P., and Iacoviello, D. Experimental damage evaluation of open and fatigue cracks of multi cracked beams by using wavelet transform of static response via image analysis. *Structural Control and Health Monitoring 24*, 4 (2017).

[2] Bendat, J. S., and Piersol, A. G. *Random Data: Analysis and Measurement Procedures*. Wiley Series in Probability and Statistics. Wiley, 2011.

[3] Cao, M., Radzieński, M., Xu, W., and Ostachowicz, W. Identification of multiple damage in beams based on robust curvature mode shapes. *Mech. Syst. Signal Proc. 46*, 2 (2014), 468–480.

[4] Fan, W. , and Qiao, P. Vibration-based damage identification methods: A review and comparative study. *Struct. Health Monit. 10*, 1 (2011), 83–111.

[5] García, I., Zubia, J., Durana, G., Aldabaldetreku, G., Illarramendi, M., and Villatoro, J. Optical fiber sensors for aircraft structural health monitoring. *Sensors 15*, 7 (2015), 15494–15519.

[6] Gentile, A., and Messina, A. On the continuous wavelet transforms applied to discrete vibrational data for detecting open cracks in damaged beams. *Int. J. Solids Struct. 40*, 2 (2003), 295–315.

[7] Guillaume, P., Verboven, P., Vanlanduit, S., Van Der Auweraer, H., and Peeters, B. A poly-reference implementation of the least-squares complex frequency-domain estimator. In *Proceedings of 21st International Modal Analysis Conference* (2003), vol. 21, pp. 183–192.

[8] Jiang, Y., Tang, B., Qin, Y., and Liu, W. Feature extraction method of wind turbine based on adaptive Morlet wavelet and SVD. *Renewable Energy 36*, 8 (2011), 2146–2153.

[9] Katunin, A. Modal-based non-destructive damage assessment in composite structures using wavelet analysis: A review. *Int. J. Compos. Mat. 3*, 6B (2013), 1–9.

[10] Katunin, A. Stone impact damage identification in composite plates using modal data and quincunx wavelet analysis. *Arch. Civ. Mech. Eng. 15*, 1 (2015), 251–261.

[11] Katunin, A., Dańczak, M., and Kostka, P. Automated identification and classification of internal defects in composite structures using computed tomography and 3D wavelet analysis. *Arch. Civ. Mech. Eng. 15*, 2 (2015), 436–448.

[12] Katunin, A., and Przystalka, P. Damage assessment in composite plates using fractional wavelet transform of modal shapes with optimized selection of spatial wavelets. *Eng. Appl. Artif. Intell. 30* (2014), 73–85.

[13] Limongelli, M., Siegert, D., Merliot, E., Waeytens, J., Bourquin, F., Vidal, R., Corvec, V., Gueguen, I., and Cottineau, L. Damage detection in a post tensioned concrete beam - Experimental investigation. *Engineering Structures 128*, Supplement C (2016), 15–25.

[14] Mallat, S. *A Wavelet Tour of Signal Processing*. Academic Press, London, 1999.

[15] Montanari, L., Spagnoli, A., Basu, B., and Broderick, B. On the effect of spatial sampling in damage detection of cracked beams by continuous wavelet transform. *J. Sound Vibr. 345* (2015), 233–249.

[16] Ovanesova, A. V., and Suárez, L. E. Applications of wavelet transforms to damage detection in frame structures. *Eng. Struct. 26*, 1 (2004), 39–49.

[17] Panopoulou, A., Fransen, S., Gomez-Molinero, V., and Kostopoulos, V. Experimental modal analysis and dynamic strain fiber Bragg gratings for structural health monitoring of composite antenna sub-reflector. *CEAS Space J. 5*, 1-2 (2013), 57–73.

[18] Rajendran, P., and Srinivasan, S. M. Identification of added mass in the composite plate structure based on wavelet packet transform. *Strain 52*, 1 (2016), 14–25. STRAIN-1064.R1.

[19] Ren, W.-X., and Sun, Z.-S. Structural damage identification by using wavelet entropy. *Eng. Struct. 30*, 10 (2008), 2840–2849.

[20] Rucka, M. Damage detection in beams using wavelet transform on higher vibration modes. *J. Theor. Appl. Mech. 49*, 2 (2011), 399–417.

[21] Rucka, M., and Wilde, K. Application of continuous wavelet transform in vibration based damage detection method for beams and plates. *J. Sound Vibr. 297*, 3-5 (2006), 536–550.

[22] Shao, X., and Ma, C. A general approach to derivative calculation using wavelet transform. *Chemometrics and Intelligent Laboratory Systems 69*, 1-2 (2003), 157–165.

[23] Solís, M., Algaba, M., and Galvín, P. Continuous wavelet analysis of mode shapes differences for damage detection. *Mech. Syst. Signal Proc. 40*, 2 (2013), 645–666.

[24] Solís, M., Benjumea, A. J., Algaba, M., and Galvín, P. Analysis of stationary roving mass effect for damage detection in beams using wavelet analysis of mode shapes. *Journal of Physics: Conference Series 628* (2015), 012014.

[25] Strang, G., and Nguyen, T. *Wavelets and Filter Banks*. Wellesley- Cambridge Press, 1996.

[26] Surace, C., and Ruotolo, R. Crack detection of a beam using the wavelet transform. In *Proceedings of the 12th International Modal Analysis Conference* (1994), pp. 1141–1147.

[27] Taha, M. M. R., Noureldin, A., Lucero, J. L., and Baca, T. J. Wavelet transform for structural health monitoring: A compendium of uses and features. *Struct. Health Monit. 5*, 3 (2006), 267–295.

[28] Ulriksen, M., and Damkilde, L. Structural damage localization by outlier analysis of signal-processed mode shapes – Analytical and experimental validation. *Mech. Syst. Signal Proc.*, 68-69 (2016), 1–14.

[29] Unger, J., Teughels, A., and De Roeck, G. System identification and damage detection of a prestressed concrete beam. *Journal of Structural Engineering 132*, 11 (2006), 1691–1698.

[30] Xu, W., Cao, M., Ostachowicz, W., Radzieński, M., and Xia, N. Two-dimensional curvature mode shape method based on wavelets and Teager energy for damage detection in plates. *Journal of Sound and Vibration 347* (2015), 266–278.

[31] Xu, Y., Zhu, W., Liu, J., and Shao, Y. Identification of embedded horizontal cracks in beams using measured mode shapes. *J. Sound Vibr. 333*, 23 (2014), 6273–6294.

[32] Yang, B. *Stress, Strain, and Structural Dynamics*. Elsevier, 2005.

[33] Yi, T.-H., Li, H.-N., and Zhao, X.-Y. Noise smoothing for structural vibration test signals using an improved wavelet thresholding technique. *Sensors (Basel, Switzerland) 12*, 8 (2012), 11205–20.

[34] Zhong, S., and Oyadiji, S. O. Analytical predictions of natural frequencies of cracked simply supported beams with a stationary roving mass. *J. Sound Vibr. 311*, 1-2 (2008), 328–352.

[35] Zhong, S., and Oyadiji, S. O. Detection of cracks in simply-supported beams by continuous wavelet transform of reconstructed modal data. *Comput. Struct. 89*, 1-2 (2011), 127–148.

[36] Zhong, S., Oyadiji, S. O., and Ding, K. Response-only method for damage detection of beam-like structures using high accuracy frequencies with auxiliary mass spatial probing. *J. Sound Vibr. 311*, 3-5 (2008), 1075–1099.

.

# Appendix B
# Paper B

Ma, Q. and Solís, M. (2017). "Damage localization and quantification in simple supported beams using static test data", *Journal of Physics: Conference Series* **842** 012007

The original paper can be found on: https://iopscience.iop.org

Journal: Journal of Physics: Conference Series

ISSN: 17426588, 17426596

SCIMAGO (2017))

- Physics and Astronomy: Q3 (893/1731)

# Damage localization and quantification in beams from slope discontinuities in static deflections

Qiaoyu Ma and Mario Solís

Department of Continuum Mechanics and Structural Analysis,
Escuela Técnica Superior de Ingeniería, Universidad de Sevilla,

**Abstract** A novel simple method using static test data for damage detection, localization, and quantification in beams is presented in this paper. The method is based on the change of the deflections of the beam between a reference and a damaged state. For simply supported beams with a single damage, the maximum value of the change of deflections indicates the location of damage. Once the damage is located, one could estimate the rotational stiffness at the damaged cross section by applying a superposition scheme to isolate the effect of damage and by using basic structural analysis equilibrium equations. Afterwards, damage extent is evaluated through an existing relation between rotational stiffness and damage severity. Several static tests of a simply supported steel beam with a point load at different locations were conducted to exam the performance of the strategy. The damage is artificially introduced as an opened crack located at the bottom of the beam. The deflections of the beam were measured by using a Digital Image Correlation system. The results show that the method can accurately detect and quantify the damage. The method is non-model based and can be easily conducted. No specific loading positions are required and damage identification objective can be achieved from just one single static test.

## B.1 Introduction

The fundamental objective of damage detection is to identify the change of properies in a structure caused by damage, which includes natural frequencies, dampings, stiffness or flexibility matrix, mode shapes, and etc [3]. Many methodologies and techniques proposed by researchers are based on system identification or parameter estimation through the dynamic response of the structure. Various numerical methods are applied for damage detection and localization, such as the transimissibility function [10–12], the BAT algorithm [4], etc.

Some researchers also applied similar ideas using static response data of the structure. Caddemi and Morassi [8] identified a single crack in beams with different boundary conditions using the static displacements. Lee and Eun [6] presented a method for locating damage through the change of curvature of static deflections. Bakhtiari-Nejad, Rahai and Esfandiari [1] developed an algorithm based on the change of stored strain energy in the elements using static noisy data for damage detection. Seyedpoor and Yazdanpanah [9] also illustrated a method through the change of strain energy using static noisy data.

In this paper, a novel non-model based simple method for single crack damage detection and localization of beams is presented. Firstly, the theory of the method is presented to illustrate how the change of pre- and post-damaged static displacements of the beam under external loads can be used for damage localization. From the information about the damage location, a damage quantification method based on structural analysis is introduced. Next, a series of experimental tests of a cracked simply supported beam were conducted to exam the performance of the method.

## B.2 Theory background

It is known that the prescence of a crack will cause a reduction in the local stiffness at the cracked cross section. Hence a single damaged beam could be modeled as a rotational spring at the cracked

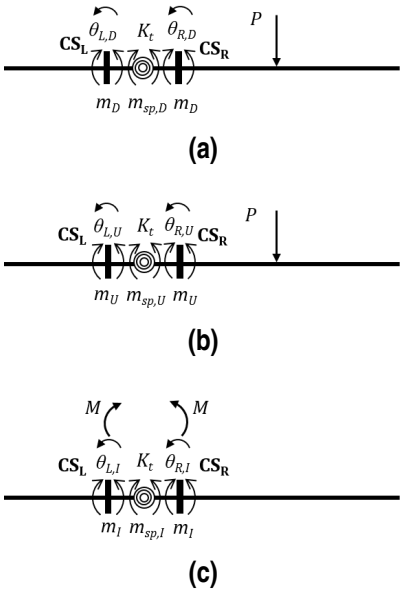


**Figure B.1** States of the superposition scheme: (a) Damaged State (D) , (b) reference or Undamaged State (U) and (c) Incremental State (I).

location that connects two undamaged parts of the beam [2]. The problem of a cracked beam under some external forces ($P$) (*Damaged State*, $D$) can be decomposed into an *Undamaged State* ($U$) plus an *Incremental State* ($I$) (Fig.B.1). Thus, the deformation ($U$) and internal forces ($f$) can be written as

$$U_D = U_U + U_I \quad \text{and} \quad f_D = f_U + f_I \tag{B.1}$$

In figures Fig. B.1 (a), (b) and (c), $CS_L$ and $CS_R$ are the left and right sides of the damage cross section respectively, $K_t$ is the rotational stiffness of the spring that models the cracked cross section, $m$ is the internal bending moment at $CS_L$ and $CS_R$ (they are equal to each other), $m_{sp}$ is the internal torsional moment of the spring, $\theta_L$ and $\theta_R$ are the rotations at $CS_L$ and $CS_R$, respectively, and the footnotes $U$, $D$, and $I$ stand for the *Undamaged* (or reference), *Damaged*, and *Incremental States* respectively. In the *Undamaged State*, the rotations at $CS_L$ and $CS_R$ are set to be equal ($\theta_{L,U} = \theta_{R,U}$), which indicates the spring is not present in the undamaged beam. It is found that this superposition is valid when the applied moment ($M$) in the *Incremental State* is equal to the internal bending moment at damage location ($m_U$) in the *Undamaged State*.

The damage locations are revealed in the overall deformed shape of $U_I$ since the external forces will introduce slope (rotation) discontinuities at damaged cross sections (Fig. B.1 (c)). For a single cracked simply-supported beam, the shape of $U_I$ is piecewise linear and it is independent from the loading position. Its magnitude depends on the magnitude of external loads, the severity of damage and the relative position of the load and the damage.

A finite element model of a simply-supported Timoshenko beam with a 1200mm length ($L$) and a $100 \times 20$mm rectangle cross section was built in ANSYS (mesh size 120mm). A spring with a rotational stiffness ($K_t$) of $1.8e^5$N/m$^2$ was used to model the crack at $0.4L$ from the left end. A concentrated load, 1kN, was applied at $0.6L$ from the left end. The deflections of the beams for the *Damaged* and *Undamaged States* are shown in Fig B.2 (a). The deflection under a self-equilibrated bending moment $m_U$ corresponding to the *Incremental State* ($U_I$) and the difference between the displacements of the *Undamaged* and *Damaged States* ($\Delta U$) are shown in Fig. B.2 (b). It is shown that $U_I$ is equal to $\Delta U$. The discontinuity in the slope indicates the damage location precisely. The

slight difference between $\Delta U$ and $U_I$ is due to numerical errors.

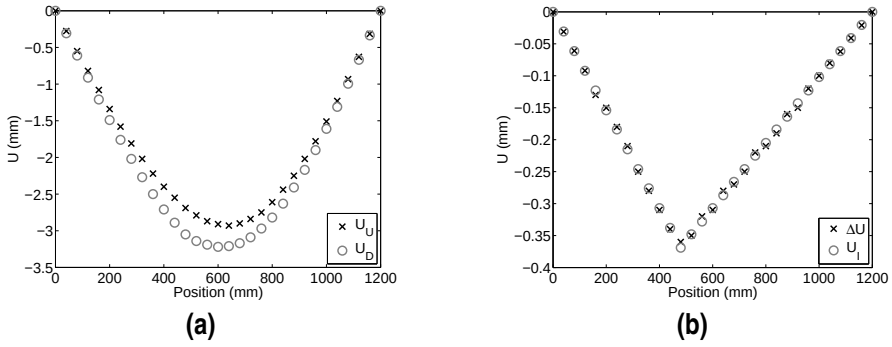


**Figure B.2** Deflection results of the finite element model: (a) $U_D$ and $U_U$ of simply-supported beam; (b) $\Delta U$ and $U_I$ of simply-supported beam.

Once the damage is localized, the rotational stiffness of the cracked beam could be estimated from the *Incremental State* using the following expression:

$$K_i = \frac{m_{sp,I}}{(\theta_{L,I} - \theta_{R,I})} = \frac{m_{sp,I}}{\Delta\theta_I} \tag{B.2}$$

The rotation discontinuity ($\Delta\theta_I$) can be directly computed from $\Delta U$ ($U_I$) and the moment absorbed by the spring ($m_{sp,I}$) can be automatically calculated for a statically determinate beam since the reactions of the beam for the *Incremental State* are null and therefore $m_{sp,I}$ equals $M$ (and $m_U$, as indicated previously). Once the rotational stiffness of the damaged cross-section is determined, the extent of damage can be estimated by comparing it with an existing correlation between damage size and rotational stiffness.

## B.3 Experimental Test of A Simply-Supported Beam

### B.3.1 Test Setup

An experimental test of a simply-supported steel beam was conducted to test the performance of the methodology. The dimension of the beam was $1200 \times 100 \times 20$mm. A notch was cut at the bottom of the beam at $0.35L$ (425mm) from the left end. The depth of the notch was set to be 7mm (35% of the beam height). A Digital Imagine Correlation(DIC) system (Fig. B.3 (a), (b) and (c)) was used for measuring the deflection of the beam under loading. A total number of 241 measuring points (damage at the 86th) were marked along the beam with an equal spacing of 5mm. A concentrated force was applied on the beam vertically through hanging a 120kg mass on it. 21 tests were performed by putting the mass at 21 equally distributed positions along the beam. The scheme of the test is shown in Fig. B.3 (d).

### B.3.2 Implementation of the methodology

Due to the effect of noise on the measured data, a trend estimate function named $l1$ Trending Filter is used to estimate the overall shape of $\Delta U$. The $l1$ Trending Filter produces trend estimation that is piecewise linear through minimize the objective function in Eqn. (B.3), where $\lambda$ is a nonnegative

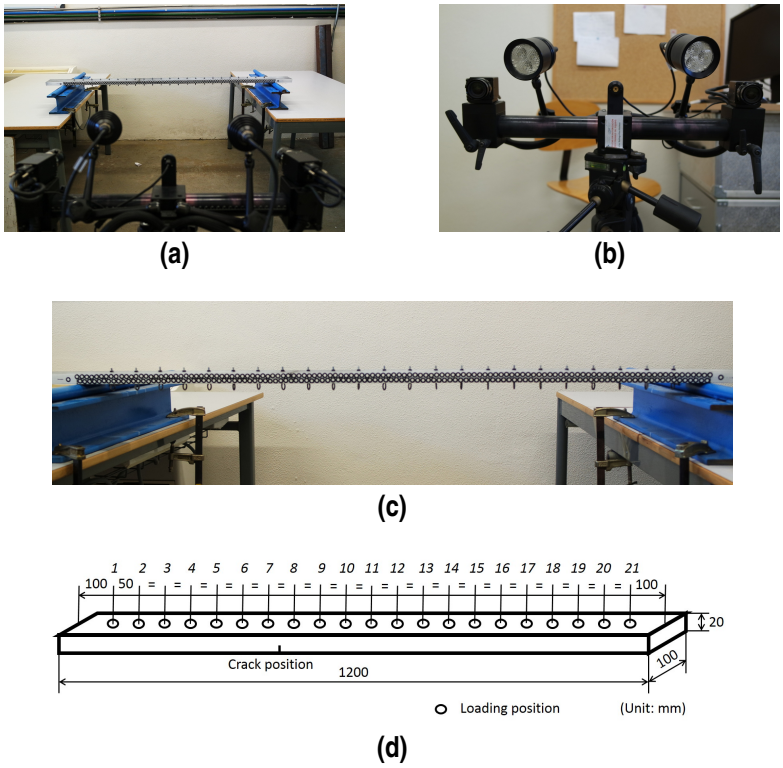


**Figure B.3** (a) Experimental setup, (b) DIC measuring system, (c) Tested beam and (d) Test scheme.

parameter. $x_t$ is the estimated trend and $y_t$ is the signal [5]. This trending filter automatically identifies the turning point along the piecewise shape data.

$$(1/2)\sum_{t=1}^{n}(y_t - x_t)^2 + \lambda \sum_{t=2}^{n-1} |x_{t-1} - 2x_t + x_{t+1}|^2 \tag{B.3}$$

The results of $\Delta U$ and the application of $l1$ Filter to $\Delta U$ ($\Delta U_{l1}$) are displayed in Fig. B.4 and B.5. For all 21 loading positions, the shape of $\Delta U$ was estimated correctly. The effect of noise only takes a relative high influence when the loading positions are close to supports of the beam (at positions 1, 20 and 21). The position where the maximum value of $\Delta U_{l1}$ takes place is considered as the damage location. The predicted results are listed in table B.1. All the predicted damage locations fall into a small range from the correct location. The furthest predition is at point 93 (for loading position 20), which is 35mm to the right of the real damage. Therefore, it is shown that the methodology can successfully localize the damage for this damage scenario.

For a notch type opened cracked on an elastic beam with rectangular cross-section, the equivalent rotational stiffness of the damaged cros-section ($K_t$) proposed by Rizos, Aspragathos, and Dimarogonas [7] (Eqn. (B.4) and (B.5)) is used in this paper for damage extent estimation:

$$K_t = 1/c \qquad c = 6\pi h J(\xi)/EI \tag{B.4}$$

where $h$ is the height of the beam, $E$ the elastic modulus of the material of the beam, $I$ the inertia of the cross-section and $J$ is the following function of the ratio ($\xi$) between the notch depth and the height of the beam.

$$\begin{aligned} J(\xi) = {} & 1.86(\xi)^2 - 3.95(\xi)^3 + 16.375(\xi)^4 - 37.226(\xi)^5 + 76.81(\xi)^6 \\ & - 126.9(\xi)^7 + 172.5(\xi)^8 - 143.97(\xi)^9 + 66.56(\xi)^{10} \end{aligned} \tag{B.5}$$

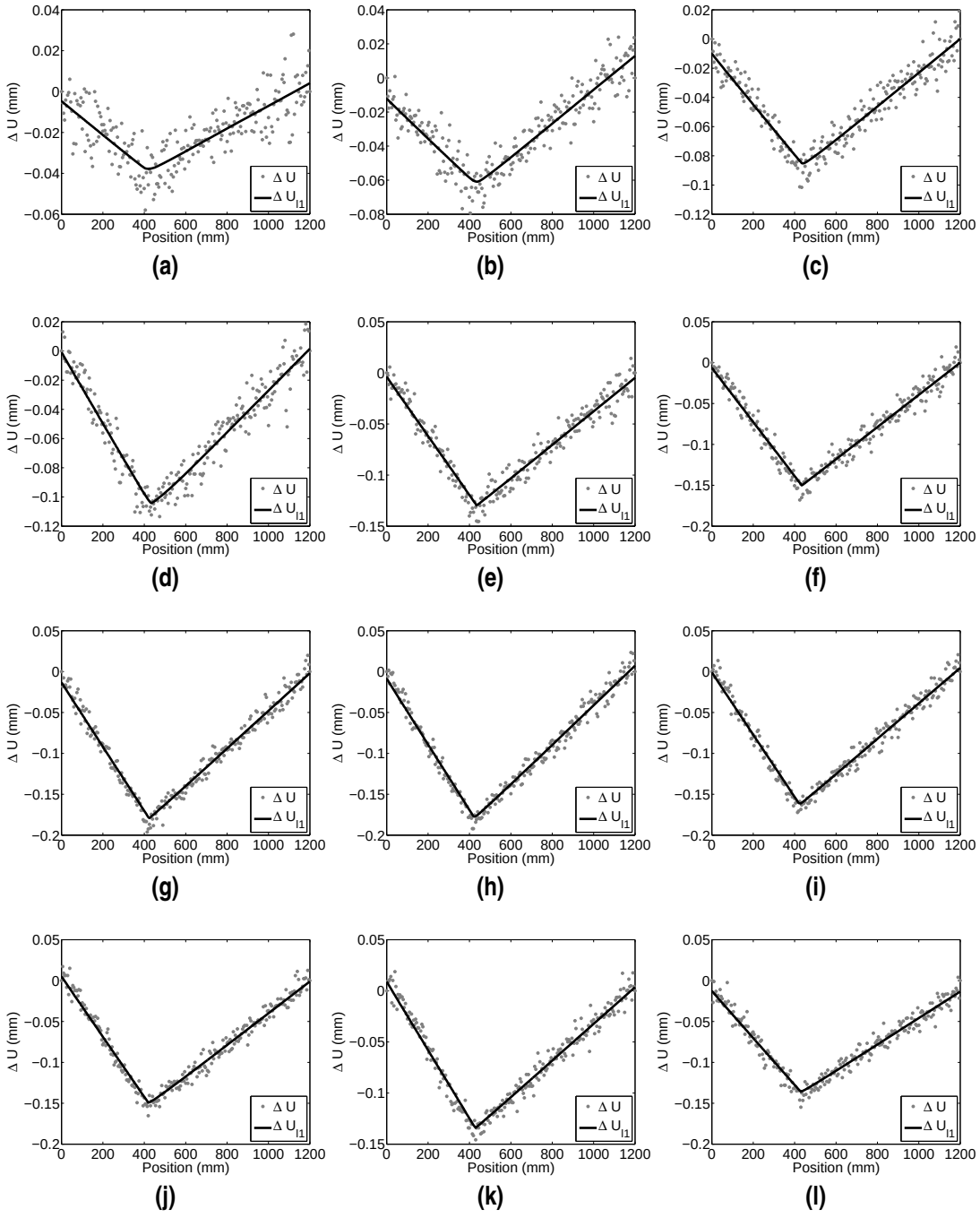


**Figure B.4** $\Delta U$ and $\Delta U_{l1}$ with loading at positions 1 (a) to 12 (l).

By using this empirical relationship, damage severity can be estimated from the experimentally identified rotational stiffness ($K_t$) in Eqn.(B.2). The rotation discontinuity ($\Delta\theta_I$) can be evaluated using a piecewise linear regression function of $U_I$, whereas $m_{sp,I}$ (equivalent to $m_U$) can be easily computed from equilibrium equations of the undamaged beam. The estimated damage extent for each test are also listed in table B.1. All of the estimated damage severities are bigger than the real value. This may indicate some discrepancy between the analytical model of the crack as a rotational spring and the actual behavior of the damaged cross section. However, for all the loading positions, the method provides predictions with high accuracy even for those with low signal to noise ratio.

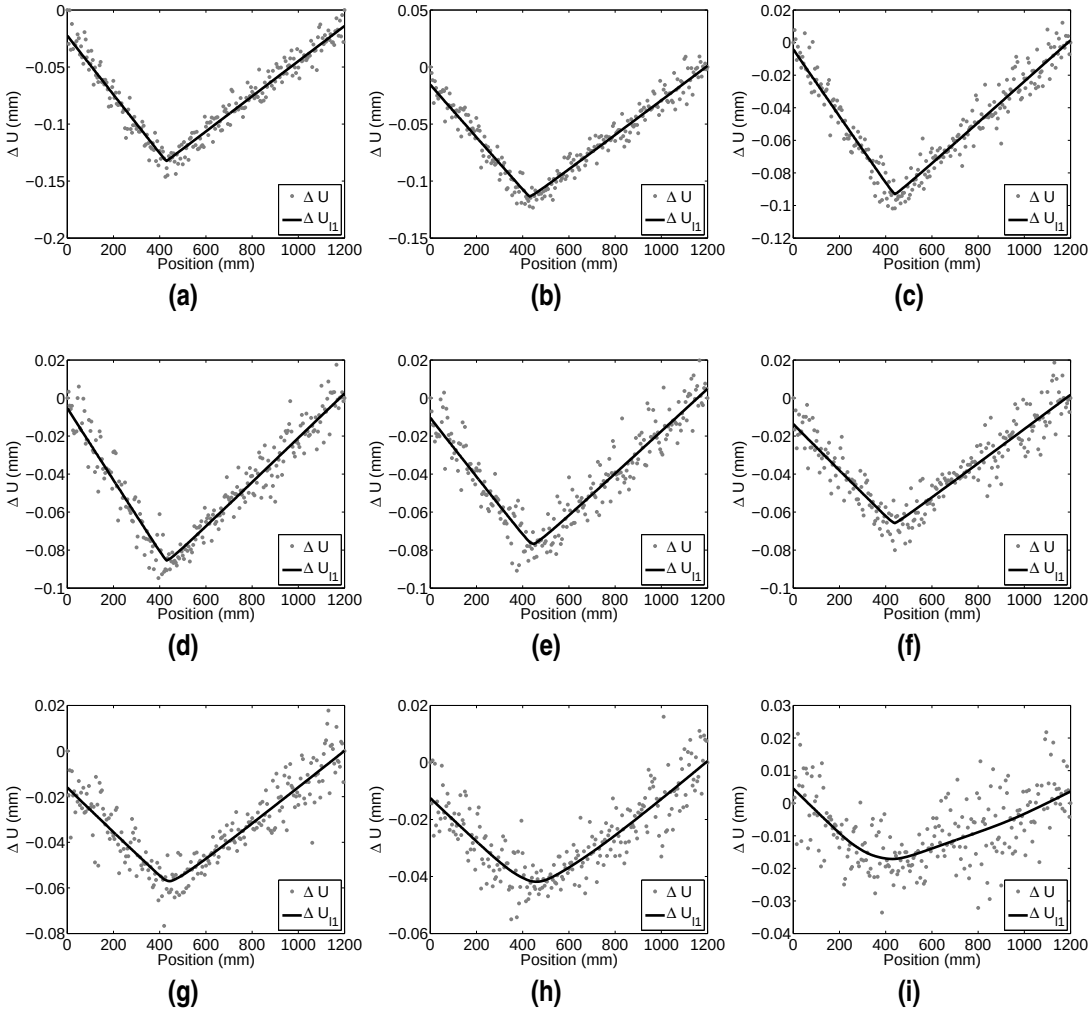


**Figure B.5** $\Delta U$ and $\Delta U_{l1}$ with loading at positions 13 (a) to 21 (i).

## B.4 Conclusion

A non-model based damage detection and localization methodology based on the static displacements is presented in this paper. No specific loading positions are needed for the experimental test and structural identification is not required. Experimental results of a simply-supported steel beam with a single crack are provided. The methodology successfully predicts the crack location with a very high accuracy for all loading positions. From the predicted damage locations, the damage extent can be estimated using an existing analytical correlations between damage extent and rotational stiffness of the damaged cross section. The method provides results with high accuracy as well. In summary, the paper proves the efficiency and simplicity of the method for practical purpose.

## Acknowledgement

This work was supported by the Consejería de Economía, Innovación, Ciencia y Empleo of Andalucía (Spain) under project P12-TEP-2546. The financial support is gratefully acknowledged.

**Table B.1** Estimated damage location and severity and their errors.

| | | Localization | | Quantification | | |
|---|---|---|---|---|---|---|
| Loading Position | Measuring Point | Location (mm) | Deviation (mm) | Severity (mm) | Error (mm) | Error (%) |
| 1 | 85 | 415 | 5 | 7.5 | 0.5 | 7 |
| 2 | 89 | 440 | 15 | 7.7 | 0.7 | 10 |
| 3 | 89 | 440 | 15 | 7.7 | 0.7 | 10 |
| 4 | 88 | 435 | 10 | 7.9 | 0.9 | 13 |
| 5 | 88 | 435 | 10 | 7.8 | 0.8 | 11 |
| 6 | 88 | 435 | 10 | 7.8 | 0.8 | 11 |
| 7 | 86 | 425 | 0 | 7.8 | 0.8 | 11 |
| 8 | 86 | 425 | 0 | 7.8 | 0.8 | 11 |
| 9 | 87 | 430 | 5 | 7.8 | 0.8 | 11 |
| 10 | 85 | 415 | 5 | 7.9 | 0.9 | 13 |
| 11 | 87 | 430 | 5 | 7.8 | 0.8 | 11 |
| 12 | 87 | 430 | 5 | 7.7 | 0.7 | 10 |
| 13 | 87 | 430 | 5 | 7.7 | 0.7 | 10 |
| 14 | 87 | 430 | 5 | 7.8 | 0.8 | 11 |
| 15 | 89 | 440 | 15 | 7.7 | 0.7 | 10 |
| 16 | 87 | 430 | 5 | 8.0 | 1.0 | 14 |
| 17 | 91 | 450 | 25 | 7.8 | 0.8 | 11 |
| 18 | 89 | 440 | 15 | 7.8 | 0.8 | 11 |
| 19 | 90 | 445 | 20 | 7.9 | 0.9 | 13 |
| 20 | 93 | 460 | 35 | 7.7 | 0.7 | 10 |
| 21 | 87 | 430 | 5 | 7.7 | 0.7 | 10 |

## References


[1] Bakhtiari-Nejad, F., Rahai, A., and Esfandiari, A. A structural damage detection method using static noisy data. *Engineering Structures 27* (2005), 1784–1793.

[2] Dimarogonas, A. D. Vibration of cracked structures: a state of the art review. *Engineering Fracture Mechanics 55*, 5 (1996), 831–857.

[3] Hajela, P., and Soeiro, F. J. Recent develoments in damage detection based on system identification methods. *Structural Optimization 2* (1990), 1–10.

[4] Khatir, S., Belaidi, I., Serra, R., Abdel Wahab, M., and Khatir, T. Numerical study for single and multiple damage detection and localization in beam-like structures using BAT algorithm. *Journal of Vibroengineering 18* (2016), 202–213.

[5] Kim, S. J., Koh, K., Boyd, S., and Gorinevsky, D. l1 Trending Filtering. *Society for industrial and Applied Mathematics 51*, 2 (2009), 339–360.

[6] Lee, E. T., and Eun, H. C. Damage detection of damaged beam by constrained displacement curvature. *Journal of Mechanical and Technology 22* (2008), 1111–1120.

[7] Rizos, P. F., Aspragathos, N., and Dimarogonas, A. D. Identification of crack location and magnitude in a cantilever beam from the vibration modes. *Journal of Sound and Vibration 138*, 3 (1990), 381–388.

[8] S.Caddemi, and Morassi, A. Crack detection in elastic beams by static measurements. *Solids and Structures 44* (2007), 5301–5315.

[9] Seyedpoor, S. M., and Yazdanpanah, O. An efficient indicator for structural damage localization using the change of strain energy based on static noisy data. *Applied Mathematical Modelling 38* (2014), 2661–2672.

[10] Zhou, Y. L., and Abdel Wahab, M. Rapid early damage detection using transmissibility with distance measure analysis under unknown excitation in long-term health monitoring. *Journal of Vibroengineering 18* (2016), 4491–4499.

[11] Zhou, Y. L., Maia, N. M., and Abdel Wahab, M. Damage detection using transmissibility compressed by principal component analysis enhanced with distance measure. *Journal of Vibration and Control 24* (2016), 2001–2019.

[12] Zhou, Y. L., Maia, N. M., Sampaio, R. P., and Abdel Wahab, M. Structural damage detection using transmissibility together with hierarchical clustering analysis and similarity measure. *Structural Health Monitoring 16* (2016), 711–731.

# Appendix C
# Paper C

Ma, Q. and Solís, M. (2018). "Damage localization and quantification in beams from slope discontinuities in static deflections", *Smart Structures and Systems*, 22(3):291-302.

The original paper can be found on: https://www.techno-press.org

DOI: 10.12989/sss.2018.22.3.291

Journal: Smart Structures and Systems

ISSN: 1738-1584, 1738-1991

Journal Citation Reports (2017): Impact factor: 2.231

- Engineering, Civil: Q1 (32/128)
- Engineering, Mechanical: Q2 (32/128)

SCIMAGO (2017)

- Control and Systems Engineering: Q2 (86/948)

# Damage localization and quantification in beams from slope discontinuities in static deflections

Qiaoyu Ma and Mario Solís

Department of Continuum Mechanics and Structural Analysis,
Escuela Técnica Superior de Ingeniería, Universidad de Sevilla,

**Abstract** This paper presents a flexibility based method for damage identification from static measurements in beam-type structures. The response of the beam at the Damaged State is decomposed into the response at the Reference State plus the response at an Incremental State, which represents the effect of damage. The damage is localized by detecting slope discontinuities in the deflection of the structure at the Incremental State. A denoising filtering technique is applied to reduce the effect of experimental noise. The extent of the damage is estimated through comparing the experimental flexural stiffness of the damaged cross-sections with the corresponding values provided by analytical models of cracked beams. The paper illustrates the method by showing a numerical example with two cracks and an experimental case study of a simply supported steel beam with one artificially introduced notch type crack at three damage levels. A Digital Image Correlation system was used to accurately measure the deflections of the beam at a dense measurement grid under a set of point loads. The results indicate that the method can successfully detect and quantify a small damage from the experimental data.

**Keywords** damage identification, static deflection, beams, digital photogrammetry

## C.1 Introduction

Damage detection in structures is based on the identification of the change of structural properties induced by damage. Extensive research on vibration-based damage identification has been developed in the last decades [10, 16, 17, 30, 37]. For damage detection in beam-type structures, comparative studies on frequency-based and mode-shape-based algorithms have shown that mode-shape-based methods are advantageous for damage localization [18, 19, 23]. Pandey et al. [26] demonstrated that changes in the curvatures of the mode shapes (second-order derivative) reveal the damage location in a beam-like structure and the curvatures of mode shapes are a better indicator for damage localization than the mode shapes. Numerical studies of beams and practical applications in bridges show that the change in curvatures of mode shapes is feasible for multiple damage scenarios detection [1, 4, 13]. The first-order derivative of mode shapes has also been considered an excellent damage indicator for beams and plates by Abdo and Hori [3]. Higher order derivatives (third and fourth) of beam-like structures have been used for damage localization purpose as well [35]. Moreover, other numerical techniques implicitly related to differentiation can be applied to mode shapes for damage localization. For instance, the wavelet transform has been applied to mode shapes [28], curvatures of mode shapes [8], and changes in mode shapes [32]. Some research studies have also proposed non-baseline methods by using the discontinuities in the derivatives as a damage indicator (see Reference [9] for instance). In the work of Xu et al. [36], they propose the use of slopes in longitudinal displacements by exciting the beam with an axial force.

For dynamic-based methods, the effect of damage is distributed among all modes. However, in practice, the number of modes that can be experimentally identified and analyzed is always limited. For instance, for large-scale structures such as bridges, the higher modes are usually not captured in day-to-day monitoring. This inevitable truncation can lead to damage identification errors [1, 4]. In contrast, the static response provides more complete and straightforward information about the

structural behavior. In addition, data processing for a static test is simpler and less time-consuming than for an experimental modal analysis.

Structural diagnosis techniques that employ static response have been proposed through parameter estimation, solving inverse problem or using strain energy [5, 6, 21, 31, 38, 39]. For damage detection in beam-type structures, several methods based on deflection measurements or its derivatives have been presented [2, 11, 29, 34]. The main difficulty for solving inverse problems of damage detection in beams is that they are usually ill-conditioned. Nonetheless, Caddemi and Morassi [6] proposed a simple one-dimensional analytical model of cracked beams with typical boundary conditions, such as simply-supported and fixed-fixed, for damage localization. Later, the authors [7] presented a more explicit analytical model for multiple cracks in beams for damage localization and quantification. Choi et al. [11] developed a load theorem that uses the influence line of the moment of the conjugate beam for damage localization in statically determinate beams. Stöhr et al. [34] presented a method using influence lines of slope difference measured by one inclination sensor for damage localization in bridges. Abdo [2] perfomed a parametric study on damage localization by applying the Grey Relation Coefficient with the displacement curvature difference.

The main drawback for using the static response is the difficulty in accurately and efficiently measuring the static displacement at a high enough number of measurement points. In Structural Health Monitoring (SHM) application for bridges, various techniques have been developed to measure the static deflection, such as deformation sensors, inclinometers, strain gauges, and fiber optic sensors [12, 33, 40]. As an alternative, non-contact optical measuring techniques can be used to overcome this issue [22]. Rucka and Wilde [28] used a digital still camera to measure the static displacements of a cantilever beam and applied wavelet analysis directly to the measured data for damage localization.

On the other hand, the problem of a cracked beam under some external static forces can be decomposed into an undamaged state plus an incremental state where a traction field is applied on the crack surface [20]. Moreover, Caddemi and Morassi [6] demonstrated the relationship between damage severity and the response of the structure at this incremental state. This paper is also based on this type of decomposition approach. The aim is to develop a fast and robust method for damage identification in beams with cracks through direct experimental measurements without neither solving inverse problems nor estimating any model parameter.

A straightforward and simple damage localization and quantification method that utilizes the static deflection difference between the Reference and Damaged States is proposed. A slope discontinuity in this deflection difference reveals the location of damage. The main concern when dealing with derivatives of experimental mode shapes or static displacements is that they usually can not be directly measured and their computation is subjected to numerical instabilities due to experimental noise. A proper trending filter is proposed in this paper to denoise the data in order to avoid this difficulty. Moreover, the extents of damage can be estimated from the experimentally determined flexural stiffness of the damaged cross-sections.

The rest of the paper is outlined as follows. First, the decomposition scheme and the principle of the method are introduced. Next, the paper presents a general methodology for damage localization and quantification based on the detection of slope discontinuities in the deflection differences between the Reference and the Damaged States. Then, a numerical example is presented to verify the method. Details and performance of the methodology are disscussed through an experimental application on simply supported beams with a single crack. Lastly, the conclusions are drawn.

## C.2 Theoretical Background

The structural behavior of a cracked beam is a complex problem that has been the subject of many studies over the years. It has been addressed from different perspectives (fracture mechanics, finite

element models, experimental tests, etc.) and different parameters have been considered (stress-intensity factors, local flexibility, etc.) [14]. The presence of a crack causes a reduction in the local stiffness of the cross-section. Thus, a damaged cross-section can be macroscopically modeled as a massless rotational spring with a specific stiffness that links the two parts of the beam at both sides of the crack. The ideal lumped model of local stiffness reduction and its vicinity are depicted in Fig. C.1.

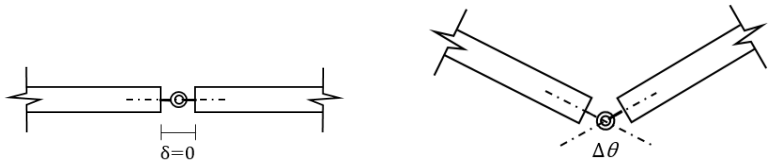


**Figure C.1** Ideal lumped damage model: (a) undeformed; (b) deformed.

In the book of Dimarogonas et al. [15], the authors provided correlation equations of the flexual stiffness and the damaged cross-section for different shapes of cross-section and various types of damage. For a notch type opened crack on an elastic beam with a rectangular cross-section, the equivalent flexural stiffness of the damaged cross-section ($K_{ana}$) can be estimated from Eqs. (C.1)-(C.2) [27], assuming that the notch has a uniform depth and a sufficient small width to maintain open under loading condition:

$$K_{ana} = 1/c \qquad c = 5.346hJ(\xi)/EI \tag{C.1}$$

where $h$ is the height of the cross-section, $E$ is the elastic modulus of the material of the beam, $I$ is the moment of inertia of the cross-section, and $J$ is defined by the following function of the ratio $\xi$ between the notch depth and the height of the cross-section.

$$\begin{aligned} J(\xi) = {} & 1.8624(\xi)^2 - 3.95(\xi)^3 + 16.375(\xi)^4 - 37.226(\xi)^5 \\ & + 76.81(\xi)^6 - 126.9(\xi)^7 + 172(\xi)^8 - 143.97(\xi)^9 + 66.56(\xi)^{10} \end{aligned} \tag{C.2}$$

The problem of a beam with cracks subjected to a general external load is represented from a macro mechanical perspective in Fig. C.2. The damage in the beam is modeled as a massless rotational spring with a stiffness $K$ in the one-dimensional beam model. The beam is under some arbitrary external loads $F$ that can produce non-zero internal moments at damage locations. The external loads remain unchanged after the occurrence of damage. To better demonstrate the scheme, only one single damage is considered in Fig. C.2 but the theoretical analysis would be identical for multiple damage scenarios. The response of the structure at Damaged State (State D, Fig. C.2(a)) can be understood as the superposition of the response at the Reference State (State R, Fig. C.2(b)) plus the effect of applying a certain concentrated self-equilibrated moment, $M$, at the damage position at the Incremental State (State I, Fig. C.2(c)). The presented theory is valid for any boundary conditions that are properly established, i.e. no rigid body motion is allowed and the beam is stable. Therefore, for simplicity and generality, no boundary conditions are specified in Fig. C.2. The following list defines the notations plotted in Fig. C.2:

Nomenclature

$\mathbf{CS_A}$, $\mathbf{CS_B}$ the cross-sections at the left and right sides of the damage, respectively;

$\theta_A$, $\theta_B$ the rotations of $\mathbf{CS_A}$ and $\mathbf{CS_B}$, respectively;

$m$ the internal bending moment at $\mathbf{CS_A}$ and $\mathbf{CS_B}$ (they are equal to each other because of moment equilibrium at the damage location);

$m_{sp}$ the internal torsional moment of the spring.

Subscripts $D$, $R$, and $I$ stand for the Damaged, Reference, and Incremental States, respectively.

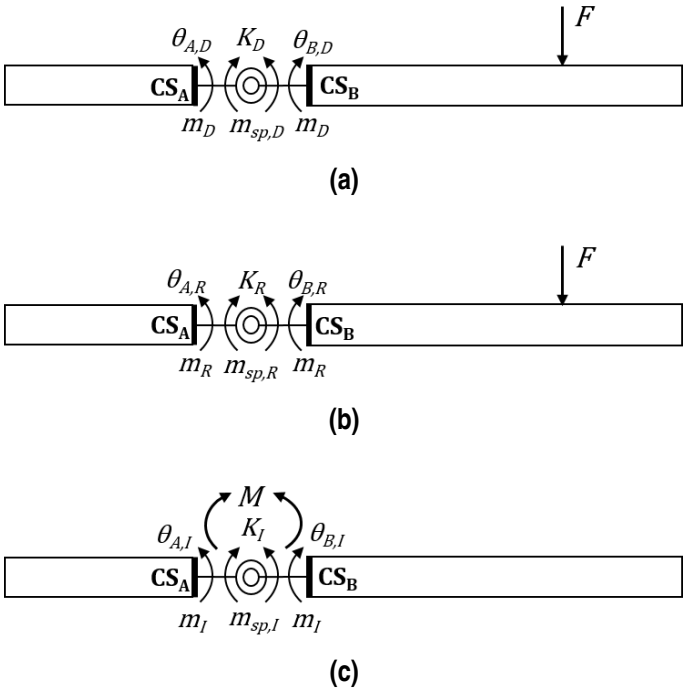


**Figure C.2** States of the superposition scheme: (a) Damaged State, (b) Reference State and (c) Incremental State.

According to the superposition scheme, the following relationships can be written,

$$m_D = m_R + m_I \tag{C.3}$$

$$m_{sp,D} = m_{sp,R} + m_{sp,I} \tag{C.4}$$

$$\theta_{A,D} = \theta_{A,R} + \theta_{A,I} \quad \text{and} \quad \theta_{B,D} = \theta_{B,R} + \theta_{B,I} \tag{C.5}$$

At any state, the constitutive law of the spring states that:

$$m_{sp} = K \cdot (\theta_B - \theta_A) \tag{C.6}$$

At State R, the following compatibility condition is imposed since there is no damage:

$$\theta_{A,R} = \theta_{B,R} \tag{C.7}$$

Thus, Eq. (C.6) determines that the internal moment of the spring at this state is null:

$$m_{sp,R} = K_R \cdot (\theta_{B,R} - \theta_{A,R}) = 0 \tag{C.8}$$

Equation (C.8) implies that the spring has no effect at State R since any value of $K_R$ can satisfy the equation. By subtracting $\theta_{A,D}$ from $\theta_{B,D}$ in Eqs. (C.5), and considering Eq. (C.7) the following equation is obtained:

$$\theta_{B,D} - \theta_{A,D} = \theta_{B,I} - \theta_{A,I} \tag{C.9}$$

Equations (C.4) and (C.8) indicate that:

$$m_{sp,D} = m_{sp,I} \tag{C.10}$$

From Eqs. (C.6), (C.9) and (C.10), it is verfied that the stiffness of the springs in State D and I are the same:

$$K_D = K_I = K \tag{C.11}$$

At State D, from moment equilibrium, the following equation is obtained:

$$m_D = m_{sp,D} \tag{C.12}$$

At State I, the moment equilibrium can be written as:

$$M = m_{sp,I} - m_I \tag{C.13}$$

Equation (C.13) means that the externally applied moment $M$ is partially transmitted to the beam and partially taken by the spring. By introducing Eqs. (C.3), (C.10), and (C.12) in Eq. (C.13), it is obtained that:

$$M = m_R \tag{C.14}$$

Therefore, in a general situation with multiple damages, the proposed superposition scheme is valid when the external moments applied at State I equal the internal bending moments at damage locations at State R. The applied moments ($M$) at State I clearly lead to rotational discontinuities between the two sides of the beam connected by the rotational springs. The damage can therefore be localized where the slope discontinuities are identified in the deflection of State I ($u_I$). According to the superposition scheme, this deflection can be computed from the displacement fields measured at States R ($u_R$) and D ($u_D$).

$$u_I = \Delta u = u_D - u_R \tag{C.15}$$

The flexural stiffness of each cracked section (the rotational stiffness of the springs) can be estimated by applying Eq. (C.6) to State I:

$$K = \frac{m_{sp,I}}{(\theta_{B,I} - \theta_{A,I})} = \frac{m_{sp,I}}{\Delta\theta_I} \tag{C.16}$$

From Eqs. (C.10) and (C.12), Eq. (C.16) can be written as:

$$K = \frac{m_D}{\Delta\theta_I} \tag{C.17}$$

From the flexural stiffness of the damaged cross-sections, the extents of damage can be assessed by comparing the rotational stiffness estimate with existing correlations. For instance, Eqs. (C.1) and (C.2) can be used to estimate the crack depth in a rectangular cross-section. In order to obtain the rotational stiffness from Eq. (C.17), $m_D$ and $\Delta\theta_I$ at the corresponding damaged cross-section have to be estimated first.

For statically determinate beams, the internal bending moment of the beam at State D can be calculated accurately through structural analysis. For statically indeterminate beams, $m_D$ has to be estimated through numerical analysis or analytical models. The rotation discontinuities can be determined and computed from the deflection difference, as it will be discussed in next sections.

## C.3 Damage Identification Methodology

### C.3.1 General Procedure

The general procedure for damage localization and quantification in beams through experimental measurements is summarized as follows:

1) Measure the static deflections of the structure at States R ($u_R$) and D ($u_D$);
2) Compute the deflection increment ($\Delta u$) between $u_R$ and $u_D$ using Eq. (C.15);
3) Compute the value of the slope discontinuities ($\Delta\theta_I$) of $\Delta u$ and localize damage;
4) Compute the internal bending moment of damaged cross-sections at State D;
5) Compute the flexural stiffness or rotational stiffness ($K$) at damage locations using Eq. (C.17);
6) Estimate the damage severity through a previously obtained correlation between damage size and flexural stiffness (such as Eqs. (C.1) and (C.2)).

In practice, the corresponding change of the slope in Step 3) can be computed through a finite difference procedure at each measurement point. Given three equally spaced measurement points and their corresponding deflection measurements $[\Delta u(i-1), \Delta u(i), \Delta u(i+1)]$, the numerical evaluation of the slope difference at point $i$ can be estimated by Eq. (C.18), where "$\theta_I^+$" and "$\theta_I^-$" are the slope of $\Delta u$ from forward differencing approach and backward differencing approach, respectively, and $\Delta x$ is the distance between adjacent measurement points.

$$\begin{aligned}\Delta\theta_I(i) &= \theta_I^+(i) - \theta_I^-(i) \\ &= \frac{\Delta u(i+1) - 2\Delta u(i) + \Delta u(i-1)}{\Delta x}\end{aligned} \tag{C.18}$$

### C.3.2 Numerical Validation

A numerical example with two damages are presented to illustrate the theory of the superposition scheme and the proposed damage detection methodology. A finite element model of a simply-supported one-dimensional Timoshenko steel beam with a length of 1200 mm, a width of 100 mm, a height of 20 mm, and a 200 GPa modulus of elasticity was built. Two springs with equal rotational stiffness, $K_1 = K_2 = 1.8\text{e}^5$ N·m/rad (equivalent to 50% damage severity according to Eqs. (C.1)-(C.2)), were used to model two cracked cross-sections ($D_1$ and $D_2$). They are located at $1/3$ (400 mm) and $2/3$ (800 mm) of the beam. A concentrated load, $F = 1000$ N, was applied at 1000 mm from the left end (arbitrarily selected position). The models for State R, D, and I are presented in Fig. C.3, where $M_1$ (66.67 N·m) and $M_2$ (133.33 N·m) equal the internal bending moments at the associated cross-sections at State R.

The deflections of the numerical models of States R and D are shown in Fig. C.4(a). It can be seen that there is a difference between the two deflections but there is no evidence of the presence and location of damage from simple inspection. The deflection of State I ($u_I$) and the deflection increment ($\Delta u$) obtained by subtracting $u_R$ from $u_D$ are shown in Fig. C.4(b). The consistency of $u_I$ and $\Delta u$ verifies the superposition scheme presented in section 2.

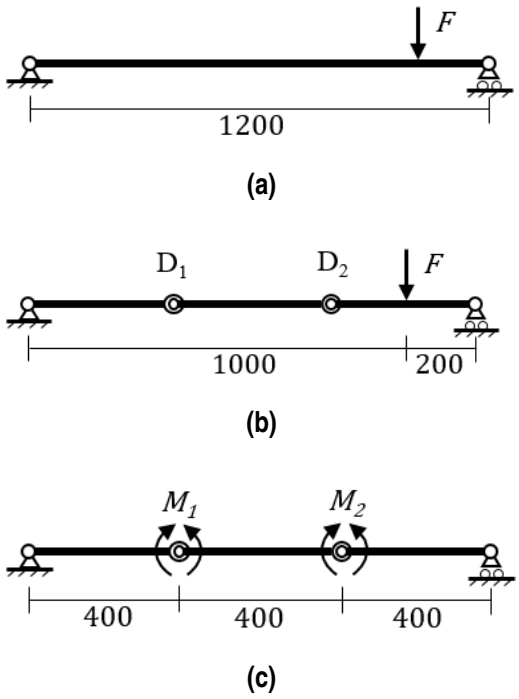


**Figure C.3** Scheme of the simply supported beam models: (a) model for State R; (b) model for State D; (c) model for State I (unit: mm).

In practical applications, in which only measurements of $u_D$ and $u_R$ can be available, the deflection of the Incremental State can be calculated by subtracting $u_D$ and $u_R$ ($\Delta u = u_I = u_D - u_R$). Then, the corresponding slope discontinuities ($\Delta\theta_I$) can be estimated by using Eq. (18). The results in Fig. 4(c) show that the peak values of the rotation difference of the deflection increment reveal the damage locations precisely. The estimates of the damage locations and rotational stiffness of the springs from the deflection difference are listed in Table 1. Neglecting numerical roundup errors, both of the predictions are consistent with the model information.

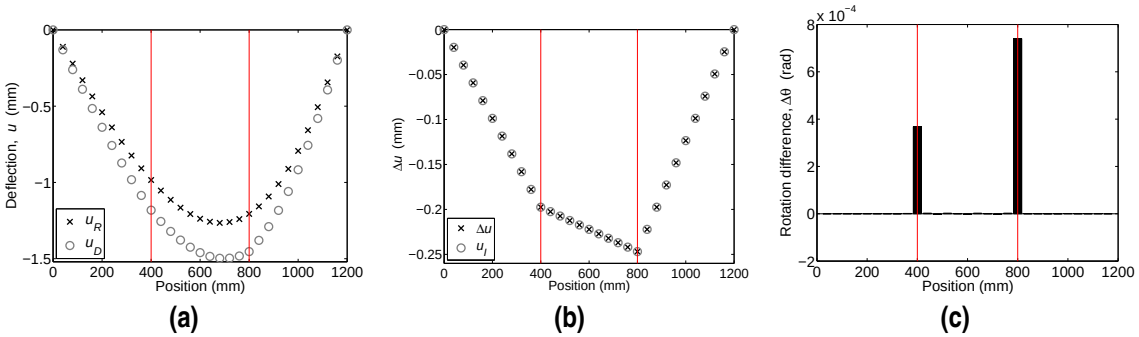


**Figure C.4** (a) Deflections of the finite element model of State R ($u_R$) and State D ($u_D$); (b) deflections of the finite element model of State I ($u_I$) and the difference between $u_D$ and $u_R$ ($\Delta u = u_D - u_R$); (c) Slope difference of $\Delta u$ (The red lines mark the damage locations.).

From this numerical example, the proposed methodology has been verified for damage localization and quantification in noise-free conditions.

**Table C.1** Numerical results.

| Damage | Predicted locations (mm) | Change in rotation $\Delta\theta$ (rad) | Estimated stiffness $K$ (N·m/rad) |
|---|---|---|---|
| D1 | 400 | $3.68e^{-4}$ | $1.81e^{5}$ |
| D2 | 800 | $7.40e^{-4}$ | $1.80e^{5}$ |

### C.3.3 Denoising in practical applications

In practical applications, due to the presence of noise, the challenge is to detect and identify the slope discontinuities associated with damage from noisy data. The computation of slope discontinuities can not be done in a straightforward way from the experimental raw data. A denoising function is required to estimate the shape of $\Delta u$. In this paper, since many practical implementations of SHM for beam-type structures are of simply supported cases (especially in bridges), details for applying the methodology in this case are provided.

For simply supported beams, the deflection of the beam at State I ($\Delta u$) is piecewise linear with turning points at damage locations since the internal forces of undamaged cross-sections at State I are null. Each part of the beam moves as an undeformed rigid body. Therefore, the $l1$ Trending Filter developed by Kim et al. [24] is proposed as a mathematical tool for denoising. The experimentally obtained $\Delta u$ is treated as a spatially distributed signal and the $l1$ Trending Filter estimates the piecewise linear trend of the data through minimizing the objective function in Eq. (C.19)

$$(1/2)\sum_{i=1}^{N}(\Delta u(i) - \Delta u_{l1}(i))^2 + \lambda\sum_{i=2}^{N-1}|\Delta u_{l1}(i-1) - 2\Delta u_{l1}(i) + \Delta u_{l1}(i+1)| \quad \text{(C.19)}$$

where $\Delta u(i)$ is the experimental value of $\Delta u$ at measurement point $i$, $\Delta u_{l1}(i)$ is the estimate of the piecewise linear trend at that point, and $N$ is the number of measurement points. $\lambda$ is a nonnegative parameter which controls the trade-off between the "smoothness" of $\Delta u_{l1}$ and the residual between the original data ($\Delta u$) and the estimated linear trend ($\Delta u_{l1}$). As $\lambda$ approaches 0, $\Delta u_{l1}$ equals the original data. As $\lambda$ approaches an upperbound value ($\lambda_{max}$) $\Delta u_{l1}$ is the best linear regression fit (a straight line) of the data. This upperbound value is defined as:

$$\lambda_{max} = \left|\left|(DD^T)^{-1}D\Delta u\right|\right|_{\infty} \quad \text{(C.20)}$$

$$D = \begin{bmatrix} 1 & -2 & 1 & & & \\ & 1 & -2 & 1 & & \\ & & \ddots & \ddots & \ddots & \\ & & & 1 & -2 & 1 \end{bmatrix}_{(n-2)\times n} \quad \text{(C.21)}$$

where $||\bullet||_p$ means the $p$th-norm. It has been proved that $\lambda_{max}$ can be computed with $O(n)$ arithmetic steps [24]. The $l1$ Trending Filter can be applied with a Matlab function coded by the authors [25]. Since the value of $\lambda$ has an influence on how the piecewise linear trend of $\Delta u_{l1}$ is estimated, it therefore affects the damage localization results. A preliminary inspection on how results are affected by this parameter is necessary in order to select a reasonable value.

A more detailed discussion of the influence of $\lambda$ and the use of rotation difference in practical applications for damage identification are provided in the experimental study in Section C.4.

## C.4 Experimental Results

### C.4.1 Test Setup

An experimental test of a simply supported steel beam was conducted to test the performance of the methodology. Pictures of the experimental setup and the scheme of the test are shown in Fig. C.5. The length of the beam is 1200 mm, and the cross-section is 80 mm wide and 20 mm high. A transversal edge-type notch on the top of the beam at 425 mm from the left end (Fig. C.5(a)) was introduced by a saw cut. The depth of the notch is constant through the width of the cross-section. Three depths (damage severity) were introduced progressively, 2 mm, 4 mm, and 7 mm. They represent 10%, 20% and 35% of the beam height, respectively. It should be noted that, in practice, the depth of the beam is usually higher than its width. However, in the present research, the damage severity is simply defined by the ratio of the crack depth to the beam height and therefore the results are not influenced by the width dimension. The only issue is that the stiffness of the beam is proportional to the width and therefore consistent proportional static loads would be required to obtain the same deflection for different beam widths.

A Digital Imagine Correlation (DIC) system was used to measure the deflection of the beam under static loads (Fig. C.5(b)). For each test, 50 images were captured at a sample rate of 1 Hz. Erratic images were discarded and the average values of displacements were computed from the remaining pictures in order to enhance the accuracy of the results. A total number of 241 measurement points were marked along the beam with an equal spacing of 5 mm.

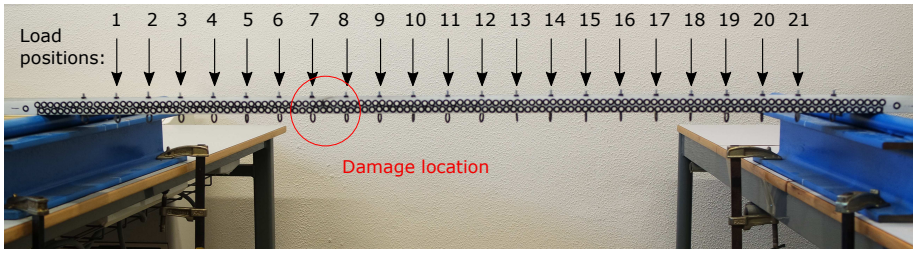


(a)

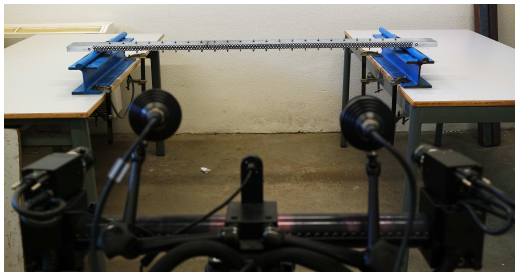

(b)

**Figure C.5** Experimental setups: (a) the tested beam and the load positions, (b) the DIC measuring system.

### C.4.2 Static Loads

From a theoretical point of view, the method is independent from the distribution and magnitude of the load provided that it produces a non-zero bending moment at damage location. However, in practice, a load that produces a measurable value of deflection increment should be applied. For a single damage case with a concentrated force, the maximum increment is generated by applying the load at the damage location. Therefore, when the damage location is unknown, a distributed load would be preferred rather than a single point load in order to capture a deflection increment as big

as possible. However, in practice, a distributed load is more difficult to apply than a concentrated force. One way to approach a distributed load effect is to apply multiple distributed concentrated forces at the same time. The other option is to apply a single concentrated load at multiple positions one at a time and later aggregate the results. In this experimental test, the second method is used. This approach has the advantage of using a small load to obtain a big deflection difference.

A static concentrated force was applied on the beam by hanging a 120 kg mass at 21 equally distributed positions with a spacing of 50 mm (Fig. C.5(a)) individually. The static deflection data were stored for both States R and D, respectively. By combining the experimental deflections for each load position ($u_j$), the resultant value due to a simultaneous application of all the loads ($u_{sum}$) can be obtained from Eq. (C.22).

$$u_{sum} = \sum_{j=1}^{21} u_j \tag{C.22}$$

The measured maximum static deflection of the beam at State R among all load positions is smaller than 4 mm, which is below a usual serviceability limit state requirement. However, the maximum aggregate deflection is 58 mm. This process amplifies the damage effect and therefore can capture small damage effects. Then, these experimental data are processed using the methodology presented in Section C.3. The obtained results are presented and discussed in the following sections.

### C.4.3 Raw Measurements

The sum of deflections of all load positions at States R and D ($u_{R,sum}$ and $u_{D,sum}$, respectively) are shown in Figs. C.6(a), C.7(a), and C.8(a) for 10%, 20%, and 30% damage, respectively. It can be seen that the effects of damage are imperceptible by comparing $u_{R,sum}$ with $u_{D,sum}$ for all three levels of damage. A piecewise linear shape of the deflection differences ($\Delta u_{sum}$) that points to damage are observed in Figs. C.6(b), C.7(b), and C.8(b). The trend is more clear for higher damage level due to the decrease of noise level. Nonetheless, the rotation difference of $\Delta u_{sum}$ computed by using Eq. (C.18) in Figs. C.6(c), C.7(c), and C.8(c) indicate that the computation of rotation difference directly from raw data is unstable and damage can not be localized even for 35% damage severity. Next, the results with the application of the proposed denoising technique are shown.

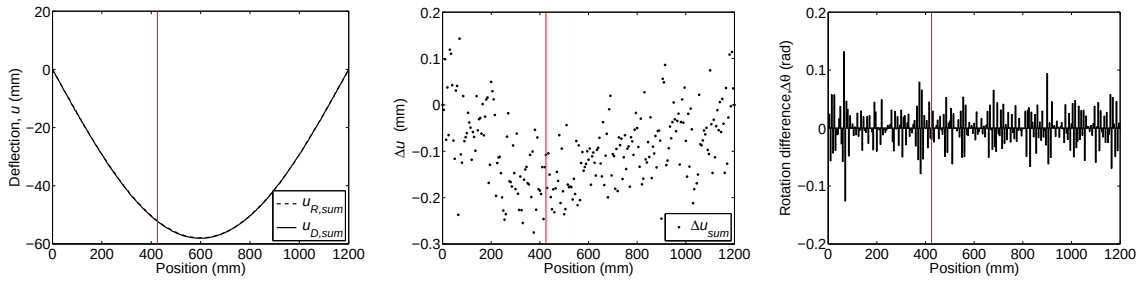


**Figure C.6** Results of direct measurements for 10% severity: (a) the deflection sum at State R ($u_{R,sum}$) and D ($u_{D,sum}$); (b) the difference of the deflections ($\Delta u_{sum}$); (c) the rotation difference of $\Delta u_{sum}$ ($\Delta\theta$). (The red line marks the actual damage location.).

### C.4.4 $l1$ Trending Filter: Selection of $\lambda$

As mentioned in the preceding section, the application of the $l1$ Trending Filter requires a pre-selected value of $\lambda$. At this point, the influence of $\lambda$ should be analyzed in order to obtain good results. The upperbound values for each damage severity are provided in Table C.2. Three different

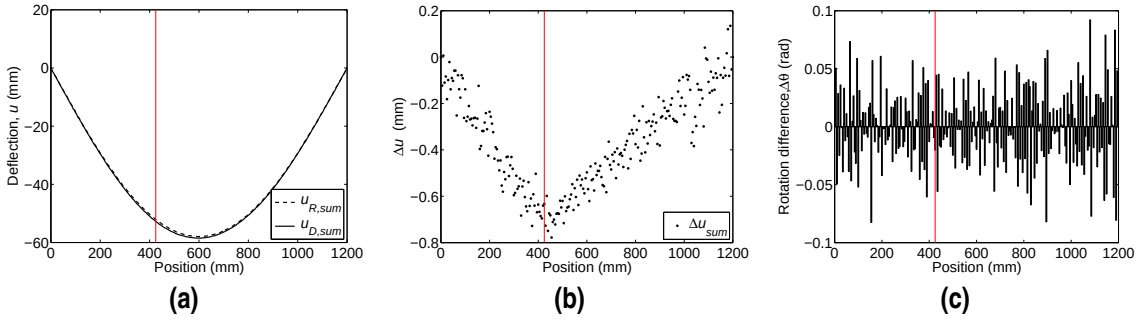


**Figure C.7** Results of direct measurements for 20% severity: (a) the deflection sum at State R ($u_{R,sum}$) and D ($u_{D,sum}$); (b) the difference of the deflections ($\Delta u_{sum}$); (c) the rotation difference of $\Delta u_{sum}$ ($\Delta\theta$). (The red line marks the actual damage location.).

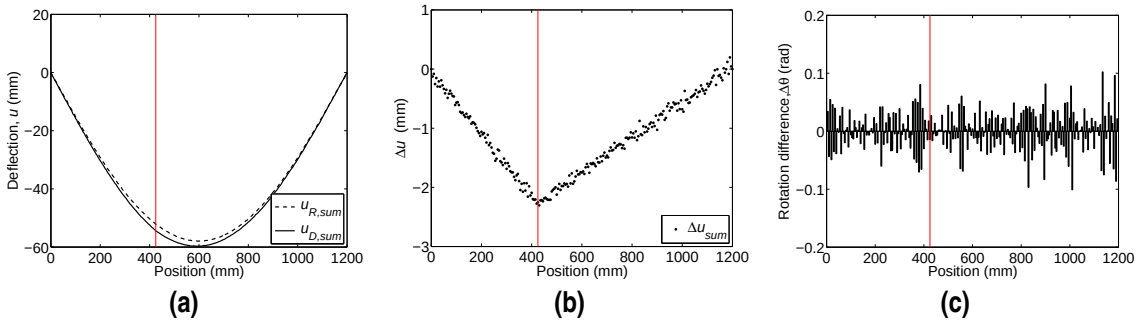


**Figure C.8** Results of direct measurements for 35% severity: (a) the deflection sum at State R ($u_{R,sum}$) and D ($u_{D,sum}$); (b) the difference of the deflections ($\Delta u_{sum}$); (c) the rotation difference of $\Delta u_{sum}$ ($\Delta\theta$). (The red line marks the actual damage location.).

**Table C.2** Cases definition and their corresponding $\lambda$ value.

| Case | $\lambda/\lambda_{max}$ (%) | Damage Severity (%) | | |
|---|---|---|---|---|
| | | 10 | 20 | 35 |
| | 100 | 180.2 | 732.9 | 2454.2 |
| 1 | 1 | 1.8 | 7.3 | 24.5 |
| 2 | 10 | 18.0 | 73.3 | 245.4 |
| 3 | 20 | 36.0 | 146.6 | 490.8 |

$\lambda$ values defined as a percentage of $\lambda_{max}$ are considered in this case study (Cases 1, 2, and 3 in Table C.2). From Eq. (C.19), it is intuitive that a higher value of $\lambda/\lambda_{max}$ is preferred for higher noise level, and vice versa.

### C.4.5 Identification Results

#### 10% Damage

The denoised data from $l1$ Trending Filter ($\Delta u_{sum,l1}$) for 10% damage are plotted in Fig. C.9. It is evident that the $l1$ Trending Filter is capable of denoising the experimental data efficiently. For Case 1, Fig. C.9(a) shows five clear rotation discontinuities. Three of them are consistent with the sign of their corresponding bending moments whereas the other two are not. Obviously, for a real damage, only a positive value of rotational stiffness from Eq. (C.17) is meaningful. Therefore, the cross-sections at 180 mm and 950 mm, where rotation differences are inconsistent with the

bending moment direction are considered undamaged. For Cases 2 and 3, two and one rotation discontinuities can be observed, respectively.

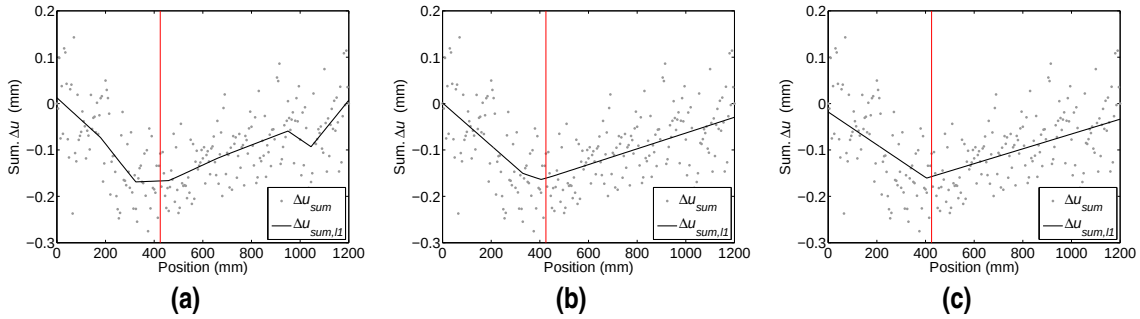


**Figure C.9** Results of $l1$ Trending Filter for 10% damage with different $\lambda$: (a) Case 1; (b) Case 2; (c) Case 3. (The red line marks the actual damage location).

By comparing the experimental rotational stiffness from Eq. (C.16) with the analytical value from Eqs. (C.1)-(C.2), the estimated crack depths at all measurement points are plotted in Fig. C.10. Three damage are identified in Case 1 at 325 mm, 460 mm and 1045 mm with depths of 2.5 mm, 1.3 mm and 4.3 mm, respectively. Fig. C.10(b) shows one damage in Case 2 at 330 mm and another at 405 mm. Both estimated crack depths are around 1.6 mm. The only damage in Case 3 is localized at 405 mm with a depth of 2.03 mm. For this damage severity, Case 3 provides the closest identification results to the actual scenario.

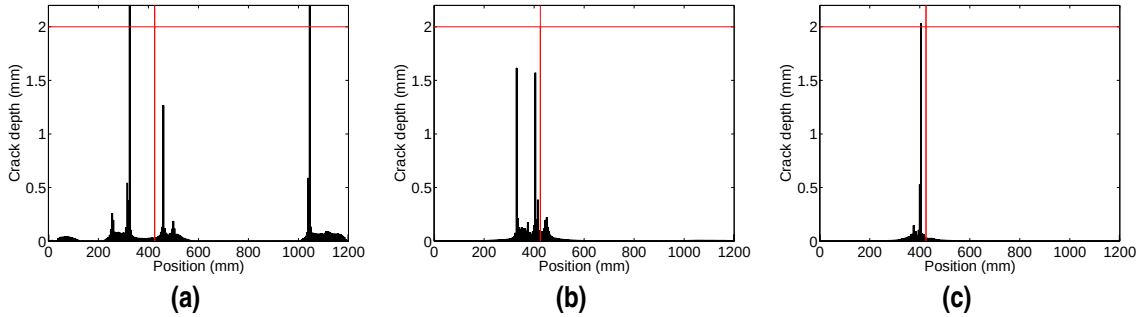


**Figure C.10** Results of estimated crack depth for 10% damage with different $\lambda$: (a) Case 1; (b) Case 2; (c) Case 3. (The red lines mark the actual crack depth and the actual crack location).

Results in Figs. C.9(a) and C.10(a) indicate that if the value of $\lambda$ is too small, the $l1$ Trending Filter provides a result close to the original data, which would lead to false positive errors due to its sensitivity to oscillations of the data. The inconsistent rotation discontinuity is an indicator of the inaccuracy of the results of Case 1.

### 20% Damage

The denoised data from $l1$ Trending Filter ($\Delta u_{sum,l1}$) for 20% damage in Fig. C.11 shows that all three cases of $\lambda$ provide reasonable estimates of $\Delta u_{sum}$. Two rotation discontinuities are observed in Case 1 while only one in Cases 2 and 3. However, Fig. C.11(c) illustrates the fact the $l1$ Trending Filter tends to approach the data with a single straight line as $\lambda$ is higher. Therefore, when $\lambda$ is too high, the predicted damage location tends to shift towards a wrong location.

The corresponding estimated crack locations and depths are plotted in Fig. C.12. Figure C.12(a) shows that one of the two potential damage regions is at 355 mm and the other is from 440 to 455 mm. All estimated crack depths are below 3 mm. In Case 2 (Fig. C.12(b)), a single crack is

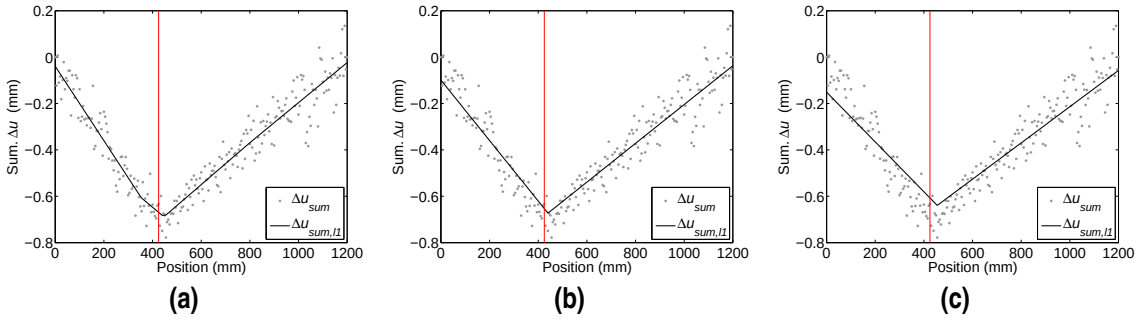


**Figure C.11** Results of $l1$ Trending Filter for 20% damage with different $\lambda$: (a) Case 1; (b) Case 2; (c) Case 3. (The red line marks the actual damage location).

predicted at 440 mm with a 4.3 mm depth. In Case 3, the crack is 4.03 mm deep and is localized at 455 mm. The prediction from Case 2 is 15 mm closer to the actual damage than the prediction from Case 3. Although the evaluated crack depth from Case 2 is 8% higher than the real value, it is considered a very accurate result from a practical point of view. Therefore, for this damage level, Case 2 provides the best damage dentification results.

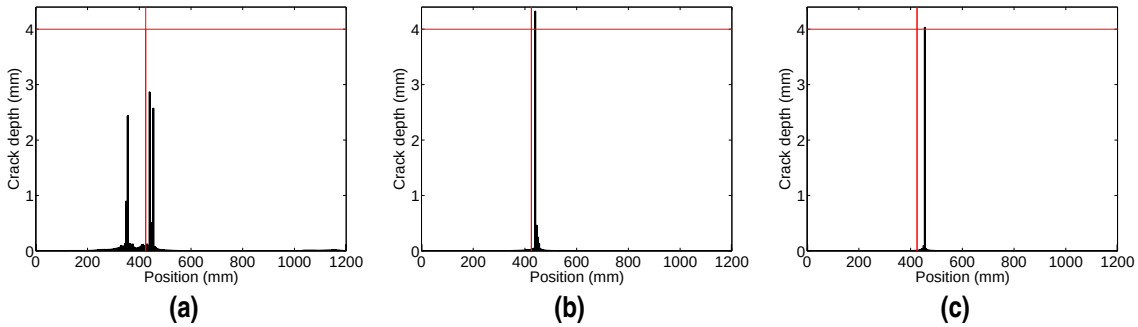


**Figure C.12** Results of estimated crack depth for 20% damage with different $\lambda$: (a) Case 1; (b) Case 2; (c) Case 3. (The red lines mark the actual crack depth and the actual crack location).

### 35% Damage

The denoised data from $l1$ Trending Filter ($\Delta u_{sum,l1}$) for 35% damage are plotted in Fig. C.13. Apparently, the estimated result from Case 1 matches the raw data better than those from Cases 2 and 3. Figures C.13(b)-(c) indicate that both values of $\lambda$ are too high.

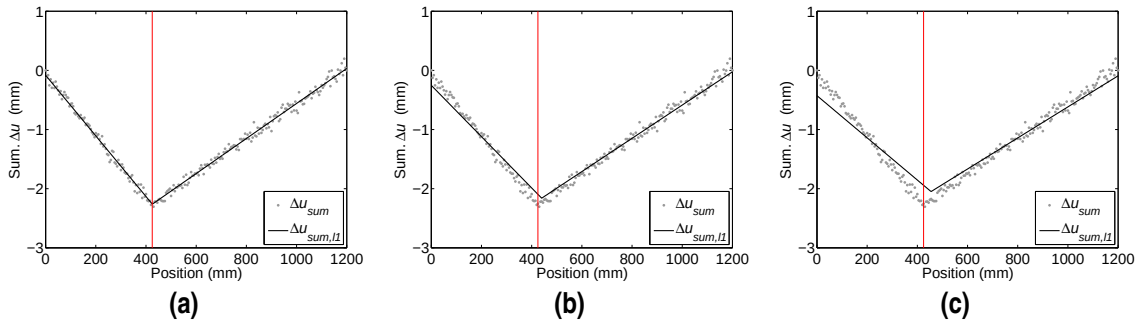


**Figure C.13** Results of $l1$ Trending Filter for 35% damage with different $\lambda$: (a) Case 1; (b) Case 2; (c) Case 3. (The red line marks the actual damage location).

The corresponding estimated crack locations and depths are plotted in Fig. C.14. Three consecutive cracks are predicted in Case 1 with the center point at 425 mm. The estimated crack depths are 3.54 mm, 6.57 mm and 3.94 mm, respectively. In Case 2, one single damage is localized at 440 mm with a depth of 7.59 mm (8% overestimated). In Case 3, two adjacent cracks at 450 mm and 455 mm are identified with 1.77 mm and 6.94 mm in depth, respectively. For this damage extent, the prediction from Case 1 is the closest to the actual damage. For this case, the damage is localized with 100% accuracy and the evaluated crack depth is 5% lower than actual value. This difference can be due to the discrepancy between the real crack influence zone and the ideal spring model. On the other hand, although the values of $\lambda$ are too high for Cases 2 and 3, the results from both cases can be considered very accurate from a practical point of view.

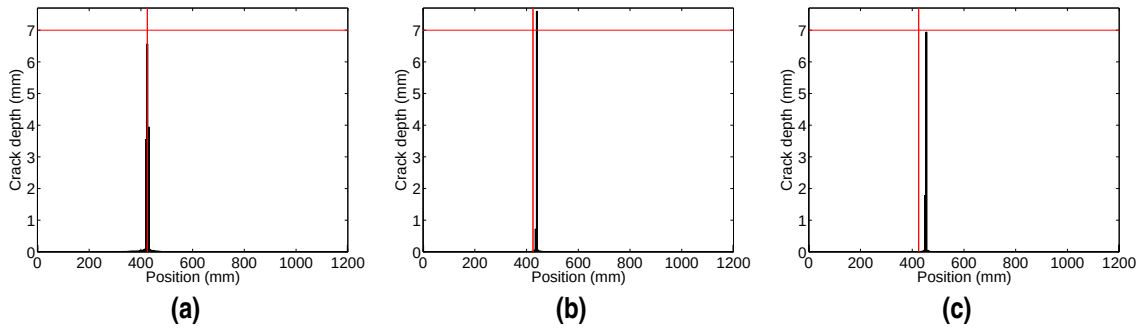


**Figure C.14** Results of estimated crack depth for 35% damage with different $\lambda$: (a) Case 1; (b) Case 2; (c) Case 3. (The red lines mark the actual crack depth and the actual crack location).

### C.4.6 Analysis of Noise Level

In this section, the denoised estimate ($\Delta u_{sum,l1}$) is used to evaluate the noise in the raw data ($\Delta u_{sum}$). In this discussion, the values of $\lambda$ that provided the best prediction of the damage are considered. The noise is evaluated by the Coefficient of Variation (CV) defined as:

$$\mathrm{CV}_{\%} = \frac{\sigma_{\Delta u_{sum}}}{\mu_{\Delta u_{sum}}} \times 100 \tag{C.23}$$

where $\sigma_{\Delta u_{sum}}$ and $\mu_{\Delta u_{sum}}$ are the standard deviation and mean value of the sum of deflection difference, defined as:

$$\sigma_{\Delta u_{sum}} = \sqrt{\frac{1}{N}\sum_{i=1}^{N}(\Delta u_{sum}(i) - \Delta u_{sum,l1}(i))^2} \tag{C.24}$$

$$\mu_{\Delta u_{sum}} = \frac{1}{N}\sum_{i=1}^{N}\Delta u_{sum}(i) \tag{C.25}$$

being $N$ is the number of measurement points on the beam.

Table C.3 shows that, the standard deviations of deflection difference for all three damage levels are similar, which indicates that the accuracy of the measuring system is consistent for all the tests. The experimental noise is mainly caused by the resolution inaccuracies of the DIC measuring system. However, as the damage severity grows, the noise level expressed by the CV decreases significantly. As a result, the damage identification is more reliable.

### C.4.7 Summary

In this case study, three $\lambda$ values corresponding to 1%, 10%, and 20% of $\lambda_{max}$ are investigated for three levels of damage severity (depth of 10%, 20%, and 35% of cross-section height). The best

**Table C.3** Summary of noise evaluation for all damage severities.

| Damage severity (%) | $\lambda$ | $\mu_{\Delta u_{sum}}$ (mm) | $\sigma_{\Delta u_{sum}}$ (mm) | CV (%) |
|---|---|---|---|---|
| 10 | Case 3 | 0.0943 | 0.0671 | 71 |
| 20 | Case 2 | 0.3652 | 0.0696 | 19 |
| 35 | Case 1 | 1.1305 | 0.0652 | 6 |

assessment results for all damage scenarios are listed in Table C.4. For different damage levels, the best choice of $\lambda$ varies. Despite the measurements are highly contaminated by noise for 10% damage, the methodology successfully localizes and quantifies the damage. As the damage level increases, a smaller portion of $\lambda_{max}$ performs better for the damage identification process. When the value of $\lambda$ is too small (see Case 1 for 10% damage Fig. C.6(a) and C.10(a)), the effect of noise could lead to false positive errors and unrealistic results. On the other hand, when the value of $\lambda$ is too high, the denoising method tends to provide inaccurate damage estimation results. When $\lambda$ is properly selected, the accuracy of both the localization and quantification results are improved.

**Table C.4** Summary of closest prediction for all damage severities.

| Damage severity (%) | $\lambda$ | Predicted locations (mm) | Estimated depth (mm) |
|---|---|---|---|
| 10 | Case 3 | 405 | 2.03 |
| 20 | Case 2 | 440 | 4.32 |
| 35 | Case 1 | 425 | 6.57 |

The results in Case 2 for 10% damage (see Fig. C.10(b)) and Case 1 for 20% damage (see Fig. C.12(a)) illustrate a similar phenomenon. A multiple damage scenario with two cracks close to the actual damage location can be identified from the peaks on the estimated rotation difference. This is due to an improper value of $\lambda$. However, the estimate of the deflection increment ($\Delta u_{sum,l1}$) seems to be well correlated with the original noisy data ($\Delta u_{sum}$) in Fig. C.9(b) and C.11(a), respectively. The fact that the estimated multiple damages are of a lower severity than the actual single crack can be regarded as the non-uniqueness of the solution in solving the inverse problem of damage identification from the estimate of the deflection increment ($\Delta u_{sum,l1}$). In other words, the effect of an actual single damage can be equivalent to that of multiple damages with lower severities near its location. Thus, results from these two cases can be considered also valid from a practical point of view. On the other hand, cross-sections with very small values of estimated crack depths in Figs. C.10, C.12 and C.14 are considered undamaged in practical applications.

## C.5 Conclusions

A damage detection and localization method in beams based on the changes in static deflections is presented in this paper. The discontinuities in the slope of the deflection difference between the pre- and post-damage states of the beam reveal the damage locations. Moreover, through theory of mechanics, the damage severities of the damaged cross-sections can be estimated. The merits of the proposed methodology are summarized as follows:

- It is efficient and simple to implement in practical applications;
- It is non-modelled based for damage detection and localization;
- It is a promising robust to noise approach;

- Theoretically, even the deflections induced by a permanent dead load on the structure could be used.

The proposed methodology has been validated by experimental test with various severities of damage. Although at this moment, the selection of $\lambda$ is based on trial and error, the authors note that a range between 1 to 20% of the maximum value would be a good initial point. The performance of the proposed methodology for multiple damage scenarios is under investigation. Questions such as the sensitivity of the method to relative damage severity and the minimum perceptible damage spacing are being studied. Moreover, specific denoising methodologies for other types of boundary conditions will be explored.

## Ackowledgements

This work was supported by the Consejería de Economía, Innovación, Ciencia y Empleo of Andalucía (Spain) under project P12-TEP-2546 and the Spanish Ministry of Economy and Competitiveness (Ministerio de Economía y Competitividad, Secretaría de Estado de Investigación, Desarrollo e Innovación) through research project BIA2016-43085-P. The financial support is gratefully acknowledged.

## References

[1] Abdel Wahab, M., and De Roeck, G. Damage detection in bridges using modal curvatures: application to a real damage scenario. *J. Sound Vib. 226*, 2 (1999), 217–235.

[2] Abdo, M. A.-B. Parametric study of using only static response in structural damage detection. *Eng. Struct. 34* (2012), 124–131.

[3] Abdo, M.-B., and Hori, M. A numerical study of structural damage detection using changes in the rotation of mode shapes. *J. Sound Vib. 251*, 2 (mar 2002), 227–239.

[4] Babu, K. R. P., Kumar, B. R., Narayana, K. L., and Rao, K. M. Multiple crack detection in beams from the differences in curvature mode shapes. *APRN J. Eng. Appl. Sci. 10*, 4 (2015), 1701–1710.

[5] Bakhtiari-Nejad, F., Rahai, A., and Esfandiari, A. A structural damage detection method using static noisy data. *Eng. Struct. 27*, 12 SPEC. ISS. (2005), 1784–1793.

[6] Caddemi, S., and Morassi, A. Crack detection in elastic beams by static measurements. *Int. J. Solids Struct. 44*, 16 (2007), 5301–5315.

[7] Caddemi, S., and Morassi, A. Detecting multiple open cracks in elastic beams by static tests. *J. Eng. Mech. 137*, 2 (2011), 113–124.

[8] Cao, M., Radzieński, M., Xu, W., and Ostachowicz, W. Identification of multiple damage in beams based on robust curvature mode shapes. *Mech. Syst. Signal Process. 46*, 2 (jun 2014), 468–480.

[9] Cao, M. S., Xu, W., Ren, W. X., Ostachowicz, W., Sha, G. G., and Pan, L. X. A concept of complex-wavelet modal curvature for detecting multiple cracks in beams under noisy conditions. *Mech. Syst. Signal Process. 76-77* (2016), 555–575.

[10] Chang, P. C., Flatau, A., and Liu, S. C. Review paper: Health monitoring of civil infrastructure. *Struct. Heal. Monit. 2*, 3 (2003), 257–267.

[11] Choi, I.-Y., Lee, J. S., Choi, E., and Cho, H.-N. Development of elastic damage load theorem for damage detection in a statically determinate beam. *Comput. Struct. 82*, 29-30 (2004), 2483–2492.

[12] Chung, W., Kim, S., Kim, N. S., and up Lee, H. Deflection estimation of a full scale prestressed concrete girder using long-gauge fiber optic sensors. *Constr. Build. Mater. 22*, 3 (2008), 394–401.

[13] Dawari, V., and Vesmawala, G. Structural damage identification using modal curvature differences. *IOSR-JMCE* (2013), 33–38.

[14] Dimarogonas, A. D. Vibration of cracked structures: A state of the art review. *Eng. Fract. Mech. 55*, 5 (1996), 831–857.

[15] Dimarogonas, A. D., Paipetis, S. A., and Chondros, T. G. *Analytical Methods in Rotor Dynamics*, 2nd ed. Springer, 2013.

[16] Doebling, S. W., Farrar, C. R., and Prime, M. B. A summary review of vibration-based damage identification methods. *Shock Vib. Dig. 30*, 2 (1998), 91–105.

[17] Fan, W., and Qiao, P. Vibration-based damage identification methods: A review and comparative study. *Struct. Heal. Monit. 10*, 1 (2011), 83–111.

[18] Farrar, C. R., and Jauregui, D. A. Comparative study of damage identification algorithms applied to a bridge: I. Experiment*. *Smart Mater. Struct. 7*, 98 (1998), 704–719.

[19] Farrar, C. R., and Jauregui, D. A. Comparative study of damage identification algorithms applied to a bridge: II. Numerical study. *Smart Mater. Struct. 7*, 5 (oct 1998), 720–731.

[20] Gudmundson, P. The dynamic behaviour of slender structures with cross-sectional cracks. *J. Mech. Phys. Solids 31*, 4 (1983), 329–345.

[21] Hjelmstad, K. D., and Shin, S. Damage detection and assessment of structures from static response. *J. Eng. Mech. 123*, 6 (1997), 568–576.

[22] Jiang, R., Jáuregui, D. V., and White, K. R. Close-range photogrammetry applications in bridge measurement: Literature review. *Meas. J. Int. Meas. Confed. 41*, 8 (2008), 823–834.

[23] Kim, J.-T., Ryu, Y.-S., Cho, H.-M., and Stubbs, N. Damage identification in beam-type structures: frequency-based method vs mode-shape-based method. *Eng. Struct. 25*, 1 (2003), 57–67.

[24] Kim, S.-J., Koh, K., Boyd, S., and Gorinevsky, D. l1Trend Filtering. *SIAM Rev. 51*, 2 (2009), 339–360.

[25] Koh, K., Kim, S.-J., and Boyd, S. l1 Trending Filtering function Matlab, 2008. (accessed 20 June 2017).

[26] Pandey, A., Biswas, M., and Samman, M. Damage detection from changes in curvature mode shapes. *J. Sound Vib. 145*, 2 (1991), 321–332.

[27] Rizos, P. F., Aspragathos, N., and Dimarogonas, A. D. Identification of crack location and magnitude in a cantilever beam from the vibration modes. *J. Sound Vib. 138*, 3 (1990), 381–388.

[28] Rucka, M., and Wilde, K. Application of continuous wavelet transform in vibration based damage detection method for beams and plates. *J. Sound Vib. 297* (2006), 536–550.

[29] Rucka, M., and Wilde, K. Crack identification using wavelets on experimental static deflection profiles. *Eng. Struct. 28* (2006), 279–288.

[30] Salawu, O. Detection of structural damage through changes in frequency: a review. *Eng. Struct. 19*, 9 (1997), 718–723.

[31] Seyedpoor, S. M., and Yazdanpanah, O. An efficient indicator for structural damage localization using the change of strain energy based on static noisy data. *Appl. Math. Model. 46*, 2 (2013), 231–244.

[32] Solís, M., Algaba, M., and Galvín, P. Continuous wavelet analysis of mode shapes differences for damage detection. *Mech. Syst. Signal Process. 40*, 2 (2013), 645–666.

[33] Sousa, H., Cavadas, F., Henriques, A., Bento, J., and Figueiras, J. Bridge deflection evaluation using strain and rotation measurements. *Smart Struct. Syst. 11*, 4 (2013), 365–386.

[34] Stöhr, S., Link, M., Rohrmann, R., and Rücker, W. Damage detection based on static measurements of bridge structures. *Proc. Int. Modal Anal. Conf. IMAC XXIV* (2006).

[35] Whalen, T. M. The behavior of higher order mode shape derivatives in damaged, beam-like structures. *J. Sound Vib. 309* (2008), 426–464.

[36] Xu, W., Zhu, W. D., Smith, S. A., and Cao, M. S. Structural damage detection using slopes of longitudinal vibration shapes. *J. Vib. Acoust. 138*, 3 (2016), 034501.

[37] Yan, Y. J., Cheng, L., Wu, Z. Y., and Yam, L. H. Development in vibration-based structural damage detection technique. *Mech. Syst. Signal Process. 21* (2007), 2198–2211.

[38] Yang, Q., and Sun, B. Structural damage localization and quantification using static test data. *Struct. Heal. Monit. 10*, 4 (2010), 381–389.

[39] Yeo, I., Shin, S., Lee, H. S., and Chang, S.-p. Statistical damage assessment of framed structures from static responses. *J. Eng. Mech. 126*, April (2000), 414–421.

[40] Yu, Y., Liu, H., Li, D., Mao, X., and Ou, J. Bridge deflection measurement using wireless mems inclination sensor systems. *Int. J. Smart Sens. Intell. Syst. 6*, 1 (2013), 38–57.

# Appendix D
# Paper D

Ma, Q. and Solís, M. (accepted). "Multiple damage identification in beams from full-field digital photogrammetry", *Journal of Engineering Mechanics.*

Journal: Journal of Engineering Mechanics - ASCE

ISSN: 0733-9399

Journal Citation Reports (2017): Impact factor: 1.799

- Engineering, Mechanical-SCIE: Q2 (60/128)

SCIMAGO (2017)

- Mechanical Engineering: Q1 (132/950)
- Mechanics of Materials: Q2 (103/480)

| | |
|---|---|
| Asunto | **Decision on Manuscript MS EMENG-4611R2 - [EMID:eb66b6ba089f48cc]** |
| De | Journal of Engineering Mechanics <em@editorialmanager.com> |
| Remitente | <em.jrnemeng.0.5fdf23.a6fc7bb8@editorialmanager.com> |
| Destinatario | Qiaoyu Ma <qma@us.es> |
| Responder a | Journal of Engineering Mechanics <journal-submissions5@asce.org> |
| Fecha | 12/12/2018 20:53 |

You are being carbon copied ("cc:'d") on an e-mail "To" "Mario Solis" msolis@us.es
CC: "Qiaoyu Ma" qma@us.es

Ref.: Ms. No. EMENG-4611R2
Multiple damage identification in beams from full-field digital photogrammetry
Qiaoyu Ma, MSc; Mario Solis, PhD

Dear Dr. Solis,

Your Technical Paper, listed above, has been accepted for publication in ASCE's Journal of Engineering Mechanics.

Your manuscript will now be forwarded to a Production Editor who will prepare it for publication. You will be notified of a publication date once your paper has been schedule for an issue.

Finally, our editors have requested that authors of accepted manuscripts serve as reviewers for Journal of Engineering Mechanics. If you are willing to serve as a reviewer, please reply to this email and let me know.

Thank you for submitting your work to ASCE's Journal of Engineering Mechanics.

Sincerely,

Taryn Dollings
Editorial Coordinator

# Multiple damage identification in beams from full-field digital photogrammetry

Qiaoyu Ma and Mario Solís

Department of Continuum Mechanics and Structural Analysis,
Escuela Técnica Superior de Ingeniería, Universitdad de Sevilla,

**Abstract** This paper addresses the identification problem of multiple open cracks in beams based on the damage-induced variations in the static deflection of the beam. A two-step non-model based damage localization and quantification methodology is proposed. First, the damage locations can be identified from the slope discontinuities in the deflection variation using a specific linear trend filtering function. Then the crack depths can be assessed from characteristic expressions of rotational spring models. An experimental case study of a simply supported beam with multiple cracks is used to exam the performance of the method. The deflections of the beam were measured with a digital photogrammetric system using partial measurements. The difference between the idealized lumped spring model for the crack and the actual effect of a real crack in the damage identification process and the performance of the method for statically indeterminate beams are illustrated through numerical examples. The paper shows that the proposed method can accurately localize and quantify multiple closely spaced cracks in beams in practical applications.

**Keywords** beams, multiple cracks identification, static deflection, digital photogrammetry.

## D.1 Introduction

Identification of cracks in beam-type structures is one of the classical problems in structural damage detection. The occurrence of cracks in beams leads to a reduction in local stiffness. This change in the properties of the beam affects the response of the structure when being excited. For crack localization in beams, comprehensive researches about the influence of cracks on the structural dynamic and static behavior have been conducted [2, 3, 6, 7, 15, 18, 19, 22, 24, 34, 38, 44].

The problem of localizing cracks in beams can be solved by identifying the discontinuities in the slope of the static deflection of the damaged beam. However, it is difficult to acquire the slope of the damaged deflection in practice.The wavelet analysis has the capability to reveal the first and second order discontinuities in the deflection of a beam directly [5]. Alternatively, the deflection difference between the damaged and undamaged beam can be used since it contains the first and second order discontinuities at damage locations as well. Gudmundson [28] indicated that the damaged deflection can be interpreted as a superposition of the predamaged deflection and an increment induced by the effect of damage solely. Therefore, the damage location can be detected by identifying the slope discontinuities in the deflection variation instead. Spanos et al.[45] applied the wavelet transform to the static deflection difference for damage detection in a numerical study of beams with multiple cracks. Caddemi and Morassi [13, 14] proposed a multiple crack detection method by solving an inverse problem based on the deflection difference of beams. Ma and Solís [36, 37] presented a more direct approach to localize the slope discontinuities in the deflection variation. Through experimental tests, the authors successfully identified the location and the severity of the damage in a simply-supported beam with a single crack.

Alternatively, based on the Maxwell-Betti reciprocal work theorem, the static deflection of the beam under a single concentrate load is equal to the deflection influence line of the loaded cross-section subjected to the same load. Štimac and Kožar [46] reported that the influence line of the deflection variation at a certain cross-section can be used as damage indicator as well as its slope

and curvature. Similarly, Stöhr et al. [47] proposed to use the slope variation of the influence lines because it can be measured from inclinometers directly in practice. In addition, He and Zhu [29] stated that the operational deflection difference of a beam under a moving load with low velocity indicated the locations of multiple cracks.

Other techniques based on the static deflection variation have been developed as well. Choi et al. [17] presented an "elastic damage load theorem"(EDLT) which points out that the shape of the deflection variation equals to the moment influence line of the conjugate beam at the point where the damage occurs. However, this theorem is limited for statically determined beams. Di Paola and Bilello [21] demonstrated that the deflection difference equals the deflection of an auxiliary beam subjected to certain superimposed curvature, which is a function of the actual bending moment distribution and damage distribution functions.

After identifying the damage locations, their extents can be evaluated with proper crack models. As classified by Friswell and Penny [26], the three ways to model cracks in beams are: 1) discrete spring models, 2) local stiffness reduction, and 3) complex finite element models in two or three dimensions. For Euler-Bernoulli beams with edge cracks, the discrete rotational spring is considered an efficient model. Based on the behavior of the crack, the spring can be modeled as linear (open crack), bilinear (switching crack), or nonlinear (breathing crack). This idealization has been used in the estimation of the mode shapes or static deflections of beams, columns and arches with cracks [1, 9–12, 16, 18, 20, 25, 32, 40, 41]. In this paper, the applicability of using five different linear rotational spring models to quantify the severities of the cracks is analyzed.

In order to successfully identify the slope discontinuities in the static deflection, a dense measurement grid is required. The implementation of close range digital photogrammetric technology in the Structural Health Monitoring (SHM) field can fulfill this demand. Applications for laboratory measurements of static structural deflection of beams and surface deformation of plates [4, 27, 43, 49] as well as for on-site measurement [30, 31, 48] have been employed. Similarly, a Digital Image Correlation (DIC) system was used to measure the deflection of the beam in the experimental tests in the present research.

The aim of this paper is to present a practical damage detection, localization and quantification methodology in beams with multiple cracks directly through experimental static deflection measurements, without neither solving inverse problem nor using any finite element model. First, the damaged locations are determined through identifying the slope discontinuities in the static deflection variation between the pre- and post-damage states by using a proper trend filter. Then, the crack depths are quantified through idealized rotational spring models. In addition, the feasibility of measuring the whole structural response by combining partial measurements is examined in the paper.

The outline of the paper is as follows. The fundamentals of the proposed method are presented in the next section. Then, the methodology is examined through an experimental case study of multiple cracks in a simply supported beam. Moreover, numerical examples are used to illustrate the difference between the actual crack effect and the idealized model as well as the performance of the method for statically indeterminate beams. Lastly, conclusions are drawn.

## D.2 Damage identification methodology

### D.2.1 Superposition scheme

Given a structure under some external loads, the occurrence of the damage leads to a change in the structural behavior. Assuming that the external conditions remain unchanged, this change in the behavior of the structure can be taken as the effect of damage only. For beam-type structures with cracks, the static response can be therefore decomposed into the static response of the beam before

damage and the variation induced by damage. In this paper, a brief review of this decomposition scheme is provided (a detailed description can be found in the work of Ma and Solís [37]).

The corresponding states to the decomposition scheme are called 'Damaged State', 'Reference State' and 'Incremental State', respectively (hereinafter referred to in abbreviated form as States D, R and I). Assuming that $n$ cracks appear at locations $0 < b_i < L$, $i = 1,2,...,n$ along the beam length $L$ and considering "$x$" a coordinate along the beam, these states are defined as follows:

**State D:** the beam, after the occurrence of damage, is under the external load $P$ which generates the internal bending moment distribution $M_D(x)$ and the beam deflection $u_D(x)$;

**State R:** the beam, before the occurrence of damage, is under the same external load $P$ which generates the internal bending moment distribution $M_R(x)$ and the beam deflection $u_R(x)$;

**State I:** the beam, after the occurrence of damage, is under a series of self-equilibrated bending moments $M_R(b_i)$ applied at the damaged cross-sections $b_i$, respectively, which generates the internal bending moment distribution $M_I(x)$ and the beam deflection $u_I(x)$, i.e. the deflection variation.

An example of a beam with three cracks ($n = 3$) is depicted in Fig. D.1. Idealized equivalent lumped rotational springs with stiffness $K_{eq,i}$ are used to model the cracks. Since the intact parts of the beam are connected by the spring, the depicted gaps among those parts are zero ($\delta = 0$). Assuming that the beam is well constrained, the boundary conditions are not specified. The external load ($P$) is represented by a concentrated force applied at a random position on the beam. The following expressions can be written based on the superposition scheme:

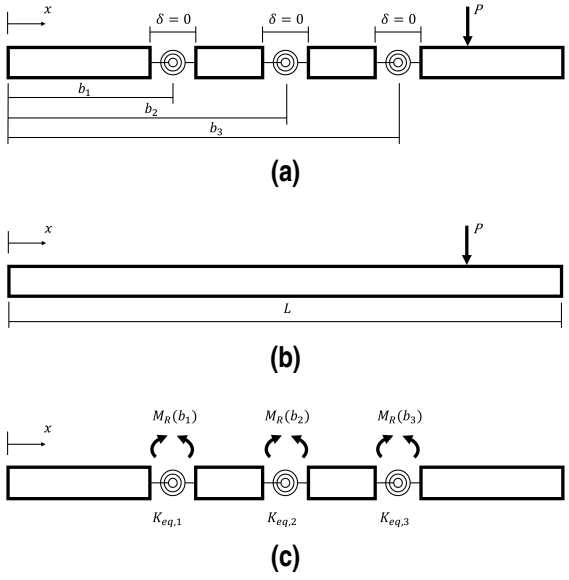


**Figure D.1** Decomposition scheme of a beam with three cracks idealized by rotational springs at (a) State D; (b) State R; (c) State I.

$$u_D(x) = u_R(x) + u_I(x) \tag{D.1}$$

$$M_D(x) = M_R(x) + M_I(x) \tag{D.2}$$

$$\theta_D(x) = \theta_R(x) + \theta_I(x) \tag{D.3}$$

where $\theta(x)$ is the rotation of the cross-section. The rotation or slope discontinuity $\phi_i$ caused by the $i$th crack at damage location $b_i$ is

$$\phi_i = \theta_D(b_i^+) - \theta_D(b_i^-) \tag{D.4}$$

where the superscripts "+" and "−" represent the right and left sides of the cross-section. Since the effect of damage only comes from State I, Eq. (D.4) can be written as:

$$\phi_i = \theta_I(b_i^+) - \theta_I(b_i^-) \tag{D.5}$$

From Fig. D.1 (c), it can be seen that the deflection variation $u_I$ is a function of the internal bending moments at the damaged cross-sections at State R, the damage severities and the constraints of the beam. The damage causes discontinuity in the first- and second-order derivatives of $u_I$ at damage locations. Therefore, the crack positions can be determined by identifying the sudden changes in the slope discontinuities in $u_I$. Note that a necessary condition for this methodology is that the applied external load produces non-zero bending moments at damaged cross-sections.

Based on the Hooke's law, the following relationship between the rotational stiffness and the rotation discontinuity caused by crack $i$ can be established:

$$\phi_i = \frac{M_D(b_i)}{K_{eq,i}} \tag{D.6}$$

where $M_D(b_i)$ is the damaged bending moment of the spring at location $b_i$. $M_D(b_i)$ depends on the boundary conditions and the damage severities, as well as the locations and amplitudes of the applied loads.

At State I, the applied moment $M_R(b_i)$ at each spring is taken partly by the spring and partly by the intact parts. The portion taken by the spring equals to the internal bending moment of the spring at State D. The other part transmitted to the intact segments can be regarded as the moment redistribution due to damage. At State D and I, the equivalent rotational stiffness of the spring can be obtained by a rewritten form of Eq. D.6:

$$K_{eq,i} = \frac{M_D(b_i)}{\phi_i} \tag{D.7}$$

By using a proper characteristic function between the crack depth and the equivalent rotational spring stiffness, the damage extent can be assessed.

### D.2.2 Detection of slope discontinuities

Analytical solutions of $u_I$ for Euler-Bernoulli beam with various boundary conditions using rotational spring models can be found in the work of Caddemi and Morassi [13]. For statically determinate beams, $u_I$ is a piecewise linear curve. In order to localize the slope discontinuities in the experimental deflection variation, a linear trend filter named $l1$ Trend Filtering [33] is used. It is a mathematical curve fitting tool which has the capability to estimate the local linear trend of the data by minimizing the following objective function

$$(1/2)\sum_{k=1}^{N}(u_{I,k} - u_{I,k}^{l1})^2 + \lambda \sum_{k=2}^{N-1} |u_{I,k-1}^{l1} - 2u_{I,k}^{l1} + u_{I,k+1}^{l1}| \tag{D.8}$$

where $u_{I,k}$ is the experimental value of the deflection variation at measurement point $k$, $u_{I,k}^{l1}$ is the estimate of the $l1$ Trend Filtering and $N$ is the number of measurement points. $\lambda$ is a non-negative parameter which controls the trade-off between the "smoothness" of the estimate

($|u^{l1}_{I,k-1} - 2u^{k}_{I,k} + u^{l1}_{I,k+1}|$) and the residual between the measurement and the estimate $(u_{I,k} - u^{l1}_{I,k})^2$. As $\lambda$ approaches 0, the estimate equals the original data. As $\lambda$ approaches an upper bound value ($\lambda_{max}$), the estimate is a straight line (the linear regression fit of the whole data set). This upper bound value is defined as:

$$\lambda_{max} = \left|\left|(DD^T)^{-1}D\Delta u\right|\right|_{\infty} \tag{D.9}$$

$$D = \begin{bmatrix} 1 & -2 & 1 & & & \\ & 1 & -2 & 1 & & \\ & & \ddots & \ddots & \ddots & \\ & & & 1 & -2 & 1 \end{bmatrix}_{(N-2)\times N} \tag{D.10}$$

where $||\bullet||_p$ means the $p$th-norm. The $\lambda_{max}$ can be computed with $O(n)$ arithmetic steps (see Reference [33] Section 5.1). The $l1$ Trend Filtering can be applied with a MATLAB function provided by the authors [35]. For convenience, since the value of $\lambda_{max}$ is case dependent, it is proposed to refer the value of $\lambda$ as a percentage of $\lambda_{max}$. As it has been shown in a previous research [37], the selection of $\lambda$ can be done by visual inspection of the fitted data. By making a trial and error search with different percentages of $\lambda_{max}$, an appropriate prediction of a piecewise linear regression, neither overfitted nor underfitted, can be obtained. The damage identification results are not very sensitive to small relative changes in the value of $\lambda$. Therefore, a proper value of $\lambda$ can be easily obtained in practice.

In practice, the slope discontinuity can be estimated through a finite difference procedure. Given three equally spaced measurement points and their corresponding deflection measurements ( $u^{l1}_{I,k-1}$, $u^{l1}_{I,k}$, $u^{l1}_{I,k+1}$), the numerical evaluation of the difference of forward and backward slopes at location $k$ can be estimated through Eq. (D.11), where $\Delta x$ is the distance between adjacent measurement points. The damage positions are localized at those cross-sections associated with high values of $\phi_k$.

$$\phi_k = \frac{u^{l1}_{I,k+1} - 2u^{k}_{I,k} + u^{l1}_{I,k-1}}{\Delta x} \tag{D.11}$$

### D.2.3 Rotational spring models for cracks

For a one-sided crack of uniform depth $d$ in a rectangular cross-section of width $B$ and height $H$, the idealized equivalent rotational stiffness of the spring model is a function of the damage severity which is defined as the ratio of the crack depth to the cross-section height ($\xi = d/H$). The equivalent rotational stiffness models can be expressed as

$$K_{eq} = \frac{EI}{H}\frac{1}{J(\xi)} \tag{D.12}$$

where $E$ is the Young's modulus of the material of the beam and $I$ is the moment of inertia of the cross-section.

Five rotational spring models proposed by different authors are used in this paper for comparison purpose:

- Rizos et al. [41]:

$$\begin{aligned} J_R(\xi) =& 5.346(1.8624\xi^2 - 3.95\xi^3 + 16.375\xi^4 - 37.226\xi^5 \\ &+ 76.81\xi^6 - 126.9\xi^7 + 172\xi^8 - 143.97\xi^9 + 66.56\xi^{10}) \end{aligned} \tag{D.13}$$

- Ostachowicz and Krawczuk [39]:

$$\begin{aligned} J_O(\xi) =& 6\pi\xi^2(0.6384 - 1.035\xi + 3.7201\xi^2 - 5.1773\xi^3 \\ &+ 7.553\xi^4 - 7.332\xi^5 + 2.4909\xi^6) \end{aligned} \tag{D.14}$$

- Chondros et al. [18]:

$$\begin{aligned} J_C(\xi) =& 6\pi(1-\nu^2)(0.6272\xi^2 - 1.04533\xi^3 + 4.5948\xi^4 - 9.9736\xi^5 \\ &+ 20.2948\xi^6 - 33.0351\xi^7 + 47.1063\xi^8 - 40.7556\xi^9 + 19.6\xi^{10}) \end{aligned} \tag{D.15}$$

- Fernánez-Sáez et al. [25]:

$$J_F(\xi) = 2\left(\frac{\xi}{1-\xi}\right)^2 \left(5.93 - 19.69\xi + 37.14\xi^2 - 35.84\xi^3 + 13.12\xi^4\right) \tag{D.16}$$

- Bilello [8]:

$$J_B(\xi) = \frac{\xi(2-\xi)}{0.9(\xi-1)^2} \tag{D.17}$$

It can be seen that, when no damage is presented ($\xi = 0$), $K_{eq} = \infty$, which means the deflection of the beam satisfies the first- and second-order derivatives continuity. Models for other shapes of cross-sections can be found in the work of Dimarogonas et al. [23] and Rubio et al. [42].

## D.3 Experimental case study

### D.3.1 Test setup

A simply supported steel beam with multiple cracks was used to test the performance of the proposed methodology. The tested beam had a length of 1200 mm and 80 mm in width and 20 mm in height. Hereinafter, all locations are measured from the left support of the beam. A total number of 4 cracks were introduced stepwise at 425 mm, 775 mm, 625 mm and 525 mm (Fig. D.2(a)) and were labeled as Crack 1, 2, 3 and 4 according to the order of appearance. All cracks were introduced as transversal edge-type notches with constant depth by a saw cut on the top of the beam. For each crack, two depths were introduced progressively, 4 mm ($\xi = 20\%$) and 10 mm ($\xi = 50\%$). A total of six cases listed in Table D.1 are examined.

**Table D.1** Damage scenarios and crack severities (%) used in the experimental tests.

| Case | Crack 1 | Crack 2 | Crack 3 | Crack 4 |
|---|---|---|---|---|
| 1 | 50 | 20 | – | – |
| 2 | 50 | 50 | – | – |
| 3 | 50 | 50 | 20 | – |
| 4 | 50 | 50 | 50 | – |
| 5 | 50 | 50 | 50 | 20 |
| 6 | 50 | 50 | 50 | 50 |

A Digital Imagine Correlation (DIC) system was used to measure the deflections of the beam (Figs. D.2(b)-(c)). A Pontos system from GOM company was used (https://www.gom.com/3d-software/gom-correlate.html). The system includes two 5 Megapixel resolution cameras. They were located at 750 mm in front of the beam. The distance between cameras was 300 mm and 8 mm lens were used. This configuration leads to a resolution of 3.2 pixels/mm. The calibration process of

the system estimated a 0.125 pixel deviation, so the expected accuracy of the measurements was 0.04 mm. For each test, 20 images were captured at a sample rate of 1 Hz. Erratic images were discarded and the average values of displacements were computed from the remaining pictures in order to enhance the accuracy of the results. High-contrast regularly shaped targets formed by a 5 mm diameter white circle in the middle of a black circle with a diameter of 10 mm were used. The central point of the target was automatically determined by the measuring system software. The contrast at the transition of small to large gray values is used. At this unique gray value gradient, a best-fit ellipse is computed whose center point is the measuring point in the left and right camera images.. A total number of 241 measurement points were marked along the side of the beam with an equal spacing of 5 mm. The targets were positioned in two arrays, 121 points above the centerline and 120 points below (see Fig. D.2(d) for the arrangement).

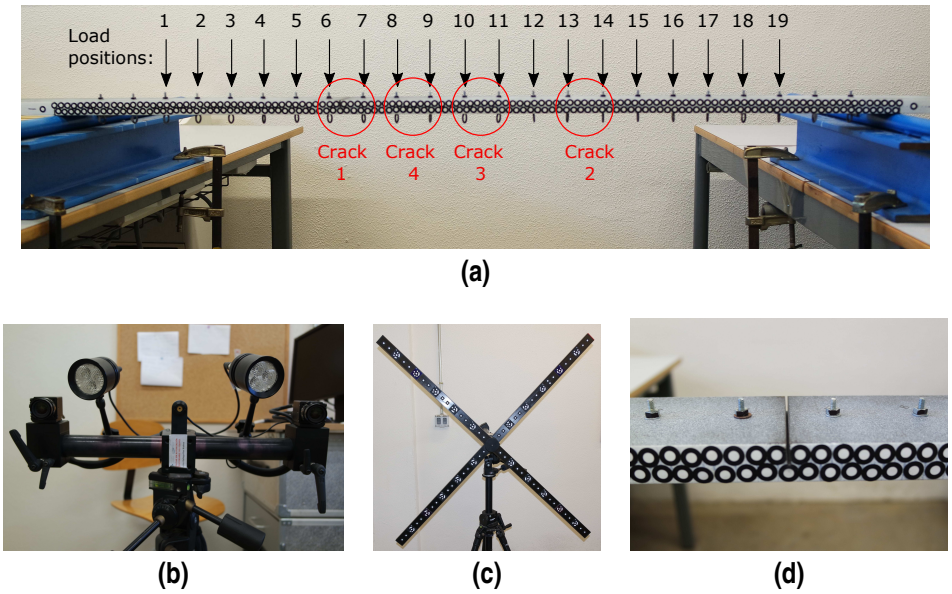


**Figure D.2** The experimental test setup: (a) the tested steel beam with the load and crack positions; (b) the DIC measuring cameras; (c) the calibration pattern; (d) a crack with 50% damage and the measurement targets.

### D.3.2 Static loads

In practice, a load combination that can produce a measurable value of the deflection variation is required. For a beam with a single crack under a concentrated force, the maximum value of the deflection variation occurs when the load is applied at the damaged cross-section. Information about damage location is usually not a prior knowledge in practical damage detection cases. Therefore, a distributed load combination that covers a wide region of the beam is used in the experimental test because it increases the chance to obtain the deflection variation when the load is applied at the damage location.

A 120 kg mass was applied at 19 equally spaced positions along the beam with a spacing of 50 mm, leaving 150 mm to both supports (Fig. D.2(a)). By combining the deflections from each load position, the equivalent value of applying all the loads simultaneously can be obtained:

$$u_{I,sum} = u_{D,sum} - u_{R,sum} \tag{D.18}$$

where $u_{I,sum}$, $u_{D,sum}$ and $u_{R,sum}$ are the sum of the deflections from each load position at State I, D and R, respectively.

The use of a linear combination of a set of concentrated loads provides an additional practical advantage. A larger resulting deflection can be achieved without exceeding a practical limit value during the tests (the serviceability limit state for instance).

### D.3.3 Measuring approach using partial measurements

The close range digital photogrammetric system has a limited measuring volume. Most of the laboratory tests are focused on small scale structures that can be captured entirely within the measuring volume of the system, i.e. the space defined by the configuration of the system (lenses, relative distance and angle between cameras) in which the targets can be accurately identified. However, in practice, many structures exceed this measuring volume. In other words, the digital photogrammetric systems could only capture part of the real structure. Therefore, an approach for obtaining the static deflections of the entire structure by assembling partial measurements is used.

In this case study, first, two parts of the tested beam were measured separately using Setups A and B shown in Fig. D.3. The coordinates of the targets were measured by using the DIC system before and after applying the load. The deflections of the two parts were obtained by subtracting the unloaded coordinates from the loaded ones. The configuration and setup of the DIC system remained unchanged during the whole measuring process. The obtained deflections were denoted by $u^A$ and $u^B$ accordingly. A set of 4 common points were measured in both setups as reference points for the combination process. Then, the partial measurements were combined to construct the deflection of the beam by applying the following steps (see Fig. D.4 for the scheme of the combination process).

1. Extract the deflections of the common points $u_c^A$, $u_c^B$ from the measurements and calculate the difference $\delta = u_c^A - u_c^B$ (Fig. D.4(a));
2. Form the entire deflection ($u$) by aligning $u^B$ to $u^A$, $u'^B = u^B + \bar{\delta}$, where $\bar{\delta}$ is the average value of $\delta$;
3. Update the deflections of common points with $u_c$ in $u$, where $u_c$ is the average value from $u_c^A$ and $u_c'^B$ (Fig. D.4(b)).

Although theoretically only 1 common point is sufficient for joining the two measured parts of the beam, more points are preferred in practice in order to reduce the errors induced by measurement noise. In the present research, an overlapping of 4 points provided accurate results.

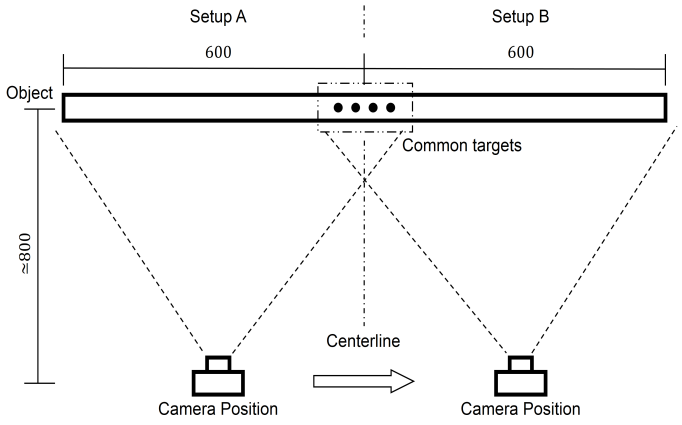


**Figure D.3** The measuring scheme with Setups A and B.

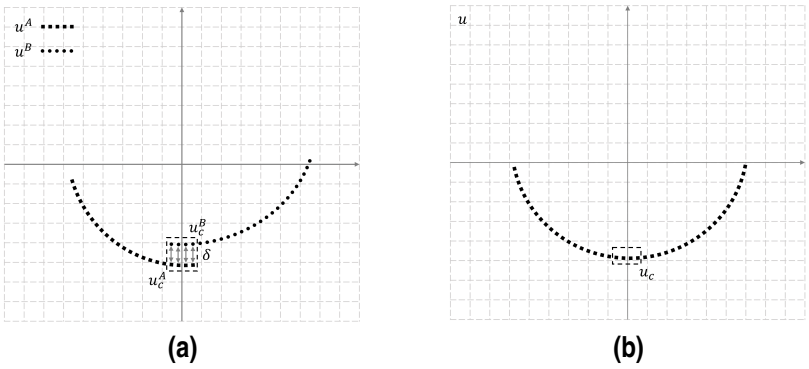


**Figure D.4** Scheme of the deflection combination process (a) measurements from Setups A and B; (b) combined deflection.

### D.3.4 Damage localization results

Following the procedure described in Section D.3.3 and using Eq. (D.18), the sum of deflection variations $u_{I,sum}$ of each damage scenario is obtained (Fig. D.5). Through direct observation on the deflection variations, the effect of 50% damage can be clearly identified in all cases while the 20% can not be distinguished along with 50% cracks in Figs. D.5(a), (c) and (e). Besides, through comparison of Figs. D.5(b), (d) and (f), it can be observed that the slope discontinuities appear to be less obvious as the distance between cracks shortens.

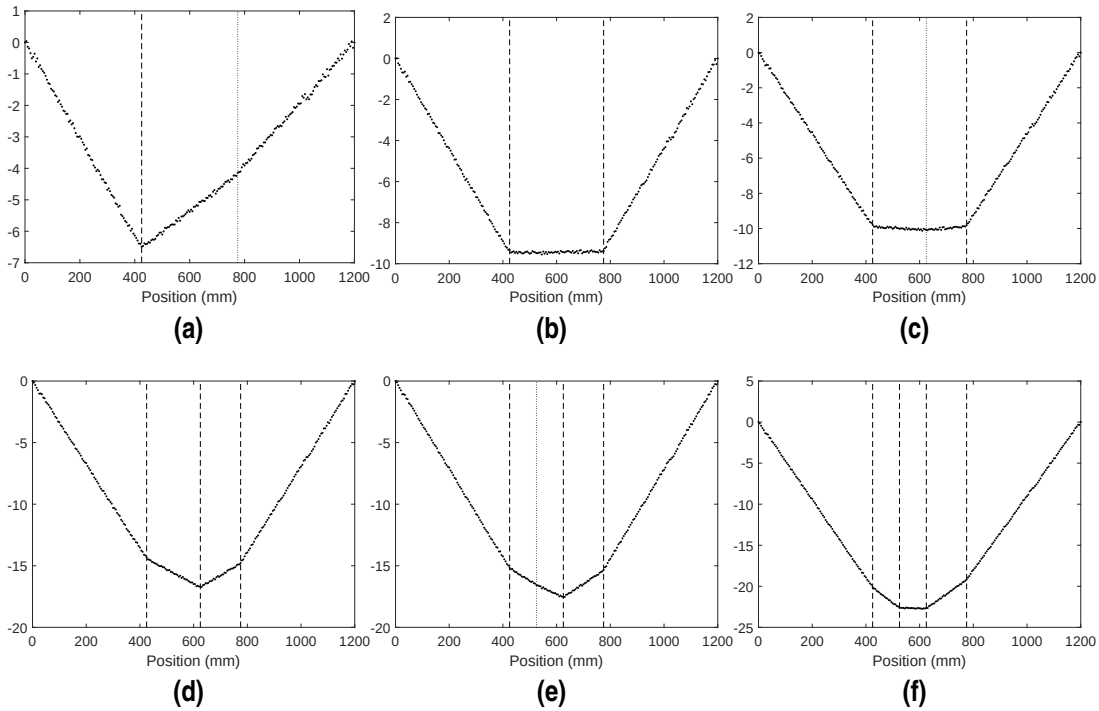


**Figure D.5** Deflection variations (mm) of (a) Case 1; (b) Case 2; (c) Case 3; (d) Case 4; (e) Case 5; (f) Case 6 (dashed lines mark the actual location of 50% cracks, dotted lines mark the actual location of 20% cracks).

After trying several different $\lambda$ values and inspecting their corresponding results for estimating $u_{I,sum}$, the values listed in Table D.2 are used. The slope discontinuities of each measured cross-

section are obtained from Eq. (D.11) and plotted in Fig. D.6. Peak values can be easily seen at the locations of 50% damage. At the vicinity of those cross-sections (within 25 mm to both sides), relative low peak values can be observed as well. Moreover, several small peak values can be observed at locations of 20% damage in Figs. D.6(a), (c) and (e). Although the values of the slope discontinuities near 50% damage locations are higher than those at 20% damage locations, they should be considered the affected region of one single crack instead of a set of closely spaced cracks. More details of the actual effect of a real crack on the identification results will be discussed in the next section.

**Table D.2** Values of $\lambda$ used in the localization process.

| | Case 1 | Case 2 | Case 3 | Case 4 | Case 5 | Case 6 |
|---|---|---|---|---|---|---|
| $\lambda_{max}$ | 7.5e$^3$ | 1.29e$^4$ | 1.37e$^4$ | 2.18e$^4$ | 2.29e$^4$ | 3.01e$^4$ |
| $\lambda/\lambda_{max}$ | 5‰ | 1‰ | 1‰ | 0.5‰ | 0.2‰ | 0.2‰ |
| $\lambda$ | 37.5 | 12.9 | 13.7 | 10.9 | 4.58 | 6.02 |

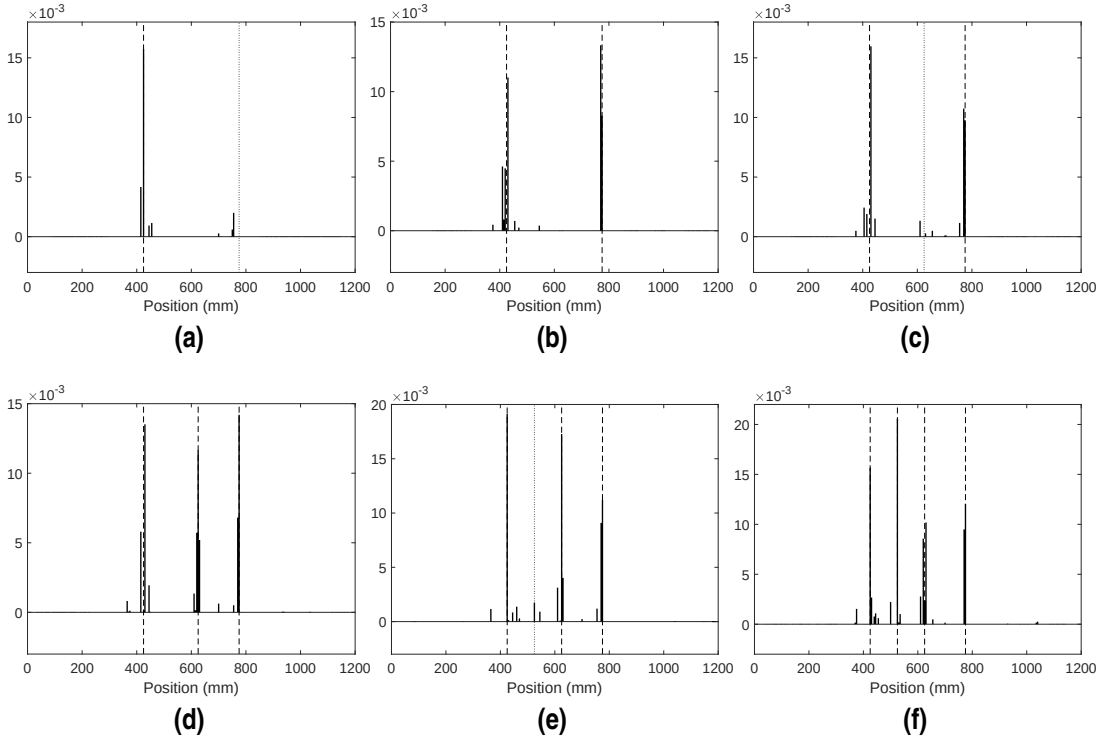


**Figure D.6** Estimated changes in rotation (rad) of (a) Case 1; (b) Case 2; (c) Case 3; (d) Case 4; (e) Case 5; (f) Case 6 (dashed lines mark the actual location of 50% cracks, dotted lines mark the actual location of 20% cracks).

Therefore, the potential damage locations are determined at the cross-sections corresponding to the maximum value of the slope discontinuities within a region of 50 mm. The predicted results listed in Table D.3 show that the proposed method can accurately detect and localize cracks with 20% and 50% severities simultaneously in all cases. In addition, the results from Case 6 indicate that cracks with a spacing of 100 mm can be distinguished.

**Table D.3** Predicted damage locations (mm).

| Case | Crack 1 (425 mm) | Crack 2 (775 mm) | Crack 3 (625 mm) | Crack 4 (525 mm) |
|---|---|---|---|---|
| 1 | 425 | 755 | – | – |
| 2 | 430 | 770 | – | – |
| 3 | 430 | 770 | 610 | – |
| 4 | 430 | 775 | 625 | – |
| 5 | 425 | 775 | 625 | 525 |
| 6 | 425 | 775 | 630 | 525 |

### D.3.5 Damage quantification results

Once the crack locations are identified, the corresponding equivalent rotational stiffness of the spring $K_{eq}$ can be estimated by using Eq. (D.7). As the beam is statically determinate, the damaged internal bending moments at the predicted damaged cross-sections can be calculated from equilibrium Eqs. ($M_D(b_i) = M_R(b_i)$). The crack depths were estimated by using the equivalent spring models listed in Section D.2.3 (Eqs. (D.12)-(D.17)) and the results are shown in Table D.4. When applying Eq. D.12, a Young modulus of 210 GPa was considered for the steel beam.

**Table D.4** Predicted damage depths (mm).

| Case | Actual depth (mm) | Rotational model | | | | |
|---|---|---|---|---|---|---|
| | | $J_R$ | $J_O$ | $J_C$ | $J_F$ | $J_B$ |
| 1 | 10 | 10.4 | 9.7 | 9.8 | 9.6 | 9.6 |
| | 4 | 4.3 | 3.8 | 4.0 | 3.8 | 2.7 |
| 2 | 10 | 9.2 | 8.4 | 8.6 | 8.4 | 8.2 |
| | 10 | 9.8 | 9.1 | 9.2 | 9.0 | 8.9 |
| 3 | 10 | 10.4 | 9.7 | 9.8 | 9.6 | 9.6 |
| | 10 | 9.1 | 8.3 | 8.5 | 8.3 | 8.1 |
| | 4 | 3.3 | 3.0 | 3.1 | 3.0 | 1.8 |
| 4 | 10 | 9.8 | 9.1 | 9.3 | 9.1 | 9.0 |
| | 10 | 10.0 | 9.3 | 9.5 | 9.2 | 9.2 |
| | 10 | 9.0 | 8.3 | 8.5 | 8.3 | 8.1 |
| 5 | 10 | 11.0 | 10.5 | 10.5 | 10.2 | 10.3 |
| | 10 | 9.2 | 8.5 | 8.7 | 8.5 | 8.3 |
| | 10 | 10.4 | 9.7 | 9.8 | 9.6 | 9.6 |
| | 4 | 3.9 | 3.5 | 3.6 | 3.5 | 2.3 |
| 6 | 10 | 10.4 | 9.7 | 9.8 | 9.6 | 9.6 |
| | 10 | 9.5 | 8.7 | 8.9 | 8.7 | 8.6 |
| | 10 | 8.6 | 7.8 | 8.1 | 7.9 | 7.6 |
| | 10 | 11.0 | 10.4 | 10.4 | 10.2 | 10.3 |

The estimated crack depths show that the model proposed by Rizos et al. [41] ($J_R$) provides the most severe damage estimates among all the models while the the model of Bilello [8] ($J_B$) predicts the lowest crack depths especially for 20% damage severity. The results from models of Ostachowicz and Krawczuk [39] ($J_O$), Chondros et al. [18] ($J_C$) and Fernández-Sáez et al. [25] ($J_F$) lead to similar estimates of crack depths with a difference within 0.3 mm. For these three models, the deviation of the estimated crack depth from real values are less than or equal to 2 mm for 50%

cracks and 1 mm for 20% cracks. For simplicity, the model of Ostachowicz and Krawczuk [39] is selected for the numerical studies (both modeling and quantification) in the next sections. .

The results indicate that the methodology can not only successfully identify the locations of multiple closely spaced cracks in a simply supported beams but also their severities. The size of the damage affected region for each crack (50 mm) serves as an estimate of the maximum spacing between measurement points to accurately locate the damage. Obviously, as the spacing between measurement points increases, the accuracy of the localization and quantification results decreases. In addition, the spacing between targets defines the minimum distance between adjacent cracks that could be identified. If cracks are more closely spaced than the measurement points, then they will be identified as just one single damage.

## D.4 Limitation on the use of the spring model

The issue of crack modeling in beams has been discussed exhaustively in the work of Friswell and Penny [26]. A real crack has a complex local effect on stiffness and stress distribution due to its size, orientation and location. Although the simplification of a crack by a spring is acceptable in many cases of beams subjected to bending, the difference shall be noted. For the simple notch open crack type of the tests, the neutral axis changes continuously around the crack region. The slope of the deflection variation in that region changes continuously and rapidly, which is different from the idealized spring model where there is a lumped slope discontinuity at the spring location only.

In this section, two different numerical models corresponding to Case 1 (defined in Table D.1) are used to analyze the influence of this difference in the damage quantification process. One of the models is a 3-D solid model built with 20-node homogeneous solid elements (Fig. D.7(a)). The crack width is 1 mm (Fig. D.7(b)). The other model is a 1-D model built with linear beam element using rotational springs to model the cracks according to Eqs. (D.12) and (D.14). The loads and measurement points are considered as in the experimental tests. A modulus of elasticity of 210 GPa was considered for both models of the steel beam. The numerical deflection variation of the beam and the corresponding slope discontinuities are shown in Fig. D.8.

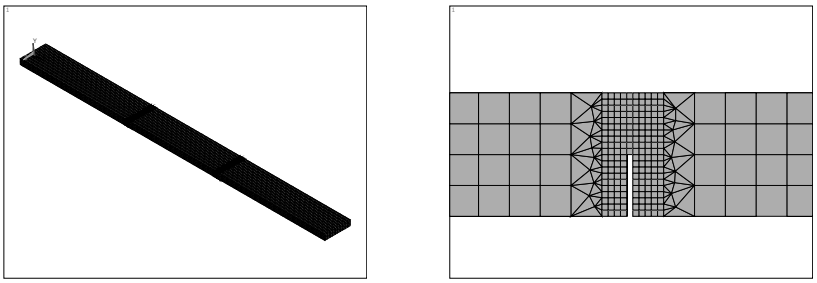


**Figure D.7** The 3D FE model: (a) the meshed beam; (b) the crack with $\xi = 50\%$.

As the experimental results, the effect of 20% damage can not be perceived directly from the deflection variation in Fig. D.8(a) since it is masked by the presence of the 50% damage. The relative difference between the slope discontinuities of 50% and 20% damage is obvious in Figs D.8(b)-(c). The 3-D model exhibits not only peak values of the slope discontinuities at the crack locations but also various additional smaller peaks at their vicinities (within 25 mm to both sides of the crack) (see Fig. D.8(b)). Therefore, a region of 50 mm centered at the crack can be regarded as the damage affected area. This result is consistent with the experimental results in Fig. D.6. In the 1-D model using idealized lumped spring models, only single peak values of rotation discontinuities exist at the precise damage locations (see Fig. D.8(c)).

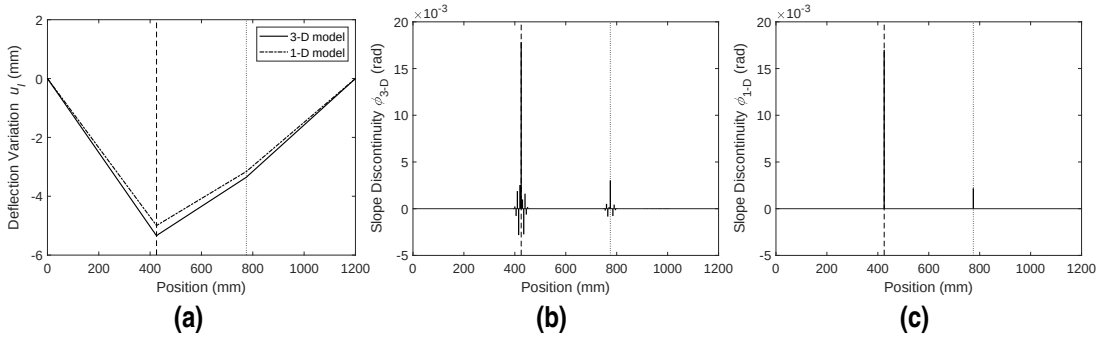


**Figure D.8** Numerical results of the simply-supported beam at State I without noise: (a) deflection variations ($u_I$) (mm); (b) slope discontinuity of 3-D model ($\phi_{3\text{-D}}$) (rad); (c) slope discontinuity of 1-D model ($\phi_{1\text{-D}}$) (rad) (dashed lines mark the actual location of 50% cracks, dotted lines mark the actual location of 20% cracks).

In Fig. D.8(a), it can be seen that there is a difference between the deflection variations of the two numerical models. From Eqs. (D.7), (D.12) and (D.14), the estimated crack depths from the results of the 3-D model are 10.2 mm for the 50% crack and 4.7 mm for the 20% crack. This result shows that even using a numerical model in noise-free conditions, there are errors in the estimation of crack depths. These errors are caused by the discrepancy between the characteristic correlations of equivalent spring models and the behavior of the actual crack. It is noted that similar errors are obtained from the experimental tests. Nevertheless, the use of rotational spring models is acceptable for quantification in practical applications since the errors are small from a practical point of view.

## D.5 Application in statically indeterminate beams

Unlike statically determinate beams, the deflection variation of a statically indeterminate beam is a piecewise polynomial curve and the bending moment distribution at State D ($M_D$) can not be easily obtained. In order to extend the application of the proposed damage identification methodology for multiple damage in statically indeterminate beams, a 3-D numerical example of a fixed-fixed beam is presented for discussion. The properties of the beam are the same as the previous sections. The solid model contains two cracks of 50% severity, one at the bottom side at the mid-span (600 mm), the other at the top side close to the support (1155 mm) (Fig. D.9).

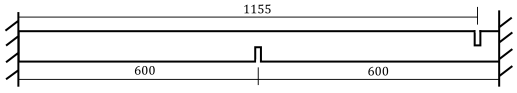


**Figure D.9** Scheme of the fixed-fixed beam with two 50% cracks (unit: mm).

In order to simulate the results from a real test, artificial noise with the same properties as the the experimental noise is added to the results from the finite element model. The experimental noise can be characterized from the undamaged deflection measurement, for which a noise-free reference can be formed by using a fourth order polynomial curve fitting approach. The mean value ($\mu$) and the standard deviation ($\sigma$) of the noise in $u_{R,sum}$ can be obtained by using Eqs. (D.19) and (D.20), being $N$ the number of measurement points on the beam and $u_{R,sum,fit}$ the fitted sum of deflections at State R. Therefore, assuming that the measurement noise is independent and follows a normal distribution, two sets of Gaussian artificial noise with the same mean and standard deviation are added to the simulated damaged and undamaged deflections. The obtained value of $\mu$ is $5.07\text{e}^{-15}$ mm (which is a zero value in practice as expected) and the value of $\sigma$ is 0.060 mm. This value is in

agreement with the theoretical resolution of the measuring system (0.04 mm), given the cameras resolution (5 MP), the distance to the measuring object (750 mm) and the results of the calibration process (0.125 pixel deviation).

$$\mu = \frac{1}{N}\sum_{k=1}^{N}(u_{R,sum,k} - u_{R,sum,fit,k}) \tag{D.19}$$

$$\sigma = \sqrt{\frac{1}{N}\sum_{k=1}^{N}(u_{R,sum,k} - u_{R,sum,fit,k})^2} \tag{D.20}$$

### D.5.1 Damage localization

The noise-free deflection variation, the noisy deflection variation and the $l1$ Trend Filtering fitted results are plotted together in Fig. D.10(a). It can be seen that the application of the $l1$ Trend Filtering, which results in a local linear fit process, can provide a good estimate of nonlinear curves. Peak values of rotation discontinuities are found at both crack positions in Fig. D.10(b). Multiple peak values are also identified at various locations along the beam. From Fig. D.4(c), it is clear that the rotation of the spring should be consistent with the applied undamaged bending moment. Therefore, valid potential damage locations should be determined by examining the rotation discontinuity along with the undamaged bending moment diagram.

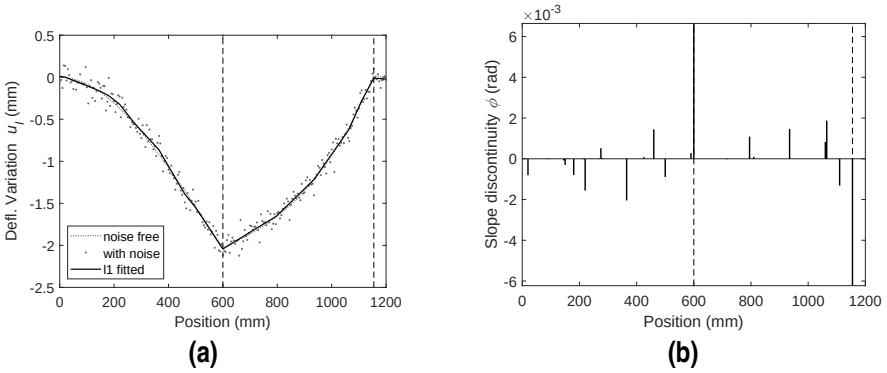


**Figure D.10** Numerical results of the fixed-fixed beam at State I: (a) deflection variation (mm); (b) change in slope (rad) (dashed lines mark the actual location of 50% cracks).

For Euler-Bernoulli beams, the bending moment distribution of an undamaged beam can be experimentally obtained by computing curvatures from its deflection and applying Strength of Materials relationships (Eq. (D.21)). In practice, it can be computed by using Eq. (D.22) following a finite difference computation of curvatures. The simulated noisy deflection and the fitted deflection of the beam at State R are plotted in Fig. D.11(a). The internal bending moment diagram obtained from the fitted deflection is shown in Fig. D.11(b).

$$M(x) = EI\frac{d^2u_R(x)}{dx^2} \tag{D.21}$$

$$M_k = EI\frac{u_{R,k+1} - 2u_{R,k} + u_{R,k-1}}{\Delta x^2} \tag{D.22}$$

The cross-sections at 255 mm and 945 mm locations where zero bending moment values appear should be interrogated by other load combinations that can produce non-zero bending moments at

these locations. Combining Figs D.11(b) and D.10(b), negative peak values of rotation discontinuities from 0 mm to 255mm and 945 mm to 1200mm as well as positive peak values between 255 mm and 945mm should be considered potential damage locations. From Fig. D.10(a), it is clear that only peak values at 600 mm and 1155 mm are caused by damage and the rest can be considered a consequence of the local linear fit process. Despite of these noisy peaks, the $l1$ Trend Filtering has the capability of identifying the sudden changes in the slope of a nonlinear curve.

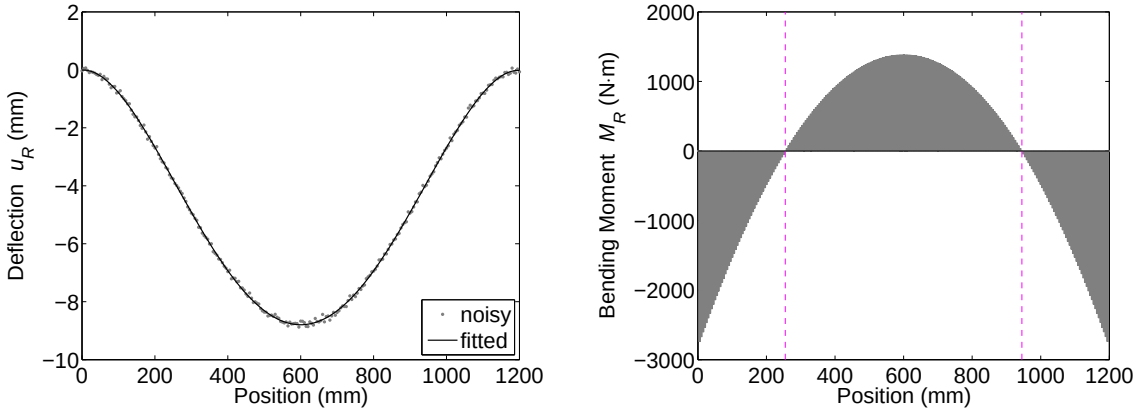


**Figure D.11** Numerical results of the fixed-fixed beam at State R: (a) the noisy deflection and the fitted result (mm); (b) the internal bending moment diagram (N·m) (dashed lines mark the zero bending moment cross-sections).

### D.5.2 Damage quantification

The damaged local bending moments at damage locations, required in the quantification process, are difficult to acquire through neither experimental tests nor numerical modeling for statically indeterminate structures. On the other hand, the bending moments of an undamaged beam can be estimated from its deflection directly through Eq. (D.22) as described in the previous section. For practical applications, this section examines the possibility of using the undamaged bending moments at the damage locations instead of the damaged ones in Eq. (D.7). It is presumed that the pre- and post-damage bending moments are similar.

In order to explore the difference between the bending moments at States R and D, an example of a fixed-fixed beam with a single damage (depicted in Fig. D.12) is presented for illustration purpose. The damaged cross-section modeled by a rotational spring with an equivalent stiffness $K_{eq}$ is situated at $L_1$ from the left support over the beam length $L$. In State I of the beam (Fig. D.1(c)), the applied bending moment $M_R(L_1)$ at the spring is caused by some external load. Denote the vertical deflection of spring by $u(L_1)$ and the left and right rotations of the cross-section at $x = L_1$ by $\theta(L_1^-)$ and $\theta(L_1^+)$ respectively. Then from the matrix structural analysis, the following equation can be established:

$$\begin{bmatrix} \frac{12EI}{L_1^3}+\frac{12EI}{L_2^3} & -\frac{6EI}{L_1^3} & \frac{6EI}{L_2^3} \\ -\frac{6EI}{L_1^3} & \frac{4EI}{L_1}+K_{eq} & -K_{eq} \\ \frac{6EI}{L_2^3} & -K_{eq} & \frac{4EI}{L_2}+K_{eq} \end{bmatrix} \begin{Bmatrix} u(L_1) \\ \theta(L_1^-) \\ \theta(L_1^+) \end{Bmatrix} = \begin{Bmatrix} 0 \\ -M_R(L_1) \\ M_R(L_1) \end{Bmatrix} \tag{D.23}$$

where

$$L_2 = L - L_1 \tag{D.24}$$

By solving Eq. (D.23) and applying the results into Eq. (D.6), the ratio of $M_D(L_1)$ over $M_R(L_1)$

can be obtained and written as a function of the relative location of damage ($\alpha$) and its relative stiffness ($\beta$) in the form of Eq. (D.25).


**Figure D.12** Scheme of a fixed-fixed beam with single crack.

$$\frac{M_D}{M_R} = \frac{1}{1+\beta(3\alpha^2-3\alpha+1)} \tag{D.25}$$

where

$$\alpha = \frac{L_1}{L} \tag{D.26}$$

$$\beta = \frac{4EI}{K_{eq}L} \tag{D.27}$$

The ratio variation of $M_D/M_R$ is plotted against the relative location $\alpha$ of the crack with various damage severities in Fig. D.13. It can be seen that in this case, the ratio increases as the damage location gets away from the supports and reaches its maximum value at the mid-span. For different severities, the difference between $M_D$ and $M_R$ gets bigger as the damage severity increases. For a crack with 50% severity, the ratio varies from 85% to 96%. Considering other uncertainties coming from errors in the rotation discontinuity estimation or from the spring models, the error in using $M_R$ instead of $M_D$ can be acceptable for practical purpose. We note that the issue may be more complicated in multiple damage scenario since the ratio depends on the positions of the cracks as well as boundary conditions.

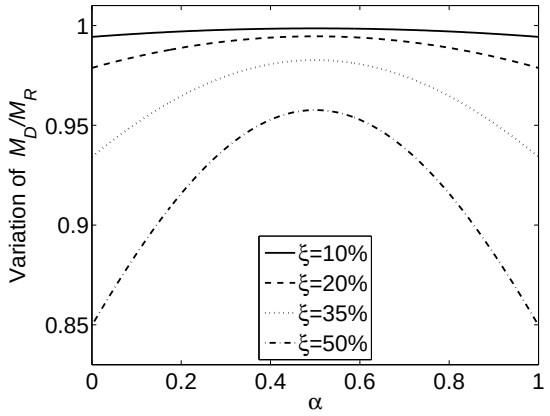


**Figure D.13** The variation of the damaged to undamaged bending moment at damage location in a fixed-fixed beam with single crack.

By substituting $M_D$ by $M_R$ in Eq. (D.7), the predicted crack depths using the spring model from [39] (Eq. (D.14)) are 10.2 mm and 8.2 mm for the mid-span crack and support crack, respectively. The results demonstrate the feasibility of estimating the crack depths by using the undamaged internal bending moments to substitute the damaged bending moments in practice.

## D.6 Conclusions

This paper proposes a simple methodology for multiple damage identification in beams with different boundary conditions. The experimental and numerical results show that the $l1$ Trend Filtering is a promising damage localization tool to detect the damage-induced variations in the static deflection. Once the damage is localized, the crack depth can be estimated by using characteristic equations of spring models. For statically indeterminate beams, an approximate evaluation can be obtained by using the undamaged internal bending moments at damage locations instead of the damaged ones, thereby a non-model based methodology is established.

The experimental application of the DIC measuring system in this paper shows the viability of acquiring the whole structural deflection by combining partial measurements. It is shown that close-range photogrammetric technology can be favorable in large scale structure measuring in practical SHM.

The merits of the proposed methodology can be summarized as follows. First the experimental setup can be easily employed in various conditions. Secondly, the localization and quantification procedures can be applied without building any model of the structure. In addition, the results of case studies not only imply that low severity cracks (20% depth) can be detected and distinguished from severe cracks (50% depth) but also show that multiple cracks closely spaced can be identified with high accuracy.

.

## Acknowledgments

This work was supported by the Consejería de Economía, Innovación, Ciencia y Empleo of Andalucía (Spain) under project P12-TEP-2546 and the Spanish Ministry of Economy and Competitiveness (Ministerio de Economía y Competitividad, Secretaría de Estado de Investigación, Desarrollo e Innovación) through research project BIA2016-43085-P. The financial support is gratefully acknowledged.

## References

[1] Andreaus, U., and Baragatti, P. Fatigue crack growth, free vibrations, and breathing crack detection of aluminium alloy and steel beams. *J. Strain Anal. Eng. Des. 44*, 7 (2009), 595–608.

[2] Andreaus, U., and Baragatti, P. Cracked beam identification by numerically analysing the nonlinear behaviour of the harmonically forced response. *J. Sound Vib. 330* (2011), 721–742.

[3] Andreaus, U., and Baragatti, P. Experimental damage detection of cracked beams by using nonlinear characteristics of forced response. *Mech. Syst. Signal Process. 31* (2012), 382–404.

[4] Andreaus, U., Baragatti, P., Casini, P., and Iacoviello, D. Experimental damage evaluation of open and fatigue cracks of multi-cracked beams by using wavelet transform of static response via image analysis. *Struct. Control Heal. Monit. 24*, 4 (2017), 1–16.

[5] Andreaus, U., and Casini, P. Identification of multiple open and fatigue cracks in beam-like structures using wavelets on deflection signals. *Contin. Mech. Thermodyn. 28*, 1-2 (2016), 361–378.

[6] Andreaus, U., Casini, P., and Vestroni, F. Frequency reduction in elastic beams due to a stable crack: Numerical results compared with measured test data. *Engng. Trans. 51*, 1 (2003), 87–101.

[7] Andreaus, U., Casini, P., and Vestroni, F. Non-linear dynamics of a cracked cantilever beam under harmonic excitation. *Int. J. Non. Linear. Mech. 42*, 3 (2007), 566–575.

[8] Bilello, C. *Theoretical and experimental investigation on damaged beams under moving systems*. Ph.d. thesis, Universitá degli Studi di Palermo, Italy, 2001.

[9] Biondi, B., and Caddemi, S. Closed form solutions of Euler-Bernoulli beams with singularities. *Int. J. Solids Struct. 42*, 9-10 (2005), 3027–3044.

[10] Caddemi, S., and Caliò', I. Exact solution of the multi-cracked Euler-Bernoulli column. *Int. J. Solids Struct. 45*, 5 (2008), 1332–1351.

[11] Caddemi, S., and Caliò, I. Exact closed-form solution for the vibration modes of the Euler-Bernoulli beam with multiple open cracks. *J. Sound Vib. 327*, 3-5 (2009), 473–489.

[12] Caddemi, S., Caliò, I., and Marletta, M. The non-linear dynamic response of the Euler-Bernoulli beam with an arbitrary number of switching cracks. *Int. J. Non. Linear. Mech. 45*, 7 (2010), 714–726.

[13] Caddemi, S., and Morassi, A. Crack detection in elastic beams by static measurements. *Int. J. Solids Struct. 44*, 16 (2007), 5301–5315.

[14] Caddemi, S., and Morassi, A. Detecting multiple open cracks in elastic beams by static tests. *J. Eng. Mech. 137*, 2 (2011), 113–124.

[15] Caddemi, S., and Morassi, A. Multi-cracked Euler-Bernoulli beams: Mathematical modeling and exact solutions. *Int. J. Solids Struct. 50*, 6 (2013), 944–956.

[16] Cannizzaro, F., Greco, A., Caddemi, S., and Caliò, I. Closed form solutions of a multi-cracked circular arch under static loads. *Int. J. Solids Struct. 121* (2017), 191–200.

[17] Choi, I.-Y., Lee, J. S., Choi, E., and Cho, H.-N. Development of elastic damage load theorem for damage detection in a statically determinate beam. *Comput. Struct. 82*, 29-30 (2004), 2483–2492.

[18] Chondros, T., Dimarogonas, A., and Yao, J. A continuous cracked beam vibration theory. *J. Sound Vib. 215* (1998), 17–34.

[19] Christides, S., and Barr, A. D. One-dimensional theory of cracked Bernoulli-Euler beams. *Int. J. Mech. Sci. 26*, 11-12 (1984), 639–648.

[20] Cicirello, A., and Palmeri, A. Static analysis of Euler-Bernoulli beams with multiple unilateral cracks under combined axial and transverse loads. *Int. J. Solids Struct. 51*, 5 (2014), 1020–1029.

[21] Di Paola, M., and Bilello, C. An integral equation for damage identification of Euler-Bernoulli beams under static loads. *J. Eng. Mech. 130*, 2 (2004), 225–234.

[22] Dimarogonas, A. D. Vibration of cracked structures: A state of the art review. *Eng. Fract. Mech. 55*, 5 (1996), 831–857.

[23] Dimarogonas, A. D., Paipetis, S. A., and Chondros, T. G. *Analytical Methods in Rotor Dynamics*, 2nd ed. Springer, 2013.

[24] Ebrahimi, A., Behzad, M., and Meghdari, A. A bending theory for beams with vertical edge crack. *Int. J. Mech. Sci. 52*, 7 (2010), 904–913.

[25] Fernández-Sáez, J., Rubio, L., and Navarro, C. Approximate calculation of the fundamental frequency for bending vibrations of cracked beams. *J. Sound Vib. 225*, 2 (1999), 345–352.

[26] Friswell, M. I., and Penny, J. E. T. Crack modeling for structural health monitoring. *Struct. Heal. Monit. An Int. J. 1*, 2 (2002), 139–148.

[27] Ghrib, F., Li, L., and Wilbur, P. Damage identification of Euler-Bernoulli beams using static reponse. *J. Eng. Mech. 138*, 5 (2012), 405–15.

[28] Gudmundson, P. The dynamic behaviour of slender structures with cross-sectional cracks. *J. Mech. Phys. Solids 31*, 4 (1983), 329–345.

[29] He, W.-Y., and Zhu, S. Moving load-induced response of damaged beam and its application in damage localization. *J. Vib. Control 22*, 16 (2015), 3601–3617.

[30] Jiang, R., and Jauregui, D. V. Development of a digital close-range photogrammetric bridge deflection measurement system. *Meas. J. Int. Meas. Confed. 43*, 10 (2010), 1431–1438.

[31] Jiang, R., Jáuregui, D. V., and White, K. R. Close-range photogrammetry applications in bridge measurement: Literature review. *Measurement 41*, 8 (2008), 823–834.

[32] Khaji, N., Shafiei, M., and Jalalpour, M. Closed-form solutions for crack detection problem of Timoshenko beams with various boundary conditions. *Int. J. Mech. Sci. 51*, 9-10 (2009), 667–681.

[33] Kim, S.-J., Koh, K., Boyd, S., and Gorinevsky, D. l1Trend Filtering. *SIAM Rev. 51*, 2 (2009), 339–360.

[34] Kisa, M., and Brandon, J. Effects of closure of cracks on the dynamics of a cracked cantilever beam. *J. Sound Vib. 238*, 1 (2000), 1–18.

[35] Koh, K., Kim, S.-J., and Boyd, S. l1 Trending Filtering function Matlab, 2008.

[36] Ma, Q., and Solís, M. Damage localization and quantification in simply supported beams using static test data. *J. Phys. Conf. Ser. 842*, 1 (2017).

[37] Ma, Q., and Solís, M. Damage localization and quantification in beams from slope discontinuities in static deflections. *Smart Struct. Syst. 22*, 3 (2018), 291–302.

[38] Mazanoglu, K., Yesilyurt, I., and Sabuncu, M. Vibration analysis of multiple-cracked non-uniform beams. *J. Sound Vib. 320*, 4-5 (2009), 977–989.

[39] Ostachowicz, W. M., and Krawczuk, M. Analysis of the effect of cracks on the natural frequencies of a cantilever beam. *J. Sound Vib. 150*, 2 (1991), 191–201.

[40] Palmeri, A., and Cicirello, A. Physically-based Dirac's delta functions in the static analysis of multi-cracked Euler-Bernoulli and Timoshenko beams. *Int. J. Solids Struct. 48*, 14-15 (2011), 2184–2195.

[41] Rizos, P. F., Aspragathos, N., and Dimarogonas, A. D. Identification of crack location and magnitude in a cantilever beam from the vibration modes. *J. Sound Vib. 138*, 3 (1990), 381–388.

[42] Rubio, L., Muñoz-Abella, B., and Loaiza, G. Static behaviour of a shaft with an elliptical crack. *Mech. Syst. Signal Process. 25*, 5 (2011), 1674–1686.

[43] Rucka, M., and Wilde, K. Crack identification using wavelets on experimental static deflection profiles. *Eng. Struct. 28* (2006), 279–288.

[44] Sinha, J. K., Friswell, M. I., and Edwards, S. Simplified models for the location of cracks in beam structures using measured vibration data. *J. Sound Vib. 251*, 1 (2002), 13–38.

[45] Spanos, P. D., Failla, G., Santini, A., and Pappatico, M. Damage detection in Euler-Bernoulli beams via spatial wavelet analysis. *Struct. Control Heal. Monit. 13*, 1 (2006), 472–487.

[46] Štimac, I., and Kožar, I. Damage detection from displacement-in-time function. In *4th Youth Symp. Exp. Solid Mech.* (Castrocaro Terme, Italy, 2005), University of Rijeka, Croatia, pp. 5–6.

[47] Stöhr, S., Link, M., Rohrmann, R., and Rücker, W. Damage detection based on static measurements of bridge structures. In *Proc. Int. Modal Anal. Conf. IMAC XXIV* (St. Luis, Missouri, USA, 2006).

[48] Valença, J., Júlio, E. N., and Araújo, H. J. Applications of photogrammetry to structural assessment. *Exp. Tech. 36*, 5 (2012), 71–81.

[49] Whiteman, T., Lichti, D. D., and Chandler, I. Measurement of deflections in concrete beams by close- range digital photogrammetry. *ISPRS Comm. IV, Symp. 2002 Geospatial Theory, Process. Appl. XXXIV* (2002), 9.

# Appendix E
# Paper E

Ma, Q. and Solís, M. (2019). "Application of wavelet analysis for crack localization and quantification in beams using static deflections", *Lecture notes in Mechanical Engineering* (submitted to the 13th International Conference on Damage Assessment of Structures DAMAS 2019)

Book: Lecture notes in Mechanical Engineering

ISSN: 21954364

SCIMAGO (2017))

- Mechanical Engineering: Q4 (636/950)

# Damage localization and quantification in beams from slope discontinuities in static deflections

Qiaoyu Ma and Mario Solís

Department of Continuum Mechanics and Structural Analysis,
Escuela Técnica Superior de Ingeniería, Universidad de Sevilla,

**Abstract** Wavelet analysis has been proven to be an efficient tool for identifying singularities in signals, such as the effect of damage in structural deflections. This paper establishes a new approach applying this technique to identify cracks in beams using static measurements. The deflection difference of the beam before and after damage is a piecewise polynomial with discontinuities at crack locations. The crack positions can be identified at apexes of the continuous wavelet transform coefficients. At damage locations, a damage index can be defined from the y-intercept of the linear regression between the logarithms of wavelet coefficients and their corresponding scales. By normalizing itself to the internal bending moment at the damage location, the damage index becomes damage location independent. Through a numerical model, a reference map between the crack depth and the damage index can be established and further used for damage severity assessment.

**Keywords** Wavelet analysis, crack depth estimation, trend estimate filter

## E.1 Introduction

Since the first application of wavelet analysis in crack detection in beams [34], numerous studies of this subject have been conducted in the past two decades. Compared to other digital differentiator filters, the wavelet function has the advantage in terms of simplicity due to its characteristics [21]. At the early stage, the applications of wavelet theory for damage detection were mainly on the dynamic response of the structure in time domain. Liew and Wang [16] first applied the wavelet to the dynamic response of a beam at a certain time in space domain. Later, due to the ability of detecting singularities in a continuous signal, the focus of wavelet analysis in crack detection shifts to space domain, i.e. deflection based for static responses [1, 2, 27, 30, 33, 36–38] and mode shape based for dynamic responses [4–6, 9, 13, 14, 29, 31, 39, 40]. Moreover, Zhu and Law [42] applied the wavelet analysis to the operational deflection of a single measurement on a simply supported beam with multiple cracks subjected to a moving load. Meanwhile, issues related to the wavelet analysis have been studied comprehensively, such as the selection of mother wavelet and scale, boundary distortion using the finite length signal, sampling effects, crack size sensitivity, mode order sensitivity, et al. [8, 12, 22, 23, 27, 28, 35]. The experimental noise issue in the measurements in practical applications have been addressed as well, such as by Solís et al. [32] through using a roving mass and weighted parameter based on Signal to Noise ratio and by Cao et al. [3] via the Teager-Energy Operator.

Further, researchers have extended the use of the wavelet transform from locating the cracks to quantifying the extents. Pakrashi et al. [26] suggest that the absolute value of the wavelet coefficient of the mode shapes at the damage location can be used as a damage calibration factor. The authors also proposed to use Kurtosis analysis for crack estimation [25]. Umesha et al. [36] studied the wavelet analysis to the static deflection of a fixed-fixed beam. A generalized curve which is the envelope plot of the wavelet coefficient maximum at damage point is proposed as a reference map for crack severity calibration. However, using the absolute value of the wavelet coefficient has the drawback that it not only varies from the crack location but also depends on the scale used in the

analysis. To resolve the location dependency, Andreaus and Casini [2] applied the wavelet analysis to the static deflection difference and proposed a new location independent damage index which is the ratio between the wavelet coefficient at the damage location and its corresponding curvature of the undamaged state. To avoid the scale dependency, Andreaus et al. [1] also proposed a new damage locating factor, normalized wavelet coefficient of several scales, which can also be used to estimate the damage severity by comparing the experimental results to the numerical values.

Another scale independent damage quantification method is to use the characteristics of the irregularities in the signal (deflection or mode shape) as damage index. Mallat and Hwang [20] points out that at the crack location, the local maximum wavelet coefficient is proportional to the scales in the logarithmic form. Hong et al. [11] first suggested to use the the Lipschitz exponent which is the slope of the linear relation to estimate the crack severity. It was found out later that the intersection of the y-axis can be used as a damage quantification index as well [7, 17, 41]. In addition, Zhu et al. [41] proposed a new damage locating index which can eliminate the boundary effect.

In this paper, a damage locating index which uses the Continuous Wavelet Transform (CWT) information at different scales, and a damage severity index which is independent from both crack location and wavelet scales are proposed by applying the wavelet analysis to the static deflection difference of the damaged and undamaged beam. To examine the performance of the methodology, Gaussian wavelet with 2 vanishing moments (Gaus2) is used as the mother wavelet. A linear trend filter is applied to reduce the experimental noise effect and determine the number of cracks. The correlation between crack depth and the damage index is obtained through a numerical model.

In the following sections, first the theoretical background of the continuous wavelet analysis is introduced. Secondly, the crack locating and severity indices are presented along with a numerical example. Then, the experimental tests and results are provided with a guide of the noise filter application. Lastly, the conclusions are drawn.

## E.2 Continuous wavelet analysis

A function $\psi(x)$ is said to be wavelet if and only if its Fourier transform $\hat{\psi}(\omega)$ satisfies

$$\int_0^{+\infty} \frac{|\hat{\psi}(\omega)|^2}{|\omega|} \mathrm{d}\omega = \int_{-\infty}^{0} \frac{|\hat{\psi}(\omega)|^2}{|\omega|} \mathrm{d}\omega < +\infty \tag{E.1}$$

It means that function $\psi(x)$ has a zero mean and finite length (compact support)

$$\int_{-\infty}^{+\infty} \psi(x) \mathrm{d}x = 0 \tag{E.2}$$

The real or complex function $\psi(x)$ is used to create a family of wavelets $\psi_{u,s}(x)$, defined as

$$\psi_{u,s}(x) = \frac{1}{\sqrt{s}} \psi\left(\frac{x-u}{s}\right) \tag{E.3}$$

where real number $s$ and $u$ are the scale and translation parameters respectively. The family of wavelet functions is a dilated or stretched version of the mother wavelet $\psi(x)$.

For a given signal $f(x)$, where $x$ is time or space, the Continuous Wavelet Transform (CWT) is obtained integrating the product of the signal function and the wavelet function

$$Wf(u,s) = \frac{1}{\sqrt{s}} \int_{-\infty}^{+\infty} f(x) \psi^*\left(\frac{x-u}{s}\right) \mathrm{d}x \tag{E.4}$$

where $\psi^*(x)$ is the complex conjugate of the wavelet function. $Wf(u,s)$ is called the CWT coefficient for wavelet $\psi_{u,s}(x)$ and it measures the variation of the signal in the vicinity of $u$ whose size is proportional to $s$.

In detection of singularities of deflections, the vanishing moments has an important influence. A wavelet has $n$ vanishing moments if the following equation is carried out

$$\int_{-\infty}^{+\infty} x^k \psi(x) \mathrm{d}x = 0, \quad k = 0,1,2,...,n-1 \tag{E.5}$$

Therefore, a wavelet with $n$ vanishing moments is orthogonal to polynomials of degree $n-1$.

## E.3 Static based crack identification problem

For a beam under some time invariant static loads, denote the static deflection difference of the beam between the damaged and undamaged states by $v$. It is known that the deflection difference $v$ is caused by the bending moment applied at the damage location [10, 19]. At the vicinity of the damage location, the cracks generate a region where the curvature of the beam changes rapidly. In practice with discrete data, the problem can be transformed into identifying the discontinuities in the deflection difference measurements.

### E.3.1 Damage Locating index

If the deflection has a singularity at certain point $u$, that means it is not differentiable at $u$, then the CWT coefficient at that point will have locally maximum values (apex values) for every scale. Small scales provide higher resolution on locating singularities but is more sensitive to noise in practice while high scales are more robust to noise but provide lower location resolution. Hence, to maximize the information provided by different scales, a damage locating index (LI) defined as the sum of the normalized CWT coefficients at different scales is proposed (Eq. (E.6)). The CWT coefficient is normalized to its maximum value for each scale (Eq. (E.7)). The normalized CWT coefficient, $Wf_n$, gives the same weight to each scale in the summation. The potential damage location is taken where the local maximum value appears, i.e. $\partial \mathrm{LI}(u)/\partial u = 0$.

$$\mathrm{LI}(u) = \sum^{s} Wf_n(u,s) \tag{E.6}$$

$$Wf_n(u,s) = \frac{Wf(u,s)}{\max\limits_{u}(Wf(u,s))} \tag{E.7}$$

### E.3.2 Damage severity index

Mallat and Hwang [20] implies the connection between two indicators which can characterize the local regularity of functions, the wavelet transform and Lipschitz exponents. At the local maximum point, $u_0$, the wavelet coefficient satisfies

$$|Wf(u_0,s)| \leq As^{\alpha} \tag{E.8}$$

where $A$ is a constant and $\alpha$ is the Lipschitz exponent. By normalizing the wavelet transform coefficient at the damage location to its corresponding damaged bending moment, $M_0$, and taking the logarithmic value on both sides of the equation, one has

$$\log_2 \left| \frac{Wf(u_0,s)}{M_0} \right| \leq \log_2 \left( \frac{A}{M_0} \right) + \alpha \log_2(s) \tag{E.9}$$

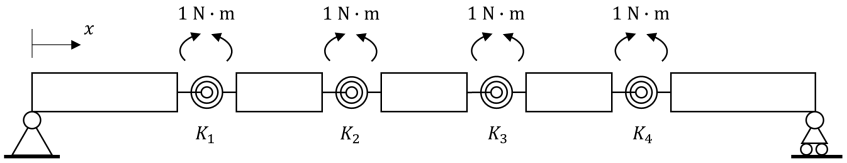


**Figure E.1** Sketch of the 1D beam model with four springs as damage.

**Table E.1** The target beam model information.

| Spring Label | 1 | 2 | 3 | 4 |
|---|---|---|---|---|
| Location, $x$ (mm) | 425 | 525 | 625 | 775 |
| Stiffness, $K$ (N·m/rad) | 2.00e$^7$ | 4.12e$^5$ | 1.73e$^5$ | 1.35e$^6$ |
| Severity[1] (%) | 10 | 35 | 50 | 20 |

[1]Crack depth to beam height ratio based on Ostachowicz's model[24]

**Table E.2** The Damage Index of the targeted damage.

| Spring Label | 1 | 2 | 3 | 4 |
|---|---|---|---|---|
| DI | −21.4 | −17.4 | −16.1 | −19.1 |

The damage index (DI) is taken as the y-axis interception

$$\mathrm{DI} = \log_2\left(\frac{A}{M_0}\right) \tag{E.10}$$

A reference correlation map between the crack depth and DI can be established through a numerical model and used for quantification purpose in practical applications.

### E.3.3 Numerical example

A simple numerical example of a simply supported beam is provided in this section to demonstrate the procedure of crack identification methodology. The crack-typed damage is idealized by a massless lumped rotational spring. The target beam modeled in ANSYS has a dimension of 1200 (length)) × 800 (width) × 20 (height) mm and Young's modulus $E = 210$ GPa. Four rotational springs with rotational stiffness $K_1$, $K_2$, $K_3$ and $K_4$, respectively, are used to model four cracks and their stiffness values are listed in Table E.1. Hereupon, all location notations are defined from the left end of the beam. For demonstration, the deflection different of the beam is generated by simultaneously implementing four pairs of unit self-equivalent bending moments on the springs respectively. The scheme of the beam is depicted in Fig. E.1.

A total number of 241 points are taken and the deflection is plotted in Fig. E.2(a). The wavelet analysis using Gaus2 wavelet is applied to the deflection difference. The scale is taken to be from 1 to 4. The normalized CWT coefficients $Wf_n$ at each scale are shown in Fig. E.2(b) and the damage locating index is shown in Fig. E.3(a). Locations where $\partial LI/\partial u = 0$ are associated with the damages at 425 mm, 525 mm 625 mm and 775 mm. At the damage locations, the linear relation between the local maximum CWT coefficients and the scales in logarithmic form can be seen clearly in Fig. E.3(b). The DI of each crack is obtained and listed in Table E.2.

A beam with the same dimension and material properties with a single spring situated at the midspan is used to establish the reference map to quantify the damage severity. The linear relation between the logarithmic wavelet coefficient and scales at the damage location of different severities

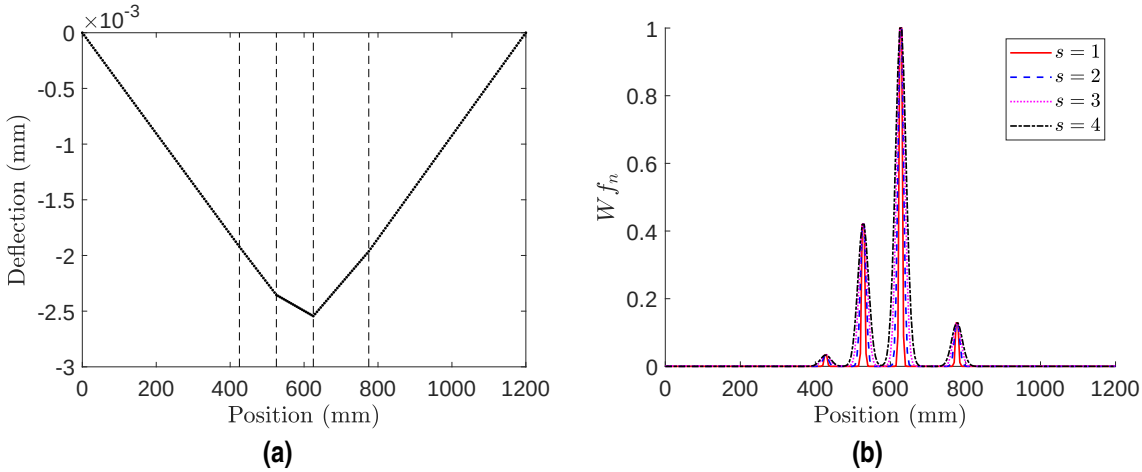


**Figure E.2** The target model: (a) deflection difference (red dash lines mark the damage locations); (b) the normalized wavelet transform coefficient of the beam.

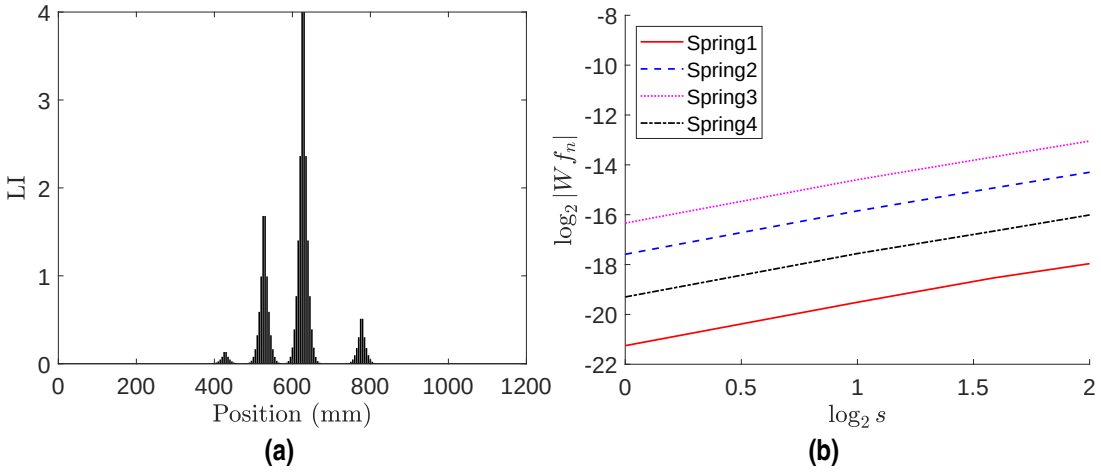


**Figure E.3** The target model: (a) the location index of the beam; (b) the CWT coefficients versus scales in logarithmic at damage locations.

**Table E.3** The reference values of Damage Index for different severities.

| Severity (%) | 10 | 20 | 35 | 50 |
|---|---|---|---|---|
| DI | −21.0 | −19.1 | −17.3 | −16.1 |

is shown in Fig. E.4. The DI of the reference model is listed in Table E.3. By matching the values in Table E.2 to the reference values in Table E.3, the crack severities can be accurately evaluated in noise free condition.

The is worthy to note that other mother wavelet can be use in place of Gaus2, though the selected one should be symmetrical and has a vanishing moment not less than 2 for statically determinate beams and 4 for statically indeterminate beams.

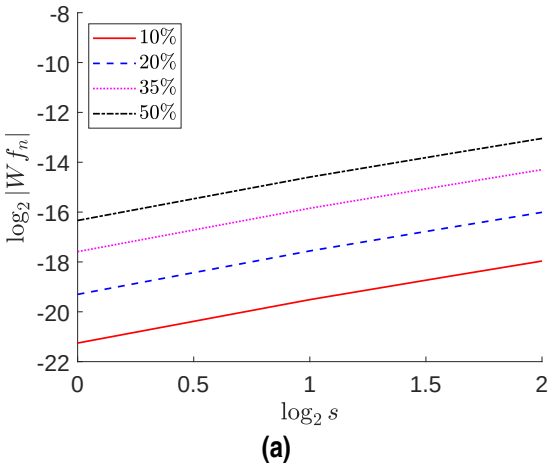


(a)

**Figure E.4** The CWT coefficients versus scales in logarithmic of various damage severities with spring located at 600 mm (reference model).

## E.4 Experimental tests

An experimental test of a simply supported beam was conducted to examined the performance of the methodology. The tested beam is 1200 mm long, 800 mm wide and 20 mm high. The material of the beam is steel with 210 GPa Young's modulus (Fig. E.5(a)). A concentrated load of 120 kg was hung at the bottom of the beam at 21 different equally distributed positions on the beam (Fig. E.5(b)). The sum of the deflections of all loads were used as the deflection base. An artificial notch crack was cut at 425 mm (Fig. E.5(c)). Two different severities were considered in the study, 20% (4 mm) and 50% (10 mm).

The deflections of the beam were measured by a Digital Imagine Correlation (DIC) system from GOM company (Fig. E.5(d)). The measurement target is a 10mm diameter black circle with a 5 mm diameter white circle in the center. The central point of the target was automatically determined by the Pontos system, part of the DIC system. For each test, 20 images were captured and the average values were taken as the target coordinates. To retain the merit of the DIC system, the whole side of the beam was covered by the targets which were placed in the forms of two lines. Both the deflections of the undamaged and damaged beams were measured. The deflection differences with crack of 20% and 50% are shown in Fig. E.6.

The deflection difference with 20% crack is about one tenth of the one with 50% crack. For static tests, the measurement noise effect is more severe for small damage than large severity. A denoising filter is applied to reduce the noise level.

### E.4.1 Noise filtering

Since the static deflection difference of a simply supported beam is linear outside of the damage region or piecewise linear in the spring model, a linear trend estimating tool named $l1$ Trend Filtering [15] is used for denoising purpose in practice. Previous studies [18, 19] have shown that the $l1$ Trend Filtering can efficiently and automatically determine the locations as well as the number of the kinks. The objective function to be minimized is

$$(1/2)\sum_{k=1}^{241}(v_k - v_k^{l1})^2 + \lambda \sum_{k=2}^{240} |v_{k-1}^{l1} - 2v_k^{l1} + v_{k+1}^{l1}| \tag{E.11}$$

where $v_k$ is the $k$th measurement and $v_k^{l1}$ is its estimate. $\lambda$ is a weighting parameter which controls the trade off between the size of the residual and the 'smoothness' of the estimate. It is obvious that

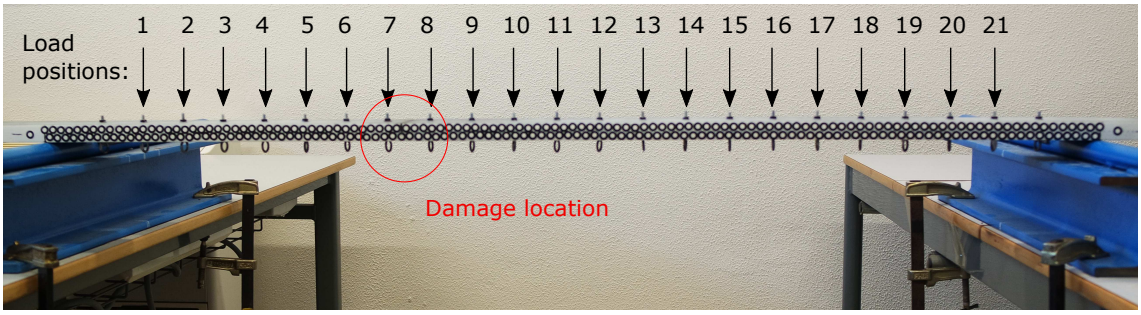


(a)

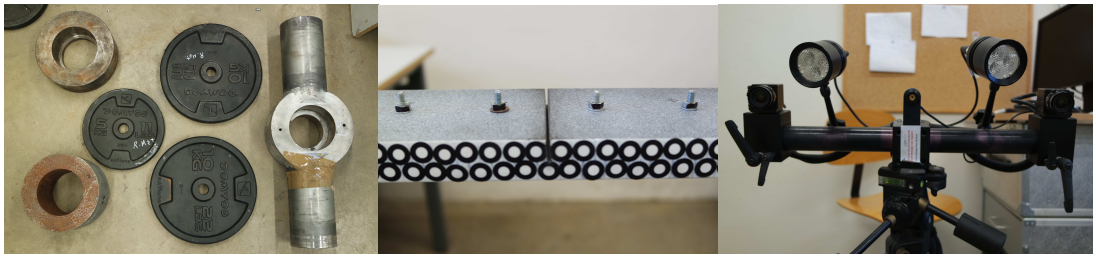

(b) (c) (d)

**Figure E.5** (a) The experimental beam with measuring points and load positions; (b) the concentrated load; (c) the artificial crack; (d) the camera of the DIC system.

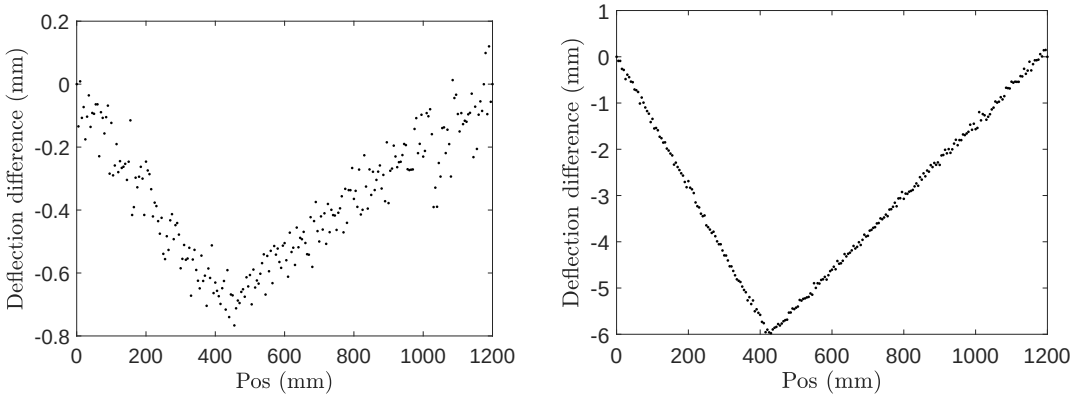


(a) (b)

**Figure E.6** The deflection difference of the damaged beam with (a) 20% (4 mm) crack; (b) 50% (10 mm) crack.

as $\lambda$ changes from 0 to $\infty$, the estimate changes from the input data inself to its linear regression fit ultimately. The size of the residual $(v_k - v_k^{l1})^2$ increases with respect to $\lambda$. Therefore, the selection of $\lambda$ is essential in this denoising process. If $\lambda$ is too small, the estimate is overfitted while if $\lambda$ is too high, the estimate becomes underfitted. There exists a range of $\lambda$ values where the estimates can be considered valid, which is named the optimal range of $\lambda$.

To evaluate the reliability of the estimates for each $\lambda$, the norm of the residual ($R$), between the estimate and the data, measured by Eq. (E.12) and the change rate of $R$ with respect to $\lambda$ ($\mathrm{d}R/\mathrm{d}\lambda$) calculated by Eq. (E.13) are used, where $i = 1,2,\cdots,n$. By trying a series of $\lambda$ values, the norms of the residual as well as its change rate are plot in Fig. E.7.

$$R = ||v_k - v_k^{l1}|| \tag{E.12}$$

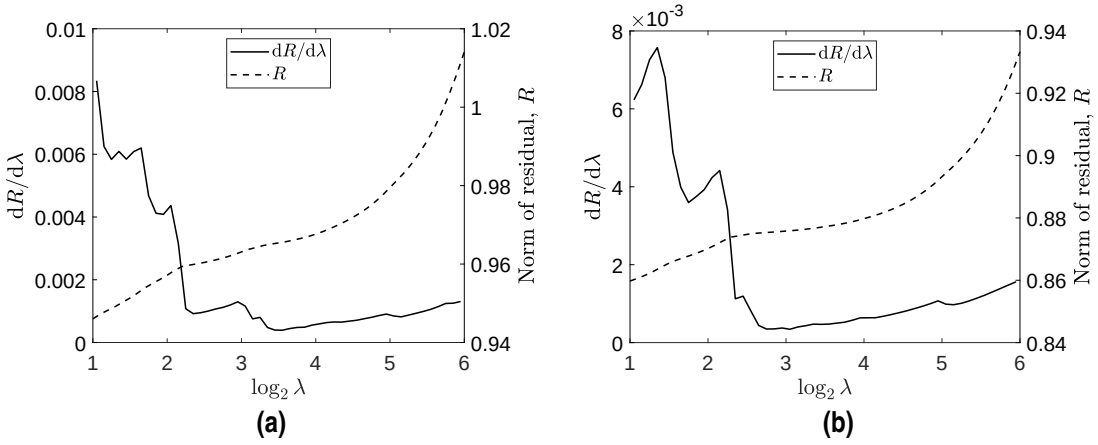


**Figure E.7** The norms of the residuals and their change rates of the beam with (a) 20% (4 mm) crack; (b) 50% (10 mm) crack.

**Table E.4** The optimal region of $\lambda$.

| Damage Severity (%) | Lower bound $\lambda_L$ | Upper bound $\lambda_H$ |
|---|---|---|
| 20% | 11 | 64 |
| 50% | 8 | 56 |

$$\frac{\mathrm{d}R}{\mathrm{d}\lambda} \approx \frac{R(\lambda_{i+1}) - R(\lambda_i)}{\lambda_{i+1} - \lambda_i} \tag{E.13}$$

It can be seen that as $\lambda$ increases from 2 ($2^1$) to 64 ($2^6$), the norm of the residual rises up at a relative fast pace but the change rate quickly drops down. The change rate reaches to the minimum at $\lambda = 13$ for 20% damage (Fig. E.7(a)) and at $\lambda = 9$ for 50% damage (Fig. E.7(b)). As $\lambda$ gets higher, the change rate increases slowly, which means that the estimate is less sensitive to the change of $\lambda$. Therefore, the $\lambda$ value correponding to the minimum point in the change rate is taken as the lower bound of the optimal region, $\lambda_L$ and estimates based on $\lambda$ values smaller than $\lambda_L$ are considered overfitted. However, there is no clear point on the chart that reveals at which point the underfitting occurs. Intuitively, the norm of the residual is a good standard to determine the point where underfitting occurs. In this case study, it is found that by keeping the norm of residual $R(\lambda)$ below $1.05R(\lambda_L)$ can prevent underfitting. Hence, the corresponding value of $\lambda$ is taken as the upper bound, $\lambda_H$. The lower and upper bound values of $\lambda$ for the two experimental cases are listed in Table E.4. The corresponding $l1$ Trend Filtering results are shown in Fig. E.8. Estimates with $\lambda$ values within this optimal range can be considered valid.

### E.4.2 Crack localization results

The $l1$ Trend Filtering leads to different kinks numbers and positions with different $\lambda$ values. For the experimental study, all integer values of $\lambda$ within the optimal range were taken into account. Therefore, the locating index (LI) in Eq. (E.6) should be written as

$$\mathrm{LI}^*(u) = \sum_{i=1}^{n} \left[ \sum_{j=1}^{m} W f_n(u, s_j) \right]_{\lambda_i} \tag{E.14}$$

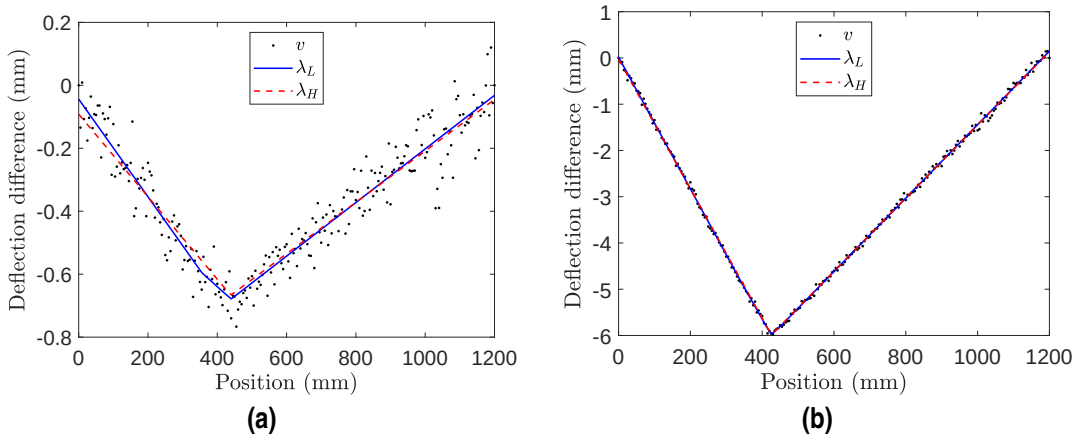


**Figure E.8** The $l1$ Trend Filtering estimates with lower and upper bond $\lambda$ values (a) 20% (4 mm) crack; (b) 50% (10 mm) crack.

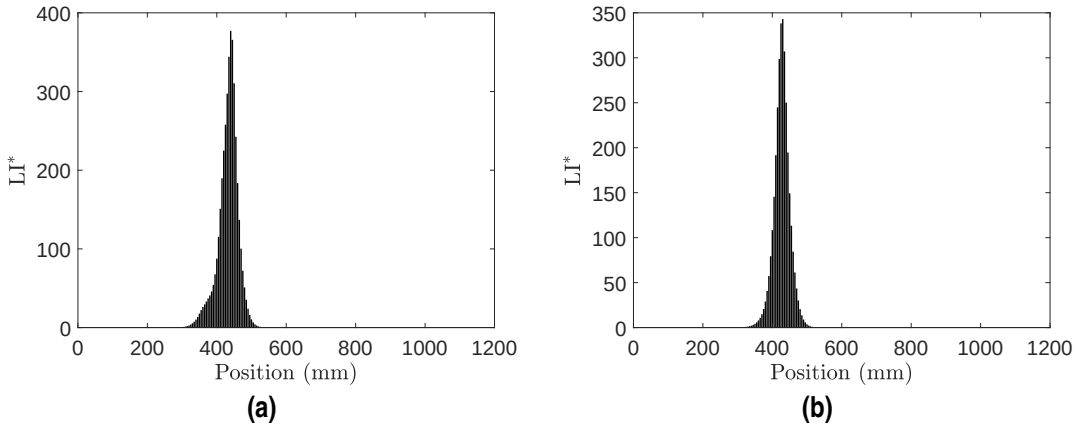


**Figure E.9** The Locating Index (LI$^*$) of the beam with (a) 20% (4 mm) crack; (b) 50% (10 mm) crack (the actual crack is situated at 425 mm).

where $n$ is the number of $\lambda$ ($n = 51$) and $m$ is the number of scales used in the wavelet transform. In this experimental study, the scales are taken from 2 to 8 ($m = 7$). From the damage locating index ($LI^*$) in Fig. E.9, the damage locations associated with $\partial LI^*/\partial u = 0$ are predicted at 440 mm for the beam with 20% crack and at 430 mm for the beam with 50% crack. In both cases, the damage location is accurately found.

### E.4.3 Crack quantification results

A 3D numerical model beam of the same dimension was built in ANSYS with the same material properties in order to establish the DI to crack depth correlation. In this model, the load is applied at 500 mm and the crack is set at 725 mm. The measurement points are taken at the same locations as in the experimental test. The reference DI values of crack severities from 5% to 60% are obtained (Fig. E.10).

The damage indices at the predicted location can be obtain for all evaluated $\lambda$ values. The corresponding crack severities can be assessed with the reference map. The average crack depth values of all considered $\lambda$ are listed in Table E.5. The estimate crack depth of 20% is 1.0 mm lower than the actual crack depth while the prediction of 50% is 0.5 mm lower than the actual value.

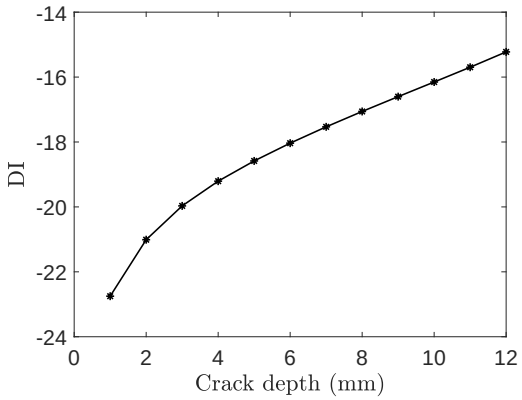


**Figure E.10** The Damage Index (DI) reference map of the beam.

**Table E.5** The estimated crack depths of the experimental tests.

| Damage Severity (%) | 20% | 50% |
|---|---|---|
| Crack depth (mm) | 3.0 | 9.5 |
| Actual depth (mm) | 4.0 | 10.0 |

## E.5 Conclusion

This paper addresses the issue of crack identification in beams using static deflection measurements. A new damage locating index as well as an location independent damage severity index based on the wavelet analysis are presented. In practice, an effective trend estimating tool is applied to reduce the noise influence. A practical guide of the application of this tool is presented. The experimental results shows that the proposed methodology can accurately locate both low severe crack and high severe crack. It is worthy to note that the proposed methodology can be applied to identify multiple cracks scenarios.

## Acknowledgments

This work was supported by the Consejería de Economía, Innovación, Ciencia y Empleo of Andalucía (Spain) under project P12-TEP-2546 and the Spanish Ministry of Economy and Competitiveness (Ministerio de Economía y Competitividad, Secretaría de Estado de Investigación, Desarrollo e Innovación) through research project BIA2016-43085-P. The financial support is gratefully acknowledged.

## References

[1] Andreaus, U., Baragatti, P., Casini, P., and Iacoviello, D. Experimental damage evaluation of open and fatigue cracks of multi-cracked beams by using wavelet transform of static response via image analysis. *Struct. Control Heal. Monit. 24*, 4 (2017), 1–16.

[2] Andreaus, U., and Casini, P. Identification of multiple open and fatigue cracks in beam-like structures using wavelets on deflection signals. *Contin. Mech. Thermodyn. 28*, 1-2 (2016), 361–378.

[3] Cao, M., Radzieński, M., Xu, W., and Ostachowicz, W. Identification of multiple damage in beams based on robust curvature mode shapes. *Mech. Syst. Signal Process. 46*, 2 (2014), 468–480.

[4] Cao, M. S., Xu, W., Ren, W. X., Ostachowicz, W., Sha, G. G., and Pan, L. X. A concept of complex-wavelet modal curvature for detecting multiple cracks in beams under noisy conditions. *Mech. Syst. Signal Process. 76-77* (2016), 555–575.

[5] Castro, E., García-Hernandez, M. T., and Gallego, A. Damage detection in rods by means of the wavelet analysis of vibrations: Influence of the mode order. *J. Sound Vib. 296*, 4-5 (2006), 1028–1038.

[6] Chang, C. C., and Chen, L. W. Detection of the location and size of cracks in the multiple cracked beam by spatial wavelet based approach. *Mech. Syst. Signal Process. 19*, 1 (2005), 139–155.

[7] Douka, E., Loutridis, S., and Trochidis, A. Crack identification in beams using wavelet analysis. *Int. J. Solids Struct. 40*, 13-14 (2003), 3557–3569.

[8] Gentile, A., and Messina, A. On the continuous wavelet transforms applied to discrete vibrational data for detecting open cracks in damaged beams. *Int. J. Solids Struct. 40*, 2 (2003), 295–315.

[9] Ghanbari Mardasi, A., Wu, N., and Wu, C. Experimental study on the crack detection with optimized spatial wavelet analysis and windowing. *Mech. Syst. Signal Process. 104* (2018), 619–630.

[10] Gudmundson, P. The dynamic behaviour of slender structures with cross-sectional cracks. *J. Mech. Phys. Solids 31*, 4 (1983), 329–345.

[11] Hong, J. C., Kim, Y. Y., Lee, H. C., and Lee, Y. W. Damage detection using the Lipschitz exponent estimated by the wavelet transform: Applications to vibration modes of a beam. *Int. J. Solids Struct. 39*, 7 (2002), 1803–1816.

[12] Janeliukstis, R., Rucevskis, S., Wesolowski, M., and Chate, A. Experimental structural damage localization in beam structure using spatial continuous wavelet transform and mode shape curvature methods. *Meas. J. Int. Meas. Confed. 102* (2017), 253–270.

[13] Janeliukstis, R., Rucevskis, S., Wesolowski, M., and Chate, A. Multiple damage identification in beam structure based on wavelet transform. *Procedia Eng. 172* (2017), 426–432.

[14] Jiang, X., Ma, Z. J., and Ren, W.-X. Crack detection from the slope of the mode shape using complex continuous wavelet transform. *Comput. Civ. Infrastruct. Eng. 27*, 3 (2012), 187–201.

[15] Kim, S.-J., Koh, K., Boyd, S., and Gorinevsky, D. l1Trend Filtering*. *SIAM Rev. 51*, 2 (2009), 339–360.

[16] Liew, K. M., and Wang, Q. Application of wavelet theory for crack identification in structures. *J. Eng. Mech. 124*, 2 (1998), 152–157.

[17] Loutridis, S., Douka, E., and Trochidis, A. Crack identification in double-cracked beams using wavelet analysis. *J. Sound Vib. 277*, 4-5 (2004), 1025–1039.

[18] Ma, Q., and Solís, M. Damage localization and quantification in simply supported beams using static test data. *J. Phys. Conf. Ser. 842* (2017), 012007.

[19] Ma, Q., and Solís, M. Damage localization and quantification in beams from slope discontinuities in static deflections. *Smart Struct. Syst. 22*, 3 (2018), 291–302.

[20] Mallat, S., and Hwang, W. L. Singularity detection and processing with wavelets. *IEEE Trans. Inf. Theory 38*, 2 (1992), 617–643.

[21] Messina, A. Detecting damage in beams through digital differentiator filters and continuous wavelet transforms. *J. Sound Vib. 272*, 1-2 (2004), 385–412.

[22] Messina, A. Refinements of damage detection methods based on wavelet analysis of dynamical shapes. *Int. J. Solids Struct. 45*, 14-15 (2008), 4068–4097.

[23] Montanari, L., Basu, B., Spagnoli, A., and Broderick, B. M. A padding method to reduce edge effects for enhanced damage identification using wavelet analysis. *Mech. Syst. Signal Process. 52-53*, 1 (2015), 264–277.

[24] Ostachowicz, W. M., and Krawczuk, M. Analysis of the effect of cracks on the natural frequencies of a cantilever beam. *J. Sound Vib. 150*, 2 (1991), 191–201.

[25] Pakrashi, V., Basu, B., and O' Connor, A. Structural damage detection and calibration using a wavelet-kurtosis technique. *Eng. Struct. 29*, 9 (2007), 2097–2108.

[26] Pakrashi, V., O'Connor, A., and Basu, B. A study on the effects of damage models and wavelet bases for damage identification and calibration in beams. *Comput. Civ. Infrastruct. Eng. 22*, 8 (2007), 555–569.

[27] Quek, S. T., Wang, Q., Zhang, L., and Ang, K. K. Sensitivity analysis of crack detection in beams by wavelet technique. *Int. J. Mech. Sci. 43*, 12 (2001), 2899–2910.

[28] Quek, S. T., Wang, Q., Zhang, L., and Ong, K. H. Practical issues in the detection of damage in beams using wavelet. *Smart Mater. Struct 10* (2001), 1009–1017.

[29] Rucka, M., and Wilde, K. Application of continuous wavelet transform in vibration based damage detection method for beams and plates. *J. Sound Vib. 297* (2006), 536–550.

[30] Rucka, M., and Wilde, K. Crack identification using wavelets on experimental static deflection profiles. *Eng. Struct. 28* (2006), 279–288.

[31] Solís, M., Algaba, M., and Galvín, P. Continuous wavelet analysis of mode shapes differences for damage detection. *Mech. Syst. Signal Process. 40*, 2 (2013), 645–666.

[32] Solís, M., Ma, Q., and Galvín, P. Damage detection in beams from modal and wavelet analysis using a stationary roving mass and noise estimation. *Strain 54* (2018), e12266.

[33] Spanos, P. D., Failla, G., Santini, A., and Pappatico, M. Damage detection in Euler-Bernoulli beams via spatial wavelet analysis. *Struct. Control Heal. Monit. 13*, 1 (2006), 472–487.

[34] Surace, C., and Ruotolo, R. Crack detection of a beam using the wavelet transform. *Proc. 12th Int. Modal Anal. Conf.* (1994), 1141–1167.

[35] Swamy, S., Reddy, D. M., and Prakash G, J. Damage detection and identification in beam structure using modal data and wavelets. *World J. Model. Simul. 13*, 1 (2017), 52–65.

[36] Umesha, P., Ravichandran, R., and Sivasubramanian, K. Crack detection and quantification in beams using wavelets. *Comput. Civ. Infrastruct. Eng. 24*, 8 (2009), 593–607.

[37] Wang, Q., and Deng, X. Damage detection with spatial wavelets. *Int. J. Solids Struct. 36*, 23 (1999), 3443–3468.

[38] Wu, N., and Wang, Q. Experimental studies on damage detection of beam structures with wavelet transform. *Int. J. Eng. Sci. 49*, 3 (2011), 253–261.

[39] Xu, Y. F., Zhu, W. D., Liu, J., and Shao, Y. M. Identification of embedded horizontal cracks in beams using measured mode shapes. *J. Sound Vib. 333*, 23 (2014), 6273–6294.

[40] Zhong, S., and Oyadiji, S. O. Detection of cracks in simply-supported beams by continuous wavelet transform of reconstructed modal data. *Comput. Struct. 89*, 1-2 (2011), 127–148.

[41] Zhu, L.-f., Ke, L.-l., Zhu, X.-q., Xiang, Y., and Wang, Y.-s. Crack identification of functionally graded beams using continuous wavelet transform. *Compos. Struct.* (2018).

[42] Zhu, X. Q., and Law, S. S. Wavelet-based crack identification of bridge beam from operational deflection time history. *Int. J. Solids Struct. 43*, 7-8 (2006), 2299–2317.

# Appendix F
# Static measurements

In this appendix, the measurement results of Experimental 1, the sum of the deflections over all load positions and their difference are plotted in Figs. F.1-F.4.

**Figure F.1** contains the measurement results of single damage scenario;

**Figure F.2** contains the measurement results of double damage scenario;

**Figure F.3** contains the measurement results of triple damage scenario;

**Figure F.4** contains the measurement results of quadruple damage scenario;

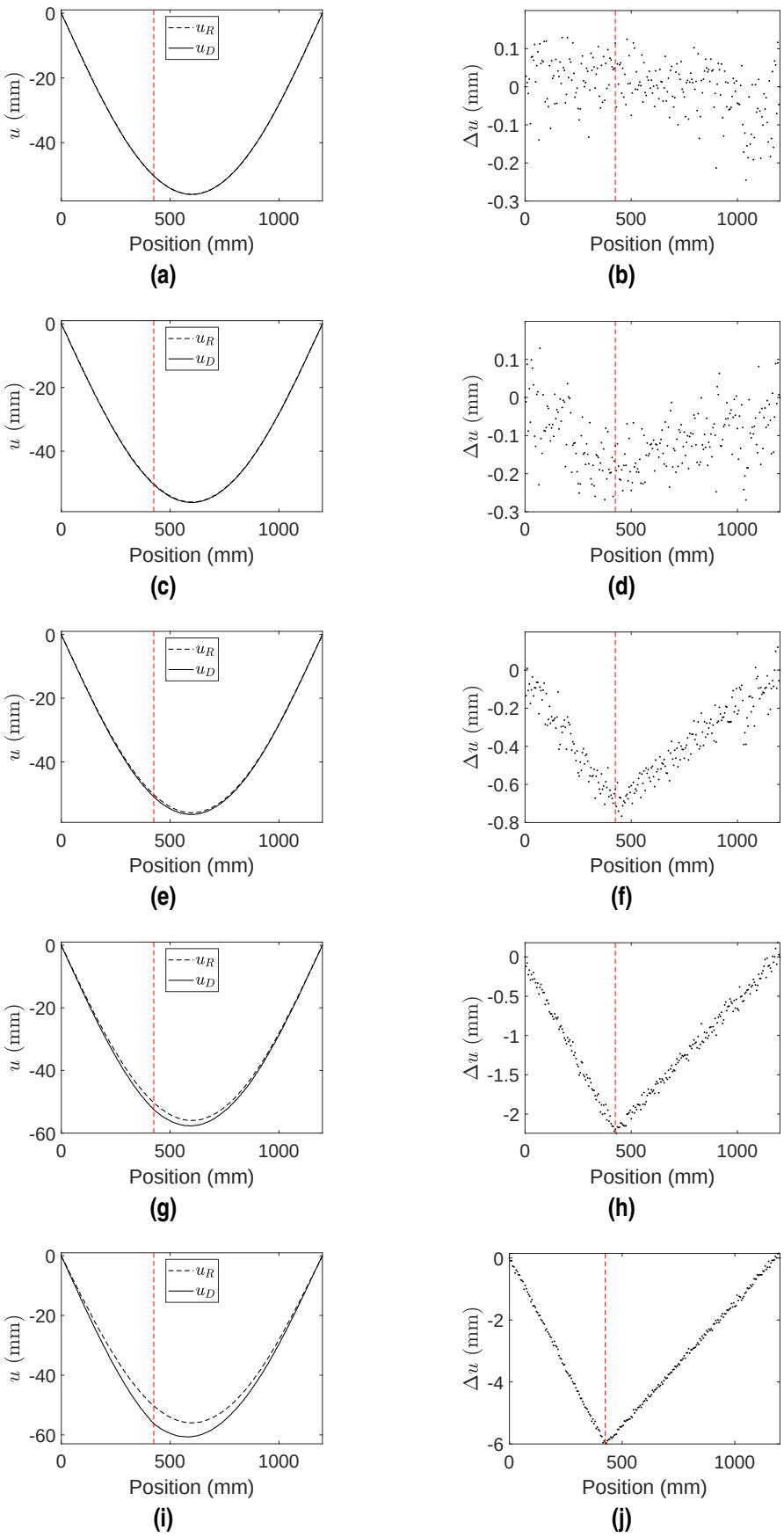


**Figure F.1** The deflection at State R ($u_R$) and State D ($u_D$): (a) Case 1.5; (c) Case 1.10; (e) Case 1.20; (g) Case 1.35; (i) Case 1.50; the deflection difference ($\Delta u$): (b) Case 1.5; (d) Case 1.10; (f) Case 1.20; (h) Case 1.35; (j) Case 1.50 (the red dashed line marks the crack location).

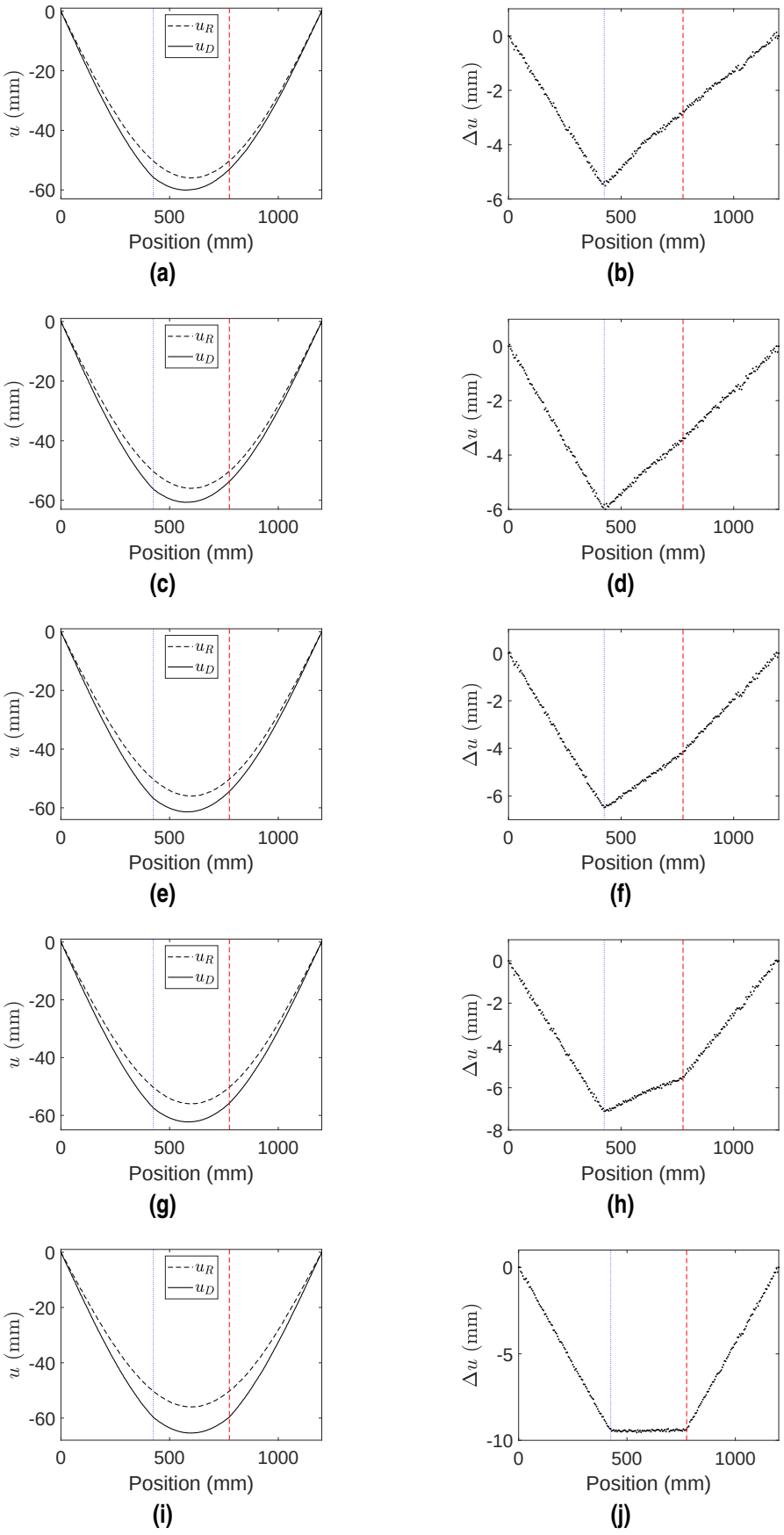


**Figure F.2** The deflection of the beam at State R ($u_R$) and State D ($u_D$): (a) Case 2.1; (c) Case 2.2; (e) Case 2.3; (g) Case 2.4; (i) Case 2.5; the deflection difference ($\Delta u$): (b) Case 2.1; (d) Case 2.2; (f) Case 2.3; (h) Case 2.4; (j) Case 2.5 (the red dashed line marks the latest crack and the blue dotted lines mark the 50% cracks).

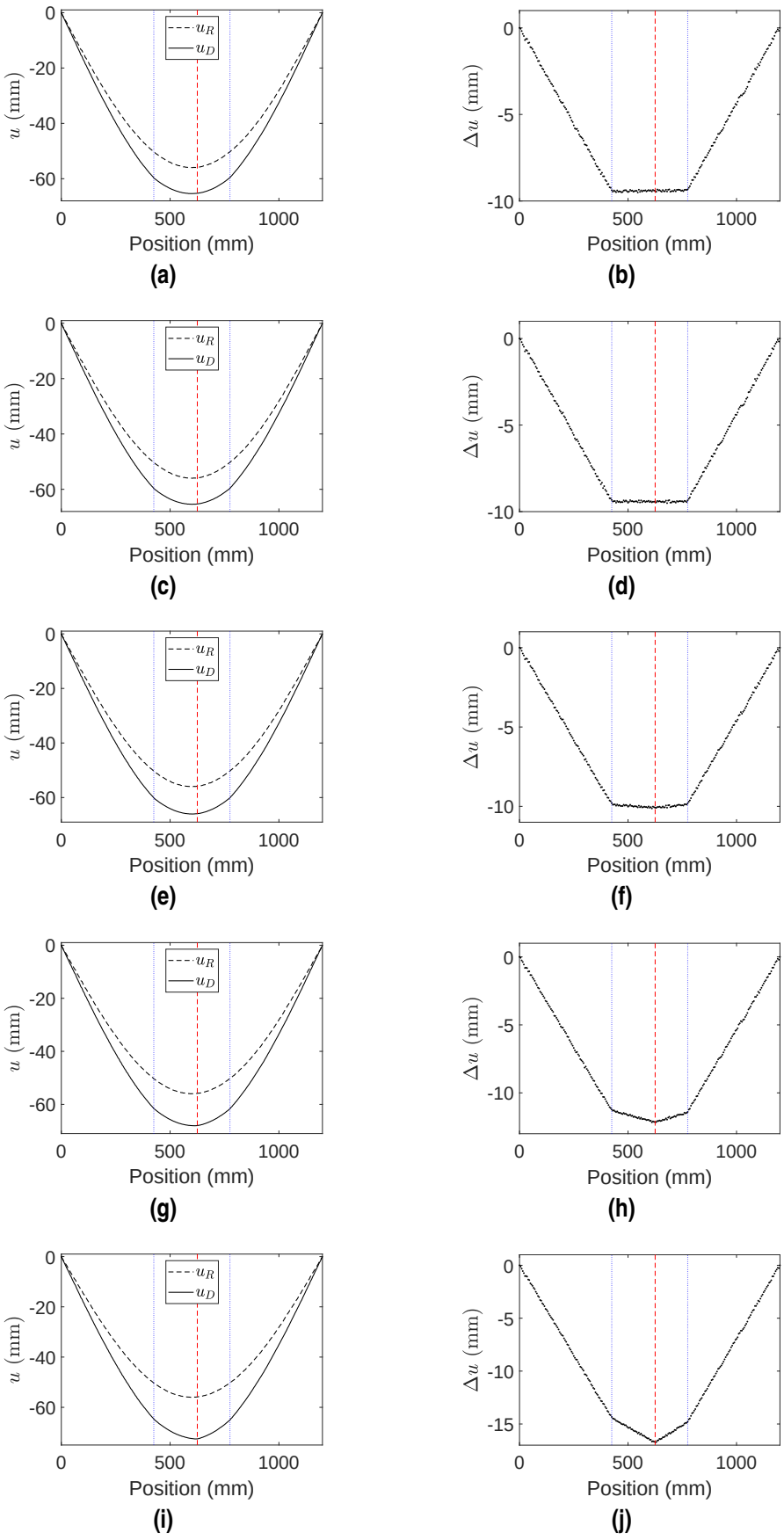


**Figure F.3** The deflection of the beam at State R ($u_R$) and State D ($u_D$): (a) Case 2.1; (c) Case 2.2; (e) Case 2.3; (g) Case 2.4; (i) Case 2.5; the deflection difference ($\Delta u$): (b) Case 2.1; (d) Case 2.2; (f) Case 2.3; (h) Case 2.4; (j) Case 2.5 (the red dashed line marks the latest crack and the blue dotted lines mark the 50% cracks).

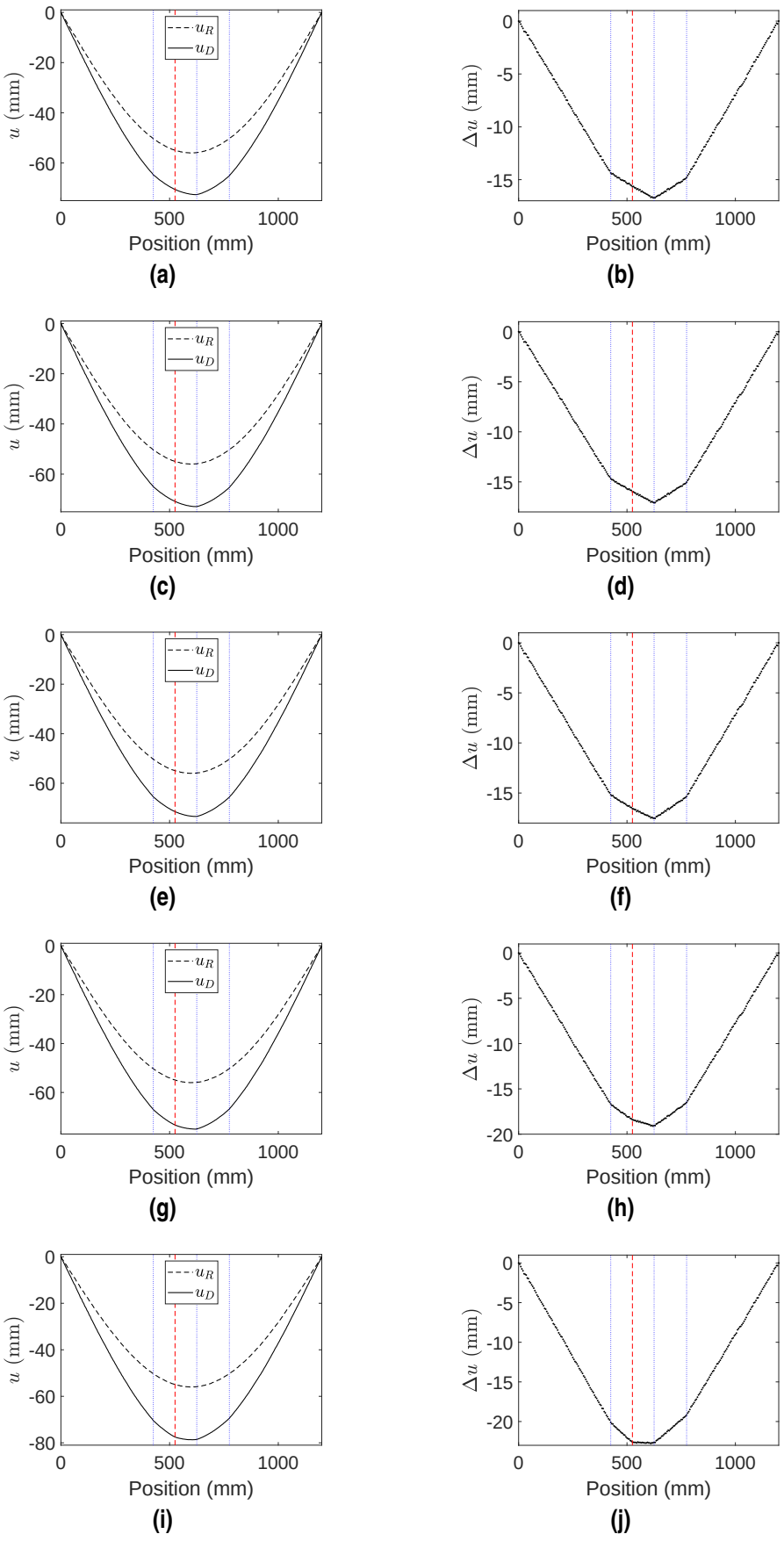


**Figure F.4** The deflection of the beam at State R ($u_R$) and State D ($u_D$): (a) Case 2.1; (c) Case 2.2; (e) Case 2.3; (g) Case 2.4; (i) Case 2.5; the deflection difference ($\Delta u$): (b) Case 2.1; (d) Case 2.2; (f) Case 2.3; (h) Case 2.4; (j) Case 2.5 (the red dashed line marks the latest crack and the blue dotted lines mark the 50% cracks).

# Appendix G
# Errata and corrigenda

In the published Paper B, Paper C and Paper D, the authors mistook the width of the test beam as 100 mm. This mistake produces no influence on the localization results but have some little effects on the quantification results. The changes in the damage severity estimates do not affect the conclusions draw in the papers. The authors sincerely apologize for the inconvenience and any potential harm to the reputation of the journals.

In the authors' opinion, this error would not undermine the scientific integrity of the published papers. Nevertheless, the authors recognize their responsibility to ensure the scientific accuracy of the published information. Therefore, the correction of the corresponding tables and figures are provided in this Appendix.

## G.1 Paper B

- **Ma, Q.** and Solís, M. (2017). "Damage localization and quantification in simple supported beams using static test data", *Journal of Physics: Conference Series* 842 012007

**Table 10** Estimated damage location and severity and their errors.

| | | Localization | | Quantification | | |
|---|---|---|---|---|---|---|
| Loading Position | Measuring Point | Location (mm) | Deviation (mm) | Severity (mm) | Error (mm) | Error (%) |
| 1 | 85 | 415 | 5 | 6.8 | 0.2 | 3 |
| 2 | 89 | 440 | 15 | 7.0 | 0.0 | 0 |
| 3 | 89 | 440 | 15 | 7.1 | 0.1 | 1 |
| 4 | 88 | 435 | 10 | 7.2 | 0.2 | 3 |
| 5 | 88 | 435 | 10 | 7.1 | 0.1 | 1 |
| 6 | 88 | 435 | 10 | 7.1 | 0.1 | 1 |
| 7 | 86 | 425 | 0 | 7.1 | 0.1 | 1 |
| 8 | 86 | 425 | 0 | 7.1 | 0.1 | 1 |
| 9 | 87 | 430 | 5 | 7.1 | 0.1 | 1 |
| 10 | 85 | 415 | 5 | 7.2 | 0.2 | 3 |
| 11 | 87 | 430 | 5 | 7.1 | 0.1 | 1 |
| 12 | 87 | 430 | 5 | 7.0 | 0.0 | 0 |
| 13 | 87 | 430 | 5 | 7.1 | 0.1 | 1 |
| 14 | 87 | 430 | 5 | 7.2 | 0.2 | 3 |
| 15 | 89 | 440 | 15 | 7.0 | 0.0 | 0 |
| 16 | 87 | 430 | 5 | 7.3 | 0.3 | 4 |
| 17 | 91 | 450 | 25 | 7.1 | 0.1 | 1 |
| 18 | 89 | 440 | 15 | 7.1 | 0.1 | 1 |
| 19 | 90 | 445 | 20 | 7.2 | 0.2 | 3 |
| 20 | 93 | 460 | 35 | 7.0 | 0.0 | 0 |
| 21 | 87 | 430 | 5 | 7.0 | 0.0 | 0 |

## G.2 Paper C

- **Ma, Q.** and Solís, M. (2018). "Damage localization and quantification in beams from slope discontinuities in static deflections", *Smart Structures and Systems*, 22(3):291-302.

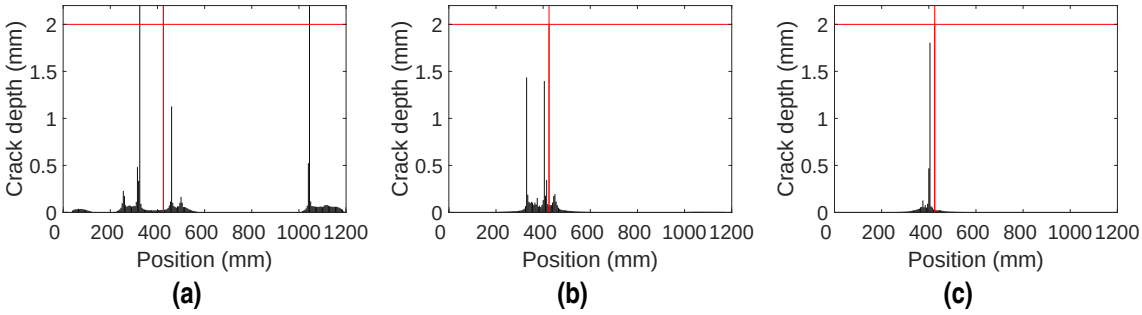


**Figure 10** Results of estimated crack depth for 10% damage with different $\lambda$: (a) Case 1; (b) Case 2; (c) Case 3. (The red lines mark the actual crack depth and the actual crack location).

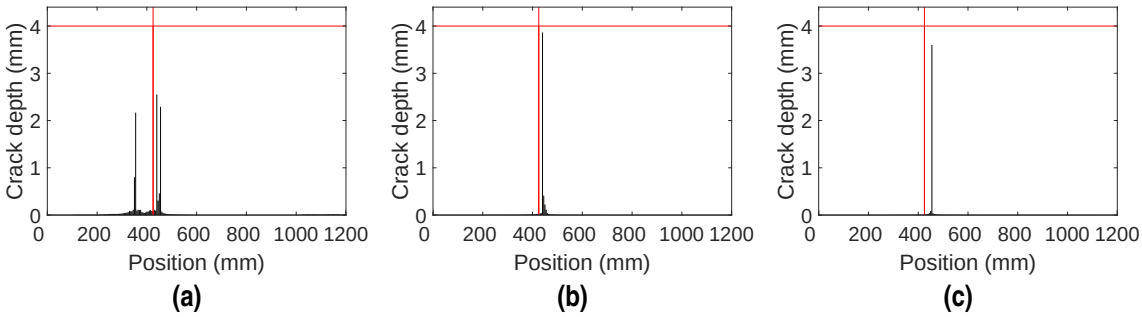


**Figure 12** Results of estimated crack depth for 20% damage with different $\lambda$: (a) Case 1; (b) Case 2; (c) Case 3. (The red lines mark the actual crack depth and the actual crack location).

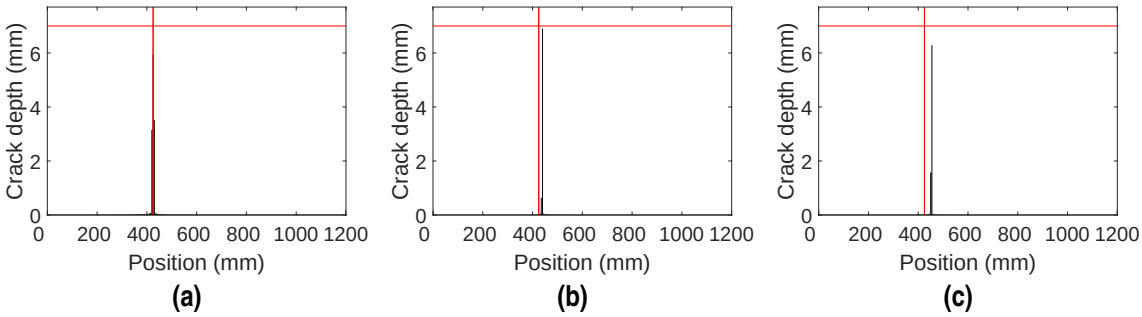


**Figure 14** Results of estimated crack depth for 35% damage with different $\lambda$: (a) Case 1; (b) Case 2; (c) Case 3. (The red lines mark the actual crack depth and the actual crack location).

**Table 4** Summary of closest prediction for all damage severities.

| Damage severity (%) | $\lambda$ | Predicted locations (mm) | Estimated depth (mm) |
|---|---|---|---|
| 10 | Case 3 | 405 | 1.80 |
| 20 | Case 2 | 440 | 3.86 |
| 35 | Case 1 | 425 | 5.93 |

## G.3 Paper D

- **Ma, Q.** and Solís, M. (accepted). "Multiple damage identification in beams from full-field digital photogrammetry", *Journal of Engineering Mechanics.*

**Table 4** Predicted damage depths (mm).

| Case | Actual depth (mm) | Rotational model | | | | |
|---|---|---|---|---|---|---|
| | | $J_R$ | $J_O$ | $J_C$ | $J_F$ | $J_B$ |
| 1 | 10 | 9.6 | 8.9 | 9.1 | 8.8 | 8.7 |
| | 4 | 3.8 | 3.4 | 3.6 | 3.4 | 2.2 |
| 2 | 10 | 8.4 | 7.6 | 7.9 | 7.7 | 7.3 |
| | 10 | 9.1 | 8.3 | 8.5 | 8.3 | 8.1 |
| 3 | 10 | 9.7 | 8.9 | 9.1 | 8.9 | 8.8 |
| | 10 | 8.4 | 7.5 | 7.8 | 7.7 | 7.2 |
| | 4 | 3.0 | 2.6 | 2.8 | 2.7 | 1.5 |
| 4 | 10 | 9.1 | 8.3 | 8.6 | 8.4 | 8.1 |
| | 10 | 9.3 | 8.5 | 8.7 | 8.5 | 8.3 |
| | 10 | 8.3 | 7.5 | 7.8 | 7.6 | 7.2 |
| 5 | 10 | 10.3 | 9.6 | 9.7 | 9.5 | 9.5 |
| | 10 | 8.5 | 7.7 | 8.0 | 7.8 | 7.5 |
| | 10 | 9.6 | 8.9 | 9.1 | 8.9 | 8.7 |
| | 4 | 3.5 | 3.1 | 3.2 | 3.1 | 1.9 |
| 6 | 10 | 9.6 | 8.9 | 9.1 | 8.9 | 8.7 |
| | 10 | 8.7 | 7.9 | 8.2 | 8.0 | 7.7 |
| | 10 | 7.9 | 7.1 | 7.4 | 7.2 | 6.7 |
| | 10 | 10.3 | 9.6 | 9.7 | 9.5 | 9.5 |

.